UNIVERSIDAD DE GRANADA

Metodología y validación experimental para el estudio de la influencia de los rellenos en el comportamiento sísmico de pórticos

By:

José Barros Cabezas

PROGRAMA DE DOCTORADO EN INGENIERÍA CIVIL

A thesis submitted in partial fulfillment of the requirements for the degree of Doctor of Philosophy

Advisors:

Dr. Manuel Chiachío Ruano

Dr. Leandro Morillas Romero

Department of Structural Mechanics & Hydraulic Engineering

University of Granada

Granada (Spain)

February 2023

Editor: Universidad de Granada. Tesis Doctorales
Autor: José barros cabeza
ISBN: 978-84-1117-788-7
URI: https://hdl.handle.net/10481/81242

Summary

Nowadays, one of the most widely used structural building systems consists of masonry infilled frames, in which the walls are intended to protect the interior of the building from environmental conditions. The construction of these walls is well known by practitioners and have been attractive for their low cost and ability to isolate different environments of a building. In most cases, the aforementioned walls are considered as non-structural elements; however, the observation made on the behaviour of this type of structures, especially after the occurrence of seismic events, has shown that these elements have an effective collaboration with the rest of the structure.

The structural system of masonry infilled frames has a large number of variables which condition its behaviour. Among the most influential variables we can mention: (1) the masonry units: the variety of materials used, the different forms of manufacture, quality and geometry, (2) the bonding mortar between masonry units: the different materials and dosages used and the bonding quality achieved between the masonry units, (3) the bonding quality between the wall and the portal frame: the existence of stress transfer elements or the direct interaction of the mortar with the frame material, (4) the construction process and the expertise of the workmanship, (5) the interaction between the behaviour of the wall in and out of its plane, (6) the existence of openings (doors and/or windows) in the wall. The aforementioned variables constitute sources of uncertainty which imply difficulty when characterizing the seismic-resistant behaviour of this system.

The main objective of this thesis is to provide effective and cost-efficient tools to evaluate existing masonry infilled frame structures. In this sense, the use of probabilistic tools has been explored to propose techniques to predict the behaviour of infilled frame buildings with quantified uncertainty. First, the use of approximate Bayesian computational algorithms is studied to infer non-linear numerical modelling parameters of masonry infilled frames, taking as a reference the results of laboratory testing. An improvement to the original ABC-SubSim algorithm is proposed, for ease of use by autonomously estimating a series of meta-parameters that influence the speed of calculation and quality of the result. This new algorithm has been named $\mathcal{A}^2$*BC-SubSim*, and has been proven to achieve a balance between computational speed and result quality, after the solution of some numerical examples. The proposed algorithm has been applied to a Bayesian inference of multiple uncertain parameters from a non-linear

multi-story infilled frame model of a building, with high efficiency.

On the other hand, the application of neural networks to predict the constitutive behaviour of the structural system was also explored. A database of existing tests has been collected in order to train such networks; however, due to the limited number of tests available in the literature, it was chosen to work with Bayesian neural networks, which have the advantage of also providing information on the quality of the prediction made by quantification of the uncertainty. Additionally, up-to-date training methods of the Bayesian neural networks have been tested. The prediction capabilities of the trained network has been checked against measurements of laboratory tests that were not part of the training group, achieving acceptable results in terms of interpolation of unobserved data, and extrapolation to unknown data.

Finally, dedicated laboratory tests have been performed to study the relationship between the out-of-plane fundamental frequency of the wall versus the stiffness of the system in the plane of the wall. With the results of these tests and a parametric study using complex numerical models, a semi-empirical non-destructive methodology has been proposed to estimate the stiffness of existing masonry infilled frames. The methodology has been checked with measurements of specimens tested on a seismic table, demonstrating the feasibility of application of the proposed methodology for existing infilled frame structures whose actual seismic behaviour want to be updated.

Resumen

En la actualidad, uno de los sistemas estructurales de edificación más utilizados globalmente consiste en la construcción de pórticos cuyos espacios libres se rellenan con muros de fábrica (también conocidos como muros de tabiquería, de bloques, de ladrillos o de *mampostería*), que tienen el objetivo de proteger el interior de la edificación de las condiciones ambientales. La construcción de estos muros es bastante conocida por el sector constructivo y ha sido atractiva por su bajo costo y su capacidad para aislar distintos ambientes de una edificación. En la mayoría de los casos, las paredes mencionadas son consideradas como elementos no estructurales; sin embargo, la observación realizada sobre el comportamiento de este tipo de estructuras, especialmente tras la ocurrencia de eventos sísmicos, ha demostrado que estos elementos colaboran efectivamente con el resto de la estructura en soportar el evento.

Al considerar a los pórticos rellenos con paredes de mampostería como un sistema estructural, nos encontramos con un gran número de variables que condicionan su comportamiento, lo que ha complicado su caracterización. Entre las variables más influyentes se pueden mencionar: (1) las unidades de mampostería: la variedad de materiales que se utilizan, las distintas formas de fabricación, calidad y geometría, (2) el mortero de unión entre unidades de mampostería: los diversos materiales y dosificaciones que se utilizan y la calidad de unión que se consigue entre las unidades de mampostería , (3) la calidad de unión entre la pared y el pórtico: la existencia de elementos de transferencia de esfuerzos o la interacción directa del mortero con el material del pórtico, (4) el proceso construtivo y el expertise de la mano de obra, (5) la interacción entre el comportamiento de la pared en y fuera de su plano, (6) la existencia de aberturas (puertas y/o ventanas) en la pared. Las mencionadas variables se constituyen en fuentes de incertidumbre que denotan la dificultad de caracterizar el comportamiento sismo-resistente de este sistema y, sobre todo, si esto se busca lograr con metodologías deterministas.

Esta tesis tiene como objetivo principal proporcionar herramientas para evaluar estructuras existentes de pórticos rellenos de mampostería. En ese sentido se ha explorado el uso de herramientas probabilistas para proponer técnicas que permitan predecir el comportamiento de edificaciones con este sistema estructural. En primer lugar, se estudia el uso de algoritmos de cálculo Bayesiano aproximado para inferir parámetros de modelación numérica no-lineal de los pórticos con paredes de mampostería, tomando como referencia los resultados de mediciones tomadas sobre especímenes de laboratorio. Se propone una mejora al algoritmo

ABC-SubSim, de manera que se facilita su uso al estimar de manera autónoma una serie de meta-parámetros que influyen en la velocidad de cálculo y calidad del resultado. Dicho nuevo algoritmo se ha denominado $\mathcal{A}^2$*BC-SubSim*, del cual se ha demostrado que permite conseguir un equilibrio entre la velocidad de cálculo y la calidad de resultado, tras la solución de algunos ejemplos numéricos. Por otro lado, también se exploró la aplicación de las redes neuronales para predecir el comportamiento constitutivo del sistema estructural, por lo que se elaboró una base de datos de ensayos existentes para poder entrenar dichas redes; sin embargo, por el limitado número de ensayos disponibles en la bibliografía, se optó por trabajar con redes neuronales Bayesianas, que tienen la ventaja de proporcionar información sobre la calidad de la predicción. La capacidad de predicción de la red entrenada se pone a prueba frente a mediciones de ensayos que no formaron parte del grupo de entrenamiento, logrando resultados prometedores.

Finalmente, se realizaron ensayos para estudiar la relación que existe entre la frecuencia fundamental de la pared fuera de su plano frente a la rigidez del sistema en el plano de la pared. Con los resultados de estos ensayos y un estudio paramétrico mediante modelos numéricos complejos, se ha propuesto una metodología semi-empírica y no destructiva para estimar la rigidez de pórticos rellenos de mampostería existentes. La metodología fue puesta a prueba con mediciones de especímenes instalados sobre una mesa sísmica, logrando demostrar la factibilidad de aplicación de la metodología propuesta.

Agradecimientos

Quisiera agradecer a mi director de mi Tesis, Dr. Manuel Chiachío Ruano, por el invaluable entrenamiento relacionado a la preparación y desarrollo de proyectos de investigación, por la dedicación, por la paciencia y por el buen ejemplo de la búsqueda de la excelencia; en particular, agradezco especialmente el hacerme parte del Laboratorio de Pronóstico Inteligente y Sistemas Estructurales Ciber-físicos, permitiéndome aprender mucho más de lo esperado de mano de los colegas y amigos. Agradezco también a mi co-director, Dr. Leandro Morillas, por compartir su amplia experiencia y conocimientos en la preparación y desarrollo de ensayos de laboratorio. A ambos les agradezco mucho por su gentileza y su muestra de amistad durante mis estancias en Granada.

Agradezco mucho a mi familia y, en especial, a mi esposa Antonieta y a mis hijos por su apoyo y paciencia durante este capítulo de nuestras vidas.

Agradezco al personal del laboratorio de estructuras de la Universidad de Granada, en particular a Santiago Díaz Osuna y a su equipo de trabajo por su labor en la fabricación, montaje y asistencia durante la campaña de ensayos en la mesa sísmica. Asímismo, agradezco a Carlos Alberto Vargas y a su equipo de trabajo en el laboratorio de estructuras de la Universidad Católica de Santiago de Guayaquil (UCSG), por compartir sus experiencias y por su esmerada colaboración durante la realización de los ensayos.

Agradezco a los ex-alumnos de la facultad de ingeniería de la UCSG, quienes contribuyeron en temas específicos que se presentan en esta investigación. Específicamente a: Frank Cabanilla, Joel Consuegra, David Suco, Bryan Coello y Sahara Hidalgo.

Agradezco al Dr. Walter Mera, al Dr. Antonio Marín y a la Dra. Irene Trelles por hacer posible el programa doctoral que he cursado. Este trabajo ha sido posible gracias al Programa de Formación Doctoral de la Universidad Católica de Santiago de Guayaquil, al proyecto SINDE Cod. Pres. # 491 y Cod. Int. # 170 *Influencia de las paredes de mampostería en estructuras de pórticos*, al apoyo del proyecto ENhANCE (`https://h2020-enhanceitn.eu/`) y el Seminario Permanente de Formación e Investigación en Ingeniería Civil UGR-UCSG.

Dedicatoria

A Dios y a la Virgen Auxiliadora, por sus innumerables bendiciones y por cuidar de mi y de mi familia.

A mi esposa Antonieta Katherine y a nuestros hijos Susana Esperanza, Isabel Aurora, Maximiliano Andrés, María De Los Ángeles y Catalina De Lourdes.

A mis padres Jorge Alberto y María Lorna, y a mis hermanos Jorge Antonio y María Lorna.

Contents

List of Figures

List of Tables

Part I

Introduction

Chapter 1

Context and motivation

Earthquake engineering is a well-established research topic that is in constant evolution. Design and construction of different structural systems have been adapted to correct the inadequate structural behaviour observed after the occurrence of seismic events. In the particular case of masonry infilled frame (MIF) structures, those masonry walls were usually considered as non-structural elements, and thus their stiffness was not taken into account during structural design. Considering the existence of a large number of buildings constructed with this structural system and criterion around the world and, particularly concerning, in areas subject to high seismic hazard, it is necessary to provide procedures to reliably assess the structural conditions of this kind of existing buildings. However, due to the occurrence of earthquakes around the world in the last decades (see Figure 1.1), it has been recognized that such walls significantly contribute to the dynamic response of buildings, and that this contribution can be either positive or negative.

Figure 1.1: World map showing seismic-prone countries where MIFs were mentioned in damage reports: Barbosa et al. (2017); Bennett et al. (1996); Fierro et al. (2011); Hak et al. (2018); Irfanoglu (2009); Kam et al. (2010); Kaushik et al. (2006); Maidiawati and Sanada (2017); Perrone et al. (2018); Tarque et al. (2015); Urich and Beauperthuy (2012); Villalobos et al. (2018).

Indeed, during the 2016 earthquake in Ecuador, specifically ocurred in Guayaquil city (200 km away from the epicenter), several mid-rise structures suffered severe damage on the masonry infills, as shown in the example of Figure 1.2. Clearly, the post-earthquake evaluation showed that the masonry wall contributed to the overall lateral shear strength of the building, avoiding a worst scenario. On the other hand, the masonry infill vertical irregular distribution along the height of a building may cause a neglected drift concentration in floors that usually have much less partitions than others, for example: main hallways, event rooms, ballrooms, among others. Figure 1.3 depicts one of such cases; in the right hand part of the figure it can be seen that the upper floors of the building remained undamaged after the event, whilst the ground level collapsed, showing that the lateral deformation was concentrated in that floor during the event, leading to this undesirable behaviour.

Figure 1.2: Broken wall of the sixth floor department from an eight story building, located in the center of Guayaquil city, after the seismic event of 2016.

Also, the presence of masonry infills may produce undesirable behaviour of the reinforced concrete frames, as can be seen in Figure 1.4. In the first case, the high stiffness and strength of the wall causes the well known "short column" effect, leading to a shear failure of the reinforced concrete column frame, demonstrating the need of considering the presence of these walls. On the other hand, notice that the use of a full infilled frame does not assure that the short column effect will not occur, as depicted in Figure 1.4b, where the same effect happened after the compressive crushing of the masonry corner. In the particular case of Ecuador, current standards still do not consider the masonry infills as structural

Figure 1.3: Example of a structural collapse due to the MIF irregular vertical distribution of stiffness (Landívar, 2016).

elements and they are only taken into account as dead load during design phases.

(a) Short column effect due to masonry infilled lateral restriction to the columns.

(b) Short column effect due to masonry infilled corner compressive crushing.

Figure 1.4: Examples of short column effect during 2016 Ecuadorian earthquake.

In the past decade, most research efforts rely on the development of deterministic procedures to model the complex non-linear behaviour of the MIFs. Models that consider in detail each component of the system behaviour require prohibitive amount of information which, added to the characteristic complexity of the model, makes its application limited to very rare building cases. In order to economically assess the vulnerability of most buildings in a location, simpler models are preferred. However, simpler model prediction capabilities are highly dependent on the amount of information used to calibrate the model and how that information resembles to the conditions of the existing buildings, introducing unknown uncertainties about the quality of the prediction. Therefore, the application of deterministic procedures may lead to either unsafe or too expensive decisions to reduce the seismic risk of an existing structure.

In this thesis, probabilistic (Bayesian) procedures for the evaluation of MIF structures are explored

to improve the quality of information to be used for decision making. Also, a novel non-destructive test procedure is proposed to reliably estimate the stiffness of the walls, allowing to considerably reduce time and costs related to the gathering of information of the building under evaluation. To attain these objectives, an approximate Bayesian computation (ABC) algorithm, called $\mathcal{A}^2$BC-SubSim was developed and applied.

Chapter 2

Objectives

The MIF structural system is influenced by a series of conditions that makes it difficult to predict its mechanical behaviour. Estimating the behaviour of existing structural systems could be an expensive task, mainly due to the need of acquiring enough information to properly feed complex and deterministic numerical models. One way around to avoid those complexities is the application of simpler calibrated models that account for the uncertainties, i.e. probabilistic models. Therefore, the main objective of this thesis is to provide uncertainty quantification techniques to fairly predict the mechanical behaviour of existing MIF buildings, accounting for the uncertainties of both the model and the knowledge about the material properties and without the need of destructive tests. This main objective has been reached by investigating against the following research premises:

1. ABC methods have been under continuous development since the last two decades, and a number of ABC variants have been proposed in the literature by joining the ABC principles with variational inference or Monte Carlo methods like the Kernel ABC (Park et al., 2016), Lazy ABC (Prangle, 2016), Coupled ABC (Neal, 2012), Empirical-likelihood ABC (Mengersen et al., 2013), or Bootstrap-likelihood ABC (Zhu et al., 2016). Other variants combine the ABC approach with efficient sampling algorithms like the ABC-Partial Rejection Control (Sisson et al., 2007), ABC-Sequential Monte Carlo (Del Moral et al., 2012; Toni et al., 2009), ABC-Particle Monte Carlo (Beaumont et al., 2009), ABC-Parallel Tempering (Baragatti et al., 2013), ABC by Simulated Annealing (Albert et al., 2015), and ABC by Subset Simulation (Chiachio et al., 2014). The reader is referred to Sisson et al. (2018) for a comprehensive overview of the ABC methods and to Karabatsos et al. (2018) for a comparative review.

   The majority of these ABC variants have been proposed in the form of new ABC algorithms which have been successfully used for model inference and calibration in a wide range of application fields, such as molecular dynamics (Dutta et al., 2018; Kulakova, 2017), biology (Bianconi et al., 2019), hydrology (Kavetski et al., 2018), health sciences (Da Costa et al., 2018; McKinley, Trevelyan

J. and Vernon, Ian and Andrianakis, Ioannis and McCreesh, Nicky and Oakley, Jeremy E. and Nsubuga, Rebecca N. and Goldstein, Michael and White, Richard G., 2018; Rutter et al., 2019), environmental radioactivity (Nishina et al., 2018), communications (Bharti and Pedersen, 2019) and physics (Christopher et al., 2018). Engineering applications (Sala and Soriguera, 2020), and particularly structural engineering applications, have also received attention from the ABC community mainly to infer unknown structural performance parameters from non-linear models (Ben Abdessalem et al., 2019; Betz, 2017; De et al., 2019; Lam et al., 2018; Song et al., 2019; Tiboaca, 2016).

Despite their successful contribution for solving complex problems in a wide range of applications, the ABC variants available in the literature require the definition of a number of sensitive algorithm hyper-parameters which highly influence the efficiency of the algorithm and also the quality of the inferred solution. This drawback puts some extra difficulties for extending these algorithms to real-world engineering problems since previous expertise is required to tune these parameters, thus limiting its usefulness to experienced users who can provide key expert-knowledge about the algorithm. In particular, the application of the ABC-SubSim algorithm is interesting, as it has been proven to be one of the most efficient ABC algorithms available in the literature.

Hipothesis 1: The approximate Bayesian computation method ABC-SubSim may be improved by implementing a self-adapting algorithm to avoid the case-dependent manual definition of the hyper-parameters of the algorithm.

Research Objective 1: Develop a Markov chain based approach to infer the best choice of the hyper-parameters of the ABC-SubSim method within each subset evaluation, and apply it to a complex multi-dimensional non-linear MIF structural model calibration.

2. The so called "Macro-models" rely on modelling the mechanical contribution of the masonry wall through a number of equivalent struts in the direction of each diagonal of the wall. As an example, some reference structural codes, like the *Seismic Evaluation Standards*, ASCE/SEI 41 (2017), adopt a one-strut macro-model to consider the contribution of the MIFs in the seismic response of frame-based buildings. Similar approaches can also be found in the recent literature about this topic (Bose et al., 2019; Huang et al., 2020; Liberatore et al., 2018; Mohamed and Romão, 2018; Mohammad Noh et al., 2017; Morandi et al., 2018b; O'Reilly et al., 2018). However, most of the referred methods in the literature do not consider the sources of uncertainties of this complex structural system. Indeed, recent works (Liberatore et al., 2018) claim about the need to consider the parameters uncertainties after the observation of the high variability of the deterministic methods. Thus, a probabilistic approach is required for the structural evaluation of existing MIF structures.

   The use of artificial neural networks (ANN) in engineering applications is experiencing a significant increase in recent years (Awodele and Jegede, 2009), resulting in extraordinary contributions. Their success in the engineering field is remarkable when the complexity of a problem is such that known physical laws struggle to provide acceptable solutions, hence they are an alternative given their

data-driven approach. In the literature, some approaches can be encountered (Kalman Šipoš et al., 2013) which proposed the application of deterministic ANN to predict the behaviour of MIFs; however, using deterministic neural networks carries the disadvantage of ignoring about the quality of the prediction and, therefore, there is a need to research about the application of probabilistic methods. In particular, Bayesian neural networks (BNN) have been demonstrated to be efficient in the quantification of the uncertainty (Blundell et al., 2015; Fernández et al., 2022).

Hipothesis 2: The application of data-based models can be suitable to predict the non-linear modelling parameters of uncertainty prone structural systems, such as MIFs.

Research Objective 2: Develop a database of available laboratory tests of MIFs, and train a Bayesian neural network that is capable to predict the constitutive in-plane (IP) behaviour of a MIF system with quantified uncertainty.

3. Several modelling strategies have been proposed to estimate the IP constitutive behaviour of MIFs, and they can typically be classified as *micro*, *meso* and *macro* modelling approaches (Mohammad Noh et al., 2017; Tarque et al., 2015). Authors like Sattar and Liel (2016a) and Sattar and Liel (2016b) have proposed the application of a *strut* model enhanced by the use of micro-modelling for the seismic evaluation of MIF buildings. However, the known complexities of micro-models and the big amount of input data requited (usually not available for existing old structures) limit their applicability. On the other hand, current reference standards for the seismic evaluation of existing buildings, like the ASCE/41-17 (ASCE/SEI 41, 2017), stipulate the need to "validate the use of finite element models and strut models by considering published or project specific experimental data from cyclic *quasi-static* or dynamic tests" for the MIF structural systems, due to their complex behaviour and the uncertainties affecting their response. To attain this issue, an alternative is a detailed characterization of the MIF, which would require a number of destructive tests to properly estimate their influence within the structural behaviour (Ferretti et al., 2019; Mazzotti et al., 2014). However, these tests involve a considerable increase in building assessment costs, making them unfeasible for small and medium-sized structures. This problem reveals the need of low-cost and non-destructive test for the structural evaluation of existing MIF, which can be easily applied in-situ and without the need of complex, yet expensive, equipment.

   Recently, it has been demonstrated experimentally (Cavaleri et al., 2020; De Risi et al., 2019; Misir et al., 2016; Palieraki et al., 2018) that the IP and out-of-plane (OOP) strength and stiffness of the wall are dependent of each other. As the OOP fundamental frequency can be obtained by non-destructive testing using available system identification methods (Reynders, 2012), it is plausible to use this tool to indirectly infer the IP stiffness of an existing wall.

   Hipothesis 3: The characteristic IP-OOP interactive behaviour of the wall in a MIF can be exploited to indirectly infer the IP stiffness of an existing wall.

   Research Objective 3: Propose a field-based non-destructive semi-empirical methodology to

predict the IP stiffness of existing MIF walls, based on the results obtained from a static and dynamic test campaign.

Chapter 3

Outline of contributions

This chapter shows the outline of the contributions developed to solve the research questions raised in Chapter 2, indicating where they appear in the text.

Research Objective 1: *Development of a Markov chain algorithm approach to infer the best choice of the hyper-parameters of the ABC-SubSim method within each subset evaluation.*

An introduction to the original ABC-SubSim algorithm is presented in Section 4.1. Also, an example application to infer the non-linear modelling parameters of a beam-column is presented. The importance of the hyper-parameter p_0 (conditional probability) is mentioned, along with its influence on the efficiency of the method and the difficulties that arise to properly define it in practical engineering applications. In Chapter 5, a Markov chain strategy to infer the best choice for p_0 is investigated and the algorithm $\mathcal{A}^2$BC-SubSim is proposed. The main idea behind this algorithm consists of a random selection of a group of p_0's that are tested on a portion of the total number of evaluations of the metric within each subset. The selection is made by searching for a balance between simulation efficiency and computational cost, and both conditions are achieved by exploiting the following facts: (1) the simulation efficiency can be estimated in terms of how close the acceptance ratio is to the optimum value and, (2) the computational cost may be reduced if the metric is more closely matched to the tolerance. The proposed algorithm is tested in comparison to the original one, in terms of the quality of the posterior and the number of evaluations of the metric (computational cost), showing that the former achieve better results with similar, or even lesser, number of model evaluations. Notice that the main advantage of the proposed method relies on the fact that there is no need of previous expert knowledge about the algorithm, nor the need to preliminarily run tests, to properly define the p_0 parameter.

The proposed algorithm is further tested with some application examples about the inference of non-linear models, namely: (1) a cantilever reinforced concrete beam-column with cyclic degradation (Section 5.4.1), (2) a group of cantilever reinforced concrete beam-columns with similar geometric characteristics, subjected to different levels of constant axial load along with cyclic lateral deformation and degradation

(Section 5.4.2), (3) a one-bay one-story reinforced concrete frame subjected to lateral cyclic deformation (Section 5.4.3), and finally (4) a 17-story building subjected to impulsive seismic loading (Section 5.4.4). Those examples demonstrates the broad applicability of the algorithm for the inference of structural parameters of non-linear models. Finally, a comparison between trial and error model calibration and a discussion about the importance of checking the consistency of the results, are presented in Section 5.5.

Research Objective 2: *Development of a database of available laboratory tests of MIFs, along with training of a Bayesian neural network that is capable to predict the constitutive IP behaviour of a MIF-wall system.*

First, an overview about Artificial Neural Networks (ANN), Bayesian Neural Networks (BNN) and, in more detail, about the Hamiltonian Monte Carlo (HMC) is presented in Section 4.3.1. Training data are required for the application of this method, hence, in Section 6.1, the data gathered from an extensive literature review are described. Details about training and test are presented in Sections 6.2, 6.2.1 and 6.2.2. In Section 6.3, a case study of the seismic evaluation of an existing three story building is presented.

A summary about the existing modelling strategies available for MIF structures is also presented in Sections 4.2.1 and 4.2.2, accompanied with some example applications. These models are later used in Chapter 6 for comparison of the prediction capabilities of the proposed surrogate model obtained with BNN-HMC. The gathered data are further exploited in Section 6.1.1, where a damage index formulation is proposed to estimate the collapse probability of MIF elements.

Research Objective 3: *Propose a field-based non-destructive test methodology to predict the IP stiffness of existing MIF walls.*

In the last few years, the study about the interaction between IP and OOP structural behaviour of MIFs has gained special attention among researchers (Cavaleri et al., 2020; De Risi et al., 2019; Misir et al., 2016; Palieraki et al., 2018). It has been shown that the degradation of IP stiffness and strength is associated with an equivalent degradation of the OOP stiffness and strength, and vice-versa. Accordingly, in Chapter 7, a campaign of laboratory tests was designed and performed to study the relationship between the OOP fundamental frequency of the wall and the IP stiffness of a MIF. The specimens consisted on reinforced concrete and structural steel frames infilled with un-reinforced concrete masonry units with vertical hollows, as detailed in Section 7.1. In the test procedure (see Section 7.2), the use of low-cost instrumentation was adopted so that, the method proposed later, has a broader coverage in terms of its applicability. The OOP fundamental frequency is estimated by acceleration measurements and existing system identification procedures available in the literature, as explained in Section 7.3. An equivalent strut linear-elastic model is calibrated from the laboratory test results, with the $\mathcal{A}^2$BC-SubSim algorithm. This model could be used to perform an evaluation of an existing MIF building; however, due to the limited data from the laboratory campaign, it can not be expected to be suitable for direct real application. To expand its applicability, the results of the campaign in liaison with the application of a complex non-linear

model of the structural system were used. A parametric study (see Section 7.5) was performed to gather additional information that allow us to propose a non-destructive semi-empirical method that can be applied to estimate the influence of a masonry infill on the stiffness of an existing moment frame building.

The proposed method is further validated with the dynamic tests described in detail in Chapter 8. These tests were performed on the shake table of the Structures' Laboratory in UGR and helped to further validate the proposed method by considering larger scale specimens and cyclic IP degradation due to dynamic loads. The specimens were also used to study the influence of cement-based plastering on the OOP fundamental frequency. Results showed negligible influence and, hence, the proposed method does not require any adjustment when cement-based plastering is present. Also, the dynamic test results were used to validate the MIF models proposed throughout this thesis.

Chapter 4

Theoretical fundamentals

4.1 Bayesian model updating by ABC-SubSim

The Adaptive Approximate Bayesian Computation by Subset Simulation algorithm proposed in the following chapter is based on the structure of the ABC-SubSim method, which is a Bayesian updating algorithm originally proposed in Chiachio et al. (2014). Thus, a description of ABC-SubSim is provided here to confer the reader with the basis about the method under an unified notation.

The focus of Bayesian model updating is to update the prior information about the value of a set of uncertain model parameters $\boldsymbol{\theta} \in \boldsymbol{\Theta} \subseteq \mathbb{R}^{n_p}$ from a parameterized model $\mathbf{x} = g(\mathbf{u}, \boldsymbol{\theta}) \in \mathcal{X} \subset \mathbb{R}^d$ based on the information given by the data $\mathbf{y} \in \mathcal{D} \subset \mathbb{R}^d$, where $g : \mathbb{R}^{n_u \times n_p} \to \mathbb{R}^d$, $\mathbf{u} \in \mathbb{R}^{n_u}$ are input values to g, and $\mathcal{D}$ is the *observation space*. Following the Bayesian formulation, the solution is not a single value of $\boldsymbol{\theta}$; on the contrary, Bayes' Theorem (see Equation (4.1)) takes the initial quantification of the plausibility of $\boldsymbol{\theta}$, which is expressed by the *prior* probability density function (PDF) $p(\boldsymbol{\theta})$, and updates this plausibility using the information in the dataset $\mathcal{D}$ through the *likelihood function* $p(y|x, \theta)$ to obtain the *posterior* PDF of the model parameters $p(\boldsymbol{\theta}|\mathbf{y})$. The interested reader is referred to Beck (2010) for further information about Bayesian model updating.

$$p(\mathbf{x}, \boldsymbol{\theta}|\mathbf{y}) \propto p(\mathbf{y}|\mathbf{x}, \boldsymbol{\theta}) p(\mathbf{x}|\boldsymbol{\theta}) p(\boldsymbol{\theta}) \tag{4.1}$$

However, there are situations where the likelihood function is unknown or analytically intractable, for which the Approximate Bayesian Computation (ABC) methods Marjoram et al. (2003), also known as *likelihood-free computation algorithms*, provide an efficient alternative. These methods bypass the evaluation of the likelihood function using a simulation-based approach. Through a specific tolerance parameter ξ, the method selects as posterior samples the pairs $(\mathbf{x}, \boldsymbol{\theta}) \in \mathcal{H} \subseteq \mathcal{X} \times \boldsymbol{\Theta}$ such that the model simulations $\mathbf{x} \sim p(\mathbf{x}|\boldsymbol{\theta}) p(\boldsymbol{\theta})$ lay within a specific region around $\mathbf{y}$, namely $\mathcal{B}_\xi(\mathbf{y}) = \{\mathbf{x} \in \mathcal{D} : \rho(\mathbf{x}, \boldsymbol{\theta}, \mathbf{y}) \leqslant \xi\}$, where $\rho(\cdot) : \mathbb{R}^{d \times n_p} \to \mathbb{R}$ is a user-defined metric function used to measure the closeness of the simulated

output $\mathbf{x}$ to the data $\mathbf{y}$. By this means, the ABC marginal posterior of parameters is expressed as $p_\xi(\boldsymbol{\theta}) \propto P(\mathbf{x} \in \mathcal{B}_\xi(\mathbf{y})|\boldsymbol{\theta})p(\boldsymbol{\theta})$, where $P(\mathbf{x} \in \mathcal{B}_\xi(\mathbf{y})|\boldsymbol{\theta})$ assigns the unity when $\rho(\mathbf{x}, \boldsymbol{\theta}, \mathbf{y}) \leqslant \xi$, and 0 otherwise.

ABC-SubSim (Chiachio et al., 2014) exploits the efficient simulation framework of Subset Simulation, originally proposed by Au and Beck (2001) as an estimator of small failure probabilities. By Subset simulation, a rare event simulation problem is transformed into the product of a series of simulations with larger probabilities whereby the computational effort is reduced. Indeed, in ABC-SubSim the region $\mathcal{H}$ of possible solutions is assumed to be defined as the intersection of m nested regions in the $\mathcal{X} \times \boldsymbol{\Theta}$ space, i.e., $\mathcal{H}_1 \supseteq \ldots \mathcal{H}_j \supseteq \ldots \supseteq \mathcal{H}_m = \mathcal{H}$, where:

$$\mathcal{H}_j = \left\{(\mathbf{x}, \boldsymbol{\theta}) : \rho(\mathbf{x}, \boldsymbol{\theta}, \mathbf{y}) \leqslant \xi_j\right\} \tag{4.2}$$

In the last equation, the tolerance values follow a decreasing sequence $\xi_1 \geqslant \xi_2 \ldots \geqslant \xi_m$ whose values are adaptively determined such that the sample estimate $\bar{P}_j \triangleq P(\mathcal{H}_j|\mathcal{H}_{j-1})$ satisfies $\bar{P}_j = p_0$, with $P(\mathcal{H}_j) = P((\mathbf{x}, \boldsymbol{\theta}) \in \mathcal{H}_j)$, and p_0 is a conditional probability acting as algorithm hyper-parameter defined by the modeller. The algorithm 1 shows the process followed by the ABC-SubSim method.

As an illustrative example, the ABC-SubSim is applied here to infer the parameters of a non-linear model of a structural reinforced concrete element tested in the laboratory. The element consist of a cantilever beam-column subjected to constant axial load and cyclic lateral deformation. More details about the test are presented in Section 5.4.1. The model consist of a distributed plasticity beam-column with a flexible boundary dependent on the stiffness of the cross section, as shown in Figure 4.1a. The reinforced concrete section is represented by a *fiber* section, where the cross-section is discretised in a series of elements with uniaxial behaviour, such that the axial-flexural stiffness of the section is determined by integration of the stiffness of the uniaxial elements over the section. Concrete behaviour is represented by the *Concrete01* constitutive model (see Figure 4.1b), using as inputs the recommendations proposed in Karthik and Mander (2011) and the estimation of the confinement ratio proposed in Mander et al. (1988). The steel reinforcement behaviour was modelled with the *Hysteretic* constitutive model (see Figure 4.1c) and the recommended properties of the ASCE/COPRI (2014) regulations. All the materials constitutive's values were defined with the nominal resistance reported by Gill (1979). Note also that the *Hysteretic* model allows considering resistance and stiffness deterioration by three parameters (see Figure 5.11): (1) demanded ductility of the material (named as D_1), (2) dissipated energy (called D_2), and (3) by the unloading stiffness degradation parameter (called β). Through these three parameters, the degradation of a reinforced concrete beam-column element can be modelled, which is a critical requirement for the seismic performance evaluation of a structure (Harris et al., 2009; Haselton et al., 2008).

The ABC-SubSim hyper-parameters were set to $N = 2000$ samples and $p_0 = 0.2$. The deviation of the proposal PDF was set equal to the 10% of the standard deviation of the marginal PDF of each θ_i from the previous subset. Figure 4.2 depicts the acceptance rate obtained for 100 independent runs with $p_0 = 0.2$,

Algorithm 1 ABC-SubSim

Input: $p_0 \in [0,1]$: defines the number of seeds by Np_0 and the number of Markov Chains for each subset by $\frac{1}{p_0}$;
N: number of samples per intermediate level;
ξ_f, m: final tolerance value and maximum number of Subsets, for stopping criteria;
Objective Function: $\xi = \rho\left(\theta_1, \theta_2, ..., \theta_{n_p}\right)$
Output: $\theta_1, \theta_2, ..., \theta_{n_p}$

Monte-Carlo Simulations
Sample $\left[\theta_{1,i}^{(0)}, ..., \theta_{1,i}^{(n)}, ..., \theta_{1,i}^{(N)}\right]$ for $i = 1, ..., n_p$
for $n = 1, ..., N$ **do**
    Obtain the tolerance values: $\xi_1^{(n)} = \rho\left(\theta_{1,1}^{(n)}, \theta_{1,2}^{(n)}, ..., \theta_{1,n_p}^{(n)}\right)$
end for
Subset Simulation
for $j = 2, ..., m$ **do**
    Renumber $\left[\theta_{j-1,i}^{(n)}, n : 1, ..., N, i = 1, ..., n_p\right]$ so that $\xi_{j-1}^{(1)} \leq \xi_{j-1}^{(2)} \leq ... \leq \xi_{j-1}^{(N)}$
    for $k = 1, ..., Np_0$ **do**
        Select $\left(\theta_{j-1,i}^{(k)}\right)$ as a seed
    Markov chain Monte-Carlo
        for $l = 1, ..., \frac{1}{p_0}$ **do**
            Generate child conditional samples $\theta_{j,i}^{k}$ from the seed $\theta_{j-1,i}^{k}$
            Evaluate tolerance value ξ_l
            if $\xi_l <= \xi_{j-1}^{(Np_0)}$ **then**
                Accept the child sample $\theta_{j,i}^{k}$ as new sample
            else
                Use seed $\theta_{j-1,i}^{k}$ as new sample
            end if
        end for
        Reorder $\left[\theta_{j,i}^{(k),l} : k = 1, ...Np_0; l = 1, ..., \frac{1}{p_0}\right]$ as $\left[\theta_{j,i}^{(1)}, ..., \theta_{j,i}^{(N)}\right]$
    end for
    if $\xi_j^{(Np_0)} \leq \xi_f$ **then**
        End algorithm
    end if
end for

along with the $p_0 = 0.5$ case. Although p_0 parameter selection will not considerably influence the final results, it is important for the efficiency of the algorithm. As shown in the aforementioned figure, in this particular case, the algorithm requires more subsets when $p_0 = 0.5$ to try to attain the same tolerance and, in some cases (13%), did not even reached it. Considering that (1) the optimum acceptance rate should be near 40% (Papaioannou et al., 2015), (2) that p_0 highly influence the acceptance rate, and (3) for the same p_0 value, the acceptance rate changes as the number of subsets increases; it seems that, to attain better efficiency, p_0 should be selected according to the conditions of each subset. Notice that the maximum number of *Subsets* was limited to $m = 40$, with a tolerance value ϵ_f given by the following metric function:

$$\rho = \sum_{i=1}^{N^*} (F - F^*)_i \tag{4.3}$$

where $\epsilon_f = 0.10 \sum_{i=1}^{N^*} (F^*)_i$ is the tolerance value, N^* is the number of data points of the test results and F^* is the force data values resulted from the tests, and F is the force data values resulted from

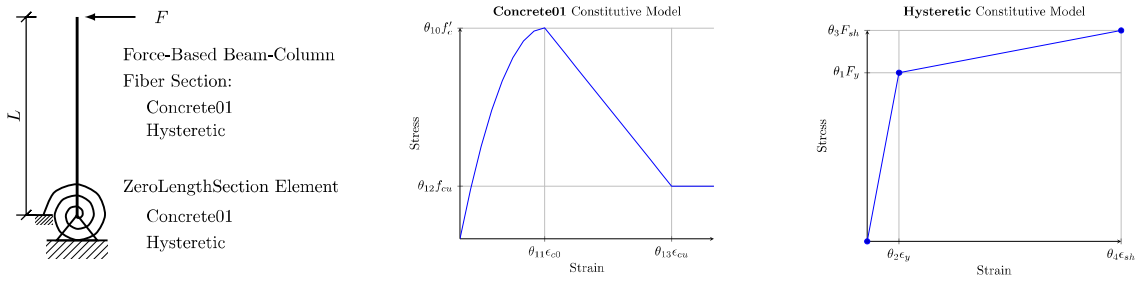

(a) Nonlinear structural model of a reinforced concrete beam-column.

(b) *Concrete01* material constitutive model and calibration parameters.

(c) *Hysteretic* material constitutive model and calibration parameters.

Figure 4.1: Example application of ABC-SubSim, on the inference of the non-linear modelling parameters of a reinforced concrete column.

Table 4.1: Parameter *a priori* information and *posteriori* results.

		θ_1	θ_2	θ_3	θ_4	θ_5	θ_6	θ_7	θ_8	θ_9	θ_{10}	θ_{11}	θ_{12}	θ_{13}
Priori	Lower Bound	0.50	0.50	0.50	0.50	0.00	0.50	0.00	0.00	0.00	0.50	0.50	0.50	0.50
	Upper Bound	1.50	1.50	1.50	1.50	0.50	1.00	0.25	0.25	0.25	1.50	1.50	1.50	1.50
	MAP	1.11	1.07	1.20	1.02	0.50	0.70	0.011	0.212	0.189	0.73	1.34	0.93	0.57
	Std (%)	0.73	1.27	0.64	3.00	0.56	0.84	0.03	1.07	0.46	0.28	0.70	1.14	0.98

the model. Thirteen model parameters have been selected for the model calibration (see Table 4.1), i.e. $\boldsymbol{\theta} = \{\theta_1, \theta_2, \ldots, \theta_{13}\}$. The parameters θ_1 to θ_4 correspond to coefficients of resistance and deformation of steel reinforcement constitutive values, as shown in Figure 4.1c. Parameters θ_5 and θ_6 define the pinching of the response of the steel reinforcement model (see Figure 5.11), θ_7 to θ_9 are degradation parameters of the hysteretic model corresponding to D_1, D_2 and β, respectively. Finally, parameters θ_{10} to θ_{13} correspond to coefficients of the resistance and deformation values for the concrete constitutive behaviour, as shown in Figure 4.1b.

Figure 4.3b compares the cyclic response of the column during the test with the maximum a posteriori (MAP) model obtained from the ABC-SubSim algorithm results. Notice that the model response agrees to the test data in terms of strength and deformation. Figure 4.3a depicts the objective function values per simulation level showing that it gets minimized as the algorithm progress. For this example, after subset number 15, the tolerance value reached almost a constant value.

Moreover, Figure 4.4 presents a multidimensional scatter-plot of the posterior samples of θ_1 to θ_6, chosen for illustration purposes. A colour code of increasing intensity is used to differentiate between subsets, where the darker colors correspond to the latest subset (15_{th} subset). The diagonal shows the probability density functions (PDFs) of each parameter, whilst the rest of the plots show paired scatter dispersion plots for every pair of parameters. Note that the uncertainty of all parameters (which can

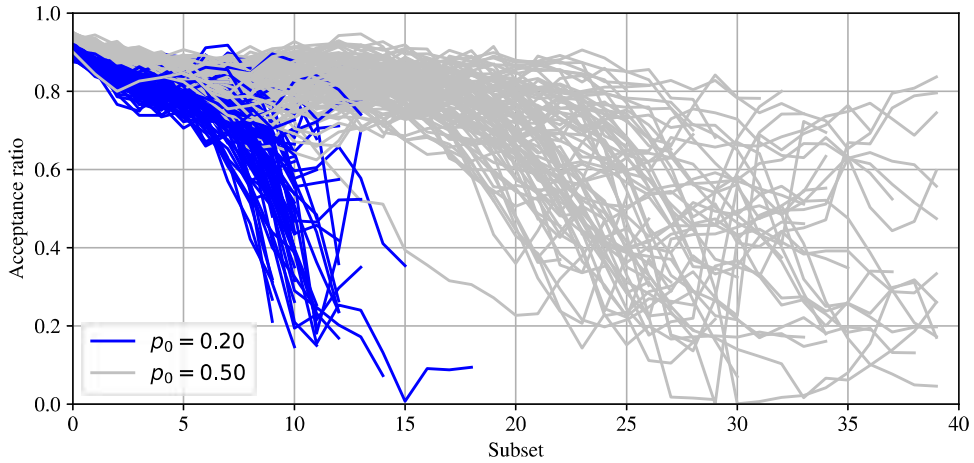

Figure 4.2: Acceptance rate after 100 independent runs of the reinforced concrete column inference problem solved with ABC-SubSim, with $p_0 = 0.2$ and $p_0 = 0.5$

be noticed by considering the spread of each PDF) is significantly reduced as they are confronted with experimental data. Also, the uncertainty is reduced as the algorithm progress towards deeper subsets, meaning that there is an effective model learning from the data. Table 4.1 summarizes the values of each model parameter at the beginning (by the *a priori* parameter range) and end of the process (by the MAP). This results show that the resulting model using the MAP values as modelling parameters is the most suitable one to reproduce the test data.

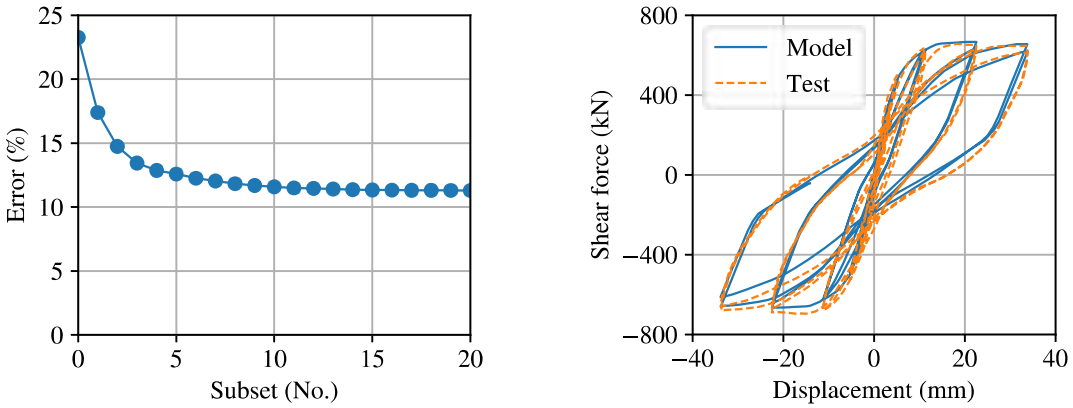

(a) Evolution of model error during calibration process.

(b) Comparison between test and calibrated model force-displacement results.

Figure 4.3: Results from the ABC-SubSim application example.

It can be noticed that the uncertainty reduction of parameter θ_4, which corresponds to the coefficient of the nominal ultimate deformation of the steel reinforcement, is significantly less than the others. Indeed,

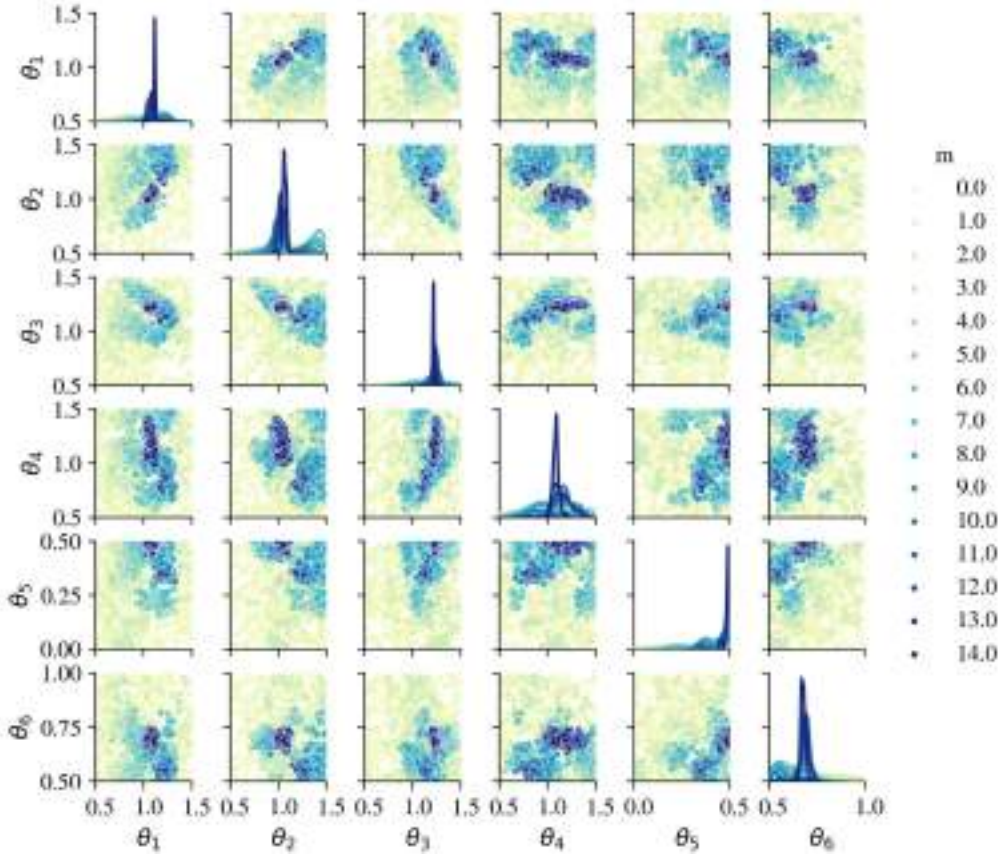

Figure 4.4: Scatter plot matrix results for θ_1 to θ_6 parameters. Axes in the diagonal display the density plots of the corresponding parameter (only 6 parameters and the initial 14 subsets are presented for clarity).

the standard deviation values of the posterior PDFs taken from table 4.1 corroborate this appreciation, showing the highest standard deviation value for θ_4. This means that this parameter is relatively insensitive to the information provided by the data and, therefore, its variation has less effect on the force-deformation response of the tested element. This result is consistent with the physical condition of the test, as this parameter modifies the ultimate deformation capacity of the steel reinforcement, which corresponds to a deformation level not reached during the test, and thus, not observed in the data.

The presented example demonstrated the capabilities of the ABC-SubSim algorithm to infer the distribution of the non-linear modelling parameters based on test results. As it was mentioned before, the definition of the conditional probability hyper-parameter, p_0, has major influence on the efficiency of the algorithm and minor, on the results, provided that a sufficient amount of simulations are employed (which some times, might be huge). Therefore, its definition should be made with caution and on a case-by-case basis. Notice that this requires to perform several runs of the problem with different p_0 values, in order to define the best choice. In Chapter 5, the algorithm is enhanced to avoid the manual selection of p_0.

4.2 Non-linear modelling of structures

4.2.1 Available frame models for reinforced concrete frames

Two different approaches are adopted in this thesis to represent the behaviour of the reinforced concrete frames, namely: (1) models with concentrated hinges at the ends of beam-column elastic elements, following the recommendations by Haselton et al. (2008); and (2) models based on beam-column elements with distributed plasticity. These two models are applied throughout this thesis, so they are summarized here for the ease of the reader. Table 4.2 shows the general formulation to obtain the constitutive parameters of the nonlinear hinges, whereas Figure 4.5a depicts the general geometry and characteristics of the model. Notice that the second approach is also used by Liberatore et al. (2018), where the concrete and steel constitutive uni-axial behaviour is discretized within the cross section, to be further integrated over the length of the beam column element. This allows us to directly consider the distribution of plasticity along the element. A similar approach was applied to model the steel frames. Additionaly, Table 4.3 and Figure 4.5b show the general geometry and characteristics of the model. The shear behaviour of the columns is not explicitly modelled since the tests within the database do not include cases with that type of failure.

Table 4.2: Reinforced concrete concentrated hinge constitutive values.

Description of constitutive parameters
$k_o = 1.1\dfrac{11EI_{40}}{L_v}$
$EI_{40} = \left[-0.02 + \dfrac{0.98P}{A_g f_c} + 0.09\dfrac{L_v}{H}\right] E_c I_g$
M_y according to Panagiotakos and Fardis (2001)
$M_c = 1.25\,(0.89)^{\frac{P}{A_g f_c}}\,(0.91)^{0.01 f_c}\,M_y$
$\theta_c = \theta_y + 0.12\,(1.55)\,(0.16)^{\frac{P}{A_g f_c}}\,(0.02 + 40\rho_{sh})^{0.43}\,(0.54)^{0.01 f_c}\,(0.66)^{0.1 s_n}\,(2.27)^{10\rho}\,F_{SYM}$
$\theta_r = \theta_c + 0.76\,(0.031)^{\frac{P}{A_g f_c}}\,(0.02 + 40\rho_{sh})^{1.02}$

Formulation of non-linear hinges according to Haselton et al. (2008), in units of N, mm and MPa. L_v: shear length, P: axial load, A_g: gross area of the cross section, f_c: concrete characteristic compressive strength, H: height of the cross section, ρ_{sh}: transverse steel ratio, s_n: rebar buckling coefficient according to Dhakal and Maekawa (2002), ρ: ratio of tension reinforcement, F_{SYM}: factor to consider asymmetric arrangement of flexural reinforcement.

As an example application of these modelling approaches for reinforced concrete frames, the test performed by Adachi et al. (2000) is modelled here with both strategies. Figure 4.6a depicts the general geometry of the model, for the concentrated hinge case. Notice that the distributed plasticity model had the same concept without the non-linear plastic hinges. The frame consisted of 200x220 mm cross-section columns with 14 longitudinal reinforcement rebars with 10 mm diameter, and 4 mm diameter stirrups with 150 mm spacing. The mid-floor beam consisted of 160x290 mm cross-section beams with 7 longitudinal rebars with 10 mm diameter as top and bottom reinforcement, and 4 mm diameter stirrups with 80 mm spacing. The concrete had a characteristic compressive strength of 18 MPa and the yield strength of

Table 4.3: Reinforced concrete and structural steel distributed plasticity uniaxial constitutive parameters.

	Concrete	Steel
Peak/Yield stress	f_c	f_y
Peak/Yield strain	$\epsilon_o = \frac{105 + f_c}{70000}$	$\epsilon_y = \frac{f_y}{E_s}$
Ultimate stress	12	
Ultimate strain	$5\epsilon_o$	
Strain hardening ratio		$\beta = 0.001$
OpenSeespy model	*Concrete01*	*Steel02*

Parameter formulation according to Karthik and Mander (2011), in units of N, mm and MPa. Recommended values of $R_0 = 18$, $CR_1 = 0.912$ and $CR_2 = 0.15$, of Steel02 model, were adopted.

the reinforcement was 342 MPa. Figure 4.6b, shows a comparison of the shear and lateral deformation behaviour of both models against the test. From the results, it can be concluded that:

- The concentrated hinge model usually over-predicts the initial stiffness of the structure and, in this particular case, also over-predicts the maximum lateral response. However, it has the capability to consider the strength degradation due to cyclic deformations, making it particularly useful to estimate the probability of collapse of this type of structures. Notice that, this phenomenological model was obtained from regression analysis of an arguably limited laboratory data; therefore, the quality of a *blind* prediction is not expected to be perfect.

- The distributed plasticity model slightly under-predicts the initial stiffness of the structure and, in this particular case, also under-predicts the maximum lateral response. Notice that this model turns to be a better representation of the physical behaviour of the materials; however, results are also dependent on the assumptions made on their constitutive behaviour.

- Even though the estimations of the models do not perfectly match the laboratory measurements, considering the sources of uncertainties (i.e the selection of parameters, modelling assumptions, neglected sources of nonlinear behaviour, the uncertainties on the laboratory measurements, to name but the most important), both models are capable to fairly predict the behaviour of reinforced concrete frames.

4.2.2 Available equivalent strut models for MIF

To physically model the shear behaviour of the MIF structural system, the framework *OpenSeespy* (Zhu et al., 2018) is used here, where a macro-modelling approach with a single strut per diagonal is applied according to three different models proposed by other researchers in Liberatore et al. (2018), Huang et al. (2020) and ASCE/SEI 41 (2017). *Pinching4* constitutive behaviour is used herein to construct the model. For the ease of the reader, the formulation of these models are summarized in Table 4.4 under a unified

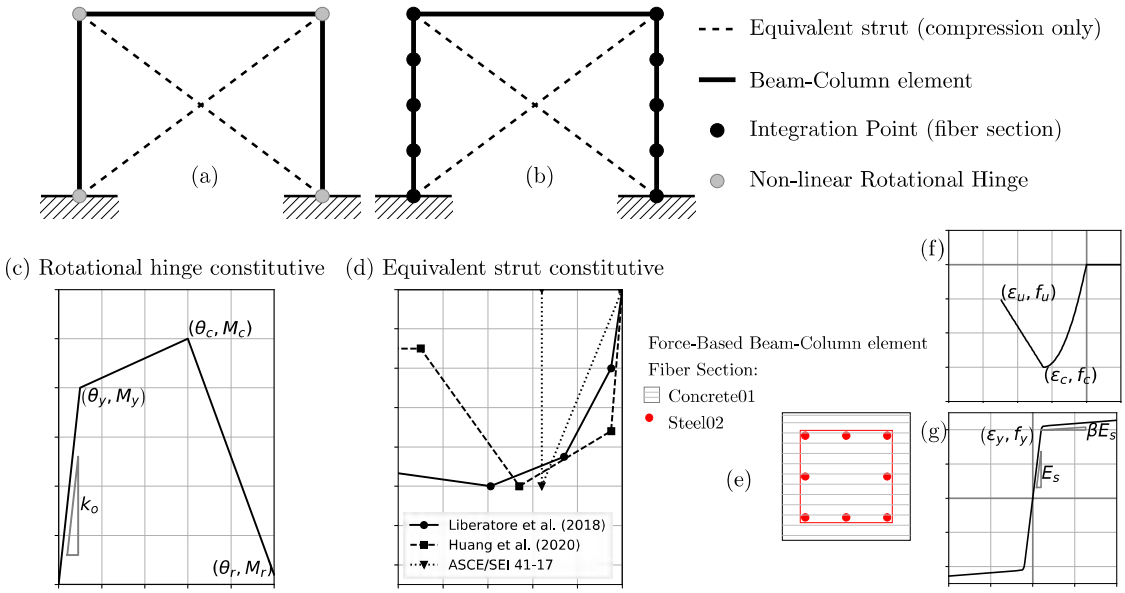

Figure 4.5: MIF models used for comparison in Section 4.2.1. (a) Frame model with concentrated hinges at the ends of beam-column elements, with a (c) tri-lineal constitutive behaviour. (b) Frame model with distributed plasticity beam-column elements, with a (e) fiber section discretized with uniaxial stress-strain behaviour of (f) concrete and (g) steel. (d) Equivalent strut shear-deformation behaviour.

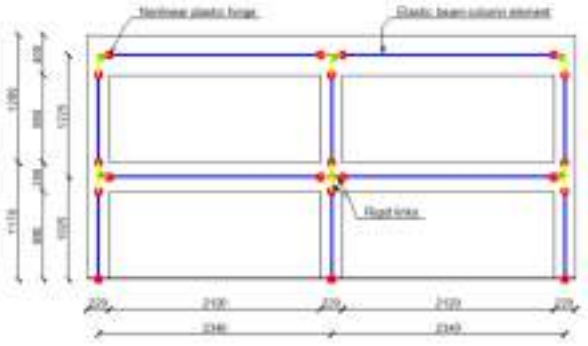

(a) Model geometry.

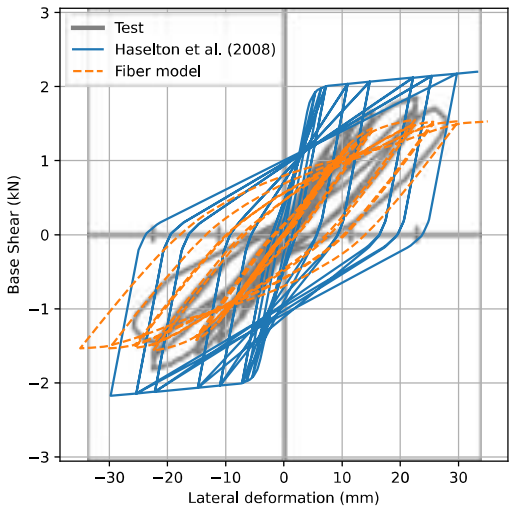

(b) Lateral displacement and shear response.

Figure 4.6: Example modelling of a building frame tested by Adachi et al. (2000).

notation. The shapes of their constitutive behavior are given in Figure 4.5d. The first model, proposed by Liberatore et al. (2018), consists of a 4-lines backbone curve where the strength is estimated according to four possible failure modes, namely: bed-joint sliding, diagonal tension, diagonal compression, and corner

compression. The formulation of the failure modes are adapted from Decanini and Fantin (1986), and corrected by a regression study using the laboratory test data of this work.

The second strut model, proposed in Huang et al. (2020), also consists of a 4-lines backbone curve; however, the characteristic strength and deformation values were obtained by a multivariate regression analysis. Finally, the third strut model, proposed in ASCE/SEI 41 (2017), consists of a 2-line backbone curve, as shown in Figure 4.5d.

Table 4.4: Macro-model constitutive parameters for three deterministic models proposed by others and used herein.

	Liberatore et al. (2018)	Huang et al. (2020)	ASCE/SEI 41 (2017)
Strength -1^{st} stiffness drop	$0.40V_p$	$0.72F_c$	-
Strength -2^{nd} stiffness drop	$0.85V_p$	-	-
Maximum strength	$V_p = \frac{\min(V_s, V_{dt}, V_{dc}, V_{cc})}{1.02}$	$F_c = \frac{f_m^{0.196} t_m^{0.867} l_d^{0.792}}{265.53}$	$V_P = v_m L_m t_m$
Residual strength	0	$0.40F_c$	0
Deformation -1^{st} stiffness drop	$0.00025H_m$	$\frac{0.72F_c}{K_e}$	
Deformation -2^{nd} stiffness drop	$0.0013H_m$	-	
Deformation - max. strength	$0.00294H_m$	$\delta_c = \frac{E_m^{-0.197} H_m^{0.978} L_m^{-0.978}}{64.94}$	$\min\left(\frac{V_P}{K_m}, \delta_r\right)$
Maximum deformation	$0.0344H_m$	$\frac{0.60F_c}{K_{pc}} + \delta_c$	

f_m, E_m: masonry characteristic compressive strength and elastic modulus, respectively. t_m: thickness of the wall, l_d, θ: length and direction of the diagonal of the wall, respectively. H_m, L_m: height and length of the wall, respectively. $V_s = [(1.2\sin\theta + 0.45\cos\theta)\,\tau_0 + 0.3\sigma_y]\,t_m L_m$: bed-joint sliding failure mode; $V_{dt} = (0.6\tau_{m0} + 0.3\sigma_y)\,t_m L_m$: diagonal tension failure mode; $V_{dc} = 1.16\tan\theta\,(\lambda_h)^{-1} f_m t_m L_m$: diagonal compression failure mode; $V_{cc} = 1.12\sin\theta\cos\theta\lambda_h^{-0.88} f_m t_m L_m$: corner compression failure mode. τ_0: bed joints basic shear strength, τ_{m0}: shear strength from diagonal compression test, σ_y: vertical stress, λ_h: Stafford-Smith coefficient (see Equation (6.1)). $K_e = 0.0143 E_m^{0.618} t_m^{0.694} H_m^{-1.096} L_m^{1.096}$: initial stiffness of the compressive strut, according to strut model 2. $K_{pc} = -1.278 f_m^{-0.357} t_m^{-0.517} K_e$: post-capping stiffness, according to strut model 2. $K_m = 1/\left(k_f^{-1} + k_s^{-1}\right)$: stiffness of the MIF system as a serial combination of frame stiffness (k_f) and shear wall stiffness (k_s). δ_r: residual deformation as a function of columns shear strength and stiffness and wall shear strength and stiffness, according to ASCE/SEI 41 (2017).

As an example application, the aforementioned models were put to the test in a blind estimation of the laboratory experiment carried out by Morandi et al. (2018b). The specimen consisted on a reinforced concrete frame with an infill wall made of clay masonry units. The columns were 350x350 mm cross section with 2.48 % of longitudinal reinforcement ratio and two 8 mm diameter stirrups at 90 mm spacing. The beam was 350x350 mm crosss section with 0.503 % of both superior and inferior longitudinal reinforcement ratio, with two 8 mm diameter stirrups at 70 mm spacing. The characteristic compressive strength of the concrete was 34 MPa, and the reinforcement yield strength was approximately equal to 500 MPa. The characteristic compressive strength of the masonry wall system was reported equal to 3.86 MPa. The masonry units were 235x235x350 mm, where 350 mm corresponds to the thickness of the wall. In Figure 4.7, a comparison is shown of the estimations of the three models against the test result. The following conclusions can be made:

- The ASCE/SEI and Liberatore models do a fair prediction of the initial stiffness of the frame. However, Huang model sub-estimates this characteristic.
- Both Liberatore and Huang models over-estimate the ultimate shear strength of the system. On the other hand, the ASCE/SEI model sub-estimates the shear strength.
- Both Liberatore and ASCE/SEI models seem to properly capture the strength degradation of the system, as the strength drops at about 40 mm of lateral deformation. In the case of Huang model, the lateral strength does not degrades during the history of deformation.
- None of the models properly captures the pinching effects.
- Even though these models have some limitations, they constitute a fair balance between simplicity of modelling and quality of the prediction. Their application on a probabilistic framework is preferable.

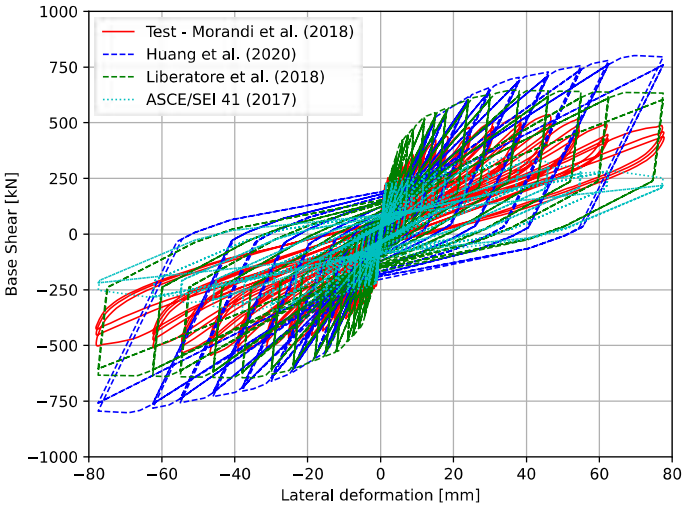

Figure 4.7: Comparison of three MIF macro-models to the test results from Morandi et al. (2018b).

4.3 Artificial Neural Networks

4.3.1 Concepts

Artificial neural networks (ANN) are a numerical method that combines machine learning and data science. In a simplified way, they can be defined as a *black box* model, in which a series of data are inserted, from which one or several results are obtained. However, the main strength of this *black box* model is that its formulation is based on observation. Internally, the model can be represented in a graph similar to the one shown in Figure 4.8, where data travels trough links from node to node, each node receives that input data, performs a task and delivers an output (see Figure 4.9). This inter-connection between nodes resembles

that between neurons in the brain, hence the name. The following characteristics can be observed in the aforementioned Figure:

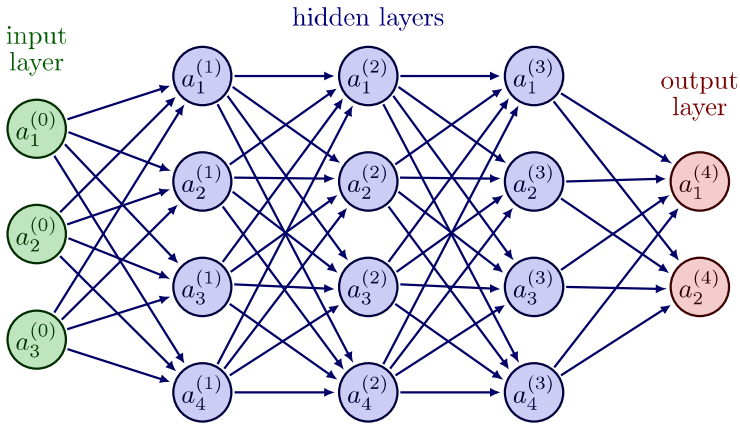

Figure 4.8: Example of an artificial neural network architecture (drawings using Neutelings (2022) libraries).

- Nodes or neurons: these are representations of mathematical functions that use the weighted sum of input values and the *bias* to calculate the output result by means of the *activation function*. The *bias* is a parameter associated to each node. Figure 4.10 shows some of the most common activation functions that are used within a neuron. Mathematically, the behavior of a neuron can be represented by the following equation:

$$y_j = \sigma\left(\sum_i a_i w_i + b_j\right) \tag{4.4}$$

  Where y_j is the output, a_i and w_i are each of the i inputs of the neuron with their corresponding weights, b_j is the bias associated with neuron j and $\sigma()$ is the activation function of that neuron.

- Links: these lines represent the path that the data take between nodes. Each link is associated to a parameter, known as *weight*, which defines the contribution of the output data of a previous neuron into the next.

- Layers: these are a set of nodes that share the arrival of the same input data. The architecture of an ANN must always contain at least one input layer and one output layer. The intermediate layers between the two previous ones are known as hidden layers.

For the ANN model to meet its objective, it is necessary to generate the parameters w_i for each link and b_j for each neuron. The process to obtain these parameters is called *training*. For this purpose, there are some algorithms that optimize the parameter values to represent the input-output relationship of known conditions. Among the existing algorithms we can mention (Bhatt and Shrivastava, 2021):

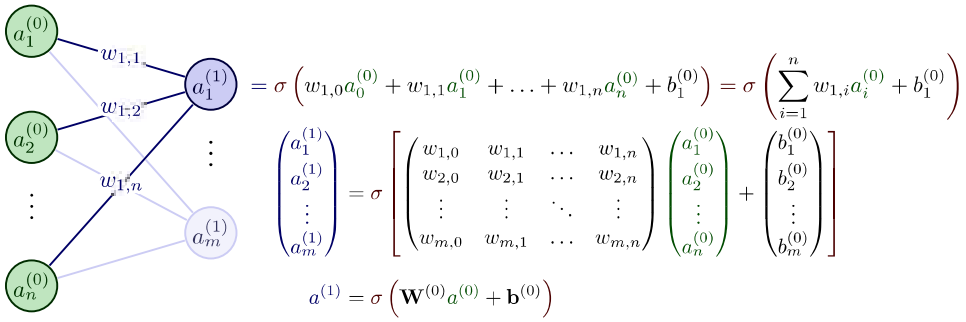

Figure 4.9: Illustration about the mathematical formulation of a neuron within an artificial neural network (drawings using Neutelings (2022) libraries).

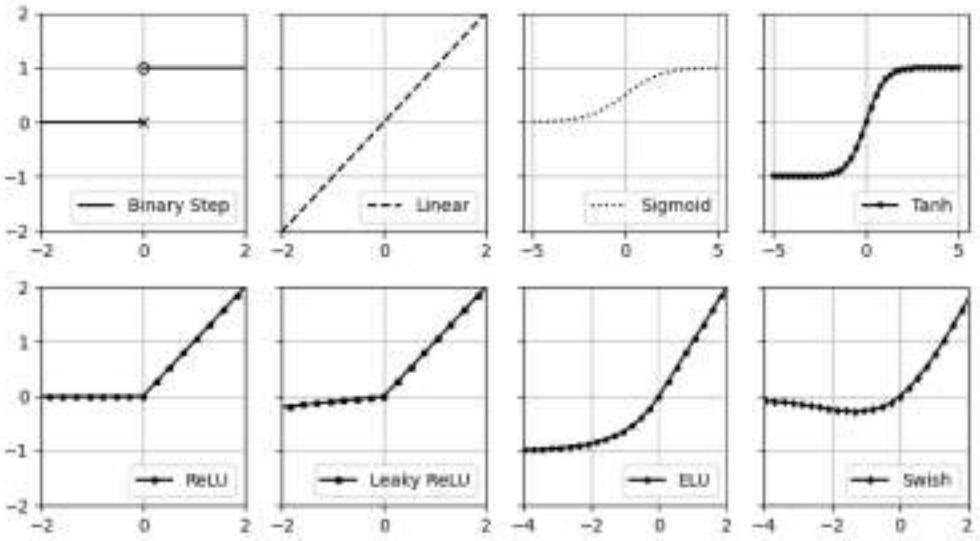

Figure 4.10: Most commonly used activation functions in ANN.

Levenberg-Marquardt, conjugate gradient, quasi-Newton and gradient descent. These models have a wide range of applications such as (Goodfellow et al., 2016) computer vision, speech recognition and natural language processing.

However, notice that the parameters defining an ANN model result from an optimization process and, therefore, do not contain information about the uncertainty inherent in a prediction (Fernández et al., 2023). This can be a disadvantage, especially when predictions are made outside the range of training data, since the model does not provide any information about the accuracy of the prediction. A particular neural network called a Bayesian Neural Network (BNN), can give a sense of accuracy of a prediction. In the BNNs, the parameters of the model are set as a distribution of plausible values and, therefore, the output is also a distribution.

4.3.2 Hamiltonian Monte Carlo based-Bayesian Neural Networks

Identifying the degree of belief in the predictions made by any model is of great importance (Ghahramani, 2015) and can be critical in the subsequent decision-making stage. Thus, BNN have been chosen as the data-driven method.

Among the state-of-the-art training algorithms for BNN, the Hamiltonian Monte Carlo (HMC) method (Neal, 1996), a variant of Markov Chain Monte Carlo (MCMC) (Gilks et al., 1996; Neal, 1993), is gaining importance and seems to be the gold standard nowadays (Benker et al., 2020). As other Bayesian training algorithms, HMC aims to find an approximation of the posterior distribution $p\left(\theta|\mathcal{D},\mathcal{M}\right)$ by sampling from a Markov Chain, where $\theta = \{w, b\} \in \Theta \subseteq \mathbb{R}^d$ represents the weights (w) and biases (b) of the BNN, $\mathcal{D}$ the data, and $\mathcal{M}$ the model class, which in this case is related to the BNN architecture.

The Hamiltonian method, in a context of conservative dynamics, is built on the premise that volumes are preserved. Every particle is defined by its position and momentum, and as a consequence, any change in the position space needs to be compensated with a change in the momentum space, so that the position-momentum phase space is maintained. In the Hamiltonian Monte Carlo context (Betancourt, 2017), the position space is replaced by the parameter space, and an auxiliary momentum variable p is adopted, hence any parameter value θ is associated with a momentum leading to the pair (θ, p). Once the momentum variable has been included and the parameter space converted to a phase space, namely $\theta \rightarrow (\theta, p)$, a joint probability distribution, namely the canonical distribution is defined as follows:

$$\pi(\theta, p) = \pi\left(\theta|q\right)\pi(q) = e^{-H(\theta,p)} \tag{4.5}$$

where $H(\theta, p)$ is the Hamiltonian function, also called as the energy at that point, and can be expressed as:

$$H(\theta, p) = -\log \pi(\theta, p) = -\log \pi\left(\theta|q\right) - \log \pi(\theta) \tag{4.6}$$

with $\pi\left(\theta|q\right)$ often assumed a Gaussian distribution $\mathcal{N}\left(p|0, M\right)$ with covariance matrix (also known as mass matrix) M, and $p \sim \mathcal{N}(0, I)$. In this method, new samples θ_n are drawn using the *leapfrog integrator* (Betancourt, 2017), with a step size ϵ and a path length L, as depicted in Algorithm 2. These samples are then accepted with probability α, as per Equation 4.7.

Algorithm 2 *Leapfrog Integrator*

1: Obtain initial samples $\theta_0 \leftarrow \theta$ and $p_0 \leftarrow p$
2: **for** $0 \leq n < {}^{L}/_{\epsilon}$ **do**
3: $\quad p_{n+\frac{1}{2}} \leftarrow p_n - \frac{\epsilon}{2}\frac{dV}{d\theta}(\theta_n)$
4: $\quad \theta_{n+1} \leftarrow \theta_n + \epsilon p_{n+\frac{1}{2}}$
5: $\quad p_{n+1} \leftarrow p_{n+\frac{1}{2}} - \frac{\epsilon}{2}\frac{dV}{d\theta}(\theta_{n+1})$
6: **end for**

$$\begin{aligned} \alpha &= min\left(1, \frac{\pi(\theta_{n+1}, -p_{n+1})}{\pi(\theta_n, p_n)}\right) \\ &= min\left(1, \frac{\exp(-H(\theta_{n+1}, -p_{n+1}))}{\exp(-H(\theta_n, p_n))}\right) \end{aligned} \tag{4.7}$$

The HMC algorithm is very sensitive to small variations in the step size and path length hyperparameters, thus finding the right values is a critical aspect of this method. The open source software *hamiltorch*[1] has been used in this thesis for the implementation of the HMC algorithm. The hyperparameters have been chosen as follows: step size $\varepsilon = 0.001$, leapfrog steps $L = 10$, the prior PDFs of θ, namely, $p(\theta)$, are chosen as Gaussian with prior precision for the parameters $\tau = 1$, likelihood output precision $\tau_{out} = 100$ and 500 samples where 250 are burned. The chosen activation function for the hidden layers is the Rectified Linear Unit *ReLu* and the activation function for the output layer is the *Sigmoid*.

[1] https://github.com/AdamCobb/hamiltorch

Part II

Methodological Contributions

Chapter 5

$\mathcal{A}^2$BC-SubSim

In this chapter, a new Approximate Bayesian Computation algorithm with reduced hyper-parameter scaling and its application to non-linear structural model calibration problems, is presented. The algorithm initially takes the ABC-SubSim algorithm structure and sequentially estimates the algorithm hyper-parameter by autonomous adaptation following a Markov Chain approach, thus avoiding the error associated to modeller's choice for these hyper-parameters. The resulting algorithm, named "Adaptive Approximate Bayesian Computation by Subset Simulation" or $\mathcal{A}^2$BC-SubSim, simplifies the application of ABC-SubSim method for new users whilst ensuring better measure of accuracy in the posterior distribution and improved computational efficiency. A first numerical application example is provided for illustration purposes and to provide a comparative and sensitivity analysis of the algorithm with respect to initial ABC-SubSim algorithm. Moreover, the efficiency of the method is demonstrated in two non-linear structural calibration case studies where the $\mathcal{A}^2$BC-SubSim is used as a tool to infer structural parameters with quantified uncertainty based on test data. The results confirm the suitability of the method to tackle with a real-life damage parameter inference and its superiority in relation to the original ABC-SubSim. Most of the content of this chapter have been covered in a publication by the author (Barros et al., 2021); however, additional examples, discussion and details are presented here for completeness.

5.1 The $\mathcal{A}^2$BC-SubSim algorithm

As seen above, the conditional probability p_0 in ABC-SubSim is an hyper-parameter which needs to be fixed in advance. As shown in Chiachio et al. (2014), p_0 has a strong influence on the computational burden of the algorithm along with the quality of the ABC posterior approximation. The *Adaptive Approximate Bayesian Computation by Subset Simulation* method avoids the manual tuning of p_0 by numerical adaptation, as shown next.

First, let us consider that $\bar{P}_j$ is not fixed to a specific value p_0 and that a sequence that follows a Markov

chain, as $\bar{P}_1, \bar{P}_2, \ldots, \bar{P}_j, \ldots, \bar{P}_m$, whose initial state $\bar{P}_1 = p_1$ is known, whilst the rest $\bar{P}_j = p_j, j \geqslant 2$, are randomly chosen from a truncated normal probability density function (PDF) given by:

$$\mathcal{N}^*(a, b, \mu, \sigma) = \frac{1}{\sigma} \frac{\phi\left(\frac{x-\mu}{\sigma}\right)}{\phi\left(\frac{b-\mu}{\sigma}\right) - \phi\left(\frac{a-\mu}{\sigma}\right)} \tag{5.1}$$

where a and b are the lower and upper truncation values, μ and σ are the mean and standard deviation respectively, $\phi(\cdot)$ is the standard normal PDF, and $\phi(\cdot)$ is its cumulative distribution function.

Next, let us consider that a sample of K values $p_j^{(1)}, p_j^{(2)}, \ldots, p_j^{(k)}, \ldots, p_j^{(K)}$, distributed following Equation (5.1) are available as possible candidates for any subset $j \geqslant 2$. To determine the best choice for p_j, let us now introduce a weighting function $\omega_k : \mathbb{R} \to [0, 1]$, which assigns a value within the $[0, 1]$ interval to each sample $p_j^{(k)}$, so that the chosen $p_j = p_j^{(k)}$ is selected with probability ω_k among the K samples. This weighting function is defined based on the following criteria:

- The expected acceptance ratio of the Markov chain Monte Carlo (MCMC) algorithm, α, which should be as near as possible to an optimum value;
- The selected p_j, which should preferably produce an associate tolerance value ξ_j as close as possible to the final tolerance, ξ_f.

The first criterion is based on Papaioannou et al. (2015) observations on the optimum acceptance ratio of a MCMC algorithm, where $\alpha \approx 0.40$ is recommended to maximize the efficiency of the Subset Simulation method; note that this allows the modeller to avoid some required pre-runs to set a hyper-parameter for the original ABC-SubSim (Chiachio et al., 2014), like the variance in the proposal PDF. The second criterion is proposed to minimize the amount of subsets required to reach the final tolerance ξ_f thus increasing the computational efficiency. Therefore, the weighting function can be mathematically expressed as:

$$\omega_k = u_k \cdot v_k \tag{5.2}$$

where u_k and v_k are ad-hoc functions to take into account the first and second aforementioned criteria, respectively. The u_k factor can be any concave downward function whose maximum is located near the recommended value 0.40. In this work, the following expression is adopted for u_k (see Figure 5.1):

$$u_k = \exp\left(-\frac{(\tilde{\alpha}_k - 0.40)^2}{2\sigma_\alpha^2}\right) \tag{5.3}$$

where $\tilde{\alpha}_k$ is the sample estimate acceptance ratio when $p_j^{(k)}$ is adopted, and σ_α is a factor to set the influence of u_k in ω_k. Further insight about the influence of σ_α on the computational efficiency is provided in Section 5.3.

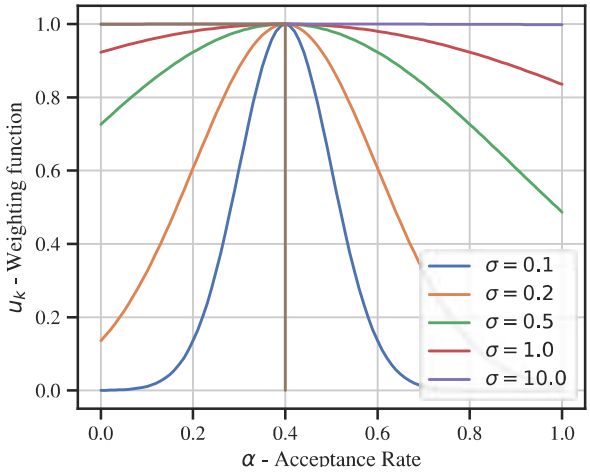

Figure 5.1: Plot of weighting function u_k in terms of the acceptance rate (α) for different values of σ_α parameter.

For the second factor v_k, a distance function is proposed as follows:

$$v_k = 1 - \frac{\xi_j^{(k)} - \xi_{\min}}{\xi_{\max} - \xi_{\min}} \tag{5.4}$$

where $\xi_{\min}$ and $\xi_{\max}$ represent the minimum and maximum metric values obtained for the $\{p_j^{(k)}\}_{k=1}^{K}$ samples. Note that Equation (5.4) makes unity when the intermediate tolerance $\xi_j^{(k)}$ associated to a trial $p_j^{(k)}$ equals $\xi_{\min}$ and zero in the opposite case. Note that the weighting function ω_k conveys a healthy balance between simulation efficiency and computational cost, which adaptively penalises the p_j values whose associated u_k or v_k are low and favours those whose balance is high. This observation is further discussed in Section 5.3, specifically in Figure 5.6c.

Finally, note that the choice of $p_j^{(k)}$ constitutes a stochastic random process and, therefore, the shape of u_k and v_k functions will not have significant influence on the behaviour of the algorithm, as long as their values lay within those proposed in Section 5.2. For instance, taking a different weighting function u_k^*, like the one in Equation (5.5), leads to similar results as denoted in Figure 5.6c, when comparing u_k^* to $\sigma_\alpha = 0.10$.

$$u_k^* = \begin{cases} 5\tilde{\alpha}_k - 1 & \text{if} \quad 0.2 < \tilde{\alpha}_k \leq 0.4 \\ 3 - 5\tilde{\alpha}_k & \text{if} \quad 0.4 < \tilde{\alpha}_k \leq 0.6 \\ 0.01 & \text{otherwise} \end{cases} \tag{5.5}$$

Similarly, taking a different weighting function v_k^*, as the following:

$$v_k^* = \left| \log \left(\frac{\xi_j^{(k)} - \xi_f}{\xi_0 - \xi_f} \right) \right| \tag{5.6}$$

where ξ_f is the final tolerance value and ξ_0 is the initial metric attained during the Monte-Carlo initialization of the algorithm, leads to similar results as depicted in Figure 5.2, where a comparison of the required number of evaluations is presented for 8 cases: (1-3) using v_k* formulation with n_k equal to 0.01, 0.05 and 0.10, (4-6) using v_k formulation with n_k equal to 0.01, 0.05 and 0.10, and (7-8) using the original ABC-SubSim algorithm with p_0 equal to 0.20 and 0.50, respectively.

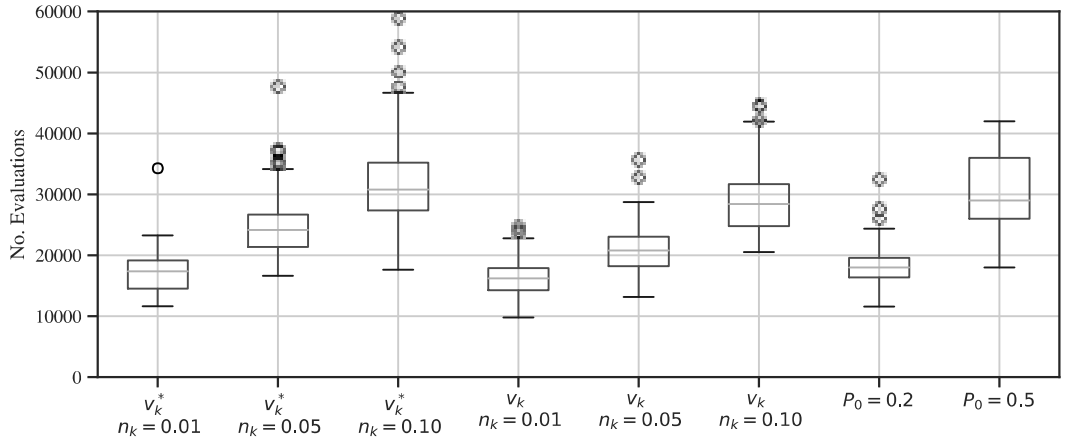

Figure 5.2: Comparison, in terms of the number of evaluations required to attain the tolerance value, of the expected computational cost of $\mathcal{A}^2$BC-SS algorithm with n_k equal to 0.01, 0.05 and 0.10, using v_k* and v_k factors. ABC-SubSim results are shown for p_0 equal to 0.20 and 0.50.

An algorithmic description of $\mathcal{A}^2$BC-SubSim is presented as Algorithm 3. The adaptive selection process of p_j values is shown in steps 8 to 22. Note that the hyper-parameter K is used to set the amount of p_j candidates to be evaluated in every subset, whereas n_k sets the algorithm runs needed to estimate the functions u_k and v_k. To alleviate computational cost, the algorithm is implemented so that similar p_j candidates (say, with less than 1% difference) are evaluated only once. A flowchart of the proposed algorithm is presented in Figure 5.3, which also depicts how the ABC-SubSim steps are integrated into the $\mathcal{A}^2$BC-SubSim.

5.2 Illustrative example

Let us consider a cantilever prismatic column (see Figure 5.4) with 0.4 [m] square cross section, 2 [m] length which is loaded at the top with a force $F = 1$ [kN]. For the sake of illustration, let us also consider that the structural material degrades at a unknown constant rate ζ affecting the Young modulus by reducing it

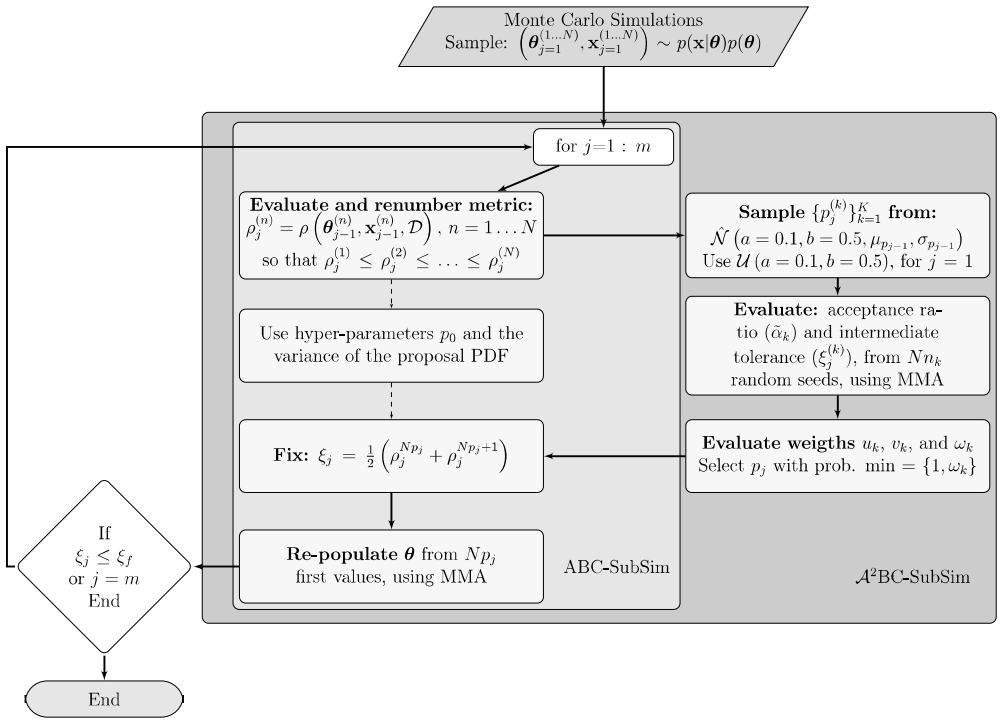

Figure 5.3: $\mathcal{A}^2$BC-SubSim algorithm flow-chart. Dashed arrows show the path of the original ABC-SubSim whilst solid ones display the proposed parameter auto-tunning steps.

from an initial value $E_0 = 40$ [MPa] following the exponential function:

$$x_n = e^{-\zeta} x_{n-1} + \upsilon_n \tag{5.7}$$

where subscript $n \in \mathbb{N}$ denotes time in weeks, x refers to the Young's modulus prediction and υ is a model error term, which is assumed to follow a Gaussian distribution with zero mean and unknown standard deviation σ, i.e. $\upsilon_n \sim \mathcal{N}(0, \sigma)$. Also, a sensor is assumed to be available at the top of the column to measure weekly deflections δ_n following a measurement equation, as follows:

$$y_n = h(x_n) + \psi_n \tag{5.8}$$

where y_n refers to the measured deflection δ_n and ψ_n denotes the measurement error term, which is assumed as a Gaussian zero-mean distribution with a known standard deviation, i.e. $\psi_n \sim \mathcal{N}(0, \sigma)$ where $\sigma_\psi = 10^{-6}$, expressed in meters units. In Equation (5.8), the function $h : \mathbb{R}_{\geq 0} \to \mathbb{R}_{\geq 0}$ and can be expressed from elasticity theory as $h = \frac{FL^3}{3x_n I}$, where I is the inertia momentum of the cross section.

In this example, the degradation rate and the standard deviations of the model error term are selected as unknown model parameters, so that $\boldsymbol{\theta} = \{\theta_1, \theta_2\} = \{\zeta, \sigma\}$. The uniform PDFs $p(\theta_1) = \mathcal{U}[0.0001, 0.02]$ and $p(\theta_2) = \mathcal{U}[0.01, 2]$, respectively, are considered as prior PDFs for the model parameters. The data for

Algorithm 3 $\mathcal{A}^2$BC-SubSim algorithm

Input: N {number of samples per intermediate level}, n_p {size of the model parameters $\boldsymbol{\theta}$ vector}, K {number of trial samples of p_j}, n_k {fraction of N to define the amount of MCMC chains in each trial}, ξ_f {final tolerance value}, m {maximum number of simulation levels allowed}, $\bar{P}_1 = p_1 \in [0,1]$ {Unconditional probability from first simulation level. Can be fixed to 1 }, σ_α, {influence parameter from Eq. (5.3) }.

Output: $\boldsymbol{\theta} = \left(\boldsymbol{\theta}_m^{(1)}, \mathbf{x}_m^{(1)}\right), \ldots, \left(\boldsymbol{\theta}_m^{(N)}, \mathbf{x}_m^{(N)}\right)$

Algorithm

Sample $\left(\boldsymbol{\theta}_1^{(1)}, \mathbf{x}_1^{(1)}\right), \ldots \left(\boldsymbol{\theta}_1^{(N)}, \mathbf{x}_1^{(N)}\right)$, where $(\boldsymbol{\theta}, \mathbf{x}) \sim p(\mathbf{x}|\boldsymbol{\theta})p(\boldsymbol{\theta})$

Subset Simulations

for $j = 1, \ldots, m$ **do**

  for $n = 1, \ldots, N$ **do**

    Evaluate $\rho_j^{(n)} = \rho\left(\boldsymbol{\theta}_{j-1}^{(n)}, \mathbf{x}_{j-1}^{(n)}, \mathcal{D}\right)$

  end for

  Renumber $\left[\left(\boldsymbol{\theta}_{j-1}^{(n)}, \mathbf{x}_{j-1}^{(n)}\right), n : 1, \ldots, N\right]$ so that $\rho_j^{(1)} \leq \rho_j^{(2)} \leq \ldots \leq \rho_j^{(N)}$

  Set $\xi_{\min} = \rho_j^{(1)}$; $\quad \xi_{\max} = \rho_j^{(N)}$

  Adaptively select p_j

  Sample $\{p_j^{(k)}\}_{k=1}^K$, **if** $j = 1$, from: $\mathcal{U}(a = 0.1, b = 0.5)$, and from: $\hat{\mathcal{N}}\left(a = 0.1, b = 0.5, \mu_{p_{j-1}}, \sigma_{p_{j-1}}\right)$, **otherwise**

  for all k **do**

    Set $\xi_j^{(k)} = \frac{1}{2}\left(\rho_j^{Np_j^{(k)}} + \rho_j^{Np_j^{(k)}+1}\right)$

    Randomly select Nn_k seeds $\left(\boldsymbol{\theta}_{j-1}^{(1)}, \mathbf{x}_{j-1}^{(1)}\right), \ldots, \left(\boldsymbol{\theta}_{j-1}^{(Nn_k)}, \mathbf{x}_{j-1}^{(Nn_k)}\right)$

    Set $q = 0$ (Auxiliary variable)

    for $i = 1, \ldots, Nn_k$ **do**

      Generate `Ceil`$[1/p_j^{(k)}]$ states of a Markov chain from the seed $\left(\boldsymbol{\theta}_{j-1}^{(i)}, \mathbf{x}_{j-1}^{(i)}\right)$ (e.g. using Modified Metropolis Algorithm (MMA) Au and Beck (2001)): $\left[\left(\boldsymbol{\theta}_j^{(i),s}, \mathbf{x}_j^{(i),s}\right)\right]_{s=1}^{1/p_j^{(k)}}$

      Evaluate the metric $\rho_j^{(i),s} = \rho\left(\boldsymbol{\theta}_j^{(i),s}, \mathbf{x}_j^{(i),s}, \mathcal{D}\right)$

      if $\rho_j^{(i),n_k} <= \xi_j^{(k)}$ **then**

        $q \leftarrow q + 1$

      end if

    end for

    Calculate the acceptance ratio as $\tilde{\alpha}_k = \dfrac{q}{n_k N}$

    Evaluate u_k, v_k, and ω_k (use Eqs. (5.3), (5.4) and (5.2), respectively)

    Set $p_j = p_j^{(k)}$ with probability min $= \{1, \omega_k\}$

  end for

  Evaluate $\mu_{p_j} = \dfrac{\sum_{k=1}^{K} p_j^{(k)} \omega_k}{\sum_{k=1}^{K} \omega_k}$ and $\sigma_{p_j} = \sqrt{\dfrac{\sum_{k=1}^{K}\left(p_j^{(k)} - \mu_{p_j}\right)^2}{K}}$ for each pair of $\left(p_j^{(k)}, \omega_k\right)$ (used further in step 8 for next j)

  Fix $\xi_j = \frac{1}{2}\left(\rho_j^{Np_j} + \rho_j^{Np_j+1}\right)$

  for $\ell = 1, \ldots, Np_j$ **do**

    Select as seed $\left(\boldsymbol{\theta}_j^{(\ell),1}, \mathbf{x}_j^{(\ell),1}\right) = \left(\boldsymbol{\theta}_{j-1}^{(\ell)}, \mathbf{x}_{j-1}^{(\ell)}\right) \in \mathcal{H}_j$

    Run MMA to generate `Ceil`$[1/p_j]$ Markov chain states lying in $\mathcal{H}_j$: $\left[\left(\boldsymbol{\theta}_j^{(\ell),s}, \mathbf{x}_j^{(\ell),s}\right)\right]_{s=1}^{1/p_j}$

  end for

  Renumber $\left[\left(\boldsymbol{\theta}_j^{(\ell),s}, \mathbf{x}_j^{(\ell),s}\right) : \ell = 1, \ldots, Np_j; s = 1, \ldots, 1/p_j\right]$ as $\left[\left(\boldsymbol{\theta}_j^{(1)}, \mathbf{x}_j^{(1)}\right), \ldots, \left(\boldsymbol{\theta}_j^{(N)}, \mathbf{x}_j^{(N)}\right)\right]$

  if $\xi_j \leq \xi_f$ **then**

    End algorithm

  end if

end for

this example are synthetically generated from Equations (5.7) and (5.8), considering $\boldsymbol{\theta}_{\text{true}} = (0.005, 0.1)$ for a time period of 200 [weeks], i.e. $\mathcal{D} = \{\delta_n\}_{n=0}^{200}$ as shown in Figures 5.5c and 5.5d (refer to the blue plot).

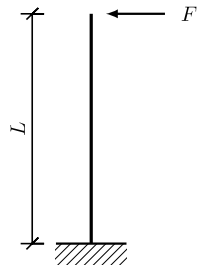

Figure 5.4: Illustration of a cantilever column with an unstable material subjected to a constant lateral load at the top.

In this exercise, the ABC-SubSim and the $\mathcal{A}^2$BC-SubSim algorithms are comparatively used to estimate the approximate posterior $p_\xi(\boldsymbol{\theta}|\mathcal{D})$, with $\xi_f = 80$ [MPa], $N = 5000$ (amount of samples per intermediate level), and using a $\mathbb{L}_1-$norm as metric function, i.e., $\rho_{(\mathbf{x},\boldsymbol{\theta},\mathcal{D})} = \sum_{n=0}^{200} \|X_n - x_n\|$, where X_n is the Young modulus obtained from Equation (5.7) using $\boldsymbol{\theta}_{\text{true}}$, acting as measured Young modulus during the 200 weeks period. The ABC-SubSim algorithm is used with $p_0 = 0.2$, whereas the $\mathcal{A}^2$BC-SubSim is scaled using $\sigma_\alpha = 0.1$, $K = 3$, and $n_k = 0.02$, according to the suggestions given in Section 5.3.

The ABC-SubSim and the $\mathcal{A}^2$BC-SubSim results are presented in Figure 5.5. In panels (a), (b) circles represent samples in the model parameter space, whereas the brighter grey circles correspond to prior samples. To reveal the uncertainty reduction, the intermediate posterior are superimposed in increasing grey tones. The results show that the approximate posterior samples (in yellow) are close to the $\boldsymbol{\theta}_{\text{true}}$ in both cases. Panels (c) to (f) provide comparative analysis in terms of model accuracy and cumulative error with respect to the data. In this numerical example, the ABC-SubSim required $m = 5$ simulation levels with $25,000$ model evaluations to reach the desired tolerance, whereas $\mathcal{A}^2$BC-SubSim employed $17,016$ model evaluations and $m = 3$ simulation levels. Observe that the $\mathcal{A}^2$BC-SubSim posterior samples are substantially closer to $\boldsymbol{\theta}_{\text{true}}$, hence better model response can be obtained if posterior samples from $\mathcal{A}^2$BC-SubSim are used to reproduce the model.

5.3 Hyper-parameters evaluation

The $\mathcal{A}^2$BC-SubSim is presented in this thesis as a variant to the original ABC-SubSim algorithm to circumvent the need of manually scaling the hyper-parameter p_0; however Section 5.1 has shown that new control parameters are required, namely K, n_κ and σ_α. In this section, a sensitivity analysis is presented to show the influence of the aforementioned $\mathcal{A}^2$BC-SubSim control parameters whereby recommendations to fix their values can be obtained.

To this end, let us start by investigating the influence of K, which sets out the amount of p_j trial samples produced at the j_{th} simulation level. Figure 5.6a shows the statistics taken from 100 independent

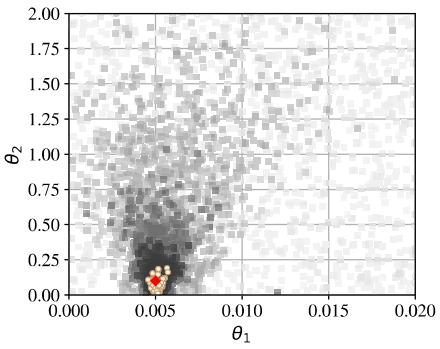

(a) $\mathcal{A}^2$BC-SubSim posterior output

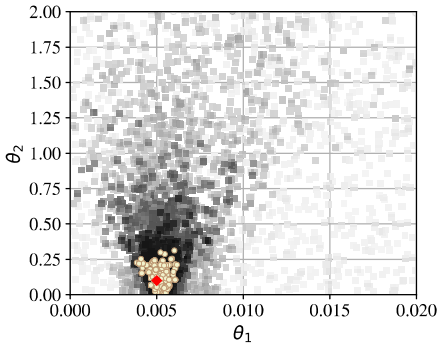

(b) ABC-SubSim posterior output

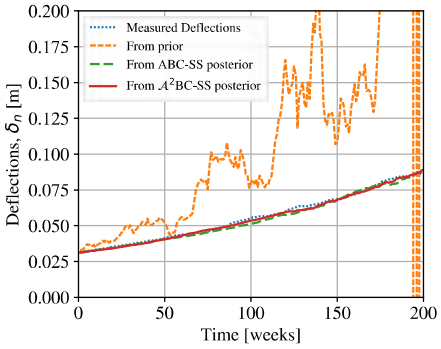

(c) Weekly evolution of column deflections

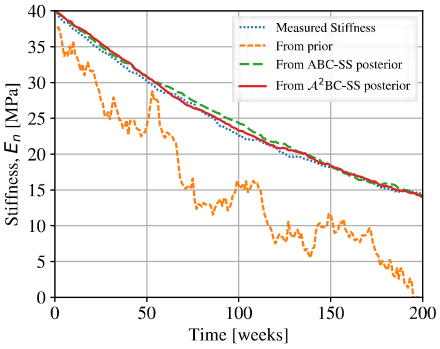

(d) Weekly evolution of Young modulus

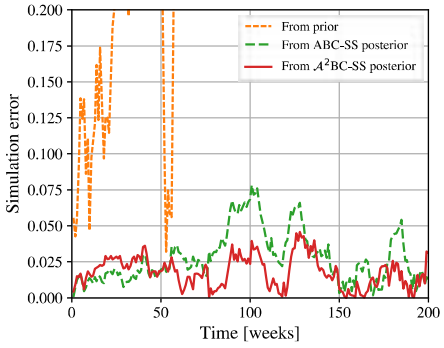

(e) Evolution of the error of simulated deflections

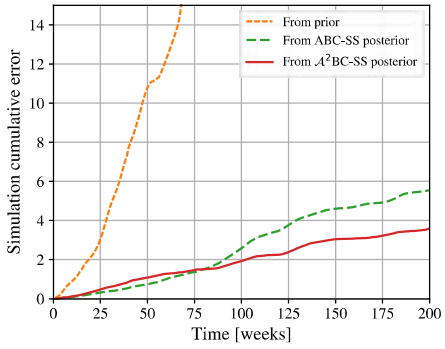

(f) Acumulated error of simulated deflections

Figure 5.5: Comparative results after the application of $\mathcal{A}^2$BC-SubSim and ABC-SubSim algorithms to the cantilever column example from Section 5.2. Panels (a) and (b) show scatter plots of posterior samples of $\boldsymbol{\theta}$ for intermediate levels, the final level (in yellow) and the true values (in red). Panels (c) and (d) represent evaluation of model response using the *Maximum a Posteriori* (MAP) values of the inferred model parameters $\boldsymbol{\theta}$. Panels (e) and (f) represent the comparative error on the simulation of the deflections.

runs of the algorithm using $K = \{3, 5, 10\}$, whereas the rest of hyper-parameters are fixed to $\sigma_\alpha = 0.1$, $n_\kappa = 0.04$, and $N = 2000$. The results are presented for the number of subsets required to reach the desired tolerance $\xi_f = 80$, amount of model evaluations, and metric evaluation. As expected, the higher the K,

the more amount of model evaluations are needed; however, the results also show that this parameter has negligible influence on the mean value and spread of the metric ρ and on the amount of required subsets.

Hence, a natural research question arises about whether a minimum K value can be defined in $\mathcal{A}^2$BC-SubSim. To this end, the weighting function ω (recall Equation (5.2)) is evaluated for two cases using $K = 3$ and $K = 10$. The results, shown in Figure 5.7 reveal that there are cases where the $\omega^{(k)}$-values can be fitted using a quadratic downward concave function, whose global maximum lies within any intermediate point of the $p_j^{(k)}$ values (panels (a) & (c)); in other cases (panels (b) & (d)) the maximum lies above the $p_j^{(k)}$ trials, corresponding to the one with higher ω-value. This suggests that, when using a quadratic downward function, $K = 3$ is enough to obtain the global maximum by interpolation.

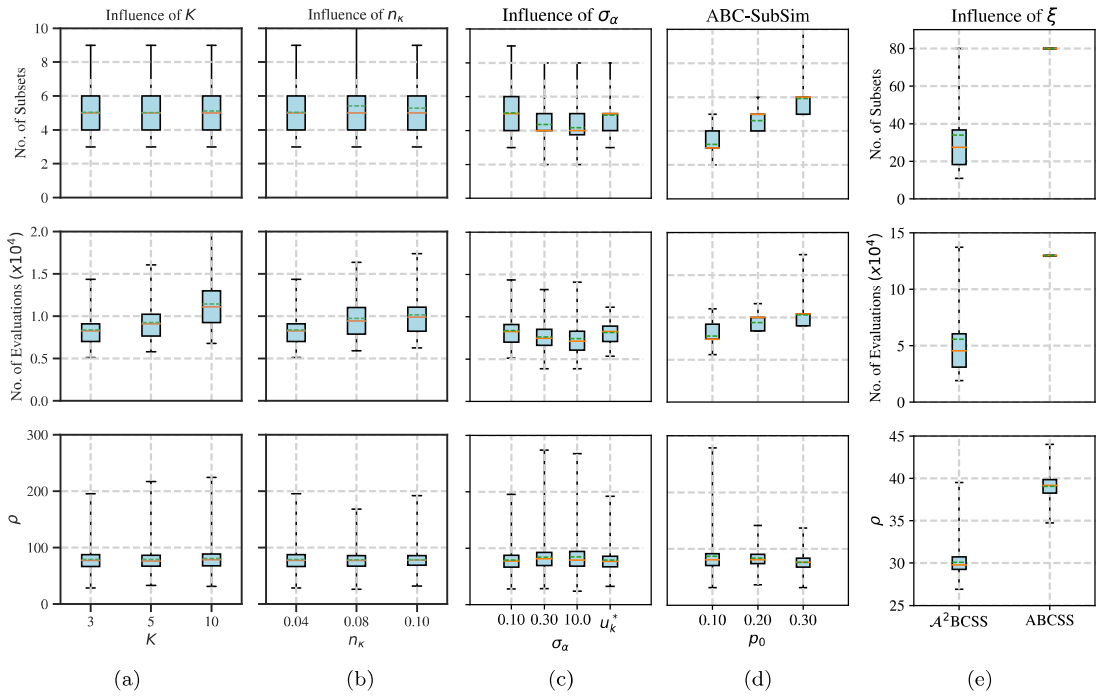

Figure 5.6: Sensitivity study using box-plots of the $\mathcal{A}^2$BC-SubSim hyper-parameters taken from 100 independent runs of the algorithm using $\xi_f = 80.0$ and $N = 2000$ for the cantilever example from Section 5.2. Panel (a) shows the algorithm response under variation of K. In panel (b), the hyper-parameters are fixed to $K = 3$, and $\sigma_\alpha = 0.10$, whereas $n_k = \{0.04, 0.08, 0.10\}$. In panel (c), $n_k = 0.04$, $K = 3$, and $\sigma_\alpha = \{0.1, 0.3, 10\}$. The term u_k^* in panel (c) refers to an alternative piecewise linear function used for comparison (refer to section 5.1). Panel (d) shows the original ABC-SubSim response using $p_0 = \{0.10, 0.20, 0.30\}$. Panel (e) shows a comparative analysis between ABC-SubSim and $\mathcal{A}^2$BC-SubSim using a more restrictive tolerance $\xi_f = 30$, and $p_0 = 0.2$ for the ABC-SubSim, and $K = 3$, $n_k = 0.04$, and $\sigma_\alpha = 0.1$ for the $\mathcal{A}^2$BC-SubSim.

Besides, panels (b) and (c) from Figure 5.6 show summarising statistics of the $\mathcal{A}^2$BC-SubSim output after the 100 runs by varying n_k and σ_α, respectively, whereas panel (e) shows the comparative performance of ABC-SubSim versus $\mathcal{A}^2$BC-SubSim using a more demanding tolerance, namely $\xi_f = 30$. As with K, the results show that the larger the n_k, the higher the amount of model evaluations required; however, its

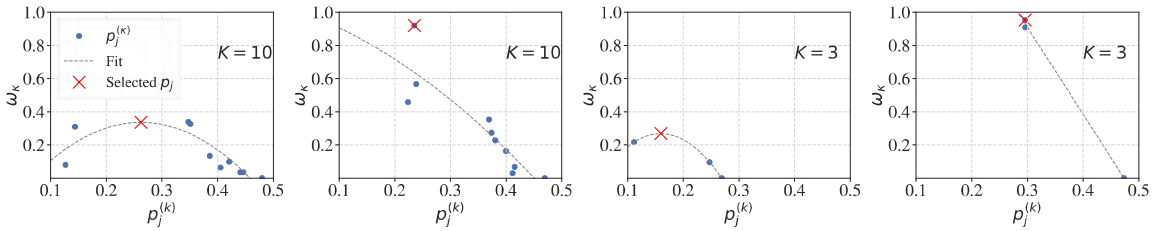

(a) (b) (c) (d)

Figure 5.7: Examples of the evaluation of weighting function ω_k for a number of $\{p_j^{(k)}\}_{k=1}^{K}$ candidates, where $K = 10$ for panels (a,b) and $K = 3$ for panels (c,d).

influence is negligible on the metric distribution and on the amount of subsets. Hence, a proper way to fix n_k is through a sampling formula like the Yamane's formula (Israel, 1992), which give us an estimation of a sample size based upon an error. Thus, the sample size $n_k N$ can be obtained as follows:

$$n_k N = \frac{N}{1 + NE^2} \tag{5.9}$$

where E is the admissible margin of error, which has been fixed to $E = 0.1$ in this work. Note from the last equation that the adopted $N = 2000$ and $E = 0.1$ lead to an estimated $n_k \simeq 0.04$.

Moreover, the results reveal that the algorithm efficiency is, in general, insensitive to the variation of σ_α, and also that, irrespective of the σ_α adopted, the algorithm behaviour is comparable to the ABC-SubSim behaviour when $p_0 = 0.1$, near the recommended value, as depicted in panel (d). Additionally, panel (e) shows that $\mathcal{A}^2$BC-SubSim turns to be considerably more efficient than ABC-SubSim when the algorithm is subjected to a more demanding tolerance. In this particular case, the results show that ABC-SubSim was unable to attain the required tolerance $\xi_f = 30$ after 80 simulation levels whereas $\mathcal{A}^2$BC-SubSim reached it using a mean of 30 simulation levels.

In summary, this analysis shows the small influence of the $\mathcal{A}^2$BC-SubSim hyper-parameters on the algorithm behaviour, hence a recommendation is to fix them to $K = 3$, $\sigma_\alpha = 0.1$, whereas n_k can be set using Yamane's formula with an admissible margin of error equal to 10%.

In addition, a comparison in terms of computational cost is carried out between $\mathcal{A}^2$BC-SubSim, using the recommended hyper-parameters (see the first result of either panel a, b or c in Figure 5.6) and the original ABC-SubSim (see panel d on the same Figure) using $p_0 = 0.2$, as recomended in Chiachio et al. (2014). The results show that, in average, the former required 12% less evaluations than the latter, depicting an improved computational efficiency. Using an Intel®Core™ i7-7700K CPU, 4.20 GHz processor, with 64 GB of RAM running on Windows 10-64 bits, on Python 3.8.3, Spyder 4.1.4, the ABC-SubSim required 504 seconds for the metric evaluations of 100 runs, while $\mathcal{A}^2$BC-SubSim required 441 seconds. Also, the $\mathcal{A}^2$BC-SubSim got better measure of the accuracy in the posterior distribution, as the metric function reached 17% lower values. These results, which demonstrate some improvement of both accuracy and

efficiency, are in addition to the significant computational savings obtained by avoiding the manual scaling of the hyper-parameter p_0.

As final exercise, the sequence of p_j has been obtained to show how these values evolve as the algorithm progresses. The results are presented in Figure 5.8a after 100 independent runs of the $\mathcal{A}^2$BC-SubSim algorithm. Note that, in average, the p_j sequence follows a random path with a marked tendency to lie within the range of $p_j = [0.2, 0.3]$. Figure 5.8b shows the corresponding acceptance rate (α) per simulation level. Displayed in Figure 5.8b are also shown the mean acceptance rate values obtained from ABC-SubSim algorithm after 100 independent runs using $p_0 = 0.1$ (in blue squares dotted line) and $p_0 = 0.3$ (green rhomboids dotted line). Observe that the mean acceptance rate values of ABC-SubSim constitute average bounds of the $\mathcal{A}^2$BC-SubSim mean acceptance rate.

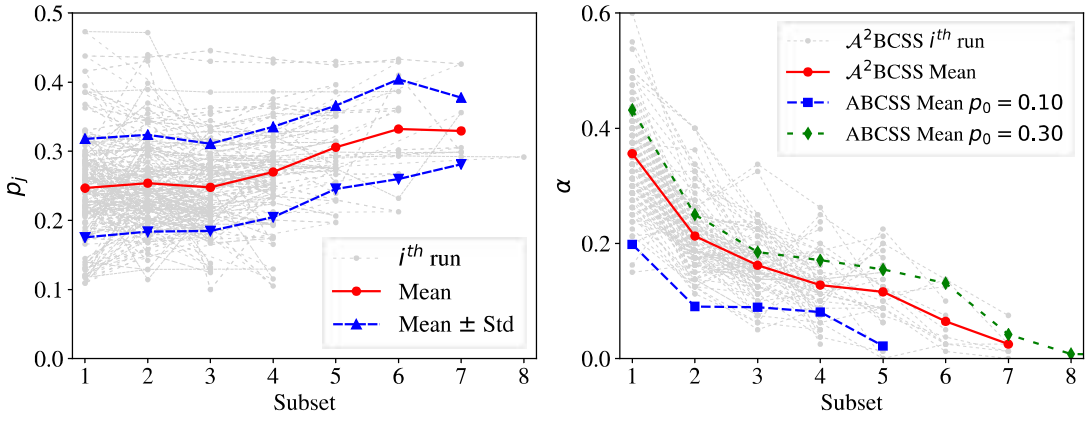

(a) Sequence of p_j values per simulation level

(b) Acceptance rate (α) per simulation level

Figure 5.8: Results from 100 independent runs using $\mathcal{A}^2$BC-SubSim, with $K = 3$, $n_\kappa = 0.04$ and $\sigma_\alpha = 0.10$ for the column example from Section 5.2. Also shown the equivalent mean results using ABC-SubSim with constant $p_0 = 0.10$ and $p_0 = 0.30$.

5.4 Application examples - non-linear model calibration

5.4.1 Cantilever Reinforced Concrete Beam-Column with cyclic degradation.

In this section the $\mathcal{A}^2$BC-SubSim algorithm is used to infer damage parameters from a non-linear mechanical model of a reinforced concrete column subjected to a constant axial load and cyclic lateral deformation. The column is 3300 [mm] high and 550x550 [mm] cross section, with longitudinal reinforcement ratio of 0.019 and 50 [mm] of coating, as depicted in Figure 5.9. The average compressive strength of the concrete is 23.1 [MPa] whereas the yield strength of longitudinal steel is 375 [MPa]. The transverse reinforcement is made of two 10 [mm] diameter stirrups with 297 [MPa] of yield strength and arranged as shown in Figure 5.9.

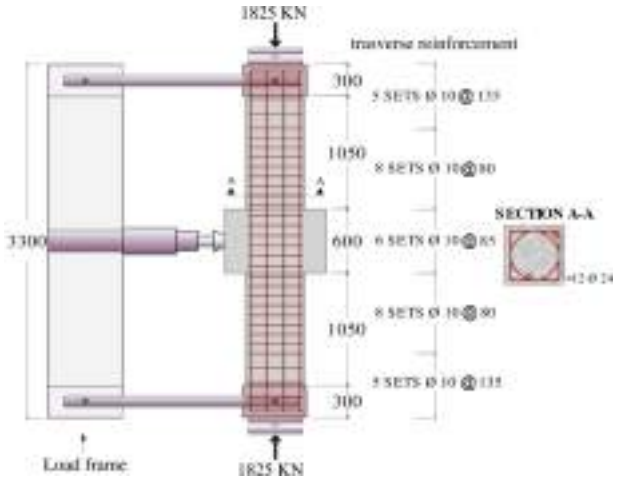

Figure 5.9: General geometry, reinforcement details, and test setup, adapted from Gill (1979). Length units are expressed in millimetres.

Non-linear forward model

The non-linear model consists of a force-based beam-column type element in cantilever along with a rotational spring modelled as a zero-length finite element, as depicted in Figure 5.10. The numerical implementation is carried out using the *OpenSeespy* software (Zhu et al., 2018). Thus, the reinforced concrete section is modelled by an OpenSees *fibre* section as shown in Figure 5.10 using the *Concrete01* material, whose input values are given in Table 5.1 for the cases of confined and unconfined concrete. These values have been set following the recommendations proposed by Karthik and Mander (2011) and the estimation of the confinement ratio proposed by Mander et al. (1988). The steel fibres for the longitudinal

Table 5.1: Input parameter values of *Concrete01* constitutive model taken for the engineering case study of Section 5.4.1.

Concrete	$\mathbf{f'_c}$ [MPa]	$\mathbf{f_{cu}}$ [MPa]	$\boldsymbol{\epsilon_{c0}}$ [%]	$\boldsymbol{\epsilon^*_{cu}}$ [%]
Confined	-34.70	-23.60	-0.641	-7.110
Unconfined	-23.10	-12.00	-0.183	-0.582

f'_c: concrete peak stress, f_{cu}: concrete ultimate stress ϵ_{c0}: concrete strain at peak stress, ϵ_{cu}: concrete ultimate strain

steel reinforcement are modelled using the OpenSees *Hysteretic* material and the recommended properties by the ASCE/COPRI (2014) regulations.

Three damage types are adopted to model the structural deterioration, namely: (1) damage due to ductility, (2) damage due to dissipated energy, and (3) unloading stiffness degradation (β), where parameters D_1, D_2, and β, are involved, respectively, as shown in Figure 5.11. The non-linear model is parameterized with a set of model parameters $\boldsymbol{\theta} = \{\theta_1, \theta_2, \ldots, \theta_8\}$, where θ_1 to θ_4 act as modifying factors of the physical parameters $\{F_y, F_{sh}, \epsilon_y, \epsilon_{sh}\}$, whilst θ_5 to θ_8 represent the parameters $\{p_x, p_y, D_1, D_2\}$,

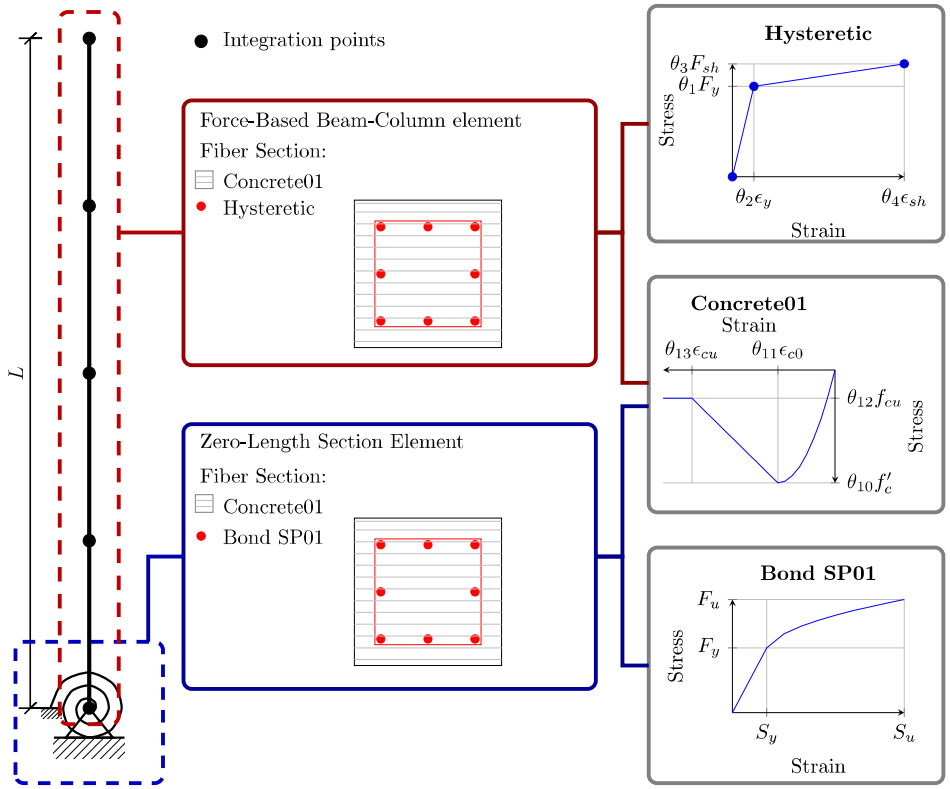

Figure 5.10: Schematic view of the proposed non-linear model of a reinforced concrete beam-column using OpenSees. On the right-side, plots of the constitutive material monotonic behaviour are presented, which include information about model parameterization.

respectively. The parameter β was also set equal to θ_8. The reader is referred to Figures 5.10 and 5.11 for a schematic description of these parameters within the context of the constitutive equations of the hysteretic material whereas the nominal values adopted for the physical parameters are provided in Table 5.2. Finally, for the case of the rotational spring element, the *Bond SP01* OpenSees material has been

Table 5.2: Nominal parameter values of *Hysteretic* constitutive model taken for the engineering case study of Section 5.4.1.

Steel	F_y [MPa]	F_{sh} [MPa]	ϵ_y [%]	ϵ_{sh} [%]
Reinforcement	375.00	468.80	0.188	1.5

adopted using the recommendations by Zhao and Sritharan (2007) to model the steel, which allows us to take into consideration the effect of strain penetration happening in the anchorage length of the steel reinforcement. Also, the recommendations by Coleman and Spacone (2001) have been adopted to define the ultimate strain corresponding to the constitutive behaviour of concrete fibres, as a function of the size of integration points of the frame beam-column elements (i.e. regularisation). In this work, Newton-Cotes

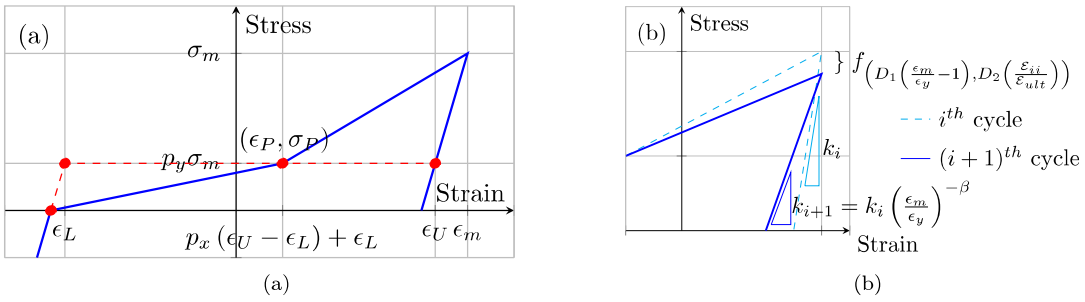

Figure 5.11: Panel (a): Schematic illustration of the in-cycle *Hysteretic* material behaviour. Panel (b): Schematic representation of the cyclic degradation (damage) parameters D_1, D_2, and β. The terms ϵ_y, $\mathcal{E}_{ii}$ and $\mathcal{E}_{ult}$, refer to the yield deformation, the i^{th}-cycle absorbed energy, and the maximum available energy, respectively.

Table 5.3: Hyper-parameter values adopted for the engineering case study of Section 5.4.1.

Parameter	K	n_k	σ_α	N	ξ_f	m
Value	3	0.05	0.10	2000	27550 $[N]$	30

integration method with five integration points is used. Indeed, the ϵ^*_{cu} values shown in Table 5.1 are obtained after the aforementioned regularisation procedure.

Then, through inference of the referred model parameters, the non-linear mechanical model can be updated based on experimental data.

Results

For the inference of parameters $\boldsymbol{\theta}$, force-displacement pairs taken from the column shown in Figure 5.9 are considered as data $\mathcal{D}$. The values are taken specifically from the specimen #1 in Berry et al. (2004) open-access database. Such specimen was axially loaded with 1815 [KN] and also subjected to a lateral cyclic displacement varying from ± 5 [mm] to ± 35 [mm]. Further information about the test and the data can be found in Berry et al. (2004). The $\mathcal{A}^2$BC-SubSim algorithm is applied by using the configuration

Table 5.4: Interval definition of the $\boldsymbol{\theta}$ parameter space for the case study of Section 5.4.1. Shown values are dimensionless.

Parameter	θ_1	θ_2	θ_3	θ_4	θ_5	θ_6	θ_7	θ_8
Lower bound	0.50	0.50	0.50	0.50	0.00	0.50	0.00	0.00
Upper bound	1.50	1.50	1.50	1.50	0.50	1.00	0.25	0.25

given in Table 5.3 and adopting a $\mathbb{L}_1$ norm as metric function over the force-displacement pairs, i.e.:,

$$\rho_{(\mathbf{x},\boldsymbol{\theta},\mathcal{D})} = \sum_{i=1}^{n_d} \|x_i - y_i\| \tag{5.10}$$

where y_i is the i^{th} lateral force data value from the test results, and x_i is the OpenSees i_{th} force value response obtained according to model parameters $\boldsymbol{\theta}$. Uniform PDFs taken over the intervals shown in Table 5.4 are adopted as a prior distribution of the model parameters $\boldsymbol{\theta}$.

The $\mathcal{A}^2$BC-SubSim results are presented in Figure 5.12 in terms of approximate posterior PDF $p_\xi(\boldsymbol{\theta}|\mathcal{D})$, whilst Table 5.5 provides some summarising statistics about the aforementioned PDFs. Note from Figure 5.12 that the approximate posterior of θ_4 and θ_8 are less informative than their component-wise counterparts, meaning that they capture less information from the data, thus their influence within the model to reproduce the data are comparatively lower. Moreover, Figure 5.20a depicts the hysteretic

Table 5.5: Posterior 5_{th} and 95_{th} percentiles, mean, standard deviation and $\boldsymbol{\theta}_{MAP}$ values of $\boldsymbol{\theta}$.

Parameter	θ_1	θ_2	θ_3	θ_4	θ_5	θ_6	θ_7	θ_8
$5^{\boldsymbol{\theta}}_{\text{th}}$	0.715	1.212	0.906	0.529	0.306	0.511	0.002	0.008
$95^{\boldsymbol{\theta}}_{\text{th}}$	0.968	1.485	1.032	1.473	0.457	0.666	0.020	0.183
Mean (μ)	0.837	1.362	0.964	0.988	0.378	0.580	0.009	0.091
Std. (σ_θ)	0.095	0.091	0.047	0.384	0.057	0.054	0.005	0.064
$\boldsymbol{\theta}_{MAP}$	0.898	1.481	0.992	1.369	0.443	0.668	0.02	0.144

response predicted by the model using the MAP of the model parameters $\boldsymbol{\theta}$ obtained by $\mathcal{A}^2$BC-SubSim versus the test curve showing that the model inferred using $\mathcal{A}^2$BC-SubSim algorithm can satisfactory reproduce the hysteric response, and that this model response is more accurate than the one using the current practice of a time-consuming and costly by-hand calibration method.

5.4.2 Group of structural tests

From the previous examples, it has been demonstrated that the $\mathcal{A}^2$BC-SubSim can be effectively used to infer structural non-linear modelling parameters from test data. In correspondence with current practice, where this kind of calibrations requires to be performed in a database of test results (Haselton et al., 2008), in the following example, the capacity of the algorithm is explored by performing a multiple-test calibration. Therefore, the data of four similar columns specimens were taken from Berry et al. (2004). All of the columns were selected from the work of Gill (1979), where the influence of axial load ratio on the flexural behaviour of reinforced concrete columns was studied. Concrete strength, transverse steel characteristics, and axial load ratio were the variables of the aforementioned investigation. The $\mathcal{A}^2$BC-SubSim is applied to calibrate the four models, assuming the axial load ratio as an independent variable to calculate the degradation parameters. The hyper-parameters of the algorithm were set as shown in Table 5.6, whereas the formulation for the degradation parameters were set as follows:

$$D_1 = \frac{P}{A_g f'_c}\theta_7 + \theta_{14} \tag{5.11}$$

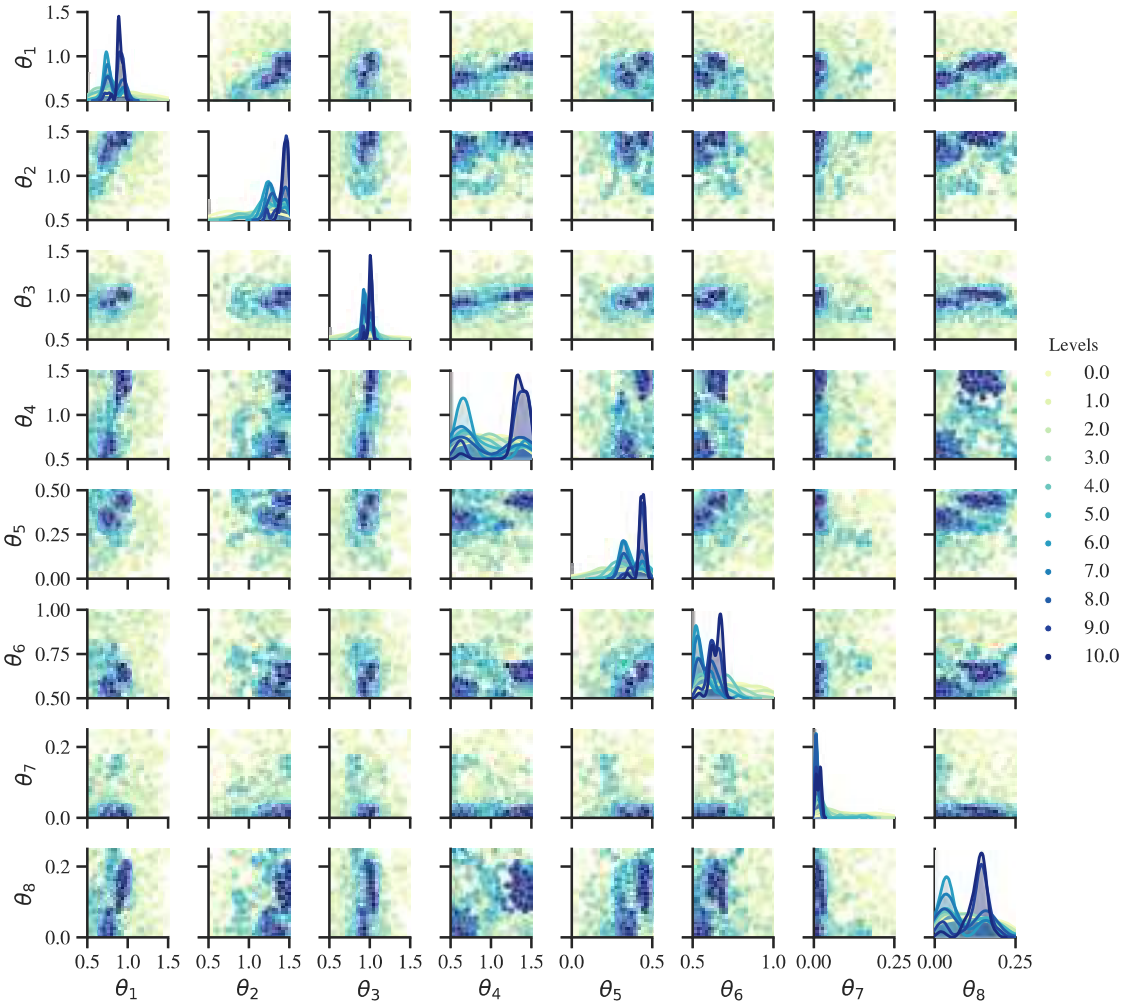

Figure 5.12: Scatter plot representation of the posterior PDF of $\boldsymbol{\theta} = \{\theta_1, \theta_2, \ldots, \theta_8\}$ as $\mathcal{A}^2$BC-SubSim output. On the diagonal, kernel density estimates are shown for the marginal posterior PDFs of the respective parameters.

Table 5.6: Algorithm hyper-parameter values adopted for the example in Section 5.4.2.

Parameter	K	n_k	σ_α	N	ξ_f	m
Value	3	0.05	0.10	5000	0.12	18

$$D_2 = \frac{P}{A_g f_c'}\theta_8 + \theta_{15} \tag{5.12}$$

$$\beta = \frac{P}{A_g f_c'}\theta_9 + \theta_{16} \tag{5.13}$$

where D_1, D_2 and β are the degradation and damage parameters (see Figure 5.11), whereas A_g denotes the concrete gross area of the cross section. *Prior* PDFs of parameters $\theta_7, \theta_8, \theta_9$ and $\theta_{14}, \theta_{15}, \theta_{16}$ are assumed as $p(\theta_7) = p(\theta_8) = p(\theta_9) = \mathcal{U}(-1.00, 1.00)$, and $p(\theta_{14}) = p(\theta_{15}) = p(\theta_{16}) = \mathcal{U}(0.00, 0.30)$, respectively. The rest model parameters along with their prior PDF definitions are considered the same as in Section 5.5.2. To directly consider the contribution of the four models, the metric is defined with the following equation:

$$\rho_{(\mathbf{x},\boldsymbol{\theta},\mathcal{D})} = 1 - \prod_{j=1}^{4} \left[1 - \frac{\sum_{i=1}^{n_d} \left\| x_i^j - y_i^j \right\|}{\sum_{i=1}^{n_d} \left| y_i^j \right|} \right] \tag{5.14}$$

where $j = 1, \ldots, 4$ is the index to consider each test contribution, and y_i^j and x_i^j are the i_{th} corresponding force value from the j_{th} test and model, respectively.

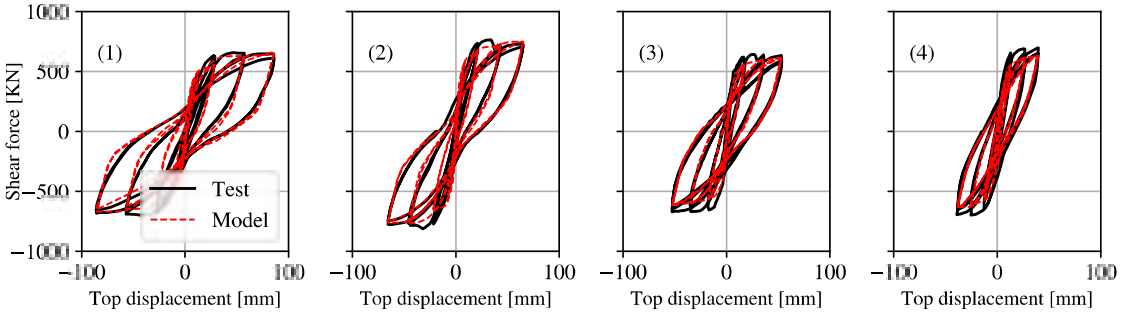

Figure 5.13: Results on the parameter inference of a group of four beam-column tests. The red dashed lines correspond to the MAP model results.

The lateral force vs deformation results are shown in Figure 5.13 denoting good agreement between the MAP model and the test results of each column of the group. The normalised difference between test and predicted model resulted equal to 16.90%, 10.15%, 9.97% and 11.80% for tests 1 to 4, respectively, achieving similar tolerance as the calibrations done in previous sections. Finally, Equations (5.11), (5.12) and (5.13) with the inferred parameters (see Figure 5.14) may be used to construct a column model that accounts for the influence of axial load ratio in the degradation of strength and stiffness.

5.4.3 A one-bay one-story reinforced concrete frame

The test configuration and results of an assemblage consisting of a single-story and single-bay reinforced concrete frame structure, subjected to a vertical constant load and a cyclic history of lateral deformation, tested by Morandi et al. (2018a), were selected from available data in the literature to demonstrate the capabilities of the proposed method.

The columns were 2950 [mm] clear high and 350x350 [mm] cross section, with longitudinal reinforcement ratio of 0.025 and 50 [mm] of coating. The beam is 4220 [mm] clear length and 350x350 [mm] cross section,

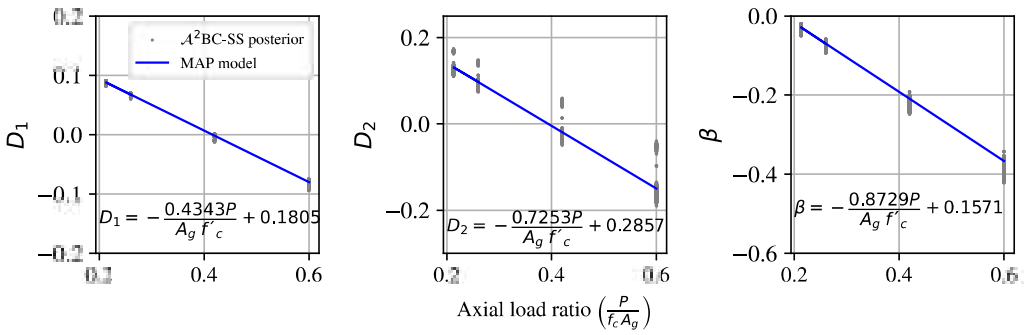

Figure 5.14: Obatained MAP degradation parameters formulation for D_1, D_2 and β in terms of the axial load ratio.

with flexural reinforcement ratio of 0.006 for both negative and positive flexure. The average compressive strength of the concrete was 34 [MPa], whereas the yield strength of longitudinal steel reinforcement was 530 [MPa]. A constant compressive load of 400 [kN] was applied and maintained to both columns during the test. The frame was subjected to several cycles of lateral deformation, where the shear force response was reported.

Parameter were set as shown in Figure 5.10 for both beam and columns, giving a parameter space of size $n_p = 26$. Figure 5.15a depicts the numerical model. Figure 5.15b demonstrates that the *blind model* can predict the dissipated energy of the assemblage only during the first cycles of lateral deformation and, after some cycles of deformation, this model under-predicts the behaviour of the frame, whereas the MAP model predictions get better agreement with the data during the entire test. Figure 5.15c shows a comparison of the reported shear force from the test, the calibrated model response using MAP values and the same model using nominal values without degradation (called *Blind model*). As can be noticed on the left panel of Figure 5.15c, the *blind model* is able to estimate the shear response of the assemblage at the first cycles of lateral deformation; however, after several cycles (see right panel), the *blind model* under-predicts the behaviour of the frame. Clearly, the MAP model prediction using $\mathcal{A}^2$BC-SubSim outperforms that of the *blind model*.

5.4.4 Complex structural model - 17 story building

In this section, the $\mathcal{A}^2$BC-SubSim algorithm is applied to infer several uncertain modelling parameters of a complex non-linear dynamical model. The data have been taken from a dynamical structural test performed by Pratap and Pujol (2021) over a 17-story physical model. In that investigation, the physical model was subjected to seismic records produced by a shake table. In this experiment, every story has approximate mass equal to 250 [kg]. Raw data from measurments, pictures and videos about this test are available at `https://datacenterhub.org/deedsdv/publications/view/564`. In this study, data from *TS1-Run2* experimental run was used to infer the modelling parameters. The data contain full

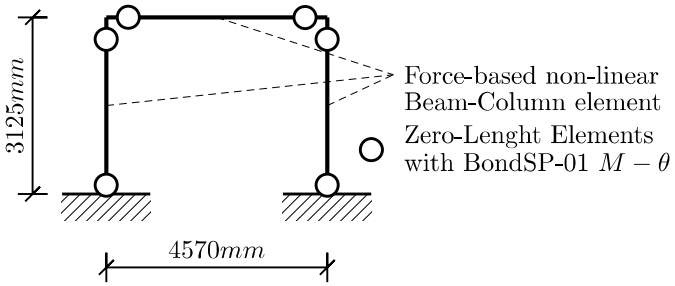

(a) Numerical model of reinforced concrete assemblage, i.e. one-bay one-story frame structure.

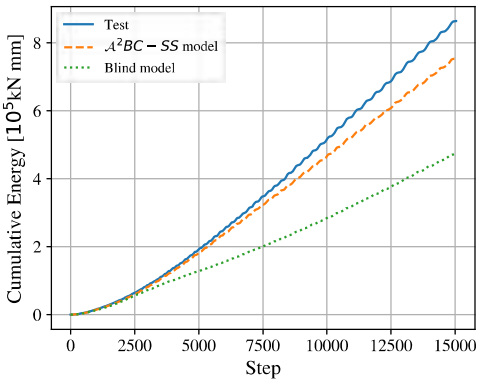

(b) Comparison of MAP model and blind model predictions in terms of cumulative energy.

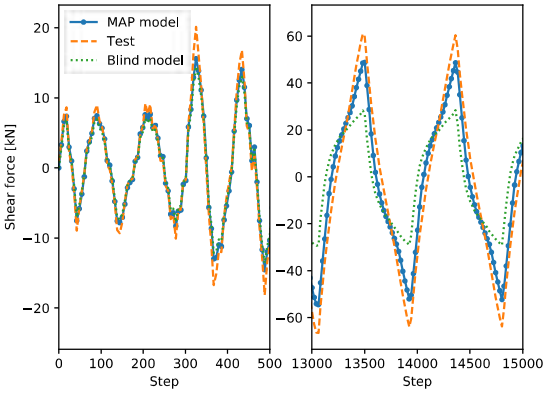

(c) Comparison of MAP model and blind model predictions in terms of shear force response.

Figure 5.15: Model and example calibration results of a structural assemblage consisting of an one-bay one-story frame test.

records of accelerations and displacements of the following stories: 4-th, 8-th, 9-th, 13-th, and 17-th. Raw measurements were read with a frequency rate equal to 1000 [Hz]. Some ppreprocessing of the data was required to eliminate noise, reduce the size of the records and rectify the condition biased results after integration of the acceleration signals; accordingly, the following post-processes were performed to the records: (1) a band-pass third-order butterworth filter between the range of frequencies 0.10 to 20 [Hz], (2) a downsampling to a frequency of 100 [Hz], and (3) a base-line correction of the acceleration records.

The mathematical model is conceived as a 17 in-series mass-spring-dashpots, where the springs are assumed to have an elastic-perfectly plastic behaviour. The parameters included in the inference are the elastic stiffness, yield strength of each floor (i.e. θ_1 to θ_{17} and (θ_{18} to θ_{34}), for each story stiffness and yield strength, respectively), and a unique damping coefficient for every dashpot (θ_{35}). The aforementioned parameters are unknown a priori, as that information is not available in the original data.

Both the ABC-SubSim and the $\mathcal{A}^2$BC-SubSim algorithms are applied to infer the referred 35 model parameters of the model. In the case of the $\mathcal{A}^2$BC-SubSim, the following hyper-parameters were adopted: $N = 3000$, $\xi_f = 0.04$, $m = 20$, along with the values recommended in Section 5.3 for the rest of

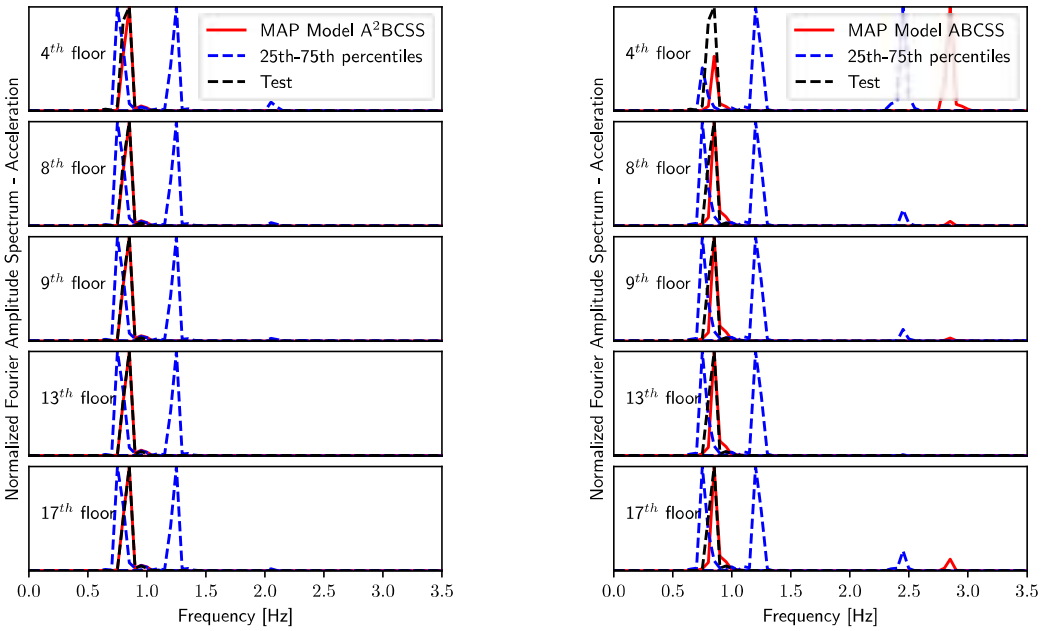

(a) $\mathcal{A}^2$BC-SubSim. (b) ABC-SubSim.

Figure 5.16: Comparison of Fourier amplitude spectrum of the acceleration records of the test measurements and those obtained from the inferred MAP model. The results are presented for stories 4, 8, 9, 13 and 17. Also, the model results using 25th and 75th percentiles of the parameters, are presented.

hyper-parameters. Uniform PDFs are considered as prior PDFs of the model parameters, such that $p(\theta_1) = p(\theta_2) = \ldots = p(\theta_{17}) = \mathcal{U}[3 \cdot 10^5, 3 \cdot 10^8]$; $p(\theta_{18}) = p(\theta_{19}) = \ldots = p(\theta_{34}) = \mathcal{U}[5 \cdot 10^5, 5 \cdot 10^8]$, and finally $p(\theta_{35}) = \mathcal{U}[1 \cdot 10^3, 1 \cdot 10^5]$, where the units are expressed in SI. In the case of the ABC-SubSim algorithm, the conditional probability was set as $p_0 = 0.2$ and the rest of the parameters were adopted in correspondence with the $\mathcal{A}^2$BC-SubSim case. The metric is defined as the relative difference of the Fourier amplitude spectrum of the modelled and measured accelerations, respectively, which is mathematically described as follows:

$$\rho = \sum_i \left| \frac{\hat{\mathbf{a}}^i - \mathbf{a}^i}{\mathbf{A}^i} \right| \tag{5.15}$$

In the last equation, the vectors $\hat{\mathbf{a}}^i$ and $\mathbf{a}^i$ contain the Fourier amplitude spectrum of the modelled and measured accelerations of the i-th story, respectively, whereas $\mathbf{A}^i$ is the resulting sum of the components of the vector $\mathbf{a}^i$. The index $i = \{4, 8, 9, 13, 17\}$ in correspondence with each story with available data.

The results of the inference using the $\mathcal{A}^2$BC-SubSim algorithm are shown in Figure 5.16a which provides a comparison of the Normalized Fourier amplitude spectrum of the accelerations obtained from the inferred MAP model, the 25th and 75th percentiles, and the spectra calculated from the measured results. Figure 5.16b shows the same results for the inference performed using the ABCSS algorithm. Notice that the MAP model obtained with the $\mathcal{A}^2$BC-SubSim algorithm outperforms the one with ABCSS.

Besides, Figures 5.17a and 5.18a respectively show the accelerations and displacements obtained after the model inference done with the $\mathcal{A}^2$BC-SubSim, in comparison to their corresponding experimental values. Note that these results are satisfactory since the algorithm has effectively inferred the model parameters so as to reproduce the experimental data with precision, measured by the MAP predictions. Notice that the inference with the ABCSS is also satisfactory but the obtained parameters resulted in a model where the second fundamental frequency becomes more participative, giving an apparent noise in the MAP model results (see Figure 5.17b), in correspondence with the results in Figure 5.16b. Similar conditions are depicted in Figures 5.18a and 5.18b

Finally, as mentioned in Barros et al. (2021), in average, the $\mathcal{A}^2$BC-SubSim algorithm required $3.5 \cdot 10^3$ [s] to perform the model inference of the 35 model parameters from this complex structural application, in contrast to the $4.0 \cdot 10^3$ [s] required by the original ABC-SubSim algorithm (approximately 15% difference). These results, which have been obtained using an Intel®Core™ i7-7700K CPU, 4.20 GHz processor, with 64 GB of RAM running on Windows 10-64 bits, and using Python 3.8.3, demonstrate that the proposed algorithm is able to perform inference in complex non-linear models with a feasible computational cost. Also, the results confirm again that the computational burden is improved with respect to the original ABC-SubSim algorithm.

5.5 Discussion.

5.5.1 Comparison with current practice trial and error model calibration

As a first step to compare the potential of the proposed methodology, a comparative analysis is carried out by considering the non-linear model response calibrated using the MAP of $\boldsymbol{\theta}$ from $\mathcal{A}^2$BC-SubSim algorithm, and the one manually calibrated following Barreiro (2018), taken as reference. In Barreiro (2018), an *ad-hoc* trial and error methodology enriched with some mechanical constraints was carried out obtaining a reasonable good model calibration using data from Berry et al. (2004). Similar handy calibrations were used by others on different structural models (i.e. Haselton et al. (2008); Sattar and Liel (2016b)) with analogous results. As pointed-out in the last section, results shown in Figure 5.19 reveal a better accuracy of the model response to the data when using the inferred parameters from the $\mathcal{A}^2$BC-SubSim method. To quantify the model prediction improvement, the Equation (5.10) is used to quantify the mismatch between the predicted and test data, rendering an output of $27,357[N]$ of accumulated error for the $\mathcal{A}^2$BC-SubSim inference procedure against $37,265[N]$ for the by-hand method by Barreiro (2018). This difference can be attributed to simplifications required for the manual scaling process leading to cumulative modelling errors. Indeed, in Barreiro (2018), parameters θ_1 to θ_6 were directly fixed from their nominal values and, therefore, they were not considered during the calibration process. Also, both the damage due to energy and the unloading stiffness degradation parameter (recall Figure 5.11) were constrained to be equal values. The output of the calibration in terms of model parameter values are shown in Table 5.7 for both methods.

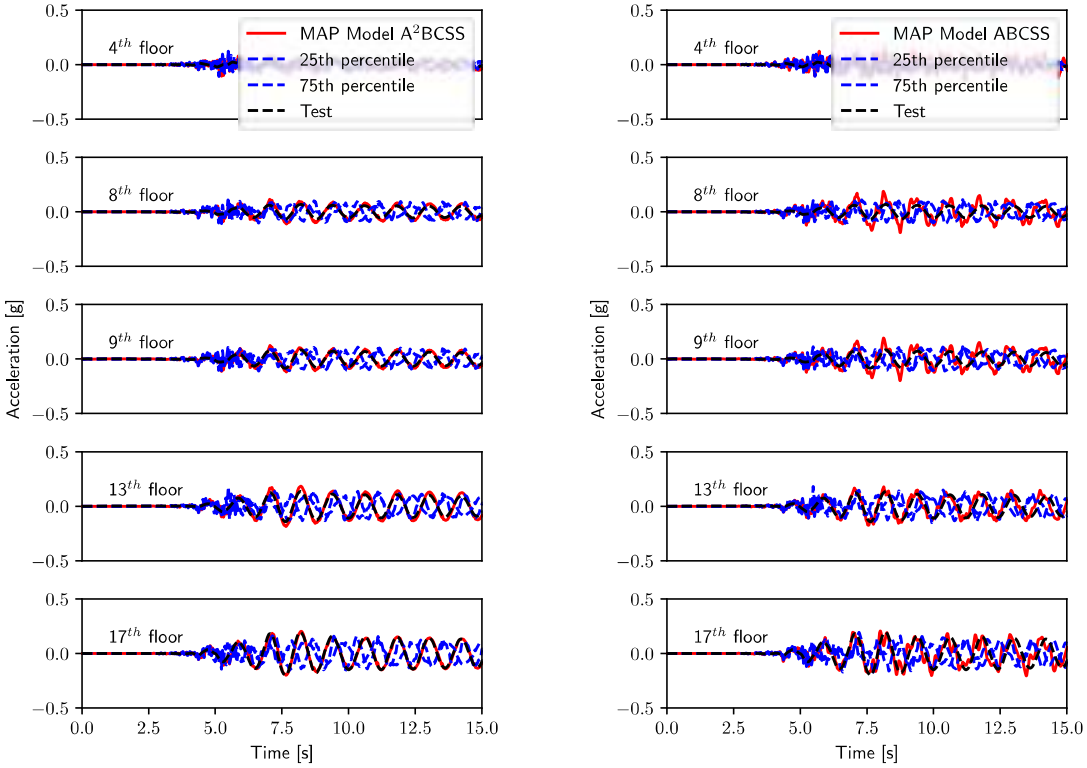

(a) $\mathcal{A}^2$BC-SubSim. (b) ABC-SubSim.

Figure 5.17: Comparison of the acceleration records of the test measurements to those obtained from the inferred MAP model and the 25th and 75th percentiles. The results are presented for stories 4, 8, 9, 13 and 17.

Parameters θ_7 to θ_9 in Table 5.7 refer to damage due to ductility, damage due to energy, and unloading stiffness degradation, respectively (note that the latter two parameters are now differentiated into θ_8 and θ_9, respectively).

Table 5.7: Calibration results from by-hand and $\mathcal{A}^2$BC-SubSim inference procedure. Results shown for the $\mathcal{A}^2$BC-SubSim case correspond to the maximum a posteriori values of the posterior PDFs.

Parameter	θ_1	θ_2	θ_3	θ_4	θ_5	θ_6	θ_7	θ_8	θ_9
$\mathcal{A}^2$BC-SubSim	0.893	1.453	0.992	1.276	0.425	0.657	0.017	0.149	0.149
By-hand	1.000	1.000	1.000	1.000	0.250	0.700	0.006	1.000	0.210

The results demonstrate that the proposed inference procedure using the $\mathcal{A}^2$BC-SubSim algorithm has the capability to reduce the human-factor error and reproduce the test data with higher accuracy than the case of using a by-hand calibration. Moreover, these results also show that an indirect inference of the model parameters can be obtained through the proposed method with quantified uncertainty, whereby robust predictions can be obtained. Thus, a richer knowledge of the actual behaviour of the constitutive

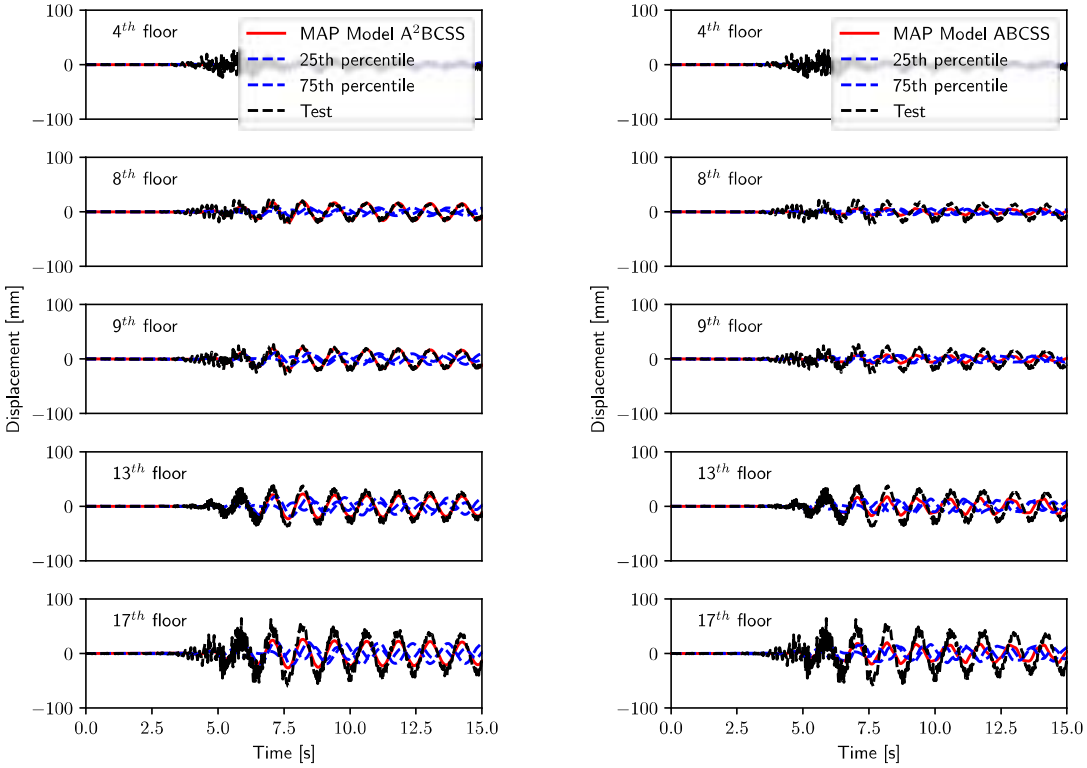

(a) (b)

Figure 5.18: Comparison of the displacement records of the test measurements to those obtained from the inferred MAP model and the 25th and 75th percentiles. The results are presented for stories 4, 8, 9, 13 and 17.

materials is possible through the information provided by the ABC posterior inference, which can be used for structural diagnostics purposes, among others.

5.5.2 Model consistency evaluation

The results shown in Sections 5.4.1 and 5.5.1 illustrate how the proposed algorithm can efficiently obtain model parameter inference for a non-linear structural case study using real-world data. However, it is worth mentioning that for this particular application the algorithm itself is unable to give a physically consistent response should the model parameters and their validity range are not properly selected. Thus, engineering judgement is required to validate the results of the model parameter inference. To illustrate this aspect, the steel constitutive model is reproduced after considering the posterior of model parameters $\boldsymbol{\theta}$ inferred using $\mathcal{A}^2$BC-SubSim. Figure 5.20a shows the inferred MAP value of the elastic module of the steel corresponding to the combined influence of parameters θ_1 and θ_2 (in red) which results about 40% lower than its nominal value (in blue). Note that the latter is inconsistent with the physical reality of the

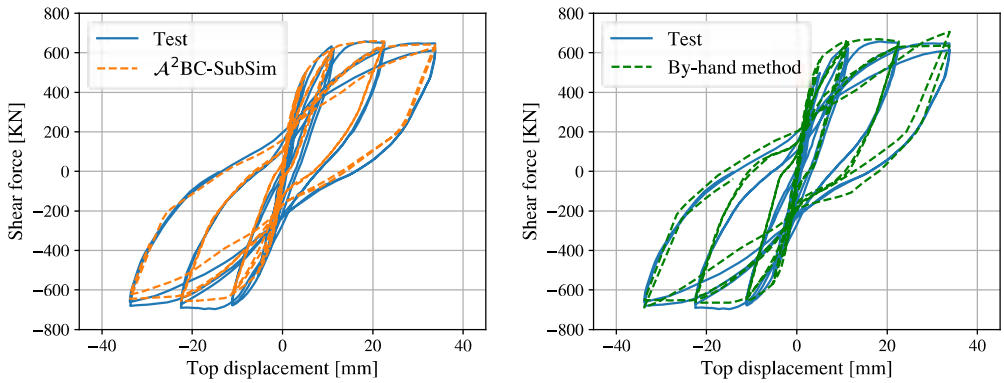

(a) $\mathcal{A}^2$BC-SubSim calibration

(b) By-hand calibration

Figure 5.19: Results of the comparative analysis of the non-linear mechanical calibration using (a) $\mathcal{A}^2$BC-SubSim method and (b) the by-hand trial and error procedure by Barreiro (2018). The blue line represents the displacement-shear force dataset from Berry et al. (2004).

steel behaviour, and an explanation to this can be given in terms of the algorithm response, which tries to converge to posterior values of the steel in liaison to the low stiffness values of the concrete due to the induced hysteretic damage.

To overcome this misbehaviour, the inference is performed again here including the following modification of model parameterization: (i) A new parameter θ_9 is used to replace θ_8 for the β parameter shown in Figure 5.11, using $p(\theta_9) = \mathcal{U}(0.00, 0.25)$ as prior PDF; (ii) Parameters θ_{10} and θ_{12} are introduced as modification factors for peak and ultimate stress values of the concrete constitutive model, as shown in Figure 5.10. The *prior* distributions adopted for these new parameters are taken as $p(\theta_{10}) = p(\theta_{12}) = \mathcal{U}(0.50, 1.50)$; (iii) Analogously, parameters θ_{11} and θ_{13} are used as modification factors for the strain values corresponding to peak and ultimate strain values of the concrete constitutive model, as shown in Figure 5.10. The *prior* distributions adopted for these parameters are assumed as $p(\theta_{11}) = p(\theta_{13}) = \mathcal{U}(0.50, 1.50)$. The

Table 5.8: Posterior 5_{th} and 95_{th} percentiles, mean, standard deviation and $\boldsymbol{\theta}_{MAP}$ values of $\boldsymbol{\theta}$, including concrete parameters.

	θ_1	θ_2	θ_3	θ_4	θ_5	θ_6	θ_7	θ_8	θ_9	θ_{10}	θ_{11}	θ_{12}	θ_{13}
$5^{\boldsymbol{\theta}}_{\text{th}}$	1.106	1.052	1.204	1.022	0.481	0.670	0.010	0.205	0.178	0.718	1.327	0.898	0.570
$95^{\boldsymbol{\theta}}_{\text{th}}$	1.131	1.093	1.222	1.128	0.499	0.699	0.011	0.240	0.194	0.727	1.350	0.931	0.594
μ	1.119	1.072	1.214	1.086	0.491	0.683	0.010	0.227	0.186	0.723	1.338	0.914	0.581
σ	0.007	0.013	0.006	0.030	0.006	0.008	0.000	0.011	0.005	0.003	0.007	0.011	0.010
$\boldsymbol{\theta}_{MAP}$	1.115	1.066	1.205	1.006	0.497	0.704	0.011	0.209	0.186	0.725	1.340	0.933	0.568

$\mathcal{A}^2$BC-SubSim algorithm configuration taken for this study is the same as the one shown in Section 5.4.1 (recall Table 5.3) except for the following changes: $n_p = 13$, $\xi_f = 20000$ $[N]$ and $m = 15$. Note that, in this case, ξ_f is set to a lower value with respect to the one chosen in Section 5.4.1, since the new parameterization allows reducing it to $\xi_f = 20000$ $[N]$ with similar computational cost. Results are

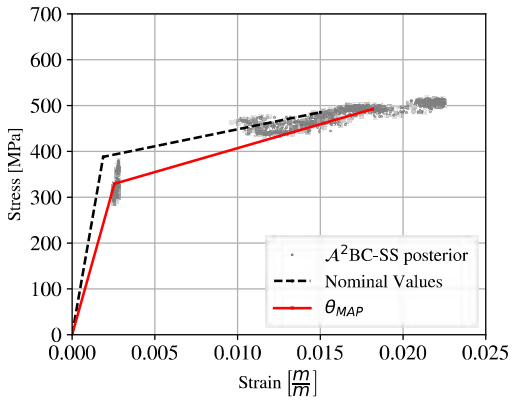

(a) Inferred steel constitutive model using parameterization given in Section 5.4.1.

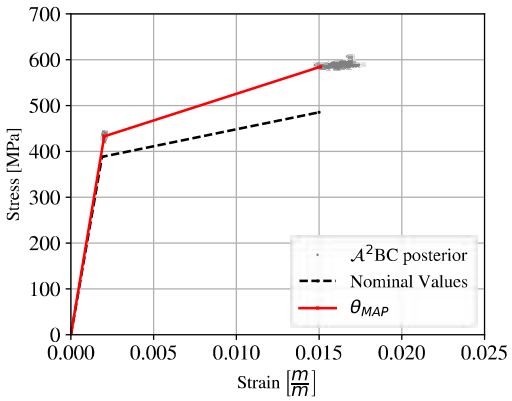

(b) Inferred steel constitutive model, including concrete behaviour modifiers in the parameterization.

Figure 5.20: Model results after calibration by ABC parameter estimation.

displayed in Table 5.8. Note that in this case, the inferred elastic module of the steel reinforcement is consistent with the expected steel behaviour, as shown in Figure 5.20b. Also, the new results are consistent with the typical dispersion expected in material stiffness, particularly for the 45% reduction of the concrete stiffness from its nominal value, which is an acceptable value. Also, a closer approximation was achieved in terms of the mismatch function, with an error equal to 23724 $[N]$ (i.e. $\xi_f \approx 11.3\%$). In summary, this discussion reveals that the solely use of $\mathcal{A}^2$BC-SubSim algorithm, as with many other inference algorithms, is not enough for an effective material diagnostics and further model calibration of complex non-linear models, and that engineering judgement is required to make the algorithm outputs consistent with the physics of the problem.

Chapter 6

Numerical modelling of masonry infilled frames

6.1 Database of IP MIF laboratory tests and mechanical model

A database of eighty five laboratory test results available in the literature has been used as input data for the analysis shown in the following sections. The tests within the database consist of one-bay and one-story MIFs, subjected only to IP lateral cyclic deformation. Table 6.1 provides an overview of the dataset considered with specification of the type of frame, masonry unit, amount of tests of each reference and presence of wall-openings. The selection of the data was limited to reported tests with complete information about the resistance and geometry of the materials, along with the force-displacement results (either graphics or tables). A summary of the information about the test can be found in Tables 6.2, 6.3 and 6.4.

The mechanical model consists of a shear one-dimensional non-linear spring with a tri-linear constitutive behaviour, as shown in Figure 6.1, which represents the shear response of the frame and the wall system as a whole. Figure 6.2 shows a distribution of a number of descriptive parameters of the MIF within the database. These parameters are the masonry unit type, failure type observed, height-to-thickness ratio, and a frame-infill stiffness relation, originally proposed by Stafford Smith and Carter (1969), also referred to as λ, which is given as follows:

$$\lambda = \sqrt[4]{\frac{E_m t_m \sin 2\gamma}{4 E_c I_c h_m}} \tag{6.1}$$

In the last equation I_c is the inertial momentum of the frame's columns, whereas E_m and E_c are the Young's moduli of the infill and frame, respectively. The terms t_m, h_m and γ, are the thickness, height and the slope of the representative diagonal of the infill, respectively.

Table 6.1: Database of experimental tests.

Reference	NT[a]	Frame / Masonry	TWO[b]
Flanagan and Bennett (1999)	13	Steel / Horizontal hollow clay brick	1
Markulak et al. (2013)	5	Steel / AAC and hollow clay bricks	0
Schneider et al. (1998)	5	Steel / Solid clay bricks	5
Tasnimi and Mohebkhah (2011)	5	Steel / Solid clay bricks	4
Morandi et al. (2018a)	4	RC / Hollow clay bricks	1
Basha and Kaushik (2016)	6	RC / Fly ash bricks	0
Calvi et al. (2004)	7	RC / Hollow clay bricks	0
Gazić and Sigmund (2016)	9	RC / Solid and hollow clay bricks	0
Guerrero et al. (2014)	3	RC / Hollow concrete bricks	0
Haider (1995)	4	RC / Solid clay bricks	0
Jiang et al. (2015a)	6	RC / AAC	0
Mansouri et al. (2014)	4	RC / Solid clay bricks	3
Mehrabi et al. (1996)	6	RC / Solid and hollow concrete bricks	0
Sigmund and Penava (2014)	8	RC / Hollow clay bricks	8

[a]NT: Number of tests
[b]Number of tests with openings

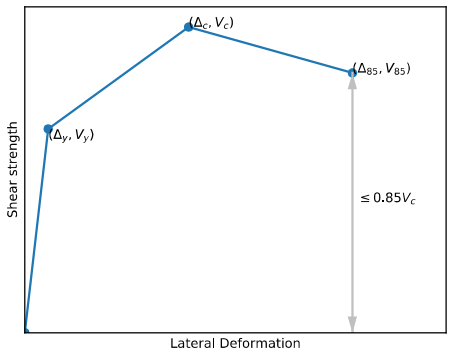

Figure 6.1: Illustration of a MIF constitutive behaviour parameters. The pairs (Δ, V) indicate the coordinates of lateral deformation (Δ) and shear (V) at key indicative points, namely yielding (Δ_y, V_y), capping (Δ_c, V_c), and residual point (Δ_{85}, V_{85}).

6.1.1 Damage index formulation

The damage index formulation stems from the well-known formulation in Park and Ang (1985); Park et al. (1985), where the damage of reinforced concrete components is quantified as a linear combination of two functions: (1) deformation ductility, i.e., the ratio of maximum deformation to yield deformation under monotonic loading, and (2) the dissipated hysteretic energy relative to the maximum energy that can be absorbed under monotonic loading. In this section, the damage index is used to set a threshold to the performance objective defined as "collapse prevention" according to ASCE/SEI 41 (2017). Here, the original equation is modified given the difficulty to determine a *yield* condition for a brittle element as a

Table 6.2: Data of masonry infilled steel frame tests (Units: mm, MPa).

Author	No.	Unit[a]	$\frac{h_m}{t_m}$ [b]	$\frac{h_m}{L_m}$	λ	$\frac{P}{A_m f_m}$ [c]	A_{is}^r [d]	A_{is}^l	Δ_y^+	Δ_y^-	Δ_c^+	Δ_c^-	Δ_{85}^+	Δ_{85}^-	V_y^+	V_y^-	V_c^+	V_c^-	V_{85}^+	V_{85}^-
Flanagan and Bennett (1999)	1	HCl	11.49	1.00	9.74	0.00%	2.79	2.79	7.92	8.96	19.73	27.94	19.98	29.58	59.30	87.09	160.28	124.41	133.86	91.98
	2	HCl	11.49	1.00	5.86	0.00%	2.79	2.79	13.38	13.44	25.91	27.24	26.15	30.40	115.34	105.80	181.64	167.94	149.37	108.27
	3	HCl	11.49	1.00	4.38	0.00%	2.79	2.79	7.03	10.10	12.91	14.59	15.00	17.34	111.57	93.13	172.98	151.69	134.16	106.04
	4	HCl	6.79	1.00	8.10	0.00%	2.79	2.79	7.55	11.99	14.11	13.31	20.02	25.74	92.15	158.58	147.68	229.49	55.19	76.36
	5	HCl	6.79	1.00	6.15	0.00%	2.79	2.79	5.22	6.35	14.11	13.31	17.19	18.94	114.54	137.20	167.46	196.01	116.49	165.63
	6	HCl	18.82	1.00	5.18	0.00%	2.79	2.79	5.22	6.35	14.11	13.31	17.19	18.94	114.54	137.20	167.46	196.01	116.49	165.63
	7	HCl	11.49	1.00	3.28	0.00%	2.79	2.79	5.03	6.61	10.85	11.05	15.19	14.60	121.17	156.78	211.83	223.97	157.45	170.66
	8	HCl	11.49	0.79	5.82	0.00%	3.61	3.61	34.94	32.09	46.78	50.11	46.78	51.70	94.84	141.74	141.76	205.42	141.76	174.59
	9	HCl	11.49	0.79	5.82	0.00%	3.61	3.61	10.82	13.03	22.79	27.03	23.11	29.24	108.10	85.88	155.99	148.58	116.79	83.80
	10	HCl	11.49	0.65	5.73	0.00%	4.61	4.61	30.16	10.84	63.98	28.34	63.98	46.24	142.04	111.41	205.26	198.95	205.26	48.48
	11	HCl	11.49	0.79	5.82	0.00%	3.61	3.61	15.99	19.79	32.90	38.09	37.94	40.72	130.99	124.12	202.14	177.32	69.32	150.23
	12	HCl	11.49	0.79	5.82	0.00%	3.61	3.61	10.13	22.08	31.43	36.37	36.89	36.89	55.94	103.56	146.44	171.45	124.38	126.46
	13	HCl	11.49	0.79	5.82	0.00%	3.61	3.25	10.62	12.90	16.00	18.79	16.41	18.97	90.57	42.33	134.18	66.98	79.36	23.15
Markulak et al. (2013)	14	AAC	12.45	0.76	4.89	0.00%	1.84	1.84	10.58	5.48	29.98	13.72	30.54	13.72	90.64	69.93	138.59	99.90	108.92	99.90
	15	HCl	12.45	0.76	3.20	0.00%	1.84	1.84	5.36	4.20	15.59	16.86	15.59	18.19	95.17	95.20	135.95	136.00	105.83	128.81
	16	AAC	12.45	0.76	4.96	0.00%	1.84	1.84	3.66	3.39	15.22	13.22	15.43	13.22	76.39	62.10	109.13	88.72	105.66	88.72
	17	AAC	12.45	0.76	4.96	0.00%	1.84	1.84	3.54	3.01	16.36	7.94	17.00	8.18	63.42	58.63	90.60	83.76	86.32	79.49
	18	AAC	12.45	0.76	4.96	0.00%	1.84	1.84	5.47	4.08	16.99	13.17	17.08	13.26	66.46	56.41	94.94	80.59	91.56	76.37
Schneider et al. (1998)	19	SCl	22.16	0.73	2.88	0.21%	1.40	1.40	5.19	10.80	16.53	24.05	26.00	25.66	29.77	51.74	65.86	82.79	55.48	70.34
	20	SCl	11.08	0.73	3.66	1.00%	1.40	1.40	11.57	4.68	23.76	22.03	39.07	34.07	122.76	79.11	180.26	177.78	141.80	149.55
	21	SCl	22.16	0.73	3.12	1.63%	1.65	1.65	6.59	8.57	13.62	20.29	26.39	25.88	79.91	87.80	125.06	125.42	103.26	105.84
	22	SCl	11.08	0.73	3.68	1.80%	1.65	1.65	8.62	12.34	20.64	32.69	29.12	41.14	133.09	133.97	196.89	194.72	167.10	128.69
	23	SCl	22.16	0.73	3.03	2.03%	1.96	1.96	8.62	12.34	13.57	20.19	29.12	41.14	133.09	133.97	196.89	194.72	167.10	128.69
Tasnimi and Mohebkhah (2011)	24	SCl	16.36	0.80	5.23	0.00%	2.31	2.31	8.14	6.27	20.00	20.00	50.20	45.39	141.76	151.03	202.51	215.75	166.98	183.36
	25	SCl	16.36	0.80	5.23	0.00%	2.06	2.06	4.11	3.46	15.25	14.59	39.12	24.91	122.05	123.49	174.36	176.41	147.56	149.55
	26	SCl	16.36	0.80	5.16	0.00%	1.78	1.78	3.89	2.83	13.80	13.53	33.91	30.05	106.76	96.28	152.52	137.54	118.83	103.86
	27	SCl	16.36	0.80	5.16	0.00%	1.63	1.63	4.56	4.12	14.93	25.00	34.74	45.58	96.34	86.32	137.63	123.32	116.23	104.77
	28	SCl	16.36	0.80	5.41	0.00%	1.51	1.51	3.91	5.88	13.95	29.75	44.79	41.18	82.17	87.88	117.39	125.54	98.23	97.83

[a] Masonry Unit types: SC: Solid Concrete, HC: Hollow Concrete, FA: Fly Ash, SCl: Solid Clay, HCl: Hollow Clay, AAC: Autoclaved Aerated Concrete

[b] h_m, t_m and L_m are the height, thickness and length of the masonry infill in [mm], respectively

[c] P is the axial load acting on the wall, $A_m = L_m t_m$ and f_m is the characteristic axial strength of the masonry wall.

[d] Area of the equivalent strut according to Holmes (1961) considering windows and doors openings, in m^2.

Table 6.3: Data of masonry infilled reinforced concrete frame tests (Units: mm, MPa).

Author	No.	Unit[a]	$\frac{h_m}{t_m}$[b]	$\frac{h_m}{L_m}$	λ	$\frac{P}{A_m f_m}$[c]	A_{is}^{r}[d]	A_{is}^{l}	Δ_y^+	Δ_y^-	Δ_c^+	Δ_c^-	Δ_{85}^+	Δ_{85}^-	V_y^+	V_y^-	V_c^+	V_c^-	V_{85}^+	V_{85}^-
Morandi et al. (2018a)	29	HCl	8.43	0.70	4.49	11.67%	7.27	7.27	12.83	12.16	45.55	44.29	47.43	46.18	395.31	414.91	564.72	592.73	508.70	570.35
	30	HCl	8.43	0.70	4.49	11.67%	7.27	7.27	10.63	10.45	46.17	46.51	62.31	78.04	382.95	388.56	547.07	555.09	456.04	453.71
	31	HCl	8.43	0.70	4.49	11.67%	7.27	7.27	8.25	11.42	28.40	30.23	29.62	30.23	329.82	333.55	471.17	476.50	365.48	476.50
	32	HCl	8.43	0.70	4.49	11.67%	4.26	4.26	8.93	6.02	31.04	31.04	31.29	31.16	203.56	207.82	290.80	296.88	264.01	273.96
Basha and Kaushik (2016)	33	FA	13.64	1.00	4.01	1.40%	1.25	1.25	2.42	1.79	11.71	13.50	36.01	26.90	45.32	43.03	64.74	61.48	54.95	52.05
	34	FA	13.64	1.00	4.01	1.40%	1.25	1.25	3.24	4.92	12.09	12.98	30.90	26.41	54.46	57.65	77.80	85.41	65.83	69.09
	35	FA	13.64	1.00	4.01	1.40%	1.25	1.25	1.49	2.35	30.54	31.30	57.71	45.38	44.60	49.13	63.72	70.19	48.81	59.50
	36	FA	13.64	1.00	4.01	1.40%	1.25	1.25	4.50	6.00	13.50	18.90	45.90	27.10	65.31	61.77	99.10	88.25	79.71	74.64
	37	FA	27.27	1.00	3.37	2.80%	1.25	1.25	1.43	3.30	10.81	15.30	35.11	31.50	62.80	47.61	89.72	68.01	65.61	56.99
	38	FA	27.27	1.00	3.37	2.80%	1.25	1.25	1.81	2.99	10.80	9.90	31.50	31.49	52.06	45.57	74.38	70.00	60.16	59.06
Calvi et al. (2004)	39	HCl	23.91	0.65	2.94	0.00%	6.87	6.87	11.50	7.19	12.00	9.39	12.08	18.26	168.16	124.70	240.22	205.44	120.58	205.44
	40	HCl	23.91	0.65	2.94	0.00%	6.87	6.87	10.78	6.01	10.60	12.17	106.78	21.42	170.78	131.80	243.98	298.19	236.75	252.24
	41	HCl	23.91	0.65	2.94	0.00%	6.87	6.87	5.80	11.79	11.10	12.00	11.85	107.61	132.21	204.56	252.79	292.23	129.18	234.09
	42	HCl	20.37	0.65	3.06	0.00%	6.87	6.87	3.83	7.30	7.30	5.22	10.78	5.42	207.00	121.34	300.00	366.58	232.14	97.45
	43	HCl	23.91	0.65	2.94	0.00%	6.87	6.87	1.97	2.54	4.70	5.64	8.89	9.14	180.00	160.00	257.14	228.57	192.86	117.13
	44	HCl	23.91	0.65	2.94	0.00%	6.87	6.87	2.29	2.15	5.35	6.03	8.97	8.62	158.12	195.47	225.89	279.25	172.53	236.56
	45	HCl	20.37	0.65	3.06	0.00%	6.87	6.87	3.47	2.23	9.14	5.61	9.17	9.22	185.44	213.39	264.92	304.84	212.90	229.72
Gazić and Sigmund (2016)	46	HCl	14.44	0.70	5.18	66.07%	1.40	1.40	1.89	2.24	4.27	3.59	5.54	5.13	110.67	89.69	158.10	137.14	132.25	114.67
	47	HCl	14.44	0.70	5.18	66.07%	1.40	1.40	1.58	2.27	3.85	4.08	5.48	5.58	116.93	94.94	168.00	138.00	136.00	115.33
	48	SCl	20.00	0.70	4.78	80.92%	1.40	1.40	2.31	1.77	21.93	12.76	24.42	24.42	139.76	111.62	199.66	159.46	175.68	113.59
	49	HCl	14.44	0.70	3.53	150.15%	1.40	1.40	0.39	0.70	6.10	2.82	8.76	11.73	54.91	53.57	78.44	76.52	65.43	56.15
	50	SCl	20.00	0.70	3.20	120.23%	1.40	1.40	0.70	0.54	15.43	2.25	21.51	24.28	30.45	23.49	43.50	34.50	33.40	28.00
	51	HCl	14.44	0.70	5.18	66.07%	1.40	1.40	6.10	5.75	22.13	18.06	22.38	24.39	41.36	40.42	61.82	57.74	50.69	50.58
	52	SCl	20.00	0.70	3.21	80.92%	1.40	1.40	1.93	1.69	5.85	13.35	6.32	14.79	116.94	118.59	167.06	169.41	135.29	141.65
	53	HCl	14.44	0.74	3.55	69.84%	1.40	1.40	1.89	2.05	10.45	5.23	12.05	12.95	154.65	145.20	220.93	218.02	186.05	177.33
	54	SCl	20.00	0.74	2.19	85.55%	1.40	1.40	3.30	2.80	10.36	17.50	10.36	18.90	208.47	202.26	297.82	288.94	235.60	280.61
Guerrero et al. (2014)	55	HC	10.33	0.65	3.88	0.00%	2.22	2.22	9.04	7.52	23.85	22.81	44.59	44.50	95.72	82.96	136.74	118.51	111.88	100.58
	56	HC	12.00	0.75	4.40	0.00%	2.48	2.48	5.07	4.81	19.00	52.00	55.80	93.95	33.95	29.05	48.50	41.50	41.20	35.26
	57	HC	12.00	0.75	4.40	0.00%	2.48	2.48	6.58	0.55	15.34	0.55	39.52	0.55	81.34	0.00	116.20	0.00	98.62	0.00

[a]Masonry Unit types: SC: Solid Concrete, HC: Hollow Concrete, FA: Fly Ash, SCl: Solid Clay, HCl: Hollow Clay, AAC: Autoclaved Aerated Concrete
[b]h_m, t_m and L_m are the height, thickness and length of the masonry infill in [mm], respectively
[c]P is the axial load acting on the wall, $A_m = L_m t_m$ and f_m is the characteristic axial strength of the masonry wall.
[d]Area of the equivalent strut according to Holmes (1961) considering windows and doors openings, in m^2.

Table 6.4: Data of masonry infilled reinforced concrete frame tests (Units: mm, MPa).

Author	No.	Unit[a]	$\frac{h_m}{t_m}$ [b]	$\frac{h_m}{L_m}$	λ	$\frac{P}{A_m f_m}$ [c]	A_{is}^r [d]	A_{is}^l	Δ_y^+	Δ_y^-	Δ_c^+	Δ_c^-	Δ_{85}^+	Δ_{85}^-	V_y^+	V_y^-	V_c^+	V_c^-	V_{85}^+	V_{85}^-
Haider (1995)	58	SCl	23.26	1.09	2.80	0.00%	2.20	2.20	9.82	9.81	20.11	20.09	40.96	35.96	138.08	151.16	216.43	221.64	177.70	188.04
	59	SCl	23.26	1.09	2.31	0.00%	2.20	2.20	12.77	17.37	30.01	34.97	71.21	62.23	169.76	193.22	242.52	289.68	172.57	246.15
	60	SCl	23.26	1.09	3.00	0.00%	2.20	2.20	13.86	6.45	29.78	25.75	29.78	25.76	95.11	69.14	136.06	188.39	130.83	177.93
	61	SCl	23.26	1.09	2.49	0.00%	2.20	2.20	12.19	14.65	30.30	30.74	40.67	61.70	149.43	188.09	213.47	268.69	149.82	224.49
Jiang et al. (2015a)	62	AAC	13.63	0.49	4.00	31.39%	10.03	10.03	3.70	6.14	40.71	43.93	64.29	65.55	409.69	466.38	585.28	666.26	496.93	566.09
	63	AAC	13.63	0.49	4.00	31.39%	10.03	10.03	21.49	24.36	54.16	73.27	76.46	99.82	343.17	311.88	490.24	468.29	402.44	431.71
	64	AAC	13.63	0.49	4.00	31.39%	10.03	10.03	21.49	24.36	54.16	73.27	76.46	99.82	343.17	311.88	490.24	468.29	402.44	431.71
	65	AAC	13.63	0.49	4.00	31.39%	10.03	10.03	18.71	14.53	48.97	53.27	51.12	58.65	354.20	288.44	511.11	488.89	414.82	385.19
	66	AAC	13.63	0.49	4.00	31.39%	10.03	10.03	15.00	17.14	63.21	45.00	101.79	79.29	299.54	248.40	490.24	504.88	402.44	428.05
	67	AAC	13.63	0.49	4.00	31.39%	10.03	10.03	20.35	16.53	80.54	74.13	100.80	107.20	312.44	292.50	446.34	475.61	343.90	402.44
Mansouri et al. (2014)	68	SCl	12.26	0.62	1.77	30.47%	1.65	1.65	16.11	17.18	43.53	51.72	45.15	57.97	79.23	81.14	113.18	115.91	69.33	79.09
	69	SCl	12.26	0.62	1.77	30.47%	1.39	1.26	14.46	12.43	58.01	27.21	58.01	45.53	53.30	57.77	76.15	83.49	76.15	65.14
	70	SCl	12.26	0.62	1.77	30.47%	1.25	1.25	11.99	10.82	28.70	27.91	45.49	44.72	62.94	62.29	89.91	88.99	57.06	46.90
	71	SCl	12.26	0.62	1.77	30.47%	1.21	1.41	10.86	8.42	34.21	17.19	35.31	33.01	58.57	63.81	83.67	92.48	63.34	78.55
Mehrabi et al. (1996)	72	HC	15.43	0.67	3.95	0.01%	1.79	1.79	1.61	2.50	11.76	10.32	20.04	16.90	111.73	104.72	159.61	149.59	135.29	125.17
	73	SC	15.43	0.48	4.50	0.01%	2.81	2.81	1.48	1.27	5.28	8.12	17.26	9.45	176.13	194.57	287.80	277.96	238.60	230.95
	74	HC	15.43	0.67	3.26	0.01%	1.79	1.79	3.04	1.69	9.85	4.38	10.19	12.94	144.22	127.23	206.03	181.76	140.09	132.05
	75	SC	15.43	0.67	4.61	0.01%	1.79	1.79	1.70	0.84	8.75	15.51	20.05	19.18	184.72	156.76	263.89	223.94	223.66	184.18
	76	SC	15.43	0.48	4.10	0.00%	2.81	2.81	0.95	2.06	6.78	8.18	7.15	17.53	252.88	242.35	361.26	346.21	306.36	293.99
	77	SC	15.43	0.67	4.44	0.01%	1.79	1.79	2.34	3.94	8.38	9.72	12.23	9.76	304.97	310.14	443.27	487.64	375.72	367.11
Sigmund and Penava (2014)	78	HCl	10.83	0.72	2.87	62.59%	1.11	1.11	1.10	1.25	6.06	4.55	6.06	5.02	160.69	172.51	257.93	246.45	257.93	183.88
	79	HCl	10.83	0.72	3.01	62.59%	1.06	1.06	1.65	1.29	6.45	4.62	7.20	4.68	209.44	183.45	299.19	290.73	245.57	224.75
	80	HCl	10.83	0.72	2.93	62.59%	1.08	1.22	1.49	1.64	8.26	10.08	13.27	10.54	194.60	182.73	278.00	261.05	184.44	255.39
	81	HCl	10.83	0.72	2.89	62.59%	1.14	1.10	1.89	1.01	14.38	13.02	17.99	13.17	208.97	153.37	298.53	219.11	242.09	202.11
	82	HCl	10.83	0.72	2.95	62.59%	1.11	1.11	1.89	1.52	4.72	4.87	10.58	5.70	216.89	194.80	309.84	278.28	261.07	195.30
	83	HCl	10.83	0.72	2.95	62.59%	1.06	1.06	1.19	2.48	7.99	6.29	13.52	14.89	180.74	214.88	258.20	306.97	220.90	261.07
	84	HCl	10.83	0.72	2.93	62.59%	1.08	1.22	1.27	1.48	13.81	9.07	14.11	12.73	197.00	193.00	281.43	275.71	281.43	261.43
	85	HCl	10.83	0.72	3.05	62.59%	1.35	1.35	1.40	0.90	4.20	3.07	4.64	3.10	195.84	123.24	279.77	275.08	138.13	158.91

[a] Masonry Unit types: SC: Solid Concrete, HC: Hollow Concrete, FA: Fly Ash, SCl: Solid Clay, HCl: Hollow Clay, AAC: Autoclaved Aerated Concrete

[b] h_m, t_m and L_m are the height, thickness and length of the masonry infill in [mm], respectively

[c] P is the axial load acting on the wall, $A_m = L_m t_m$ and f_m is the characteristic axial strength of the masonry wall.

[d] Area of the equivalent strut according to Holmes (1961) considering windows and doors openings, in m^2.

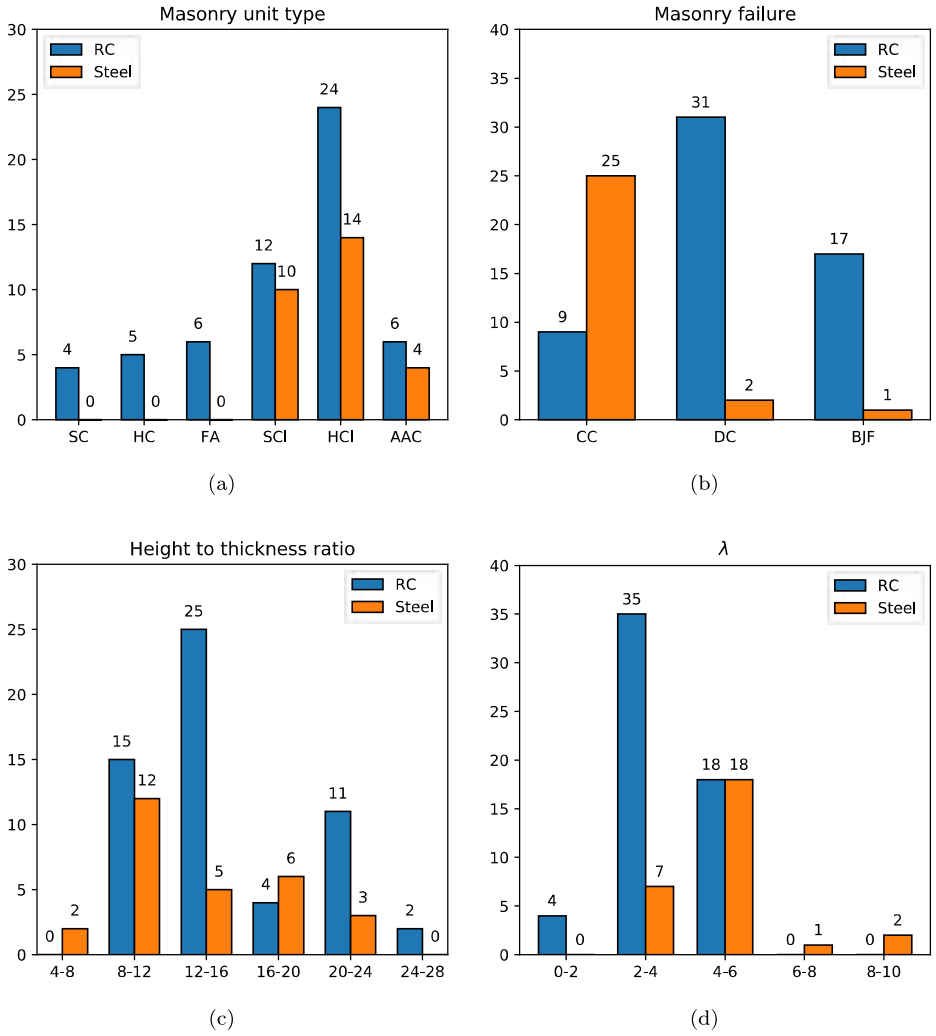

Figure 6.2: Ditribution of the following parameters within the database: (a) Masonry unit type, (b) Masonry failure observed, (c) Height to thickness ratio, (d) λ parameter. SC: Solid Concrete, HC: Hollow Concrete, FA: Fly Ash, SCl: Solid Clay, HCl: Hollow Clay, AAC: Autoclaved Aerated Concrete; CC: Corner Crushing, DC: Diagonal Cracking, BJF: Bed-Joint Failure.

masonry wall. Therefore, the following modified equation is proposed:

$$DI = \eta_1 D_1 + \eta_2 D_2 = \eta_1 \frac{\delta_i}{\delta_{max}} + \eta_2 \frac{\mathcal{E}_i}{F_{max}\delta_{max}} \tag{6.2}$$

where F_{max} and δ_{max} are the maximum shear strength and the corresponding lateral deformation, respectively; δ_i and $\mathcal{E}_i$ are the maximum deformation and the dissipated energy by deformation attained until step i, respectively; and finally η_1 and η_2 are experimentally determined coefficients which allow the normalization of the damage index value to unity. In this work it is assumed that the acceptance criteria for the collapse prevention performance level corresponds to the deformation at the point of maximum

strength, as suggested in the experimental based method in ASCE/SEI 41 (2017).

A generalized reduce gradient procedure (Lasdon et al., 1974) is used to estimate the optimum values of the parameters η_1 and η_2. The contribution of both terms is maximized restricted to the condition that the mean of the damage indices should be equal to 1.00. By applying the generalized reduce gradient procedure on the set of experimental data presented here, it is found that optimization results are $\eta_1 = 0.4948$, $\eta_2 = 0.1159$, whilst the standard deviation of the damage index leads to $\sigma = 0.184$. Figure 6.3 shows the conditional probability of reaching the collapse prevention damage state CP as a function of the damage index DI, namely $P(CP|DI)$, along with the contribution of each term $\eta_1 D_1$ and $\eta_2 D_2$ to the damage index.

Equation (6.2) and the calibrated parameters η_1 and η_2 allow the estimation of the probability of collapse of a MIF, using only the force-deformation global results obtained from a time-history analysis. In Section 6.3, this formulation is applied to assess the seismic capacity of the MIFs of a three story building.

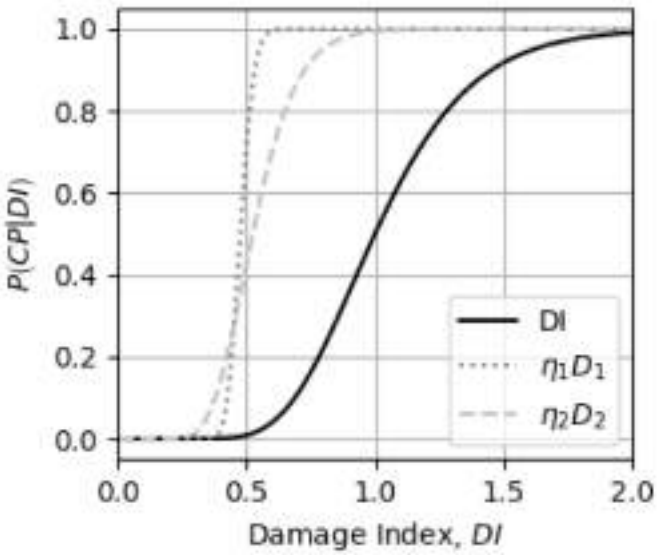

Figure 6.3: Collapse prevention limit state CDF in terms of the proposed damage index formulation.

6.2 Training of the HMC-BNN with experimental data

Here, the experimental database presented in Section 6.1 is employed to train a HMC-BNN which, as already stated above, will act as synthetic data-based model to estimate the constitutive parameters of MIFs in a probabilistic fashion.

The resulting experimental values of the constitutive behaviour of each test are summarised in Tables 6.2, 6.3 and 6.4. The HMC-BNN model consists of one input layer with ten neurons, two hidden layers with 40 neurons each, and one neuron output layer, making a total of 2121 parameters to be learned

for each constitutive value. A ReLU activation function is assigned to the neurons of the hidden layers, whilst a Sigmoid function is applied to the neuron in the output layer, as indicated in the previous section. The input layer includes neurons to account for the height-thickness ratio (h_m/t_m), height-length ratio (h_m/L_m), λ parameter (see Equation (6.1)), axial load-strength ratio ($P/A_m f_m$), equivalent infill strut area (A_{is}), masonry unit type, masonry characteristic compressive strength (f'_m), a gross parameter to consider the stiffness of the columns of the frame ($E_c I_c$), a gross parameter to consider the strength of the columns ($f_c I_c$ for reinforced concrete and $f_y I_c$ for structural steel columns), and the length of the wall (L_m). For clarity, some of those parameters have been represented in Figure 6.4. In this work, the equivalent infill strut area A_{is} is obtained as the masonry area within the equivalent strut width w_m (Holmes, 1961), whereas w_m is obtained as one third of the lenght of the wall diagonal (d_m, as indicated in Figure 6.4). This parameter is normalized to the gross area of the masonry wall and allows us to consider the presence of openings in the wall, including a way to differentiate the asymmetric cases.

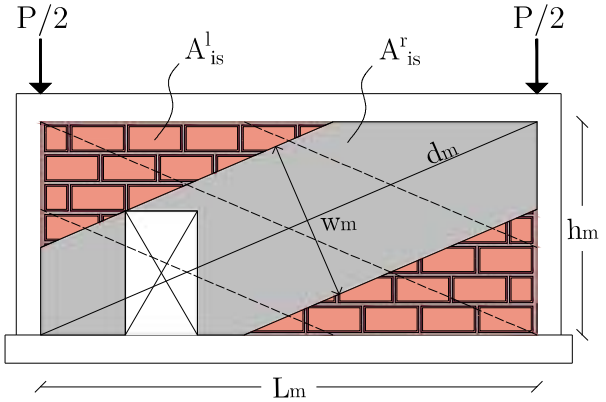

Figure 6.4: Illustration of the geometric parameters of the MIF within the database.

Correspondingly, the output layer accounts for the point of first stiffness drop (Δ_y, V_y), capping point (Δ_c, V_c) and residual strength (Δ_{85}, V_{85}) pairs of lateral deformations and shear forces (refer to Figure 6.1 for further details). Here, the capping point is defined as the Δ, V pair of the maximum strength of the envelope line of the test. The first stiffness drop corresponds to the intersection of the elastic part of a bi-linear approximation with the envelope curve of the test (similar to a yield point for ductile structural systems), whereas, the residual is the point within the envelope behaviour that is lower or equal to the 85th percent of the maximum strength.

Once trained, the HMC-BNN provides a probabilistic prediction of the three constitutive (Δ, V) pairs of a MIF characterized by specific geometrical and mechanical parameters, acting as inputs to the BNN. Figure 6.5 shows an example prediction of the trained HMC-BNN for a hollow concrete masonry infilled concrete frame with 300x300 [mm] columns. The results are obtained using the following inputs: $h_m = L_m = 3000$ [mm], $t_m = 100$ [mm], $f_m = 10$ [MPa], $E_m = 9$ [GPa], $f_c = 20MPa$, and $E_c = 21.0$ [GPa]. Notice that the prediction denotes the high level of uncertainty that affects this structural system.

Also, observe that the method allows us to perform a probability analysis of a MIF by representing the lateral behaviour of the structural system with a single shear spring.

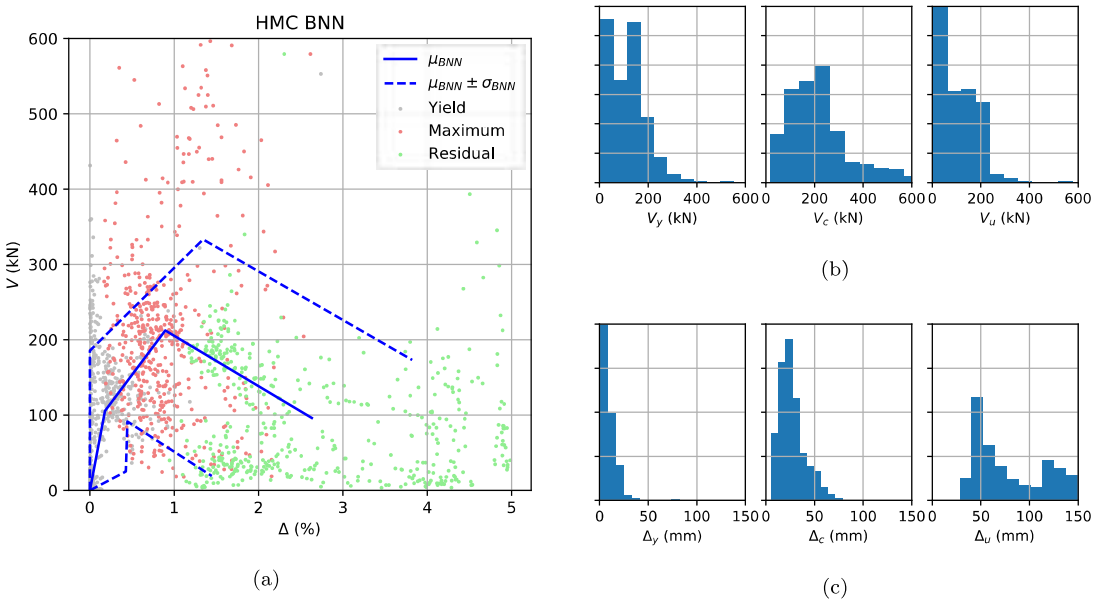

Figure 6.5: Example prediction of the constitutive values using Bayesian Neural Networks (BNN) with the Hamiltonian Monte Carlo (HMC) method. (a) Constitutive (V, Δ) pairs of the system, (b) probable distribution of the characteristic shear and (c) lateral deformation values of the trilineal approximation.

6.2.1 Prediction capabilities of the HMC-BNN within the training database

Using the modelling approaches presented in Sections 4.2.1 and 4.2.2, four MIF models are constructed and further compared to the proposed approach presented in Section 6.1. The aforementioned models are as follows:

1. Concentrated hinges frame model with a quadrilinear constitutive equivalent strut Liberatore et al. (2018);
2. Concentrated hinges frame model with a trilinear equivalent strut Huang et al. (2020);
3. Fiber section based frame model with the same equivalent strut of the first model;
4. Fiber section based frame model with a bilinear constitutive equivalent strut ASCE/SEI 41 (2017).

The BNN results are presented by its mean response and also by the scatter plots of each characteristic (V, Δ) value. Notice that the BNN model is only a one-dimensional shear spring and does not consider the separate behaviour of the frame and the infill as usual in macro-models.

Figures 6.6a to 6.6d depict the comparative results using laboratory test within the database (see Section 6.1), along with the estimation of the four models previously described, and the prediction of the

BNN. All tests correspond to reinforced concrete fully infilled frames, where solid clay, hollow clay, solid cement and hollow cement masonry units were used, respectively. From these results, the following aspects can be highlighted:

- Model 1 correctly estimates the initial stiffness and maximum strength of the system in the case of solid clay MIF. However, note that the model is not capable to capture the mechanical response after the degradation of the structure. For the cases of solid cement, hollow clay and hollow cement units MIF, the model under-predicts the initial stiffness and is not capable to capture the degradation of the system.

- Model 2 correctly captures the initial stiffness of the MIF with solid clay, solid cement and hollow cement units. However, the model over-predicts the strength of the system for solid and hollow clay units MIF, and under-predicts the strength of solid and hollow cement units MIF. In all cases, the model does not capture the mechanical response after the degradation.

- Model 3 correctly estimates the initial stiffness and maximum strength of the system with solid clay units; although, it is not capable of capturing the degradation of the structure. In the case of hollow clay units, the initial stiffness is under-predicted, whilst the maximum strength and deformation capacity is over-predicted. Finally, for the cases of solid and hollow cement units, the model under-predicts the initial stiffness and maximum strength, and does not capture the degradation of the system.

- Model 4, under-predicts in all cases the initial stiffness and maximum strength, over-predicts the deformation capacity, and does not capture the mechanical response after degradation.

- Observe that the proposed BNN model correctly predicts the initial stiffness of the system in average, for the cases of the usage of solid clay, solid cement and hollow cement units, and only under-predicts the initial stiffness of the system when hollow clay units are used. The model fairly predicts the maximum strength and captures the degradation of the system for solid clay, solid cement and hollow cement units. However, we note that for the case of hollow clay units, the BNN mean model does not properly captures the characteristic deformation nor the degradation of the system.

In general, the previous observations demonstrate that the level and sources of uncertainties of the MIF structural system should be considered when performing a structural evaluation of a building, since none of the available deterministic models can capture all of the properties of the lateral response of the system for all of the masonry unit types. On the other hand, the scatter points obtained after simulating our proposed BNN model, presented in Figures 6.6a to 6.6d, clearly capture all of the characteristics of the lateral response of the system within the prediction range. As also mentioned by Liberatore et al. (2018), this uncertainty should be accounted for to properly evaluate an existing structure.

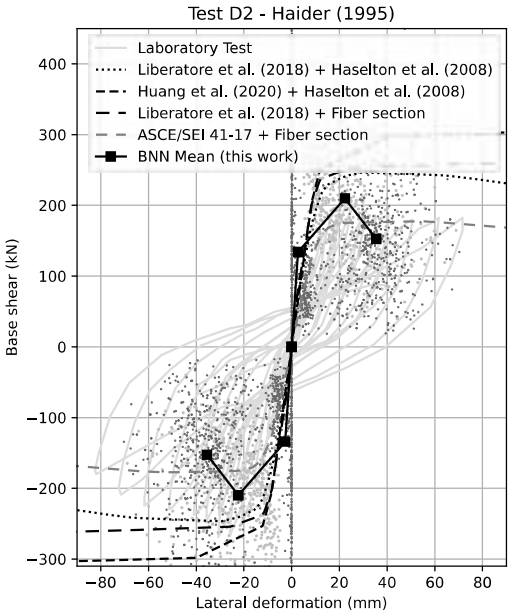

(a) Solid clay masonry infill in reinforced concrete frame.

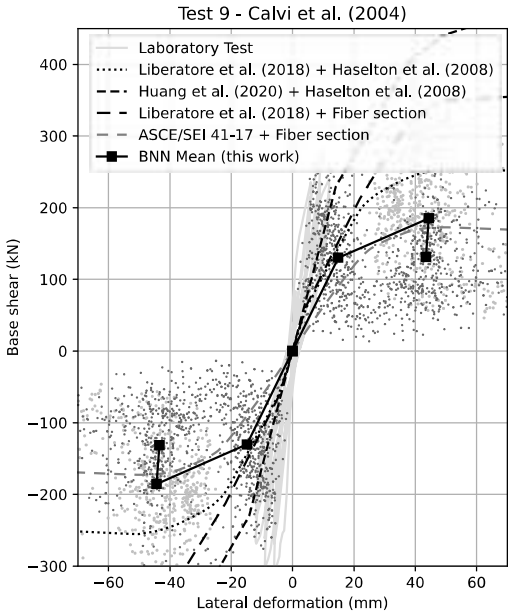

(b) Hollow clay masonry infill in reinforced concrete frame.

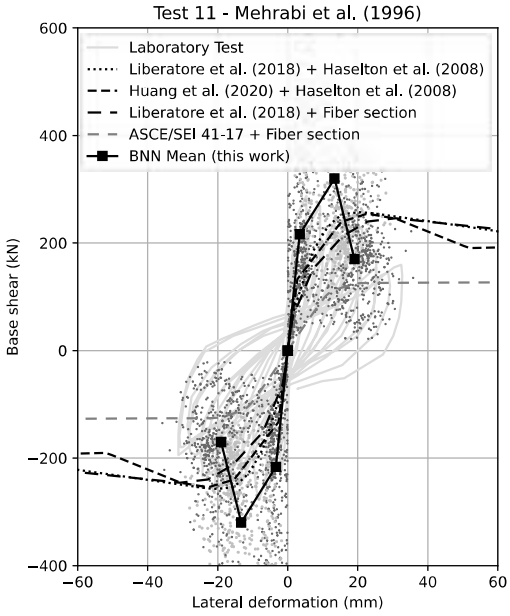

(c) Solid cement masonry infill in reinforced concrete frame.

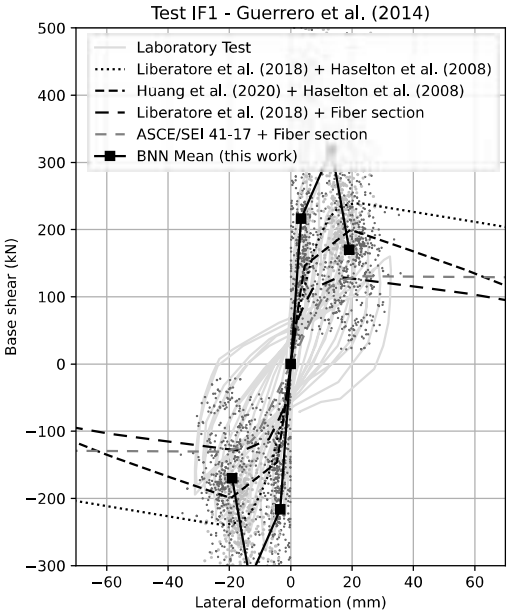

(d) Hollow cement masonry infill in reinforced concrete frame.

Figure 6.6: Masonry infilled reinforced concrete frames test results, available macro-models estimation and proposed BNN prediction comparison.

Figure 6.7a shows the measured results from a laboratory test for a case with steel frame with hollow clay masonry units. BNN mean results and scatter points are drawn along with the prediction of models 3

and 4. Model 2 was adapted by using the fiber section approach to model the behaviour of the frame. As can be seen, models 2 and 3 over predict the maximum strength and the initial stiffness of the system and do not properly capture the degradation of the structure. Model 4, on the other hand, fairly predicts the initial stiffness and maximum strength of the system, but it also fails to reproduce the degradation. The BNN mean model properly captures the maximum strength and degradation of the mechanical system, although it over-predicts the initial stiffness. Again, note that the proposed model provides a quantification of the uncertainty of the system.

Besides, Figure 6.7b shows the measured results from a laboratory test of a steel frame with hollow clay units with a non-symmetric window opening located at the upper corner of the wall. Only the model 4 can account for the reduced strength of the system due to the presence of the opening. Accordingly, only the prediction of that model is compared to the BNN model. Clearly, model 4 does not properly captures the behaviour of the system. However, observe that the BNN mean model captures the initial stiffness of the wall in the direction where the compression strut is not affected by the opening; notwithstanding, note that the stiffness is over-predicted for the opposite case. The BNN model also over-predicts the maximum strength and does not properly captures the degradation. Notwithstanding, the result is better than the available model of the literature.

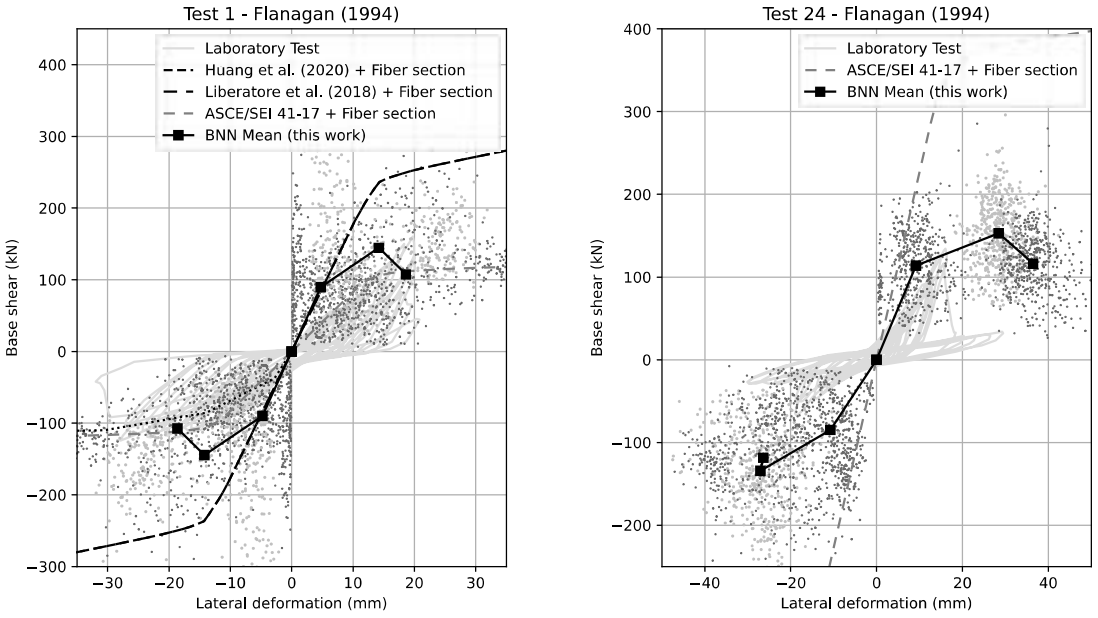

(a) Hollow clay masonry infill in structural steel frame.

(b) Hollow clay masonry infill in structural steel frame with a window opening.

Figure 6.7: Masonry infilled steel frames test results, available macro-models estimation and proposed BNN prediction comparison.

Notice that the experimental tests shown in Figures 6.6b to 6.7b were part of the training set of the

BNN, whilst the one in Figure 6.6a was part of the test set of the BNN. Figure 6.8 compares the prediction of the proposed BNN model with the force results of the first steel and concrete MIF tests from the database, showing that the probabilistic prediction of the model provides a valid envelope (represented using grey lines) of the expected real result. These results demonstrate the capabilities of the proposed BNN model to be applied on the structural probabilistic evaluation of the lateral strength of MIF existing buildings.

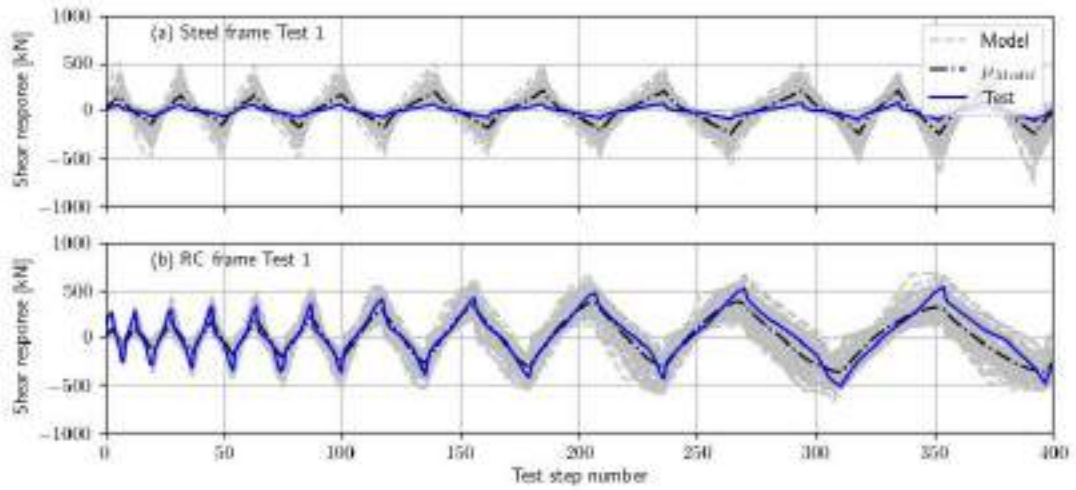

Figure 6.8: BNN-HMC model prediction in comparison to real test results, (a) a masonry infilled steel frame tested by Flanagan and Bennett (1999), (b) a masonry infilled concrete frame tested by Morandi et al. (2018a).

In the following section, the extrapolation capabilities of the model is further discussed.

6.2.2 Extrapolation capabilities of the HMC-BNN

Experimental test out from the database presented in Section 6.1 were selected to evaluate the prediction capabilities of the proposed method. First, the results of a shake-table test, performed by Benavent-Climent et al. (2018), are compared to those predicted by the proposed BNN model. According to the authors, the reinforced concrete frame was part of 11 previous seismic simulations before the masonry wall was built and, therefore, some level of degradation of the columns was expected (the authors report 1.5% maximum inter-story drift and 0.12% of residual inter-story drift). Therefore, instead of using the gross inertia as an input to the BNN model, a cracked section was used, assuming 30% of the gross section as effective. The masonry infill was tested as a retrofit system. They used 40 mm thick hollow clay units to build the wall. The beam and columns cross sections were 120x120 mm and 120x100 mm, respectively. Concrete strength was measured equal to 40 MPa on the test day. The height and length of the wall were 1400 mm and 2000 mm, respectively. As shown in Figure 6.9a, the proposed model over-predicts in average the maximum

strength, however the scatter points clearly envelopes the behaviour of the test. Considering the fact that shake-table tests introduce additional sources of uncertainties in addition to those related to the damage history of the frame, it can be concluded that the prediction obtained from the proposed BNN model is satisfactory.

To further check the efficiency of the proposed method, a second example is selected from a full-scale cyclic IP loading test performed by Furtado et al. (2018). According to the authors, the specimen consisted of a double-leaf MIF with hollow clay units. The wall was composed by a 150 mm thick external leaf, and a 110 mm thick internal leaf, with a gap of 40 mm between the leafs. Notice that the database does not consider any case of double-leaf MIF, however, the prediction was made assuming an input thickness of the masonry wall equal to the sum of the leafs of the tested system. The beam and columns cross sections were 300x500 mm and 300x300 mm, respectively. Concrete strength was measured equal to 26.8 MPa. The height and length of the wall were 2300 mm and 4200 mm, respectively. Figure 6.9b shows the BNN mean model prediction against the laboratory test results. As can be seen, the proposed model fairly predicts the initial stiffness of the system and the initial strength. Unfortunately, the test was stopped until the specimen reached 0.5% drift, so it can not be compared for the cases of ultimate strength and deformation.

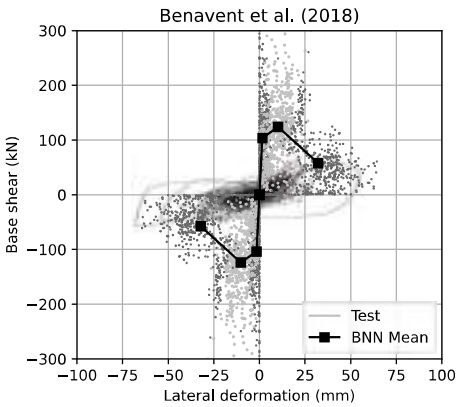

(a) Hollow clay masonry infill in reinforced concrete frame previously subjected to lateral deformation.

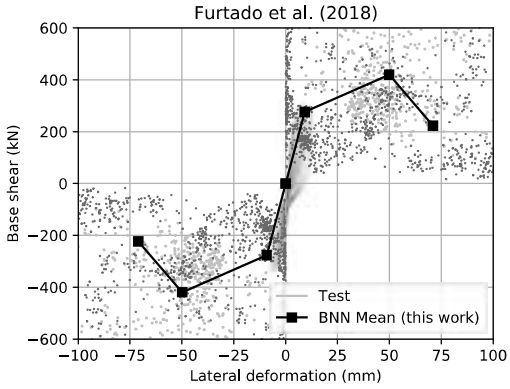

(b) Hollow clay double-leaf masonry infill in reinforced concrete frame.

Figure 6.9: Examples to test the extrapolation capabilities of the proposed BNN-HMC model.

6.3 Case study and discussion

In this section, the proposed numerical model (hereafter called "probabilistic model" to differentiate from other models) and damage index formulation are used to evaluate the seismic collapse probability of a three story masonry infilled reinforced concrete frame building. Results are compared to a code-based evaluation with ASCE/SEI 41-17, using a deterministic model available in the literature. In order to gain objectivity on the conclusions of this study, the characteristics of the building are selected to match the

properties of a one-bay and one-story laboratory test by (Morandi et al., 2018a). Accordingly, Table 6.5 shows the geometric and materials characteristics of the structure. The building is considered as 14x14 [m] plan with two MIFs as lateral resisting structure. The total mass of each floor is taken as 62000 [kg]. Figure 6.10 shows an elevation of one of the MIFs.

Table 6.5: Mean values of the geometrical and mechanical parameters of the frames used for the case study of Section 6.3. Length units are expressed in [mm], whereas strength and stiffness values (rows 9_{th} to 12_{th}) are given in [MPa]. The parameters ρ_{beam} and ρ_{col} are dimensionless.

L_m	H_m	t_m	b_{col}	ρ_{col}	b_{beam}	h_{beam}	ρ_{beam}	f'_c	f_y	f'_m	E_m
4220	2950	350	350	2.48	350	350	0.47	34	521	4.6	5299

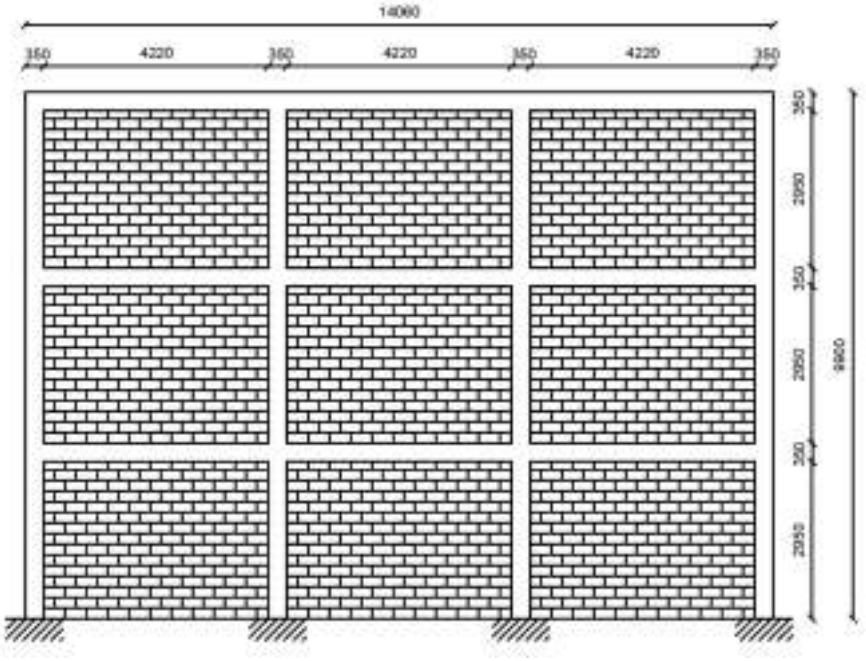

Figure 6.10: Illustration of the case study of a three story masonry infilled reinforced concrete frame.

Seismic collapse probability evaluation is estimated by means of non-linear time history analyses using far-field records data set of FEMA P695 document (Harris et al., 2009). Normalization and scaling of the seismic records are considered by means of the factors defined in Table A-3 of the aforementioned document. In the following section, three structural models are constructed, one using the proposed probabilistic approach and two deterministic models taken from the literature and adapted to ASCE 41 (ASCE/SEI 41, 2017) provisions.

6.3.1 Structural model

The probabilistic model is constructed using three sets of three in-parallel one-dimensional springs connected in-series to three equal masses.

Two deterministic models are constructed for comparison purposes. The first model corresponds to a blind prediction using a regression-based deterministic model (Huang et al., 2020), and the second model (hereafter called "deterministic modified model") is similar to the previous one but including some corrections on the constitutive values of the masonry strut, based on available laboratory test data. Figure 6.11 shows the constitutive behavior of the probabilistic estimations and the deterministic models predictions. Both deterministic models are defined using 2D elastic beam-column elements connected to nonlinear rotational springs at the ends; those springs account for beam and columns flexure inelastic behavior, using the formulation proposed by Haselton et al. (2008); a nonlinear compression strut in each principal diagonal of each frame is used to model the masonry wall effect according to Huang et al. (2020). Columns shear behavior can also be modelled according to the authors but, for this case study, shear failure is not expected because of the application of capacity design principles. The mass of each floor is set equal to that of the probabilistic model.

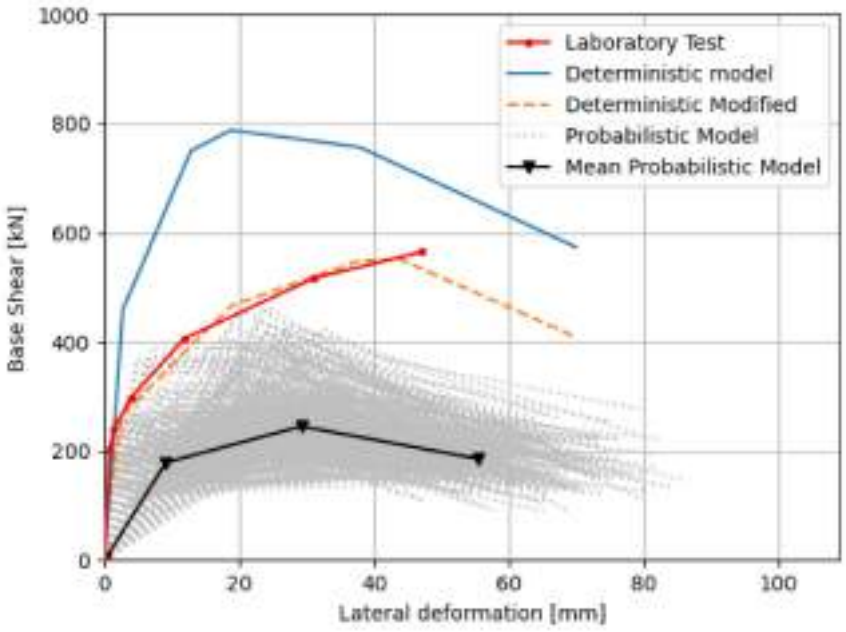

Figure 6.11: Comparison of the monotonic shear behavior of a one-bay and one-story of a laboratory tested MIF by Morandi et al. (2018a) to two deterministic models and the proposed probabilistic (Bayesian) approach.

6.3.2 Fundamental period

The distribution of fundamental period of the probabilistic model is drawn in Figure 6.12, where it can be seen that the most likely period for that structure is around 0.30 and 0.40 seconds. The deterministic (T_d) and deterministic modified (T_{dm}) fundamental period estimations are shown, and resulted as $T_d = 0.091$ [s] and $T_{dm} = 0.11$ [s]. Also, according to American Society of Civil Engineers (2016) provisions, in equation

12.8-9 reproduced here for ease of the reader, a lower bound estimation of the fundamental period can be evaluated:

$$T_a = \frac{C_q}{\sqrt{C_w}} h_n = \frac{0.0058 h_n}{\frac{1}{A_B} \sum_{i=1}^{x} \frac{A_i}{\left[1 + 0.83 \left(\frac{h_n}{D_i}\right)^2\right]}} \tag{6.3}$$

where A_B is the area of the base of the structure in m^2, x is the number of shear walls in the direction under consideration, A_i and D_i are the web area (in m^2) and the length of shear wall i (in m), respectively, and h_n is the structural height of the building in m, resulting $T_a = 0.32$ [s].

Considering the factors that affect the estimation of the structural period, i.e. epistemic uncertainties in the calculation of the mass of the structure and uncertainties in the estimation of the stiffness of the structure, related to soil stiffness, soil-structure interaction and relative deformations in wall-frame joints, among others, it is hard to conclude that the estimated fundamental period from the deterministic models matches the real structure without performing a measurement in the real structure. Therefore, approximations based on data taken from measurements of similar real structures are still more reliable. Notice that the result of Equation (6.3) lays within the range of most probable fundamental period estimated from the probabilistic model. Also, a three story building was evaluated by Varum et al. (2017) after Ghorka 2015 earthquake. Ambient vibration test were performed to identify the natural period of the structure. One of the buildings reported similar structural conditions as the presented case study. Values equal to 0.27s and 0.38s were reported for a moderate damaged structure.

A proper estimation of the fundamental period is important to perform an adequate seismic evaluation of the structure, as it directly affects the evaluation of expected deformation and, therefore, influences the damage forecast. In this particular case, considering the possibility that the fundamental period estimation of the deterministic model is low, results could lead to an underestimation of the seismic effects. Care must be taken when using deterministic models for prediction and it is strongly suggested that those models account for lower and upper bounds of the constitutive parameters or to complement the prediction with data measures taken from the real structure to be evaluated (for instance, ambient vibration of the structure).

These results suggest that the proposed model better predicts the dynamic properties of a MIF building, in comparison with the deterministic modelling approach; however, more data is required in order to achieve a more precise model.

6.3.3 Collapse evaluation by non-linear time history analysis

Non-linear time history analyses are performed using the deterministic, deterministic modified and probabilistic models presented in Section 6.3.1, and FEMA-P695 far-field records. Figure 6.13 shows the

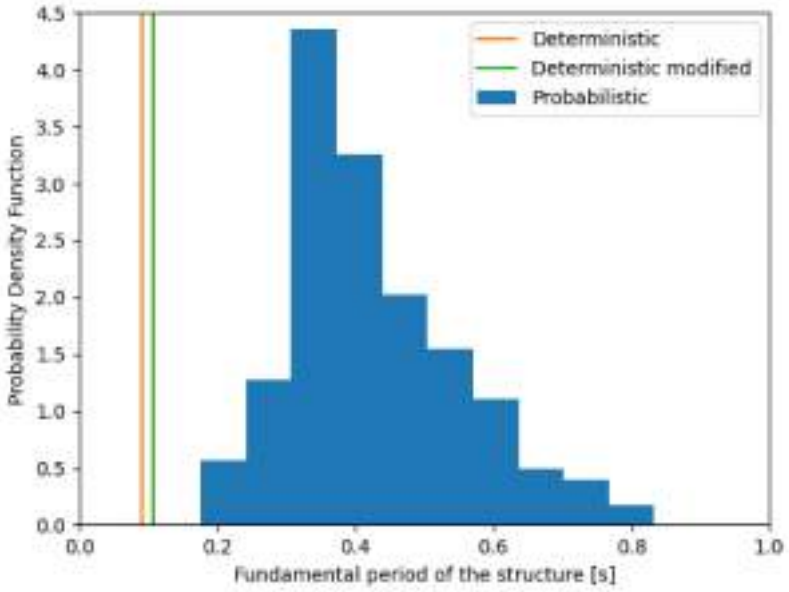

Figure 6.12: Fundamental period distribution obtained from the BNN-HMC in comparison to the deterministic model estimation.

interstory drift results corresponding to the spectral acceleration of the Maximum Considered Earthquake (MCE) level, and Figure 6.14 depicts the PDFs of the top displacements (also for MCE), for each model. Results show the impact of the overestimation of the stiffness of the structure, where the deterministic model depicts unexpected (almost negligible) deformations. The results of the deterministic modified model shows that a minimal change in the dynamic characteristics of the model (i.e. fundamental period changed from 0.091 s to 0.11 s after the modification explained in section 6.3.1), considerably modified the response of the model. Therefore, the lack of knowlegde about the dynamic characteristics of this buildings could lead to a false sense of security. Results from the probabilistic model depicts the level of uncertainty on the estimation of the behaviour of this kind of structures, even though that model is enriched with data. This results depicts the need of more investigation about this structural system.

According to ASCE 41 provisions, the deformation limit for collapse prevention performance criterion can be set from the point of maximum strength of the constitutive behavior of a structural element, based on laboratory test results. Notice that current structural evaluation provisions define deformation capacities of the structural elements in a deterministic fashion, in term of parameters that are subjected to uncertainties. This approach could lead to biased results. As shown in Figure 6.15, the deterministic model over-predicts the seismic capacity of the building, in comparison to the results obtained from the deterministic modified model (here assumed as the "true" result). In this example, it is shown the importance of obtaining reliable constitutive parameters for seismic evaluation of structures. Median regression-based parameters should be used with caution for seismic evaluation of structures.

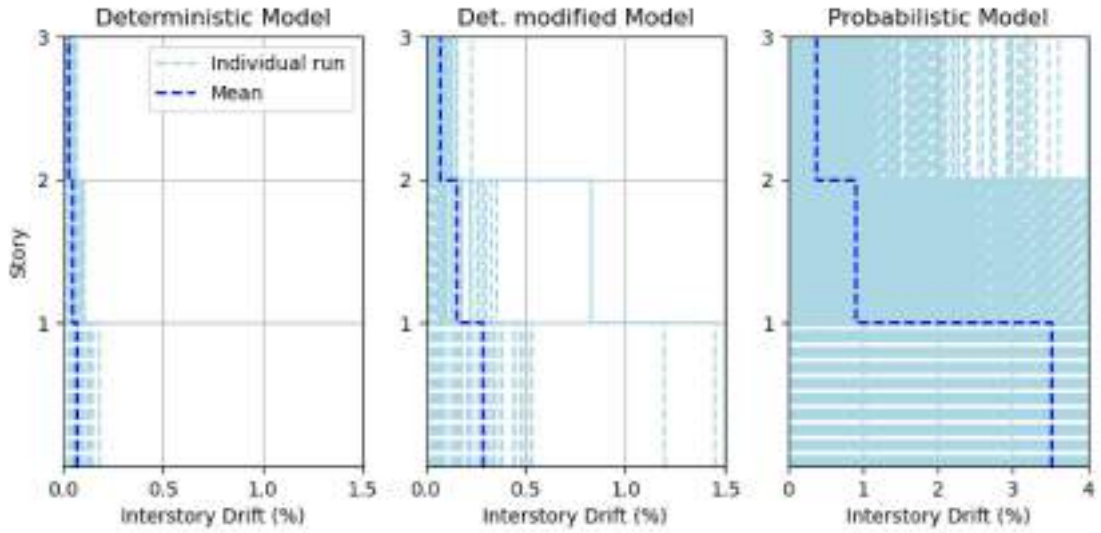

Figure 6.13: Interstory drift results of each analysis model, for every seismic record of FEMA P695, corresponding to maximum considered earthquake (MCE) hazard.

Figure 6.15 also shows the results obtained using the probabilistic approach with the presented probabilistic model. The damage index formulation presented in Section 6.1.1 is used here as the collapse prevention performance limit criterion, allowing to consider the uncertainties of the system also in the expected deformation capacity. Notice that the results from the deterministic modified model lay within the confidence interval of the probabilistic model blind-prediction. Also, the probabilistic model prediction depicts high uncertainties, giving to the structural engineer some insight about the knowledge of the expected behavior of the structure and the need for increase that knowledge in order to get a more confident result.

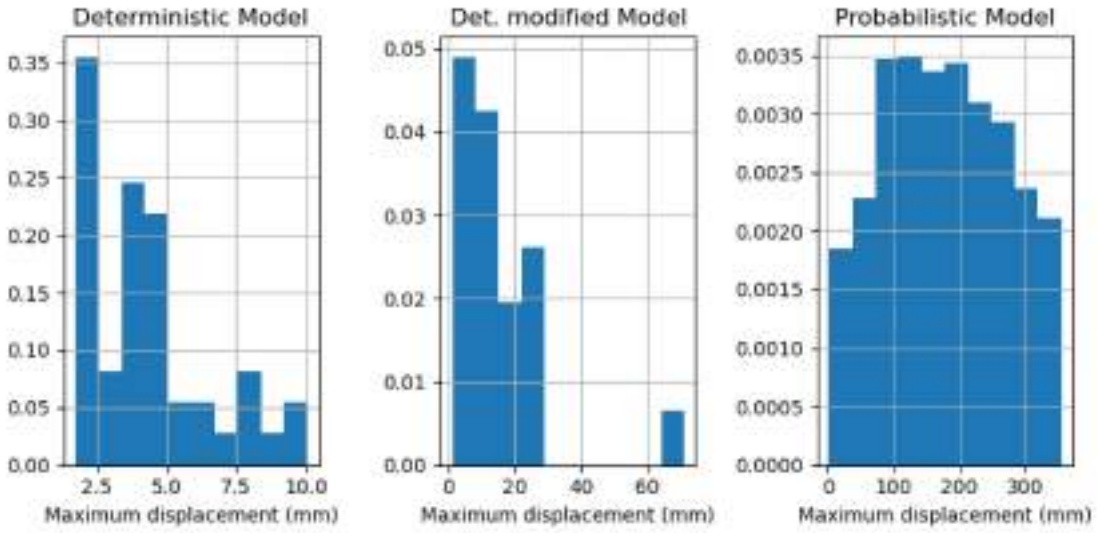

Figure 6.14: Top displacement PDF results of each analysis model, for every seismic record of FEMA P695, corresponding to maximum considered earthquake (MCE) hazard.

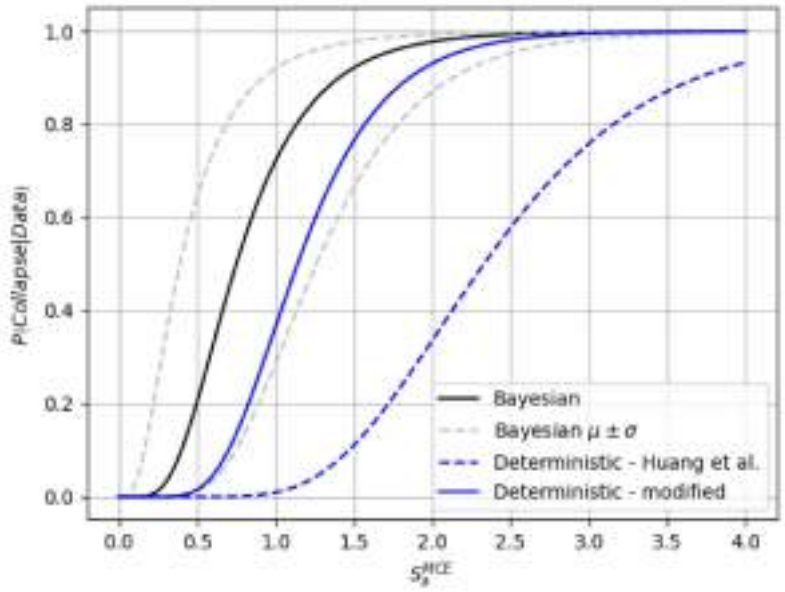

Figure 6.15: Comparison of Fragility Functions from the performed analyses.

Part III

Experimental contributions

Chapter 7

Static tests

This chapter presents a number of static tests developed during the work course of this thesis. The main objective of these tests is to propose a non-destructive and non-invasive test methodology to estimate the IP stiffness of the infills through the OOP wall dynamical response. This IP-OOP interaction has been experimentally demonstrated in some recent works (Cavaleri et al., 2020; De Risi et al., 2019; Misir et al., 2016; Palieraki et al., 2018) which state that it is possible to indirectly infer the IP stiffness of an existing wall by identifying the OOP fundamental frequency. Here, the aforementioned characteristic behaviour of the masonry wall is exploited to infer the IP stiffness of the element by a correlation with the OOP fundamental frequency of the wall. The OOP fundamental frequency can be obtained by non-destructive testing using available system identification methods (Reynders, 2012). An experimental campaign was carried out to identify correlation between the IP stiffness of the system with the identified OOP frequency of the wall.

7.1 Description of the specimens

Five one-fourth scale, one-bay and one-story MIFs were tested in the Structures Laboratory of the Catholic University of Santiago of Guayaquil, as shown in Figure 7.1. Three specimens consisted of reinforced concrete frames whereas two of them were made of structural steel. The infill walls were constructed with hollow concrete masonry units of 100x50x50 [mm], covering a wall of 750 [mm] clear height, and $\{500, 750, 1000\}$ [mm] clear bay for the three concrete frames, and $\{500, 1000\}$ [mm] for the steel frames, respectively.

Concrete columns were 75x75 [mm] cross section with longitudinal reinforcement ratio of 0.024 (i.e. four 6.5 [mm] diameter bars) and 10 [mm] of cover; transverse reinforcement consisted on one 3.5 [mm] diameter stirrup with separation of 18 [mm]. Top beam was 62.5x87.5 [mm] cross section with two 5.5 [mm] and two 4.5 [mm] bars as top and bottom reinforcement, respectively; transverse reinforcement

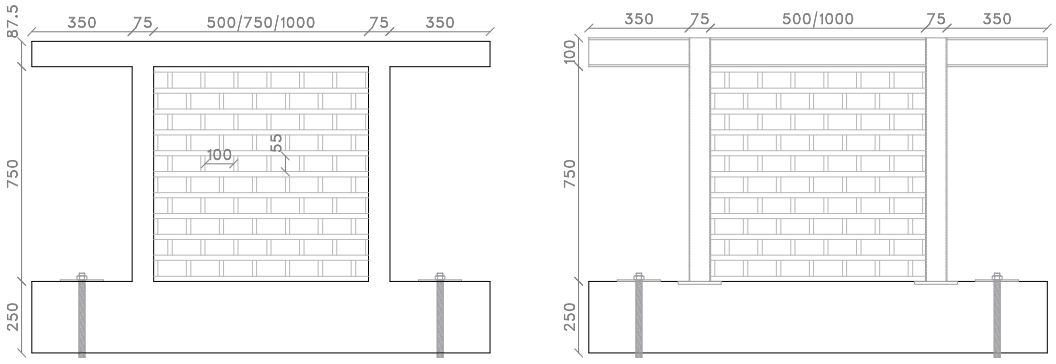

Figure 7.1: General geometric characteristics of the masonry infilled concrete and steel frame specimens.

consisted on one 2.5 [mm] diameter stirrup at 18 [mm] of separation. Steel frame columns consisted of HSS 75x75x3 [mm], and the top beam, an IPN-100 cross section. Both concrete and steel structural sections are shown in Figure 7.2.

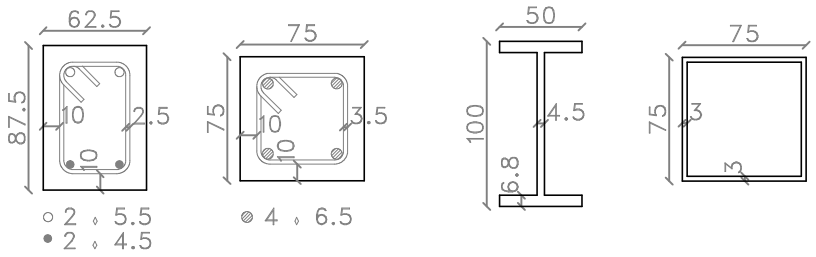

Figure 7.2: Concrete and steel beam and column sections of the specimens.

In all of the specimens, a 250x250 [mm] reinforced concrete beam with four 18 [mm] diameter longitudinal reinforcing bars and 5.5@150 [mm] stirrups was used as the bottom beam; this beam was anchored to the reaction frame with two 24 [mm] bars, as shown in Figure 7.3. Table 7.1 shows the material properties of the specimens. Additionally, two specimens of bare frames (without walls) were tested.

Table 7.1: Specimens material properties

Element	Test	Mean Results (MPa)	Standard Deviation (MPa)
Mortar	Flexure	4.1	1.517
	Compression	12.0	4.909
Masonry	Compression	0.1	0.038
Wall	Indirect tension	1.5	
Steel Reinforcement:			
3.5 mm[a]	Yield tension	441.7	
4.5 mm[a]	Yield tension	466.3	
5.5 mm[a]	Yield tension	568.8	
7.5 mm[a]	Yield tension	699.6	

[a]Only one coupon was tested for each size of steel reinforcement.

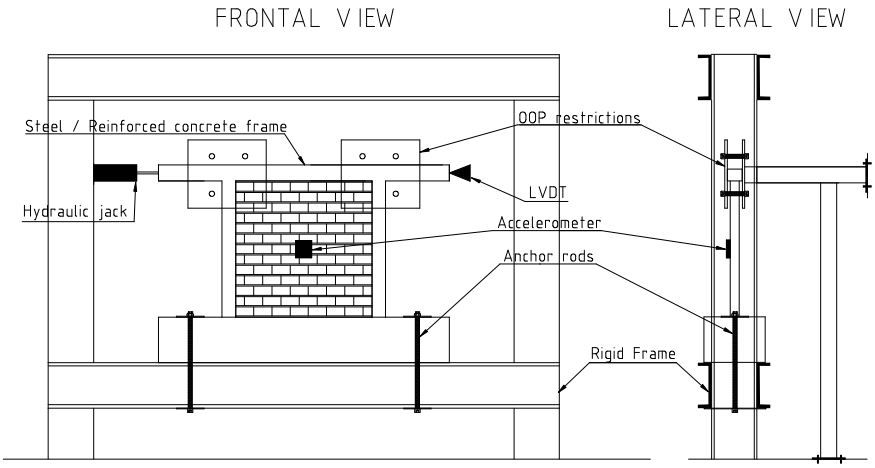

Figure 7.3: Schematic view of the test layout. Left side: frontal view, right side: lateral view.

(a) Frontal view.

(b) Lateral view.

Figure 7.4: Layout of the test.

7.2 Test procedure

The test procedure designed to assess the IP-OOP interaction behaviour of the masonry walls, has the following characteristics:

1. The MIF was anchored to the rigid frame and the measuring devices were installed.
2. The top beam of the MIF is laterally restrained against OOP movement, as shown in Figure 7.3. The plates, bolts and braces act as a restrain to the OOP movement of the top beam, modelling the restriction of an upper floor slab.
3. OOP acceleration was measured at the center point of the wall using a GY-61 arduino with an ADXL335 triaxial accelerometer (Analog Devices, 2009). A series of fists were performed with a

rubber hammer in order to induce readings of OOP acceleration of the wall. These measurements are later used to identify some of the OOP modal frequencies of the wall (see Section 7.3 for more details about the modal identification process). The aforementioned accelerometer has sufficient capabilities to identify the fundamental frequency of the down-scaled walls, with the advantages of low-cost and simple implementation.

4. After the reading of the acceleration, the bolts are released and the plates are removed. Then, IP monotonic loading is applied to the top beam until a determined lateral drift is reached, followed by the unloading. Force and deformation pairs are recorded during loading and unloading. Force was indirectly measured using a pressure gauge installed in the hydraulic jack, and top displacement was measured using a MIRAN Linear Position Sensor (Miran Sensor, 2016).

These steps were taken with increasing IP displacement cycles in order to capture the IP degradation of the wall and the corresponding OOP modal frequencies. Figures 7.5 and 7.6 display the IP force-displacement test results of the reinforced concrete MIFs and structural steel MIFs, respectively. Also, concrete and structural steel bare frames are shown in those figures. Figure 7.8 shows the secant IP stiffness in terms of the maximum deformation, δ, for each test; the tendency functions to predict IP stiffness k_{IP} are taken of the form:

$$k_{IP} = Ae^{B\delta} + C \tag{7.1}$$

where A and B can be obtained by a non-linear least squares optimization and C is set as the initial stiffness of the frame without infills (in [kN/mm]). Figure 7.8 also depicts a similar tendency of the OOP fundamental frequency, f_{OOP}, in terms of the maximum deformation demand δ, with the following equation:

$$f_{OOP} = De^{E\delta} - F \tag{7.2}$$

where D, E and F can also be obtained by non-linear least squares fitting. Similar tendencies on the stiffness degradation due to the maximum attained IP deformation were also observed by other authors (Cai and Su, 2017; Jiang et al., 2015b; Mansouri et al., 2014; Misir et al., 2016; Morandi et al., 2018b; Tasnimi and Mohebkhah, 2011; Zovkic et al., 2013). These tests results show the plausibility of the indirect inference of k_{IP} in terms of the f_{OOP} and the length of the wall. In the following section, the post processing methodology applied to identify the OOP fundamental frequency is described.

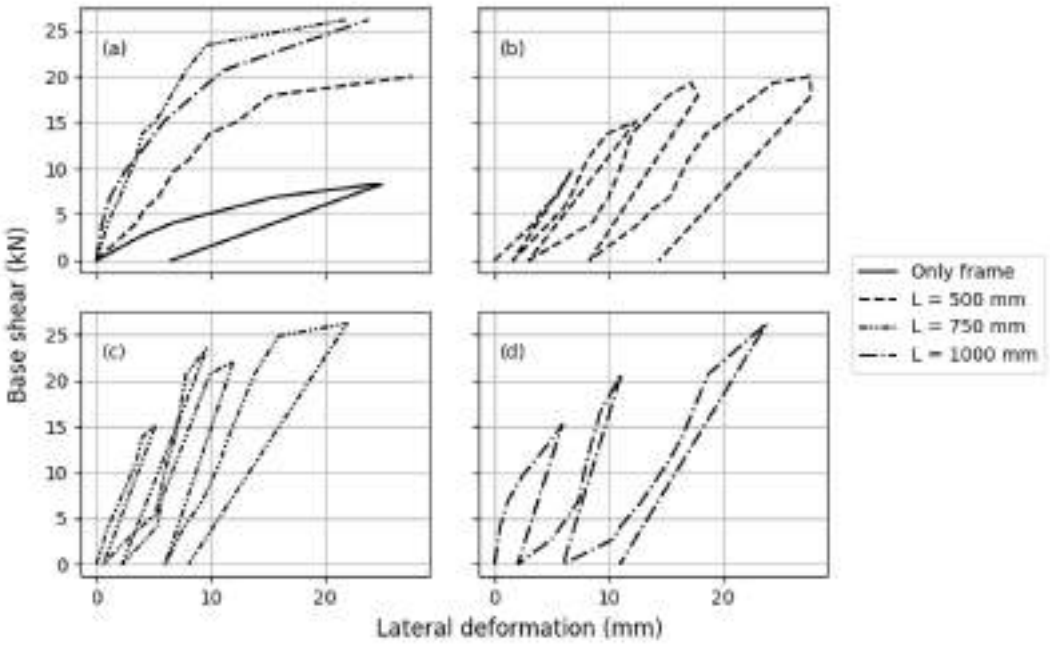

Figure 7.5: IP Test results of concrete plain frame and masonry reinforced concrete infilled frames. (a) Envelopes of each test, (b) to (d) Load-Deformation history of MIFs specimens.

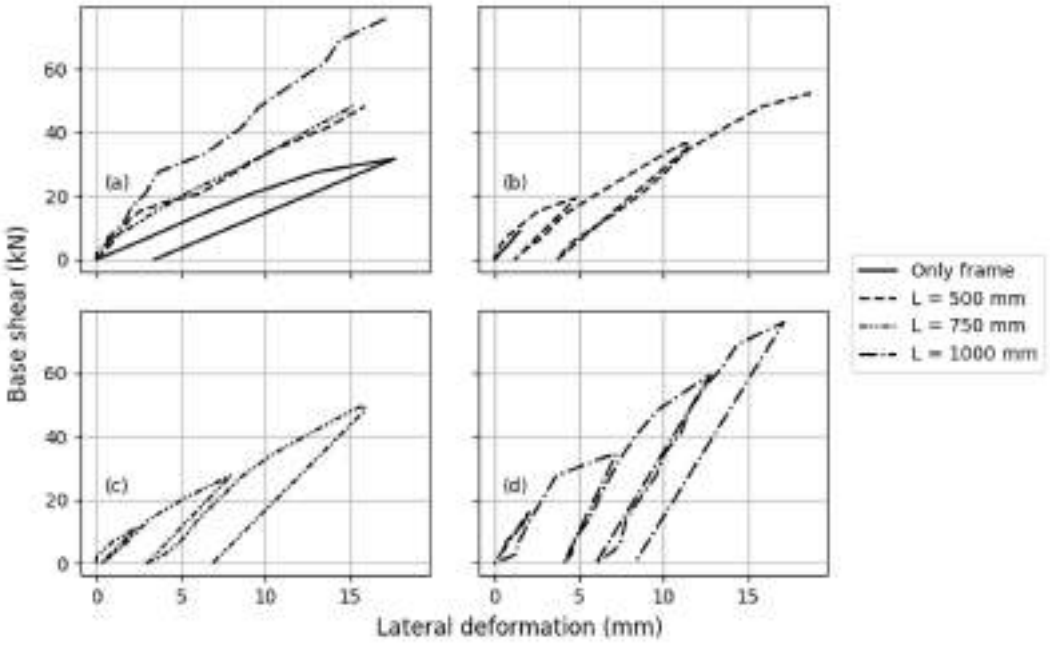

Figure 7.6: IP Test results of structural steel plain frame and masonry infilled structural steel frames. (a) Envelopes of each test, (b) to (d) Load-Deformation history of MIFs specimens.

7.3 OOP fundamental frequency identification

As mentioned before, the acceleration induced by an impulsive force applied perpendicularly to the mid point of the wall was measured in the OOP direction. This procedure is similar to EMA (Experimental Modal Analysis) method, but without an exact coincidence of the location of the application of the force and the point of measurement of the response (Allemang, 1983). The impulsive force is applied to induce energy into a broader frequency band, allowing the identification of lower frequencies. This procedure was applied to five of the specimens, after subjecting them to incremental levels of deformation on the IP direction.

Each of the acquired acceleration signals (i.e. each frame and each level of IP deformation) were subjected to a base-line correction and later passed through a band-pass filter with cutoff frequencies of 32 and 512 Hz. The cutoff frequencies were defined from an estimation made using a finite element model of the walls, where the higher cutoff frequency was set so that the first five OOP vibration modes of the stiffest specimen lie in that range. As mentioned in the third step of Section 7.2, the specimens were subjected to several impulsive hammer loading during the recording of the OOP accelerations. The measured response was split in separate impulses and the results were later used to confirm the obtained frequency from the complete record.

The Frequency Domain Descomposition (FDD) method was used here to identify the natural frequencies of the specimens. This is a non-parametric identification procedure in the frequency domain (Brincker et al., 2000), which states that the dynamic response of a system can be obtained from the convolution, in the frequency domain, between the excitation signal and the response of an unitary impulse. Then, the power density spectrum (PDS) gives the energy level of the response of the system for each frequency. Figure 7.7 depicts the PDS of the steel frame specimen S500, for each level of IP deformation. Notice that a moving average post-process was used to locate the maximum values of the PDS, along with a normalization to the maximum value. The right panel of Figure 7.8 shows the results of the identified fundamental frequencies of all specimens in terms of the maximum lateral demand.

7.4 Proposed MIF modelling approach

This section formulates the IP stiffness model based on OOP fundamental frequency of the wall, and defines a macro-model based on the aforementioned IP-OOP relation. This model is parameterized by a set of uncertain parameters, which are further inferred through Bayesian inference using the experimental data described in the previous section. A strut-based model, commonly known as *macro-model* (Tarque et al., 2015), has been adopted here to idealize the stiffening effect of the frame caused by the masonry infills. To this end, a 2D model was defined using OpenSeespy (Zhu et al., 2018), which consisted of an *elastic truss* element disposed along the principal diagonal of the frame bay, as shown in Figure 7.9. The strut section is modelled as $A_m = t_m w_m$, where t_m is the thickness of the wall and w_m is assumed as one-third of the

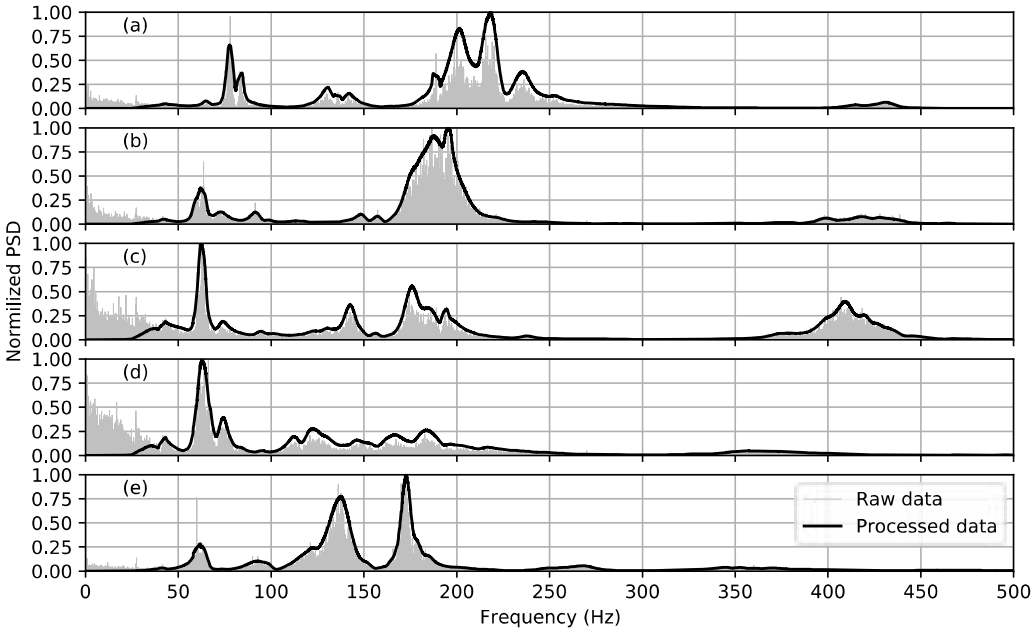

Figure 7.7: Power Density spectra of the OOP measurements of specimen S500 MIF, after each level of IP deformation: (a) Undamaged, (b) to (e) depicts the results after each increasing deformation.

length of the wall's diagonal. The strut, the beam, and the frame columns of this model are considered as elastic elements. For the stiffness k_{IP} of this strut, the exponential decay relations between the IP and OOP behaviour, observed in the previous sections (recall Equations (7.1), (7.2), and Figure 7.8), are used. Indeed, note that according to these observations, both the IP stiffness and the OOP fundamental frequency decay with the increase of lateral IP deformation. To model this fact, Equations (7.1), (7.2) are rearranged as follows:

$$\delta = \ln\left(\frac{k_{IP} - C}{A}\right)^{\frac{1}{B}} \tag{7.3}$$

$$\delta = \ln\left(\frac{f_{OOP} - F}{D}\right)^{\frac{1}{E}} \tag{7.4}$$

These equations can be combined to obtain the K_{IP} as a function of f_{OOP}, as follows:

$$k_{IP} = A\left(\frac{f_{OOP} - F}{D}\right)^{\frac{B}{E}} + C \tag{7.5}$$

Finally, with no loss of generality, the last equation can be simplified using only three parameters, now called as $\theta_1, \theta_2, \theta_3$ leading to the following expression:

$$k_{IP} = \theta_1 \left(f_{OOP} - \theta_2\right)^{\theta_3} \tag{7.6}$$

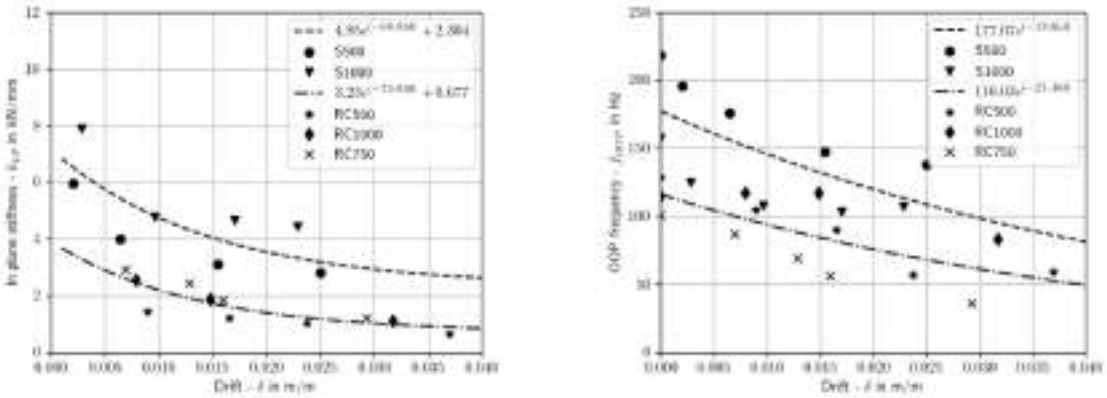

Figure 7.8: Degradation of IP stiffness (left) and reduction of OOP natural frequency (right) in terms of attained IP drift and type of frame.

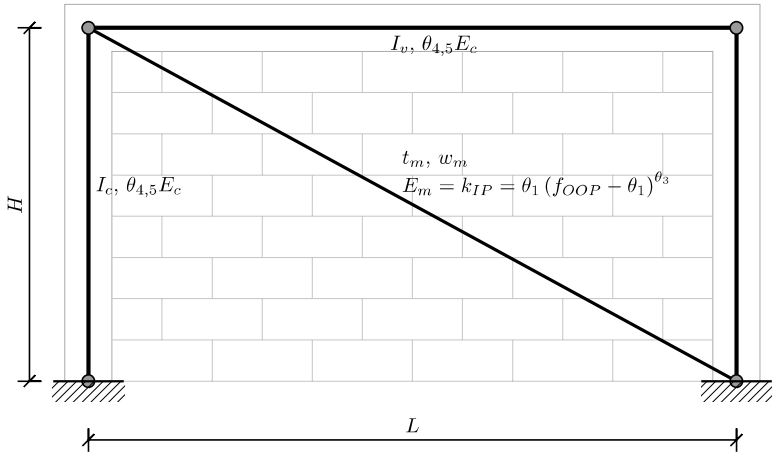

Figure 7.9: Elastic IP macro model constructed in OpenSeespy.

In the last equation, the parameters θ_1 to θ_3 are uncertain parameters and can be inferred using the tests results, as described in the following section. Additionally, the strut macro-model considers two extra parameters to account for the concrete and steel stiffness. In total, five uncertain parameters comprise the proposed strut macro-model, namely $\tilde{\boldsymbol{\theta}} = \{\theta_1, ..., \theta_5\}$, where θ_1 to θ_3 are to consider the elastic modulus of the equivalent strut, based on the OOP fundamental frequency, θ_4 is a concrete frame stiffness modifier to consider the stiffness reduction due to cracking, and finally θ_5 is a steel frame stiffness modifier, to account for base plate rotational flexibility.

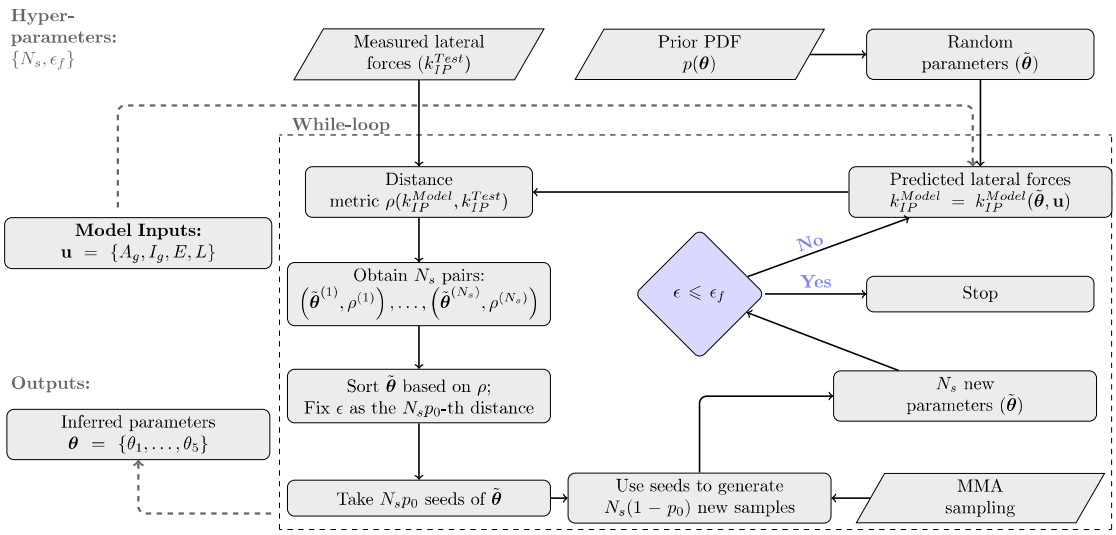

Figure 7.10: A flowchart explaining $\mathcal{A}^2$BC-SubSim, Barros et al. (2021). $\tilde{\boldsymbol{\theta}}$ parameters are defined as the modifiers of Equation (7.6). A_g, I_g, E, L are the gross area, gross inertia, elastic modulus and length of the beam-column elements of the frame, respectively.

From the tests results described in Section 7.1, the model was calibrated using the approximate Bayesian computation method (ABC) called $\mathcal{A}^2$*BC-SubSim* presented in Chapter 5. The following function was adopted as the metric:

$$\rho = \sum_i \left[\frac{\left| k_{IP}^{Model} - k_{IP}^{Test} \right|}{k_{IP}^{Test}} \right]_i \tag{7.7}$$

where i denotes each of the tests of the experimental campaign, k_{IP}^{Model} and k_{IP}^{Test} are the numerically estimated and the experimentally measured IP stiffness of the system, respectively.

Figure 7.11 depicts the *prior* and the *posterior* distribution of the inferred parameters. Figure 7.12 shows the estimated IP stiffness results from the calibrated model in comparison to the measured stiffness from the laboratory tests. These results demonstrate the plausibility to infer the IP stiffness of a MIF by identifying the OOP fundamental frequency, and using Equation (7.6) (notice that the parameters were calibrated to estimate the stiffness in units of $\frac{kN}{m}$). However, the parameters of that equation were set for a unique kind of masonry characteristics and, therefore, they are not expected to be suitable for direct application to other masonry characteristic strength or geometry. To overcome to this limitation, in the following sections a non-linear model is presented, along with its calibration to the observed data, to be used within a parametric study. The results of the parametric study are used latter to expand the applicability of the proposed method.

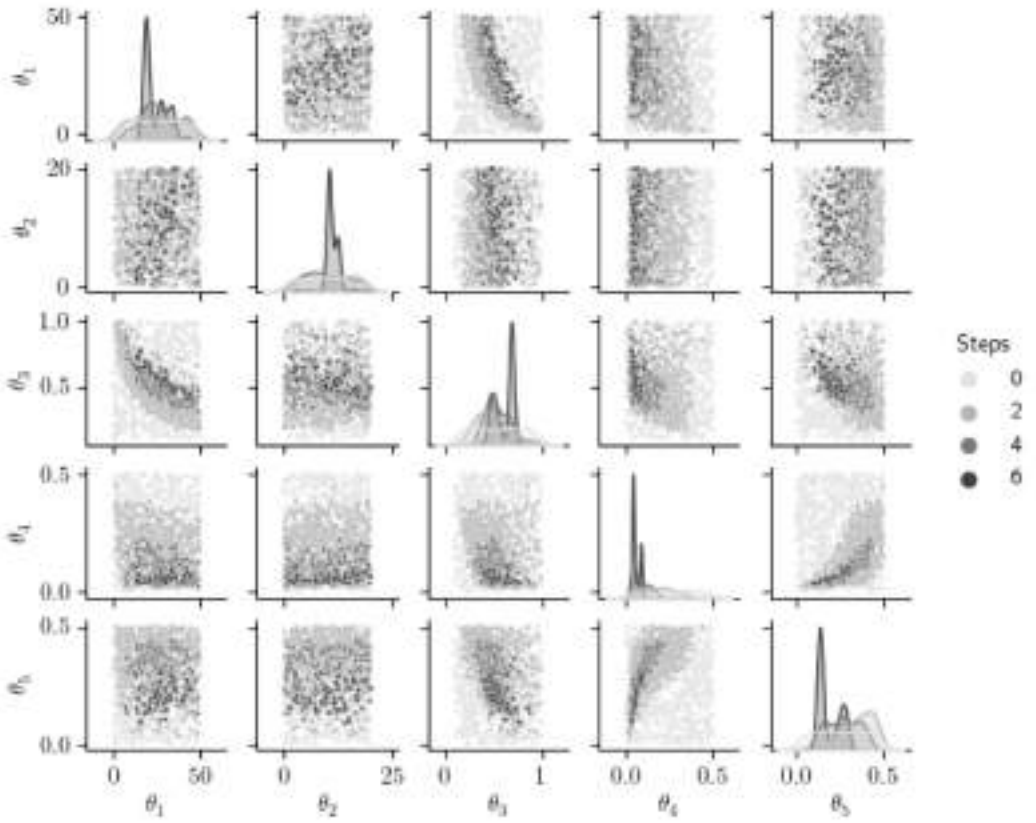

Figure 7.11: Scatter plot representation of the posterior PDF of $\boldsymbol{\theta} = \theta_1, ..., \theta_5$ as $\mathcal{A}^2$BC-SubSim output. The diagonal shows the kernel density estimates of the marginal posterior PDFs of each parameter of the simplified model of Figure 7.9.

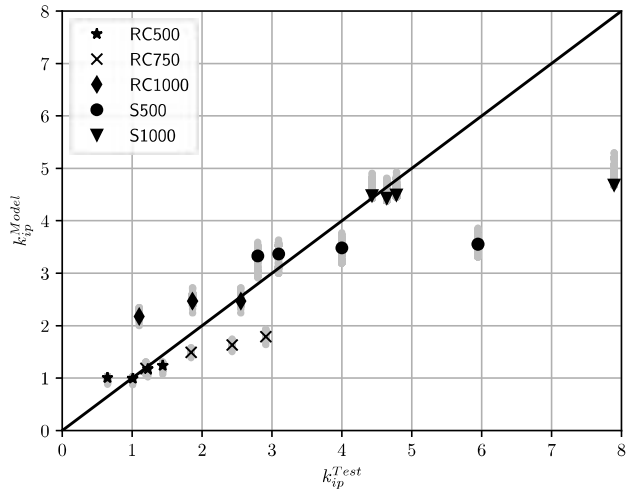

Figure 7.12: Comparison of the calibrated model K_{IP} prediction, against the measured test results. Black marks correspond to the maximum a posteriori (MAP) estimation. Silver marks depict the range of the posterior distribution that results from the Bayesian analysis.

7.5 Parametric study

There are several techniques to model the behaviour of MIFs, as mentioned in Chapter 2. In this thesis, the application of a *meso*-model called *Multi Pier*, originally proposed by Pirsaheb et al. (2020), is explored. Accordingly, the masonry wall is modelled as a 3D truss, allowing to directly incorporate the IP-OOP behaviour interaction of the masonry wall, with the advantages of being computationally cheap, robust and easily implementable in any software. In this investigation, this model was built using OpenSeespy, and was properly calibrated to capture the behaviour of the specimen RC750. In the following section, the implemented model is described and later used to study the influence of geometric parameters in the prediction of Equation (7.6). Only reinforced concrete frames were included in this study.

7.5.1 Masonry infilled frame model

The MIF model is built in OpenSeespy and consists of two main parts: (1) the reinforced concrete frame model and (2) the masonry wall model. Both parts are joined together using equal degree of freedom constraints, therefore assuming a perfect bond between the reinforced concrete frame and the masonry wall. Accordingly, the discretization of both parts of the model are defined as geometrically coincident. Figure 7.13 shows the geometric representation of the MIF model.

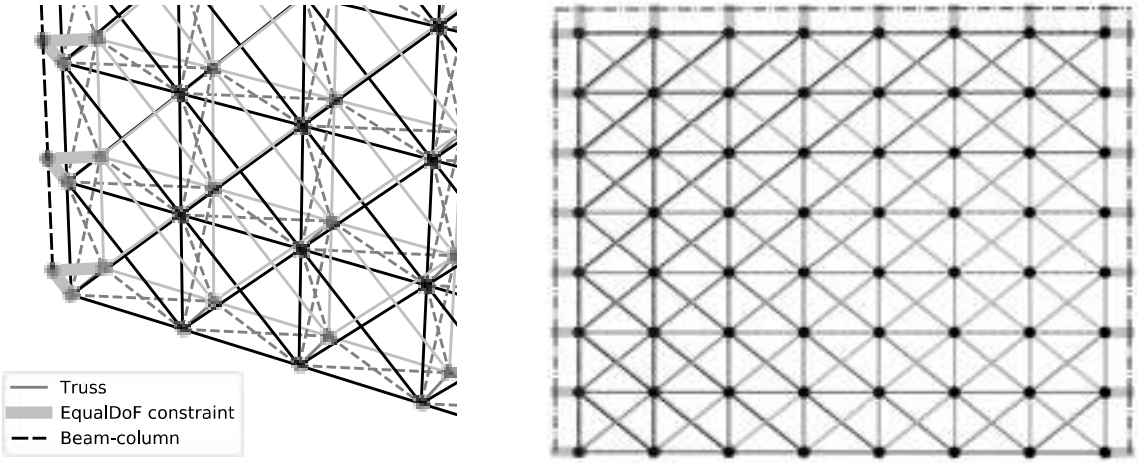

(a) Isometric view of the bottom left part of the MIF model.

(b) Front view of the MIF model.

Figure 7.13: Geometric representation of the MIF model implemented in OpenSeespy.

The first part of the model consists of distributed plasticity displacement-based beam-column elements with uni-axial constitutive models by means of a fiber section. *Concrete01* and *Steel02* constitutive models were adopted to estimate the concrete and steel reinforcement behaviour, respectively. Parameter values were evaluated from the equations proposed by Karthik and Mander (2011). Strain penetration effects

are also considered by means of a rotational spring at the base of the column. The parameters of the rotational spring are calibrated according to the bare frame test results (see Figure 7.5 and Section 7.1). The rotational spring is defined by a *Zero-Length* element and the *Hysteretic* constitutive model. Table 7.2 shows the parameter values of the fiber section and the rotational spring after the calibration process.

Table 7.2: Parameter values of frame model.

Hysteretic - Zero-Length element

θ_1^{rot}	M_1	θ_2^{rot}	M_2	$Pinch_x$	$Pinch_y$	D_1	D_2	β
0.01008	1.52	0.32215	13.05	0.06200	0.29760	0.24010	0.12173	0.26799

Concrete01 - Column Section				Steel02 - Column Section		
f_c	ϵ_0	f_{cu}	ϵ_u	f_y	E_s	b
-20.0	-0.00200	-5.00	-0.01000	500.0	200.00	0.140

The second part of the model consists of a 3D truss, composed by horizontal, vertical and diagonal elements with uni-axial behaviour. *Concrete02* constitutive model was selected for every truss. Maximum compressive strength was assumed to be equal to the characteristic compressive strength of the masonry (see Table 7.1). Notice that the characteristics of the material are defined in terms of stress and strain; however, truss models require an input in terms of force and deformation. The formulation applied for that conversion is described in detail by the original authors of the model, and the interested reader is referred to Pirsaheb et al. (2020) for additional details. RC750 specimen test results were used to calibrate the model. The tensile strength of the masonry struts was taken as 5% of the compressive strength. The compressive strain at maximum strength was set equal to 0.2%. The calibrated model was adapted to RC500 and RC1000 geometries to evaluate its prediction capabilities. Figure 7.14 depicts the comparison of the model prediction against the IP test results, and Table 7.3 shows the prediction capabilities on the OOP fundamental frequencies. It can be concluded that the model is representative of the behaviour of the MIF structural system. In the following sections, the calibrated model is applied to study the influence of geometric and strength parameters on the IP-OOP behaviour.

Table 7.3: OOP fundamental frequency comparison between Multi Pier model and laboratory test measurement.

OOP test	Model			Test			Error (%)		
	RC500	RC750	RC1000	RC500	RC750	RC1000	RC500	RC750	RC1000
1	150	102	85	129	101	115	16.3	1.0	26.1
2	128	81	63	105	87	117	21.9	6.9	46.2
3	91	79	62	90	69	117	1.1	14.5	47.0
4	79	73	48	57	56	83	38.6	30.4	42.2
5	79	73		59	36		33.9	102.8	

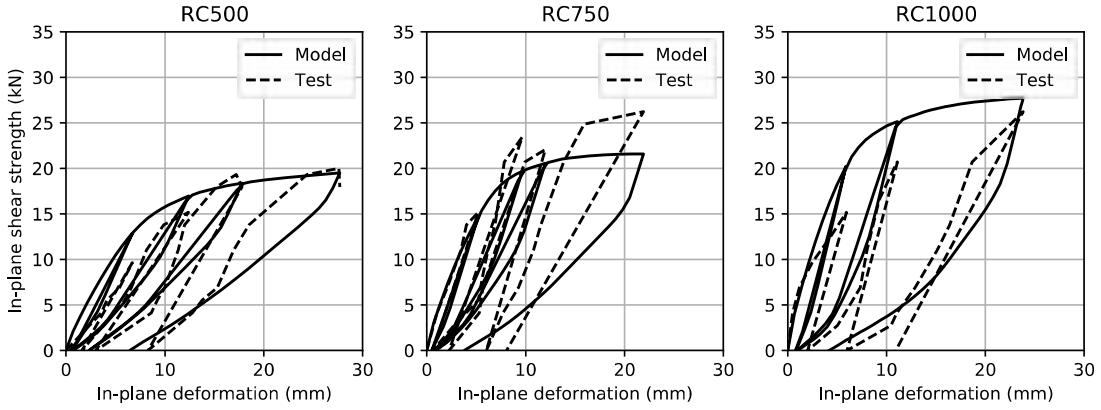

Figure 7.14: Comparison of the calibrated model estimation against the laboratory test results.

7.5.2 Influence of masonry height / length ratio

Using the model described in the previous section, the following parameters were set as constants: $f_m = 1.0$ MPa, $t_m = 50$ mm, $H_m = 750$ mm, where f_m is the characteristic compressive strength of the masonry wall, t_m, H_m and L_m are the thickness, height and length of the wall, respectively. Accordingly, the $^{H_m}/_{L_m}$ ratio was defined for several L_m values, giving the range between 0.4 and 2.0, approximately. Figure 7.15a depicts the OOP expected fundamental frequency in terms of the maximum attained IP drift and the adopted L_m values. As expected, the increasing deformation induces degradation on the wall, reducing the OOP stiffness and, therefore, the fundamental frequency.

Figure 7.15b depicts the OOP fundamental frequency in terms of the $^{H_m}/_{L_m}$ ratio, for the case of a non degraded wall (i.e. IP drift equal to 0). The $^{H_m}/_{L_m}$ tendency equation in terms of the OOP frequency is also shown in that figure, where it is demonstrated that the OOP frequency increases with an increment of the $^{H_m}/_{L_m}$ ratio. Comparing these results to the measured behaviour in Figure 7.8, seems that the RC1000 does not follow the tendency of the model. This condition may be caused by the fact that the joint between the wall and the upper beam of the frame is usually difficult to construct properly, meaning that the assumption made about the perfect bond between the frame and the wall may not be representative for the upper joint in that case. To address this issue, it would require additional tests and, as a consequence, it is left as future work of this thesis.

7.5.3 Influence of masonry height / thickness ratio

Similar to the analysis of the previous section, the following parameters were set as constants: $f_m = 1.0$ MPa, $L_m = 750$ mm, $H_m = 750$ mm. Accordingly, the $^{H_m}/_{t_m}$ ratio was defined for several t_m values, giving the range between 11 and 30, approximately. Figure 7.16a depicts the OOP expected fundamental frequency in terms of the maximum attained IP drift and the adopted t_m values. Consistent results were obtained in terms of the IP deformation and OOP fundamental frequency.

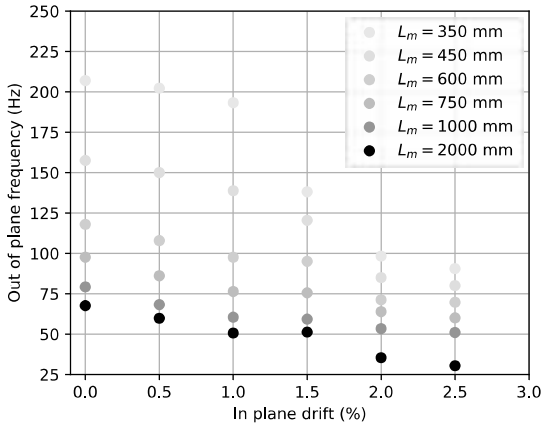

(a) Influence of masonry wall length and IP drift on the OOP frequency.

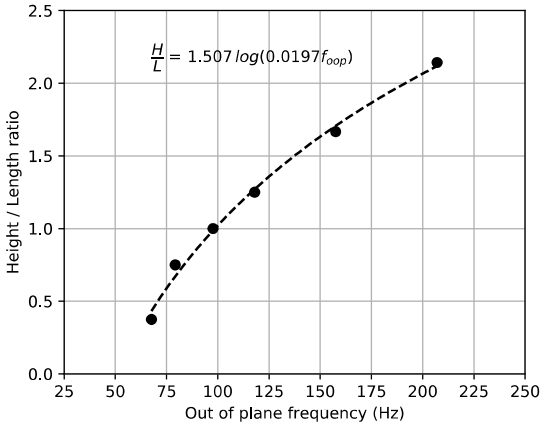

(b) Height-length ratio in terms of the measured OOP fundamental frequency for an undeformed MIF.

Figure 7.15: Influence of masonry height / length ratio on the IP and OOP stiffness.

Figure 7.16b shows the OOP fundamental frequency in terms of the $^{H_m}/_{t_m}$ ratio, for the case of a non degraded wall. The $^{H_m}/_{t_m}$ tendency equation in terms of the OOP frequency is also shown in that figure, where it is demonstrated that the OOP frequency increases as the $^{H_m}/_{t_m}$ ratio decays.

7.5.4 Influence of masonry characteristic strength

Similar to the analysis of the previous section, the following parameters were set as constants: $H_m = 750$ mm, $t_m = 50$ mm, $L_m = 750$ mm. Accordingly, the f_m characteristic strength was defined in the range between 1 and 8 MPa. Figure 7.17a depicts the OOP expected fundamental frequency in terms of the maximum attained IP drift and the adopted f_m values. Consistent results are obtained in terms of the IP deformation and OOP fundamental frequency.

Figure 7.17b shows the OOP fundamental frequency in terms of the f_m value, for the case of a non

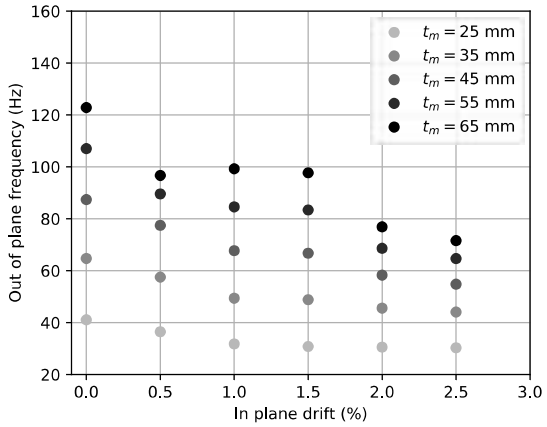

(a) Influence of masonry thickness and IP drift on the OOP frequency.

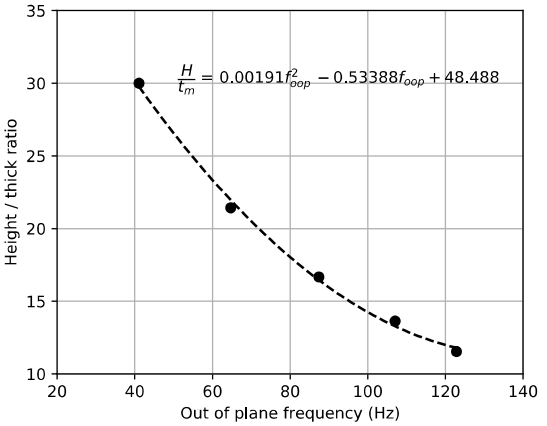

(b) Height-thickness ratio in terms of the measured OOP fundamental frequency for an undeformed MIF.

Figure 7.16: Influence of masonry height / thickness ratio on the IP and OOP stiffness

degraded wall. The f_m tendency equation in terms of the OOP frequency is also shown in that figure, where it is demonstrated that the OOP frequency increases as the f_m value gets higher.

7.5.5 Influence of scaling

Similar to the analysis of the previous section, the following parameters were set as constants: $H_m/L_m = 1$, $H_m/t_m = 15$ and $H_m = 750$ mm for the original scale. Accordingly, the scaling factor was defined in the range between 1 to 5. Figure 7.18a depicts the OOP expected fundamental frequency in terms of the maximum attained IP drift and the adopted scaling factors. Consistent results are obtained in terms of the IP deformation and OOP fundamental frequency.

Figure 7.18b shows the OOP fundamental frequency in terms of the scaling factor, for the case of a non degraded wall. The scaling factor tendency equation in terms of the OOP frequency is also shown in

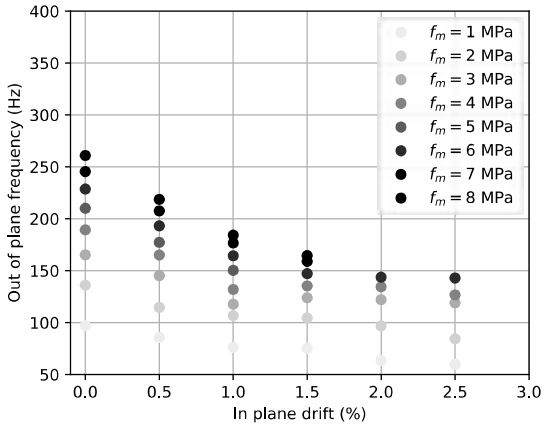

(a) Influence of masonry characteristic strength and IP drift on the OOP frequency.

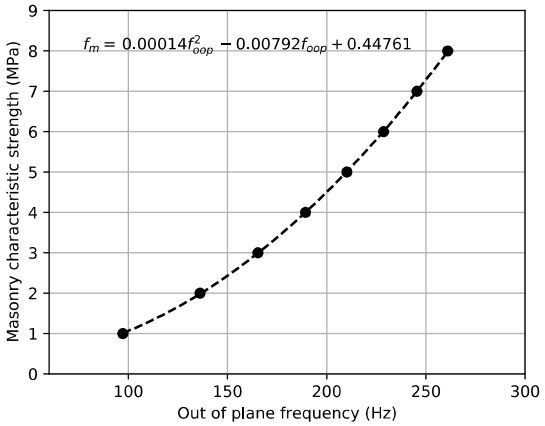

(b) Characteristic compressive strength in terms of the measured OOP fundamental frequency for an undeformed MIF.

Figure 7.17: Influence of the characteristic compressive strength of the masonry on the IP and OOP stiffness.

that figure, where it is demonstrated that the OOP frequency decreases as the scaling factor gets higher.

7.6 Non-destructive test for indirect stiffness estimation

The parametric study of the previous section demonstrated that the OOP fundamental frequency is related to the maximum historic IP drift, the strength of the materials of the wall, the boundary conditions and the geometric characteristics of the wall. This section describes a method to estimate the IP stiffness of the wall in terms of geometric parameters and OOP fundamental frequency measure.

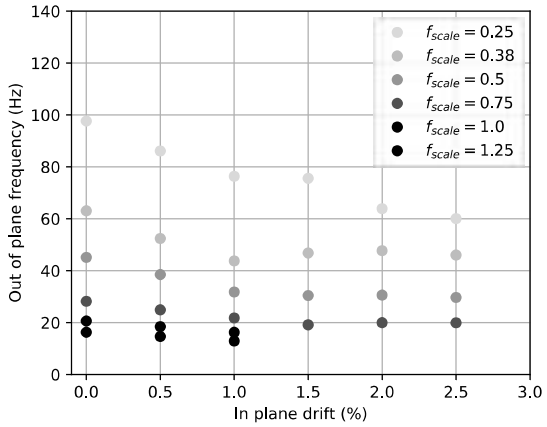

(a) Influence of scaling and IP drift on the OOP frequency.

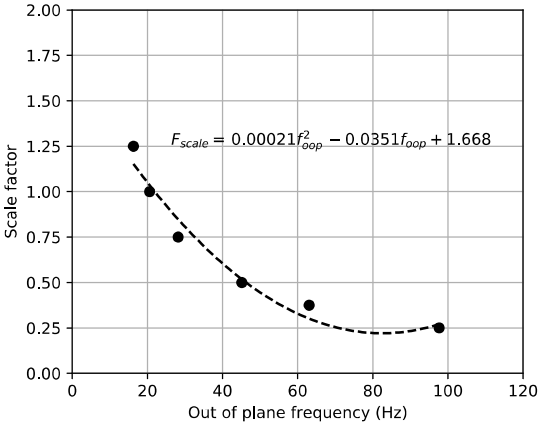

(b) Scaling factor in terms of the measured OOP fundamental frequency for an undeformed MIF.

Figure 7.18: Influence of the scaling factor of the masonry on the IP and OOP stiffness.

7.6.1 Proposed method

To consider the influence of height, length, thickness, strength and scaling of the masonry wall, Equation (7.6) is modified as follows:

$$k_{IP} = \theta_1 \left(f_{OOP} - \theta_2\right)^{\theta_3} \cdot f_{H/L} \cdot f_{H/t} \cdot f_{f'_m} \cdot f_{scale} \tag{7.8}$$

where the factors $f_{H/L}$, $f_{H/t}$, $f_{f'_m}$ and f_{scale} are modifiers of the IP stiffness of the simplified strut model that account for height/length ratio, height/thickness ratio, the strength of the wall and the scaling factor, respectively.

The modifier factors were obtained from the results of the parametric study, using the following process:

1. For each model, the IP secant stiffness was obtained for the different levels of drift and different

values of the parameters (i.e. length, thickness and strength).

2. The stiffness was normalized to the obtained stiffness of a basic case, considering the corresponding attained IP drift. For the $f_{H/L}$ modifier, $H/L = 1.00$ was adopted as the basic case, as shown in Figure 7.19a. Similarly, for the $f_{H/t}$ modifier, $H/t = 13.63$ was adopted as the basic case, as shown in Figure 7.19b. For the f_{scale} modifier, Scale = 0.25 was adopted as the basic case, as shown in Figure 7.19c. Finally, for the $f_{f'_m}$ modifier, $f'_m = 1.00$ MPa was adopted as the basic case, as can be seen in Figure 7.19d. In all cases, the basic condition was adopted from the model closer to the RC750 specimen, as it was used for the calibration of the model and, therefore, its results are the most reliable.

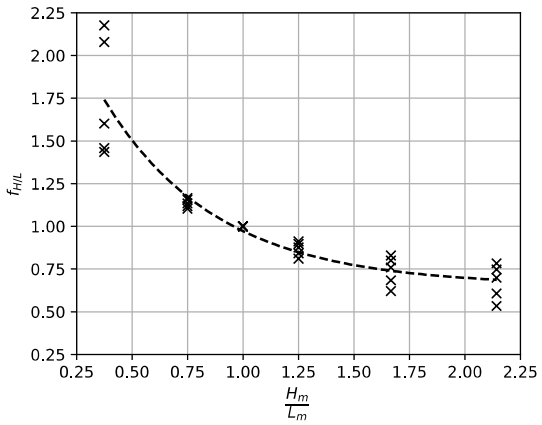

(a) Height-Length ratio modifier.

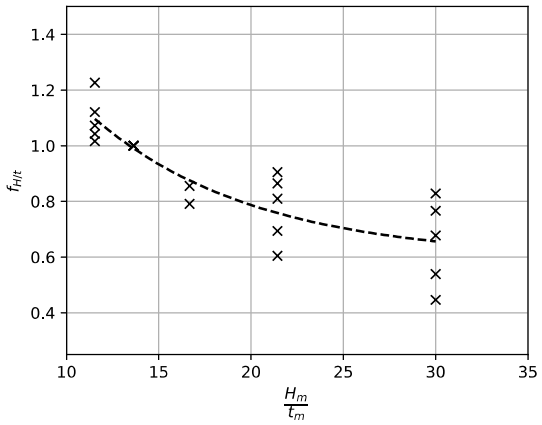

(b) Height-thickness ratio modifier.

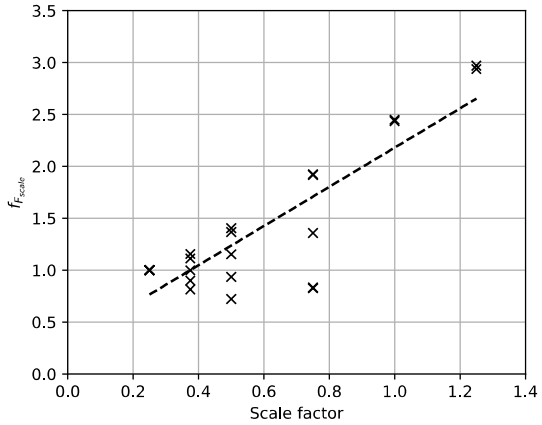

(c) Scaling factor modifier.

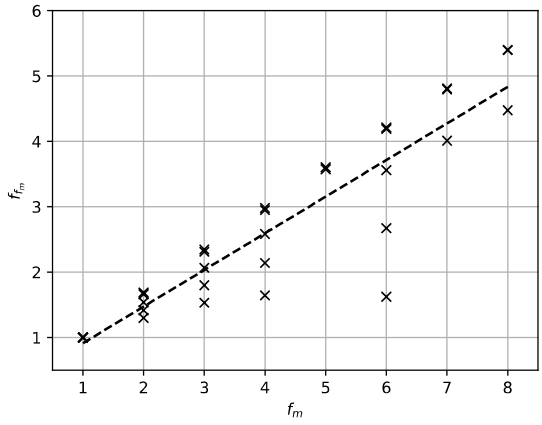

(d) Characteristic compressive strength modifier.

Figure 7.19: Functions of the modifier factors in terms of each influencing parameter.

7.6.2 Application examples

Four additional models were constructed using the Multi Pier methodology (see Section 7.5.1, to check the effectiveness of the proposed method defined by Equation (7.8) and Figures 7.19a to 7.19d. These models are used here as if they were existing MIF elements of a structure, where measured data is gathered. The geometric characteristics of each MIF are presented in Table 7.4. The OOP fundamental frequency and the IP tangent stiffness of the structural system, according to the numerical model, is also shown in that table. Finally, the modifier factors and the estimation of IP stiffness of the proposed method are presented. The cases were selected with the following criteria:

1. All cases are real size structures. Notice that the scale factor shown in the table are defined as either 0.83 or 1.00. Those values are obtained considering that a 0.25 scale corresponds to a wall height equal to 750 mm.

2. Column and beam sizes were defined equal for cases 1 and 2, and 3 and 4, respectively. Typical sizes for low-rise structures were assumed.

3. Case 1 is a tall wall, i.e the length is smaller than the height. Case 2 is a short wall, where the length is higher that the height. Cases 3 and 4 were set as squared walls.

4. Cases 1 and 2 are set to have a small height to thickness ratio, whilst cases 3 and 4 are set to a higher value.

5. Cases 1 to 3 use walls with characteristic masonry strength equal to 1.00 MPa (equal to the ones that were tested). Case 4 considers a higher strength.

6. All cases were assumed as non-degraded walls for the calculations presented in Table 7.4. Table 7.5 presents the same cases, where the MIF were subjected to a relative deformation less than 1.00% of the height.

As shown in Table 7.4, a fair prediction was obtained for the case of non-degraded MIFs, showing a difference of 4%, 15%, 25% and 34% for each case, respectively. For degraded MIFs, differences were 70%, 25%, 38% and 5%, respectively. These results are promising and seems that the proposed methodology would be a powerful tool for the stiffness evaluation of existing structures; however, it requires further laboratory testing to support some of the assumptions made.

Table 7.4: Summary of results of application examples for non-degraded MIFs from Section 7.6.2.

	Parameter	Case 1	Case 2	Case 3	Case 4
Frame sections	Column (mm)	400x400	400x400	300x300	300x300
	Beam (mm)	300x400	300x400	250x350	250x350
Wall geometry	L_m (mm)	2000	4000	3000	3000
	H_m (mm)	2500	2500	3000	3000
	t_m (mm)	200	200	150	150
	f_m (MPa)	1.00	1.00	1.00	5.00
	H_m/L_m	1.25	0.63	1.00	1.00
	H_m/t_m	12.50	12.50	20.00	20.00
	Scale factor	0.83	0.83	1.00	1.00
Multi Pier model	f_{OOP} (Hz)	44.6	29.1	17.6	38.4
	k_{IP} (kN/mm)	15.4	29.7	8.9	41.2
Geometric modifiers	$f_{H/L}$	0.90	1.25	1.00	1.00
	$f_{H/t}$	1.05	1.05	0.78	0.78
	f_{scale}	1.95	1.95	2.20	2.20
	f_m	1.00	1.00	1.00	3.20
Simplified model	k_{IP}^{mean} (kN/mm)	16.0	25.4	6.7	27.2
	k_{IP}^{std} (kN/mm)	1.30	1.91	1.17	1.22

Table 7.5: Summary of results of application examples for degraded MIFs from Section 7.6.2.

	Parameter	Case 1	Case 2	Case 3	Case 4
Multi Pier model	f_{OOP} (Hz)	26.44	20.5	13.5	27.8
	k_{IP} (kN/mm)	7.3	15.9	4.7	22.2
Simplified model	k_{IP}^{mean} (kN/mm)	12.5	20.0	2.9	21.1
	k_{IP}^{std} (kN/mm)	1.95	2.73	0.60	0.80

Chapter 8

Dynamic tests on shake table

During the last part of the thesis' work, an experimental campaign about dynamical tests on shake table were carried out. The main objectives of these tests were:

- To gather additional information about the IP-OOP interaction of MIF walls described in the previous chapter, but under excitation conditions equivalent to those encountered during a seismic event.
- To study the influence of cement-based mortar plastering on the IP initial stiffness and OOP fundamental frequency of MIFs.
- To study the influence of cement-based mortar plastering reinforced with natural fibers on the IP initial stiffness and OOP fundamental frequency of MIFs under seismic excitation.

The experimental campaign consisted on a series of dynamic tests performed on the seismic shake table of the University of Granada. Three 3/5 scaled MIFs were built with the same geometry and materials; however, the first wall was not plastered, whereas the other two were plastered with and without natural fiber reinforcement, respectively.

8.1 Description of the specimens

Three 3/5 scale, one-bay and one-story MIFs were installed on the shake table of the University of Granada, as shown in Figures 8.1a, 8.1b and 8.1c. All specimens consisted of reinforced concrete frames with infill walls constructed with hollow concrete masonry units of 400x200x90 [mm], as shown in Figure 8.2a. The clear height of the wall was 1520 mm and the clear bay length, 2090 mm. Concrete columns were 172x172 [mm] cross section with longitudinal reinforcement ratio equal to 0.0153 (i.e. four 12 [mm] diameter bars) with 15 [mm] cover; transverse reinforcement consisted on one 6 [mm] diameter stirrup with separation of 75 [mm]. The top beam was 140x175 [mm] cross section with two 10 [mm] and two 8 [mm] bars as

top and bottom reinforcement, respectively. The transverse reinforcement consisted on 6 [mm] stirrups at 90 [mm] of separation. Figure 8.2 depicts the cross section and general geometry of the MIF specimens. Nominal strength of the concrete was obtained by compressive cube testing, resulting in 20 [MPa]. Nominal compressive strength of the masonry units and yield strength of steel reinforcement are defined by suppliers as 10 [MPa] and 420 [MPa], respectively.

The construction of the walls was performed after the formwork removal of the reinforced concrete frames, following the usual construction practice in Ecuador. After completion of the three walls, each one was treated separately. The first wall was not plastered. A cement-based N-type (TMS 402/602, 2016) mortar with 1:6 proportion (i.e. 1 part of cement and 6 parts of sand) was used for plastering the second wall. The third wall was plastered with a mortar with similar proportions but adding abaca fibers as part of a parallel research.

(a) Frontal view of the reinforced concrete frames, before the construction of the walls.

(b) Frontal view of the MIF specimens.

(c) Lateral view of the MIF specimens.

Figure 8.1: Dynamic test set-up.

8.2 Test set-up and instrumentation

The MIF specimens were installed on the biaxial shake table of Granada University, which contains sensors to measure the displacement, acceleration and the induced force of the actuators, in both "x" and

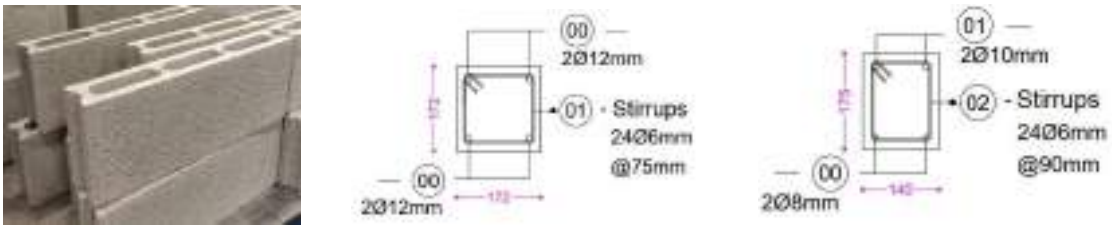

(a) Masonry units. (b) Column cross section. (c) Beam cross section.

Figure 8.2: Structural elements conforming the MIF specimens.

"y" directions. Figures 8.1 and 8.3 depicts the set-up of the MIF specimens on the shake table. Four 3000x500x35 mm steel plates were anchored to the top of the MIFs to act as additional mass (approximately 1650 kg).

Each wall was instrumented as follows (the reader is referred to Figure 8.4 for a schematic view of the sensor deployment over the walls):

- Two IL-600 laser sensors to measure displacements on the base and the top of the wall.
- One uniaxial seismic accelerometer and one uniaxial piezo-electric accelerometer installed on the top of the wall, with the measuring direction aligned to the wall length, i.e. IP direction.
- One uniaxial piezo-electric accelerometer installed in the mid lenght and height fo the wall, with the measuring direction aligned to the thickness of the wall, i.e. OOP direction.
- Two strain gauges installed on the external side longitudinal reinforcement of the MIF columns, near the bottom beam of the concrete frame.
- A strain gauge installed on the first stirrup of each column, taken from the bottom beam of the frame. An additional strain gauge was installed to the first stirrup of one of the columns, taken from the upper beam of the frame.
- Two linear variable displacement transducers (LVDT) installed on the external side of the MIF to measure vertical elongation. This measurement will be used later to estimate the rotation at the base of the wall.

The sampling rate was set to 600 Hz for every measuring instrument.

8.3 Test procedure and general results

During the dynamical tests, the specimens were subjected to a scaled acceleration record corresponding to the 2016 Ecuadorian earthquake (Singaucho et al., 2016), obtained in the Pedernales station (namely APED, East direction). To consider the dynamic influence of the downscaled geometry of the specimens,

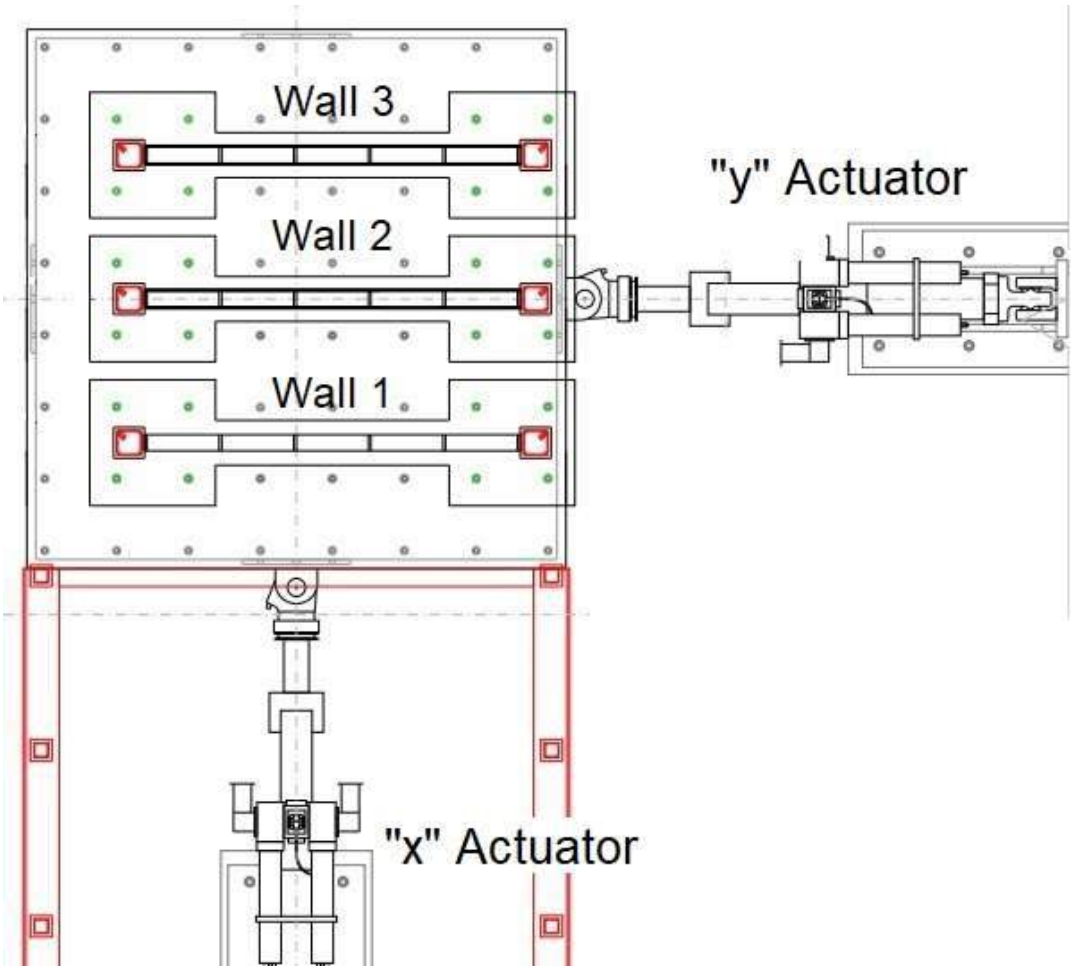

Figure 8.3: Plan view of the dynamic test setup.

the time step of the seismic record was also scaled by applying the scaling laws (Ghosh, 2011), i.e. the time was factored by $\sqrt{3/5}$. Figure 8.5 depicts the original accelerogram along with the corresponding pseudo-acceleration and pseudo-displacement response spectra.

The specimens were subjected to incrementally scaled acceleration of the original record by 25%, 50%, 75%, 100% and 150% of the original amplitude history. Correspondingly, each test is referred to as *025, 050, 075, 100* and *150*, respectively. Thereafter, a large amplitude *sine sweep* was applied after the aforementioned increments. In addition, low amplitude white noise records were applied consecutively to the 050, 075, 100 and 150. These records are labelled here as *WN1, WN2, WN3* and *WN4*, respectively. Finally, a high amplitude white noise record was applied after the sine sweep and, correspondingly labelled as *WN5*. White noise records were used to identify the fundamental frequency of the structural system after the occurrence of the corresponding seismic acceleration. Appendix A shows all of the records obtained after each dynamic test, for both raw and post-processed data. The post-processing consisted on performing an interpolation to get equally spaced data, a rolling average removal and a down-sampling to

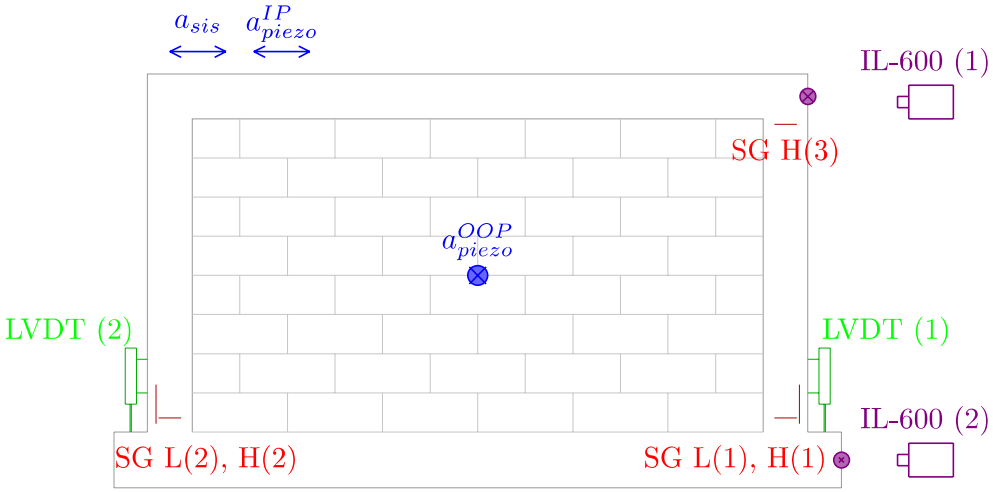

Figure 8.4: Typical frontal view of a wall with the location of the measuring devices.

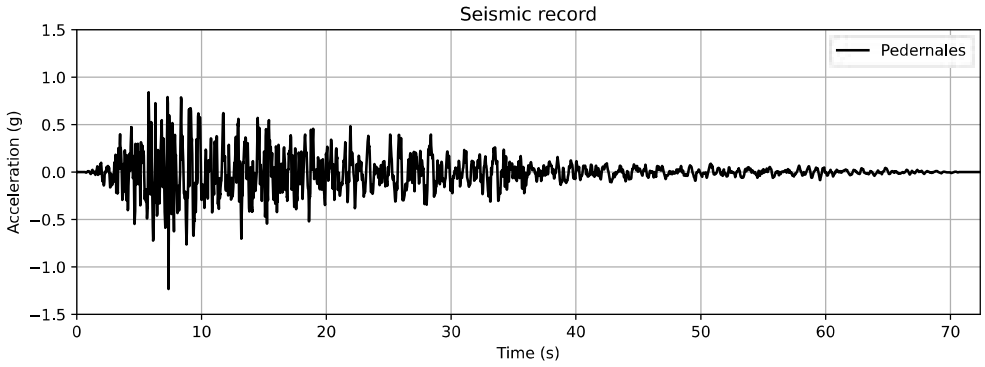

(a) Seismic record of Pedernales station.

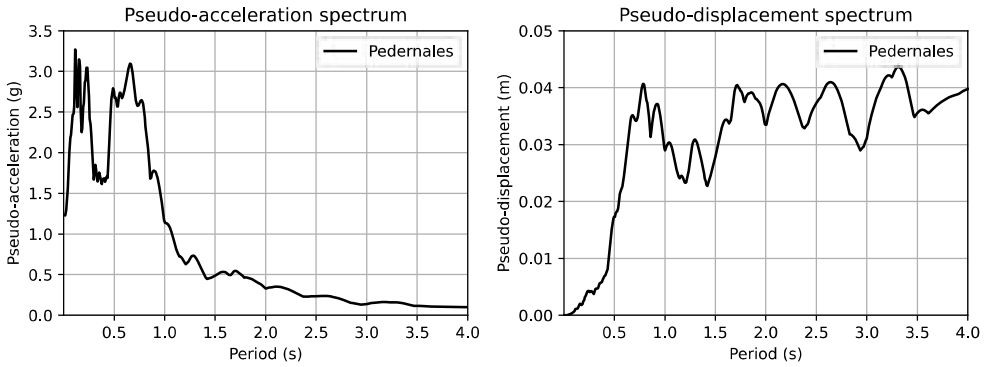

(b) Pseudo-acceleration and pseudo-displacement spectra.

Figure 8.5: Original record of 2016 Ecuadorian Earthquake, from Pedernales station.

a frequency rate of 100 Hz.

In the following sections, a general summary of the most important results are presented.

8.3.1 Results in the IP direction

Table 8.1 and Figure 8.6 summarize the maximum readings taken from the seismic accelerometers, the piezo-electric accelerometers and the difference between top and bottom displacements from the IL-600 sensors (i.e. drift) of each specimen. Notice that, in general, the white noise seismic signal test readings from both kind of accelerometers are very similar, except for the last white noise record. As can be seen in the Appendix A, most high amplitude readings from the seismic accelerometers made them overflow and, therefore, maximum values of these accelerometers are not trustworthy. On the other hand, the double integration of piezo-electric accelerometers readings are consistent with IL-600 displacement readings.

Table 8.1: Summary of maximum IP measured response

Signal	Wall 1			Wall 2			Wall 3		
	a^a_{sis}	a^b_{piezo}	Δ^c	a^a_{sis}	a^b_{piezo}	Δ^c	a^a_{sis}	a^b_{piezo}	Δ^c
025	0.93	0.69	1.90	0.77	0.69	2.06	0.80	0.74	1.18
050	1.05	1.38	2.66	0.86	1.39	2.25	1.01	3.33	1.94
WN1	0.30	0.33	1.65	0.93	0.33	1.85	0.89	0.44	1.09
075	1.23	1.99	3.13	1.08	2.07	2.28	1.10	4.28	2.13
WN2	0.29	0.31	1.40	0.73	0.28	1.86	0.85	0.45	0.92
100	1.30	2.52	2.97	1.08	2.07	2.72	1.33	2.40	2.70
WN3	0.28	0.29	1.71	0.70	0.31	1.65	1.00	0.39	1.00
150	1.16	3.13	3.36	1.28	4.54	3.38	1.39	3.22	3.67
WN4	0.28	0.31	1.56	0.51	0.27	1.94	0.87	0.38	1.16
Sine Sweep	1.46	6.15	3.58	1.29	6.04	3.18	1.28	6.57	1.65
WN5	1.23	4.83	2.98	1.25	4.33	2.42	1.25	1.82	1.40

[a] Results from uniaxial seismic accelerometer, in units of g.
[b] Results from uniaxial piezo-electric accelerometer, in units of g.
[c] Interstory drift (i.e. difference from top and bottom measurements taken from the IL-600 laser sensors), in units of mm.

8.3.2 OOP fundamental frequencies

Appendix A also shows the OOP acceleration records of the three specimens. From the post-processing of the accelerograms, the identification of the fundamental frequency of each wall is summarized in Table 8.2 and Figure 8.7. No visible damage was found in any of the specimens and, consequently, the OOP fundamental frequency stayed without variation. Also, notice that the presence of the plastering had negligible influence on the OOP fundamental frequency. Table 8.2 shows the identified frequency using two methods, namely: (1) counting the number of *zero-crossings* (ZC) and the frequency domain decomposition method by computing the *power density spectrum* (PDS).

Using Equation (7.8) and the results from Table 8.2, the mean IP stiffness of the wall can be estimated as $k_{IP} = 700\frac{kN}{mm}$. In Section 8.4.1, the models proposed in Chapter 7 are compared to the measurements obtained from the tests.

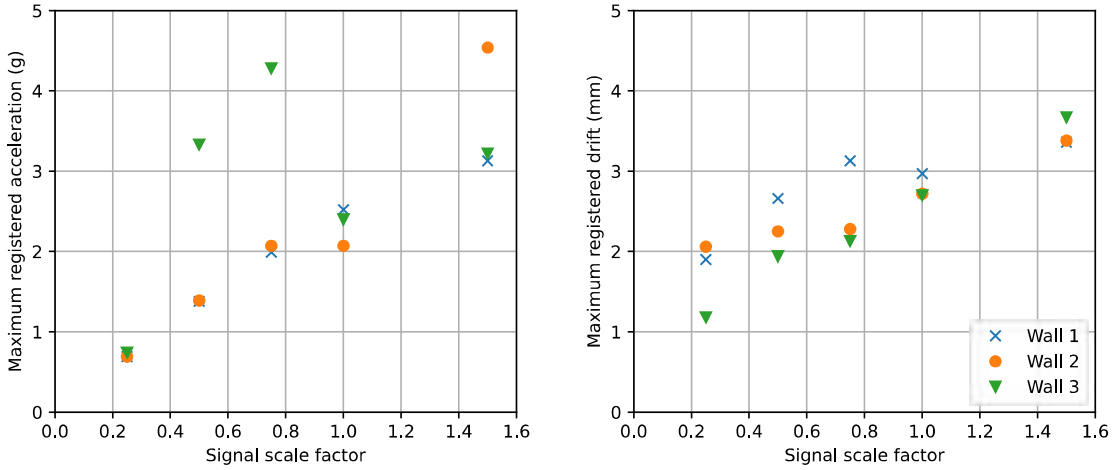

Figure 8.6: Summary of maximum IP measured response.

Table 8.2: Identified natural frequency (in Hz) of each specimen wall after the corresponding testing

Signal	Wall 1		Wall 2		Wall 3	
	ZC	PDS	ZC	PDS	ZC	PDS
025	30.52	34.01	34.70	22.92	32.97	27.87
050	30.17	39.12	30.92	21.67	30.62	27.87
WN1	31.06	34.89	33.69	22.84	31.90	25.85
075	29.22	35.95	27.61	27.58	30.19	20.95
WN2	30.98	35.75	36.08	28.03	35.04	25.57
100	30.02	49.97	26.45	33.20	29.44	21.68
WN3	31.49	36.63	35.06	21.42	34.72	24.14
150	29.36	40.53	26.50	22.75	30.87	21.73
WN4	32.68	44.88	36.60	22.51	36.10	23.70
Sine Sweep	31.33	23.37	27.67	22.64	32.81	22.38
WN5	17.07	21.61	27.13	21.80	26.26	21.80

8.4 IP MIF mathematical models

In this section, two modelling strategies were applied to predict the behaviour of the specimens. First, the method to indirectly estimate the IP stiffness of the wall from the identified OOP fundamental frequency, presented in Chapter 7 is studied and, second, a non-linear model of the MIF is proposed and calibrated with the algorithm presented in Chapter 5.

8.4.1 Linear model with equivalent strut

The model shown in Figure 7.9 is applied here. A modal damping was used and defined equal to 2% of the critical damping. From Table 8.2, notice that the fundamental OOP frequency of the walls are similar to each other. Taking all the values of the Wall 1 specimen, the mean resulted equal to 32.7 Hz, with a standard deviation equal to 7.0 Hz. Wall 2 and 3 fundamental frequency resulted 15% less than

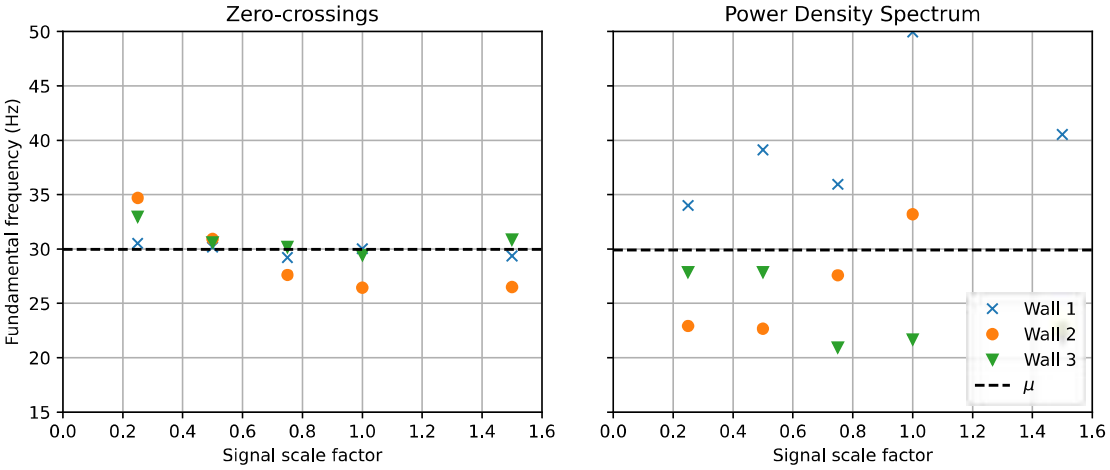

Figure 8.7: Identified natural frequency (in Hz) of each specimen wall after the corresponding testing.

Wall one, meaning that the cement-based plastering did not contribute to the stiffness of the wall, but only to the mass. Figure 8.8 depicts the IP stiffness distribution estimation obtained from Equation 7.8, where the OOP fundamental frequency was randomly modelled assuming a normal distribution with the aforementioned mean and standard deviation. In this model, θ values of Figure 7.11 were used, along with the modifier factors of Figure 7.19, namely: $f_{H/L} = 1.198$, $f_{H/t} = 0.87$, $f_{f'm} = 3.15$ and $f_{scale} = 1.42$. Figure 8.9 shows the IP deformation results obtained, with a close-up view of the time interval in which the maximum response occurs. Notice that the mean result of the proposed model is a fair prediction of the response of an existing MIF. Also, the measured result is mostly bounded within the mean $\pm$ one standard deviation of the model estimation.

8.4.2 Non-linear model calibrated with ABC

The model is a more elaborated version of the first model presented in Section 8.4.1. Here, the equivalent strut is modelled in both directions and considered as compression-only struts with dash-pots connected in parallel. Also, the base of the MIF is modelled with a spring and dash-pot that considers the plausible relative movement between the surface of the shake table and the specimen. As no visual damage was observed on the concrete frame, beam and columns are modelled as elastic elements, with a reduction factor (applied to the gross inertia) to consider the influence of cracking, along with a horizontal dash-pot connected to a external fixed node. The aforementioned dash-pots are proposed as an alternative to the classical methods of damping modelling (i.e. Rayleigh or modal damping), considering that the damping characteristics can be inferred by applying Bayesian methods. To define the constitutive behaviour parameters of the springs and dashpots, Equations (8.1) and (8.2) were applied to avoid issues due to scaling of the lower and upper bounds of the assumed uniform distribution. Figure 8.10 depicts the

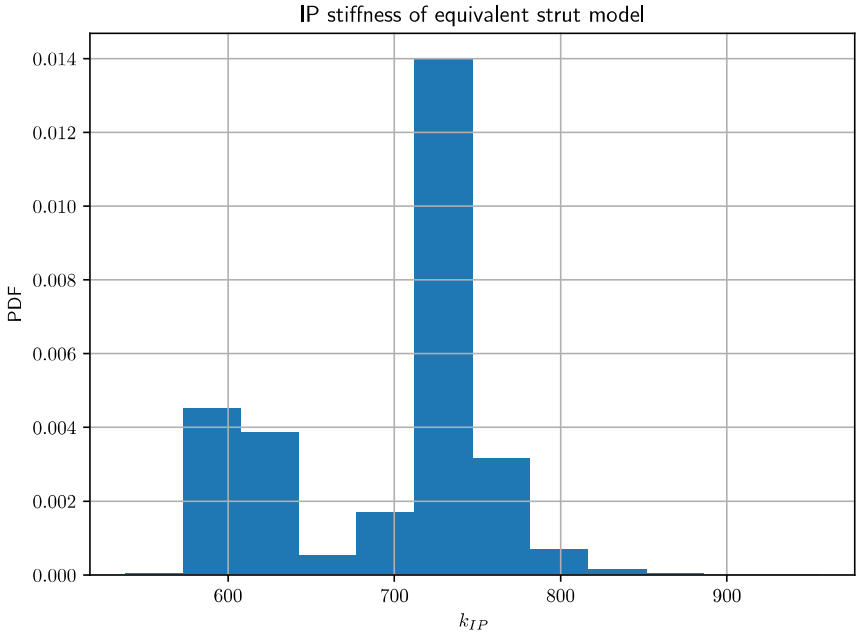

Figure 8.8: Estimated distribution of equivalent strut IP stiffness of the specimens.

geometry and general assumptions of the model.

$$K = k_1 \times 10^{k_2} \tag{8.1}$$

$$C = c_1 \times 10^{c_2} \left(\frac{d\epsilon}{dt} \right)^{c_3} \tag{8.2}$$

The $\mathcal{A}^2$BC-SS algorithm was used to obtain the parameters of the model. Fourteen parameters, namely $\boldsymbol{\theta} = \theta_1, \theta_2, \ldots, \theta_{14}$, were defined as shown in Table 8.3, where the lower (L) and upper(U) bounds of the prior uniform distribution are presented, along with the maximum a posteriori (MAP) results. Figure 8.11 compares the Fourier spectrum resulted from the test measurements to the model prediction. As can be seen, the model captures the dynamic properties of the specimen, showing a good match around the fundamental frequency. Figures 8.12, 8.13 and 8.14 compare the results from the non-linear model (for both MAP and a set of individual estimation from the parameters distributions) and the measurements, demonstrating that the proposed model can fairly estimate the expected acceleration of the MIF system. Notice that the calibration of the model was performed only with the 075 signal and, even on the extrapolation cases shown in Figures 8.13 and 8.14, the model has a good match to the measurments.

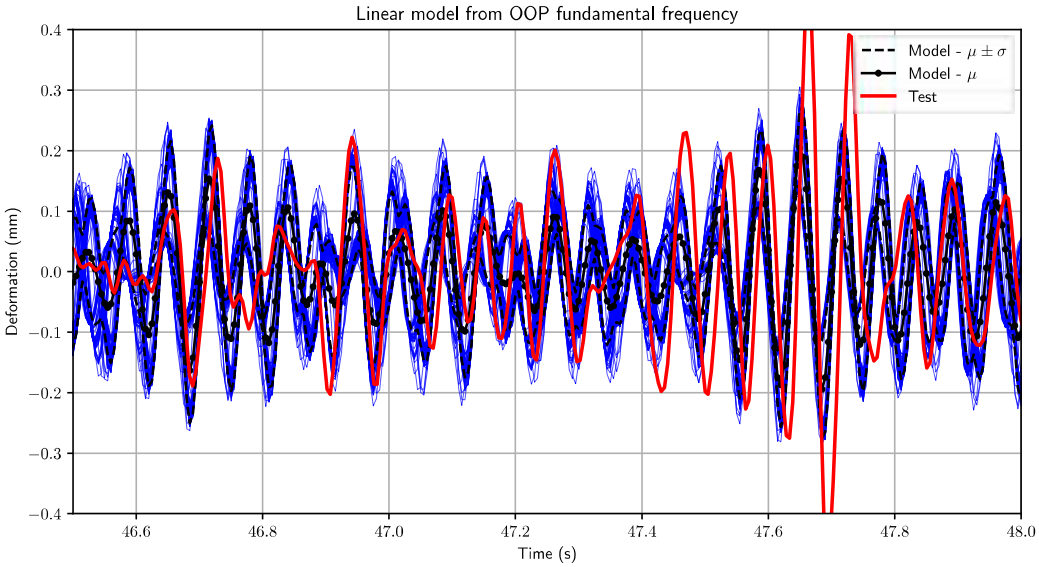

Figure 8.9: Probabilistic model estimation of deformation.

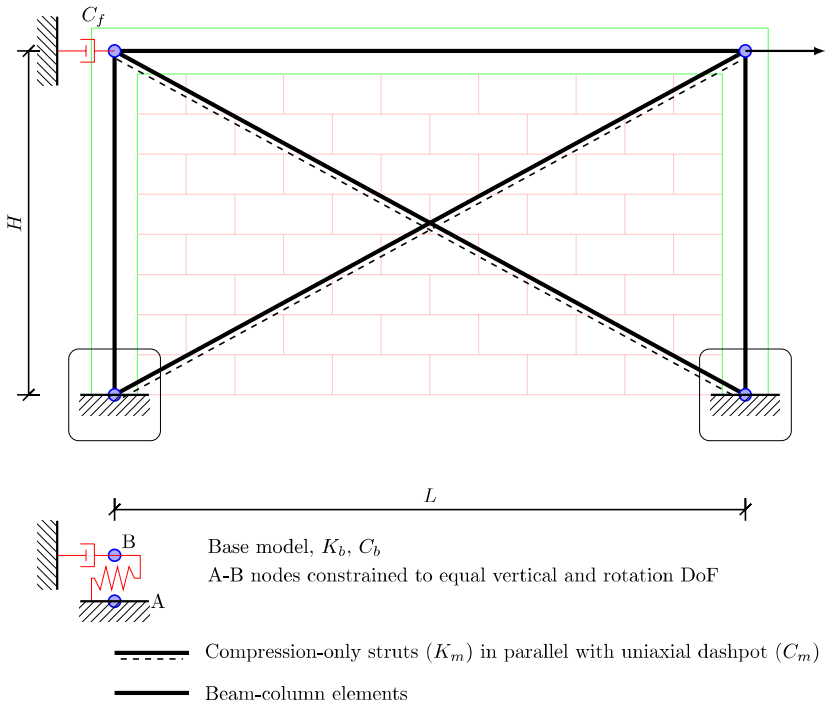

Figure 8.10: Nonlinear model calibrated with ABC methodology.

Table 8.3: Prior distributions and MAP results of the parameters of the MIF non-linear model calibrated with $\mathcal{A}^2$BC-SubSim algorithm.

θ	Prior		MAP	Part of the model
	L	U		
1	0.010	10.000	3.34	Base spring, k_1, k_2
2	0.010	10.000	4.80	
3	1000.0	1000000.0	322228.0	Base maximum lateral force
4	0.010	10.000	5.00	Base dash-pot, c_1, c_2, c_3
5	0.010	10.000	9.32	
6	0.100	1.500	0.69	
7	0.010	2.000	0.045	Frame stiffness modifier
8	500.0	10000.0	9382.30	Frame dash-pot, c_1, c_3
9	0.500	1.800	0.78	
10	0.010	10.000	5.70	Wall spring, k_1, k_2
11	0.010	10.000	2.45	
12	0.010	10.000	1.89	Wall dash-pot, c_1, c_2, c_3
13	0.010	10.000	0.71	
14	0.500	1.500	1.44	

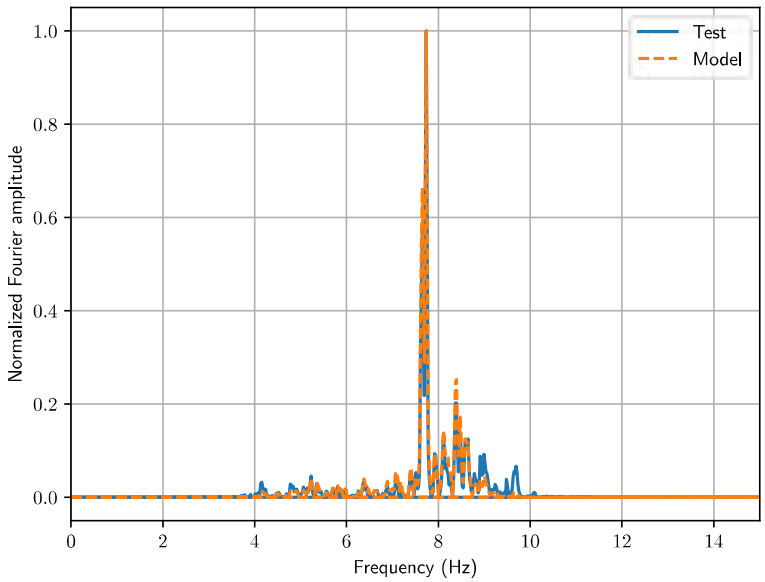

Figure 8.11: Comparison between the Fourier spectrum from the measurements during the 075-signal test and the model fed with the MAP parameters values.

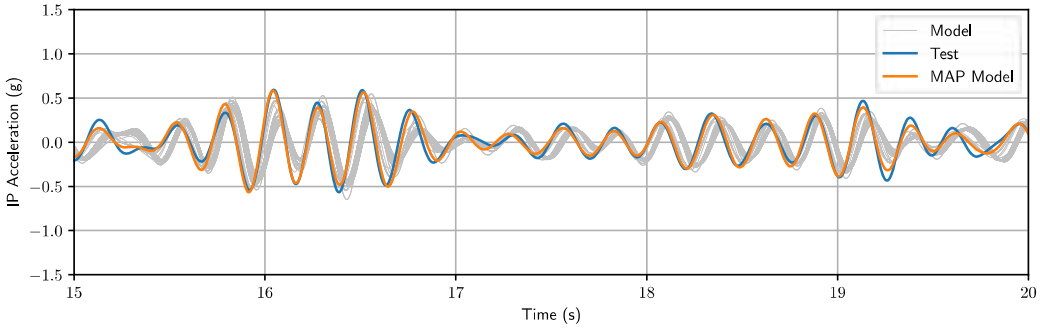

Figure 8.12: Comparison between acceleration measurements during the 075-signal test (signal used for calibration) and the model fed with the MAP parameters values.

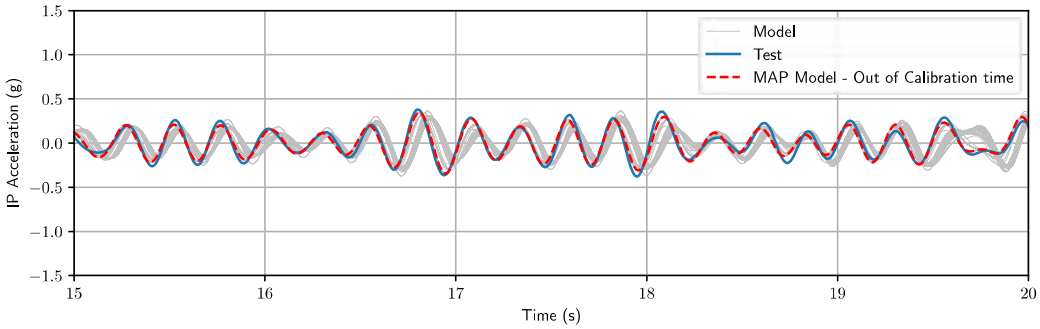

Figure 8.13: Comparison between acceleration measurements during the 100-signal test (signal not used for calibration) and the model fed with the MAP parameters values.

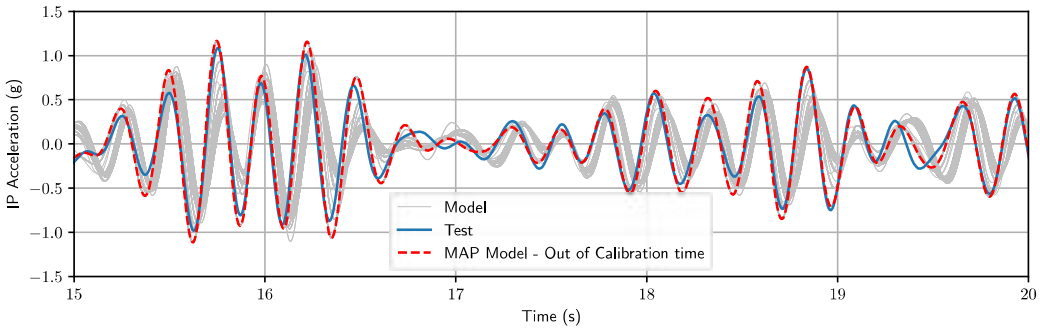

Figure 8.14: Comparison between acceleration measurements during the 150-signal test (signal not used for calibration) and the model fed with the MAP parameters values.

Part IV

Conclusions and future works

Chapter 9

Conclusions and future works

In this thesis work, at first, the methodological basis for the calibration of numerical models based on observational data is provided. The calibration method using the $\mathcal{A}^2$BC-SubSim algorithm has the advantage of dealing with the parameters of the model in a probabilistic way, allowing direct consideration of the uncertainty generated by the assumptions adopted in a model. Based on this algorithm, two methodological proposals have been developed for the evaluation of existing masonry infilled frame structures.

The first one, which consists on the estimation of constitutive parameters by means of BNN-HMC, allowing a fast evaluation of an existing structure based on information that can be collected in a very easy and economical way. This methodology will be very practical for those who manage cities and have the responsibility of preparing and implementing programs for the seismic rehabilitation of existing structures, since, at present, the definition of the sequence in which the possible interventions should be carried out is done by means of qualitative methods. Considering that the proposed model is not complex and its application is straightforward, it is estimated that it will constitute a tool that will provide more information for making this type of decisions at the macro level.

The second, which consists on the indirect measurement of the in-plane stiffness of the wall by means of a non-destructive test, allows an economic evaluation of an existing structure, helping engineers in practice to internalize the problems of masonry-filled frames and to incorporate their influence in the analyses carried out for the rehabilitation of existing structures. The simplicity of the test will allow to contemplate the influence of these walls even for minor structures.

The following are concluding remarks specialized on the scientific contributions of this thesis. About the proposed ABC algorithm, the following conclusions have been drawn:

- The algorithm is a variant of ABC-SubSim that overcomes the need to tune the hyper-parameter p_0, which highly controls the efficiency of the algorithm. This is carried out by an original adaptive selection of this parameter based on a partial evaluation of the next subset.

- The examples provided demonstrate both efficiency and efficacy for structural nonlinear model calibration based on test results. A comparison of calibrations done by conventional methods (i.e., "by-hand") demonstrate the advantages of $\mathcal{A}^2$BC-SubSim algorithm for this purpose; however, it is also advised that the specialist's judgment is required to attain consistency in the results.

- The method is extended to perform the calibration of a set of tests, allowing the inference of degradation parameters that are difficult or impossible to estimate using conventional methods. The method is applied on a complex structural application to show the capacity to perform the inference within large multi-dimensional nonlinear models using real-world structural health monitoring data. Finally, the method is applied on the calibration of a MIF model from a test performed on a seismic shake table, obtaining a close match of the numerical estimation with the measurements.

About the simplified shear spring model, where the parameters of the constitutive behaviour are predicted by a BNN, the following conclusions arise from this investigation:

- After quantifying the sources of uncertainty that affect the seismic behaviour of MIFs, the application of deterministic models to estimate the behaviour of this kind of structures, is not recommended. Indeed, results demonstrate that the application of deterministic models may lead to an incorrect estimation of the lateral initial stiffness and/or maximum strength and/or the degradation of the structure, depending on the applied model and on the type of masonry unit of the system.

- Available data about the MIF structural system are scarce and, therefore, insufficient to properly develop a good model. However, the probabilistic model proposed herein helps to better capture the expected IP lateral behaviour of the structure, with the additional advantage of giving information about the uncertainty of the prediction.

About the proposed procedure to indirectly infer the IP stiffness of MIFs by means of the OOP fundamental frequency:

- Using an experimental campaign of five one-fourth scaled MIFs, a simplified model was proposed and inferred to the data to indirectly predict the IP stiffness based on the identified OOP fundamental frequency.

- The applicability of the method was futher extended to properly cover model predictions out-of the configuration range given by the experimental data, by means of a physics-based parametric study performed with a MIF meso-model. By this means, influencing coefficients were obtained to consider the effects of height-length ratio, height-thickness ratio, the masonry characteristic strength and the scale size of the MIF. A number of applicaion examples were presented, demonstrating the capability and adequacy to predict the IP stiffness of MIFs from their OOP fundamental frequencies.

- The proposed linear model with an equivalent strut is capable to fairly reproduce the dynamic properties of the dynamic experimental results obtained with the seismic shake table.

Once the conclusions are given as a summary of the potential of the research of this thesis along with as discussion about its limitations, a number of future works arise as desirable next steps for this thesis:

- To explore the application of physics-guided neural networks to exploit the modelling capabilities of micro or meso-models within the framework of artificial neural networks.
- The proposed method to indirectly estimate the IP stiffness of a wall in terms of the OOP fundamental frequency requires additional laboratory testing to confirm the results obtained here by numerical modelling and to better capture the influence of different damage scenarios of the mansonry walls to the MIF structural system. Thus, desirable future work includes a larger scale MIF structures with consideration of varying frame-wall bond condition, among other variables.
- Case study applications of the proposed methods of structural evaluation of MIF structures of Chapters 6 and 7 demonstrated their capabilities.
- During the course of this thesis, some dynamic model parameter inference applications using the $\mathcal{A}^2$BC-SubSim algorithm, were presented. The study of the inference of these models and, after several trials to get better results with the obtained parameters, it seems that classical methods to model damping are not always the best choice. This last statement was not proven specifically, as it is out of the scope of this investigation. However, the algorithm could be an appropriate tool to search for alternative modelling strategies of the natural decaying effect of the response of civil and building structures.

Chapter 10

Conclusiones y trabajo futuro

En el presente trabajo de tesis, en primer lugar, se proporciona la base metodológica para realizar la calibración de modelos numéricos en base a datos obtenidos por medio de observación. El método de calibración utilizando el algoritmo $\mathcal{A}^2$BC-SubSim tiene la ventaja de tratar a los parámetros del problema de manera probabilista, lo que permite considerar de manera directa la incertidumbre generada por las suposiciones adoptadas en un modelo. Sobre la base de este algoritmo, se han desarrollado dos propuestas metodológicas para la evaluación de estructuras existentes de pórticos rellenos de mampostería.

La primera, que consiste en la estimación de parámetros constitutivos por medio de las BNN-HMC, permite una evaluación rápida de una estructura existente a partir de información que se puede levantar de una manera muy fácil y económica. Esta metodología resultará muy práctica para aquellas personas que administran ciudades y tienen la responsabilidad de preparar e implementar programas para la rehabilitación sísmica de estructuras existentes, ya que, actualmente, la definición del orden en que se deben realizar las posibles intervenciones se realiza por medio de métodos cualitativos. Considerando que el modelo propuesto no es complejo y su aplicación es directa, se estima que constituye en una herramienta que dará mayor información para la toma de este tipo de decisiones a nivel macro.

La segunda, que consiste en la medición indirecta de la rigidez en el plano de la pared por medio de un ensayo no-destructivo, permite una evaluación económica de una estructura existente, ayudando a los ingenieros de la práctica a interiorizar la problemática de los pórticos rellenos de mampostería e incorporar su influencia en los análisis que se realizan para la rehabilitación de estructuras existentes. La simplicidad del ensayo permitirá contemplar la influencia de estas paredes incluso para estructuras menores.

Sobre el algoritmo ABC propuesto, se han extraído las siguientes conclusiones:

- El algoritmo es una variante de ABC-SubSim que evita la necesidad de afinar el hiperparámetro p_0, que controla en gran medida la eficiencia del algoritmo. Esto se lleva a cabo mediante una original selección adaptativa de este parámetro basada en una evaluación parcial del siguiente subconjunto de prueba.

- Los ejemplos proporcionados demuestran tanto la eficiencia como la eficacia para la calibración de modelos estructurales no lineales basados en resultados de pruebas. Una comparación de las calibraciones realizadas por métodos convencionales (es decir, "a mano") demuestra las ventajas del algoritmo $\mathcal{A}^2$BC-SubSim para este fin; sin embargo, también se hace notar que se requiere el criterio del especialista para lograr consistencia en los resultados.

- El método se extiende para realizar la calibración de un conjunto de pruebas, permitiendo la inferencia de parámetros de degradación que son difíciles o imposibles de estimar utilizando métodos convencionales. Por último, el método se aplica en un caso de estudio complejo para demostrar la capacidad de realizar la inferencia dentro de modelos no lineales multidimensionales, utilizando datos de monitorización de la salud estructural.

En cuanto al modelo simplificado de resorte de corte, en el que los parámetros del comportamiento constitutivo se predicen mediante una BNN, de esta investigación se desprenden las siguientes conclusiones:

- Después de considerar todas las fuentes de incertidumbre que afectan al comportamiento sísmico de los MIFs, no se recomienda la aplicación de modelos deterministas para estimar el comportamiento de este tipo de estructuras. Los resultados demuestran que la aplicación de modelos deterministas puede conducir a una estimación incorrecta de la rigidez lateral inicial y/o de la resistencia máxima y/o de la degradación de la estructura, dependiendo del modelo aplicado y del tipo de unidad de mampostería del sistema.

- Los datos disponibles sobre el sistema estructural del MIF son escasos y, por tanto, insuficientes para desarrollar adecuadamente un modelo preciso. Sin embargo, el modelo probabilístico que aquí se propone ayuda a captar mejor el comportamiento lateral esperado en el plano de la estructura, con la ventaja adicional de dar información sobre la incertidumbre de la predicción.

Sobre el procedimiento propuesto para inferir indirectamente la rigidez IP de los MIFs mediante la frecuencia fundamental fuera del plano:

- A partir de los resultados de la campaña experimental de cinco MIFs a escala de un cuarto, se propuso un modelo simplificado que fue calibrado a los datos para predecir indirectamente la rigidez en dirección paralela al plano de la pared, basándose en la frecuencia fundamental identificada en la dirección perpendicular al plano de la pared.

- La aplicabilidad del método se amplió para cubrir adecuadamente las predicciones del modelo fuera del rango de configuración dado por los datos experimentales, mediante un estudio paramétrico realizado con un meso-modelo basado en la física del MIF. Se obtuvieron coeficientes de influencia para considerar los efectos de la relación altura-longitud, la relación altura-espesor, la resistencia característica de la mampostería y el tamaño a escala del MIF. Se presentaron varios ejemplos de

aplicación, demostrando la capacidad y eficacia para predecir la rigidez en el plano de los MIFs a partir de sus frecuencias fundamentales fuera del plano.

- El modelo lineal propuesto con un puntal equivalente es capaz de reproducir razonablemente las propiedades dinámicas del modelo experimental dinámico.

A continuación se enumeran algunos trabajos futuros deseables:

- Explorar la aplicación de redes neuronales guiadas por la física para explotar las capacidades de modelación numérica de micro o meso-modelos en el marco de las redes neuronales artificiales.

- El método propuesto para estimar indirectamente la rigidez en el plano de un muro en términos de la frecuencia fundamental fuera del plano requiere ensayos de laboratorio adicionales para confirmar los resultados obtenidos aquí mediante modelación numérica y para captar mejor la influencia de diferentes escenarios de daño de los muros de mampostería en el sistema estructural MIF. En esa dirección, resulta interesante realizar ensayos sobre especímenes de mayor escala de estructuras MIF con la consideración de la variación de la condición de unión marco-pared, entre otras variables.

- Se presentaron casos de estudio en los que se aplicaron los métodos propuestos en los capítulos 6 y 7, para la evaluación estructural de edificios MIF, en donde se demuestra su potencial.

- A lo largo de esta tesis se han presentado algunas aplicaciones de inferencia de parámetros de modelos dinámicos, utilizando el algoritmo $\mathcal{A}^2$BC-SubSim. El estudio de la inferencia de estos modelos y, después de varios ensayos para obtener mejores resultados con los parámetros obtenidos, parecería que los métodos clásicos para modelar el amortiguamiento no son siempre la mejor opción. Esta última afirmación no se demostró específicamente, ya que está fuera del alcance de esta investigación. Sin embargo, se hace notar que el algoritmo podría ser una herramienta adecuada para buscar estrategias alternativas de modelación numérica del efecto de decaimiento de las respuesta de las estructuras.

Appendix A

Data records

This appendix shows the seismic excitation and the measured response of the specimens described in Chapter 8. For each test, the following data are shown:

- Data from shake table instrumentation (in x and y directions):
  - Displacement
  - Acceleration
  - Force
  - Fourier spectra of the acceleration records
  - Acceleration and displacement response spectra of the acceleration records, corresponding to 5% of the critical damping
- Data from instrumentation installed on each wall:
  - In-plane (IP) acceleration at the top of the wall recorded with a seismic accelerometer
  - IP acceleration at the top of the wall recorded with a piezo-electric accelerometer
  - Out-of-plane (OOP) acceleration at the mid height of the wall recorded with a piezo-electric accelerometer
  - IP displacement at the base of the wall
  - IP displacement at the top of the wall
  - IP drift
  - Fourier spectra from the acceleration records at the top of the wall (IP) and at the mid height (OOP)
  - Power density spectra from the acceleration records at the top of the wall (IP) and at the mid height (OOP)

1 Data obtained from shake table instrumentation

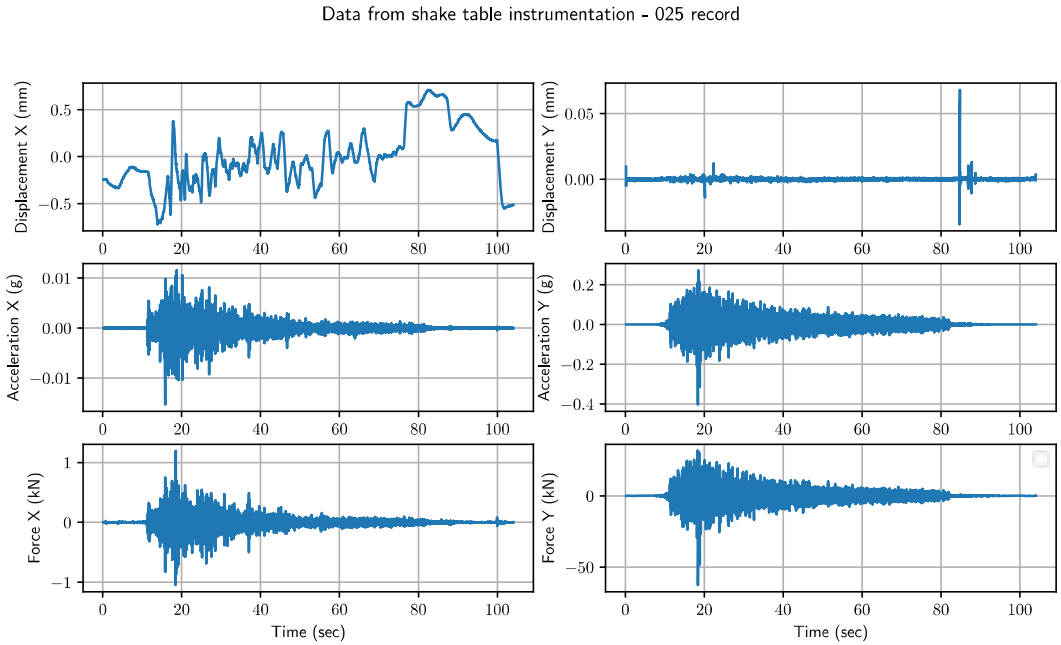

Figure 1: Shake table instrumentation data from 025 record.

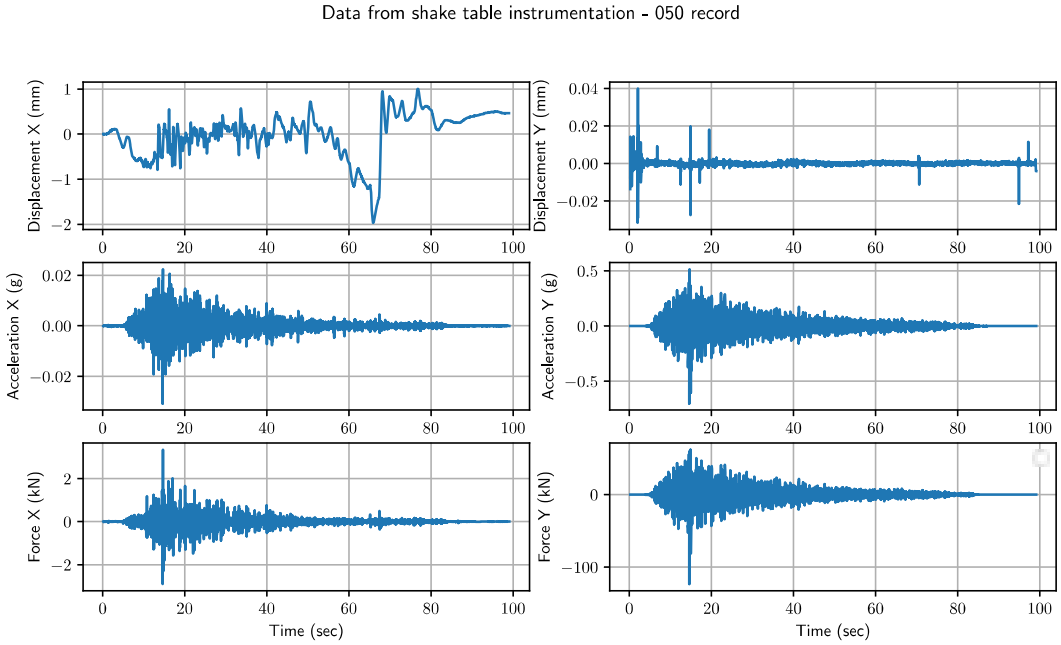

Figure 2: Shake table instrumentation data from 050 record.

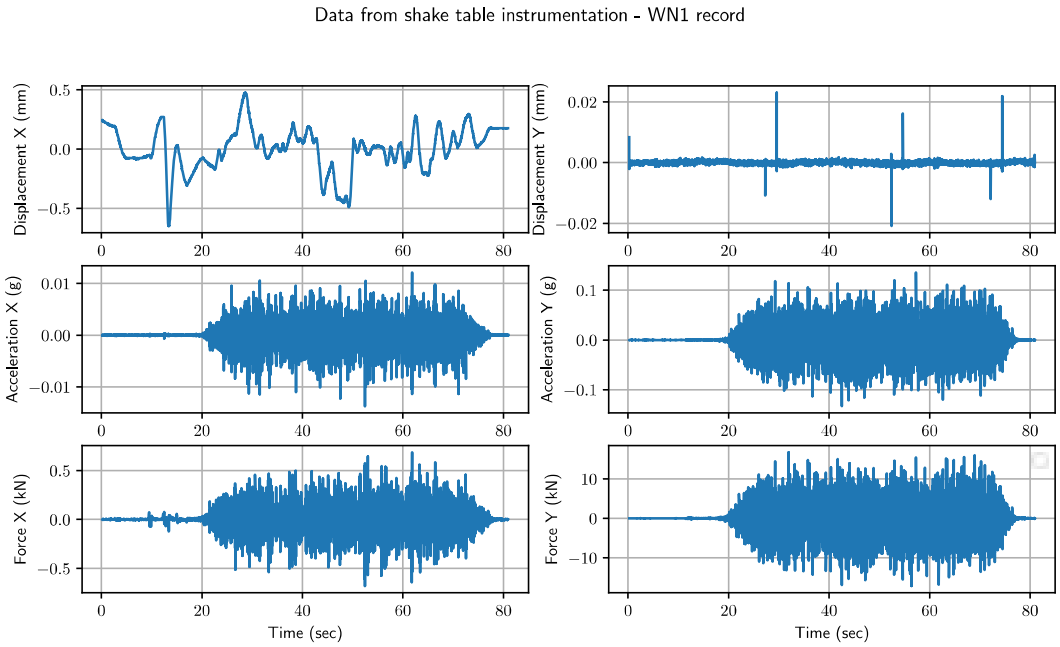

Figure 3: Shake table instrumentation data from $WN1$ record.

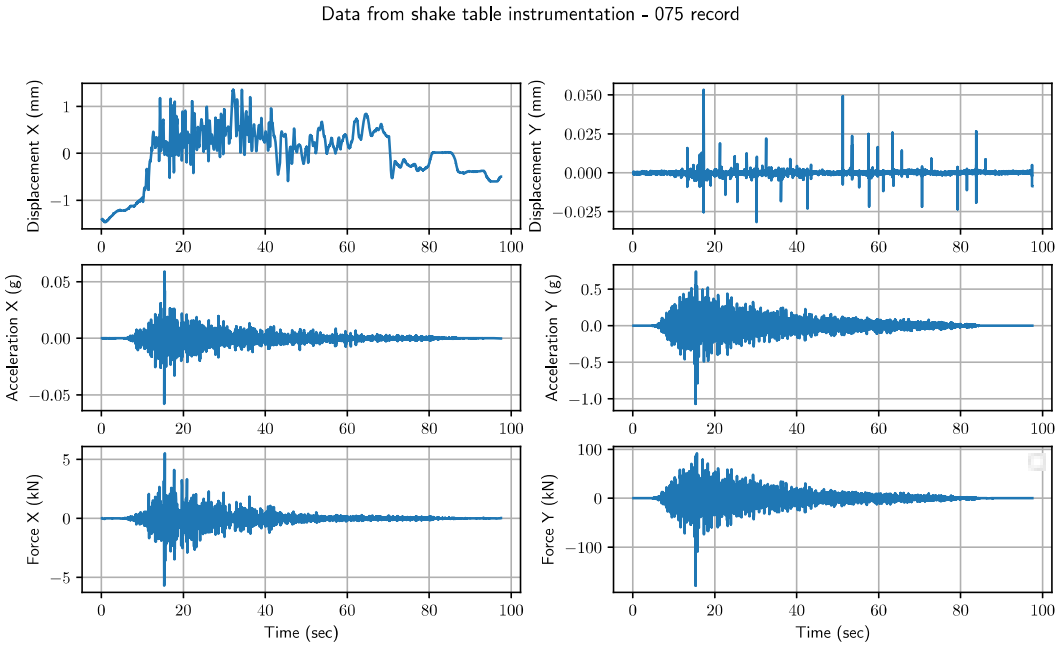

Figure 4: Shake table instrumentation data from 075 record.

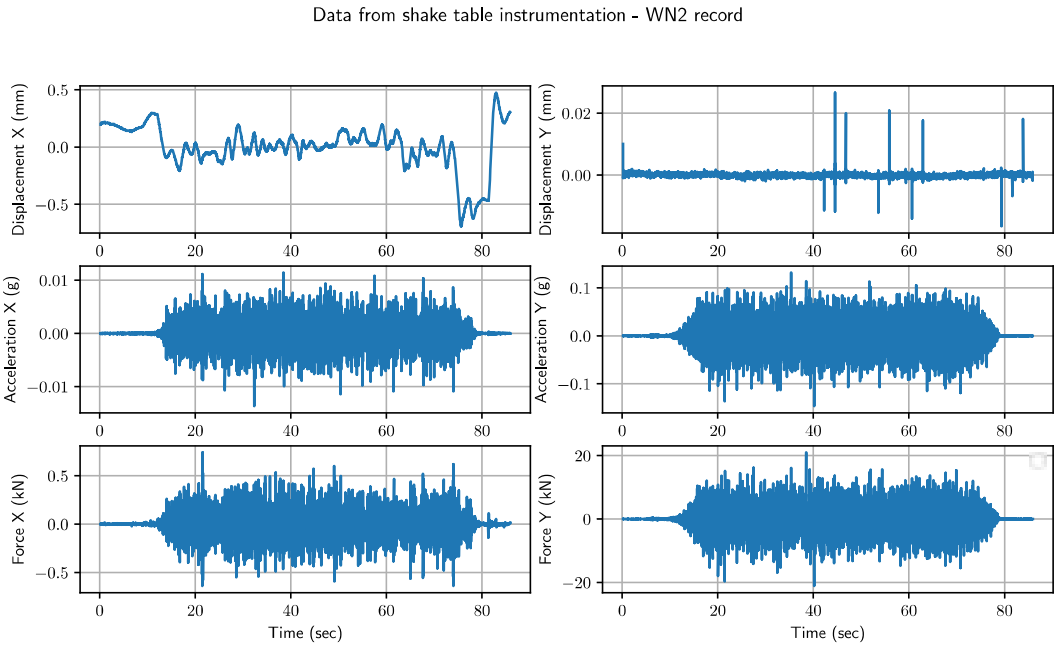

Figure 5: Shake table instrumentation data from $WN2$ record.

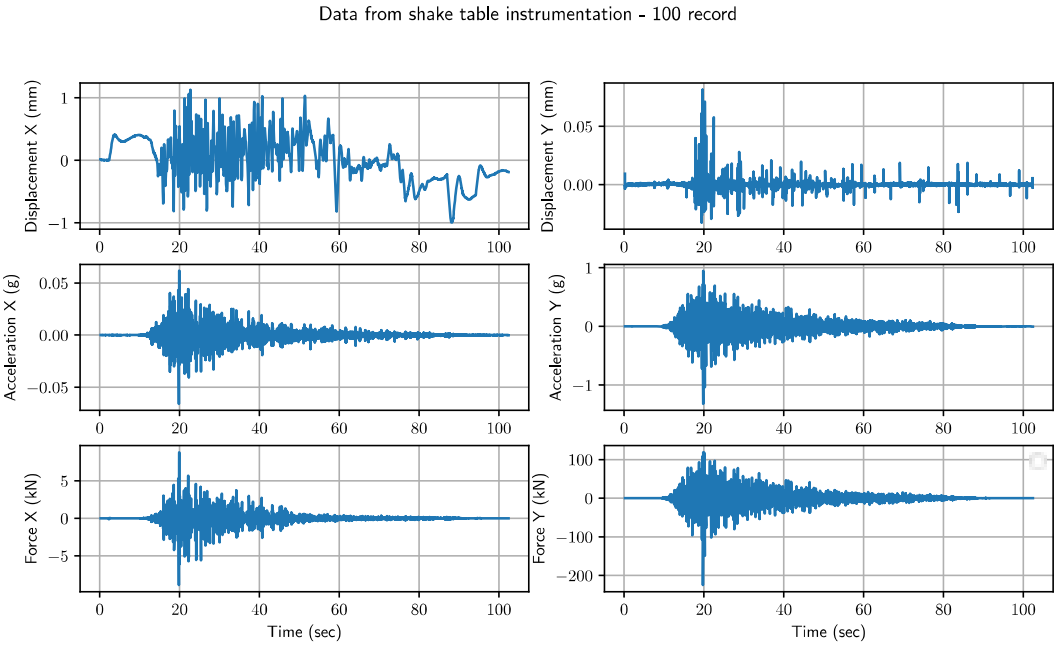

Figure 6: Shake table instrumentation data from 100 record.

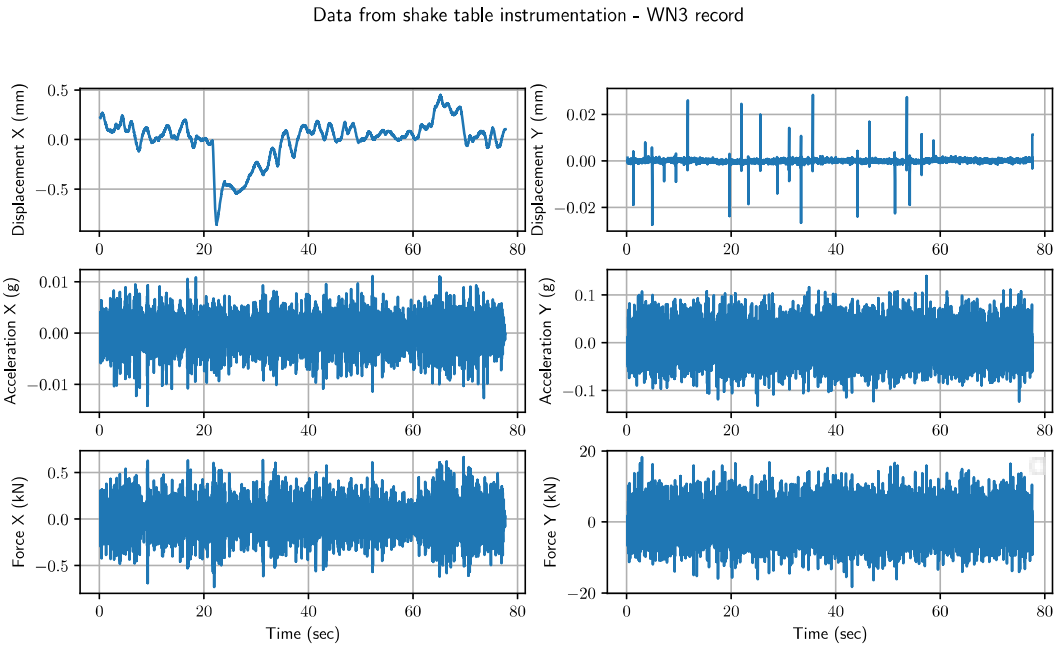

Figure 7: Shake table instrumentation data from $WN3$ record.

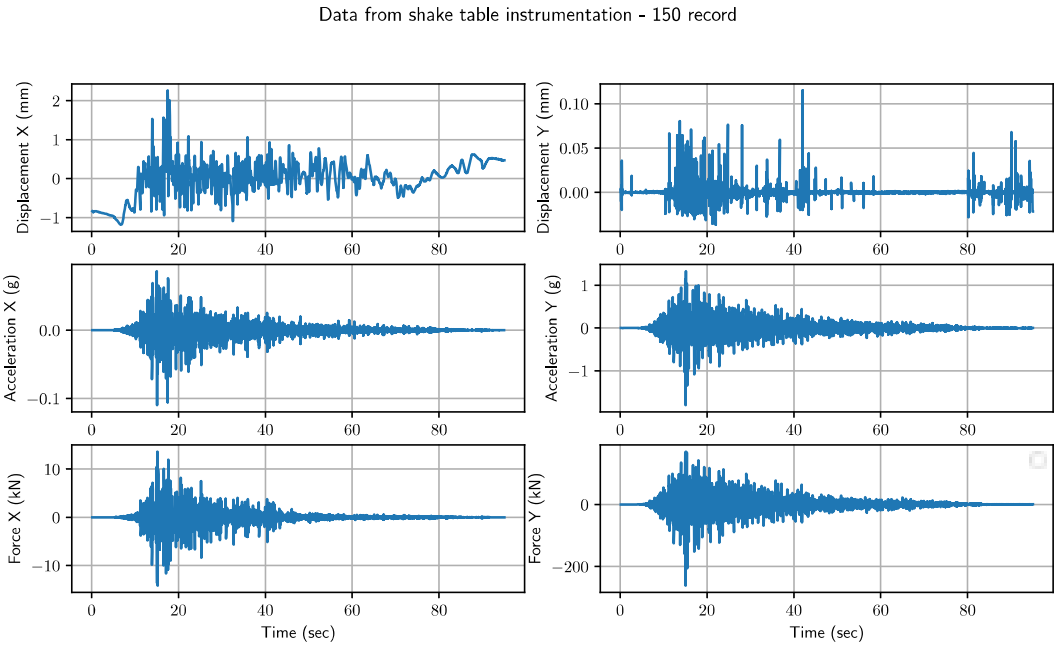

Figure 8: Shake table instrumentation data from 150 record.

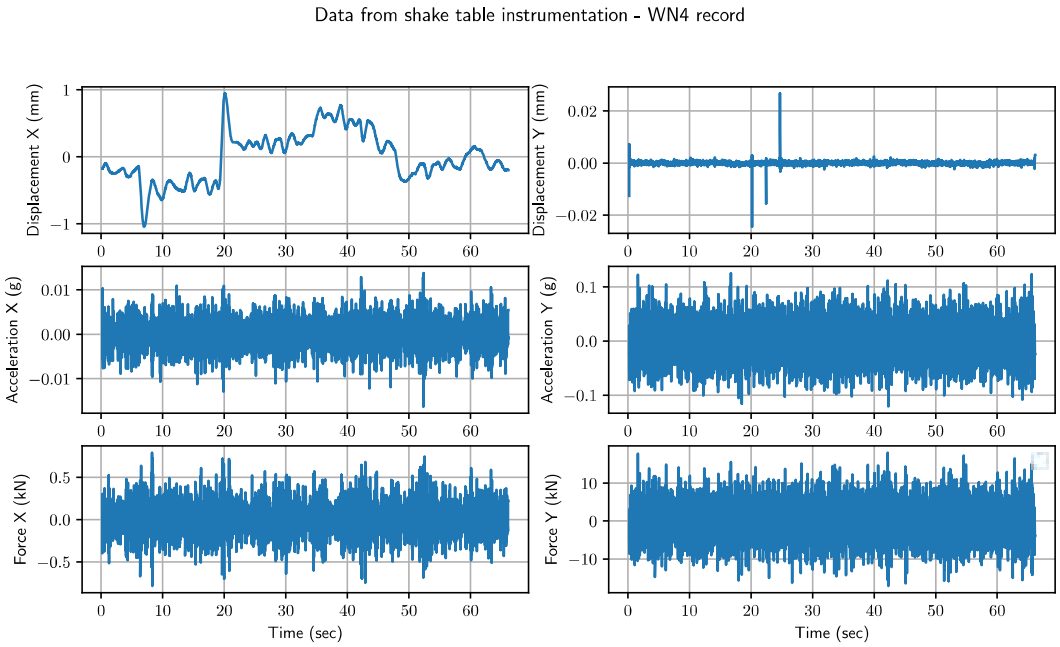

Figure 9: Shake table instrumentation data from $WN4$ record.

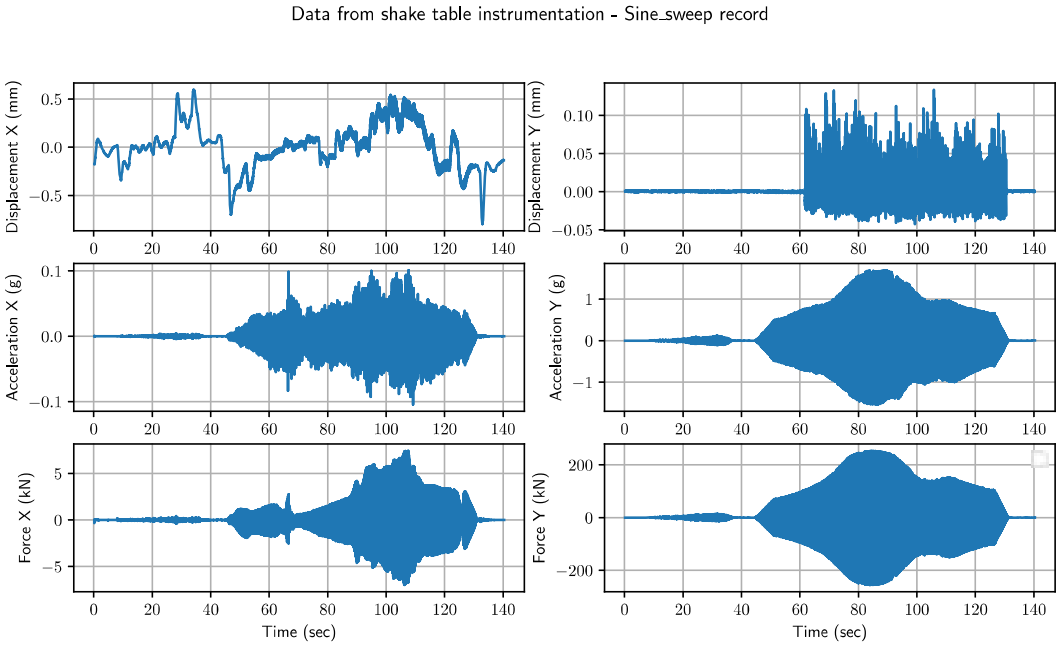

Figure 10: Shake table instrumentation data from $Sine_sweep$ record.

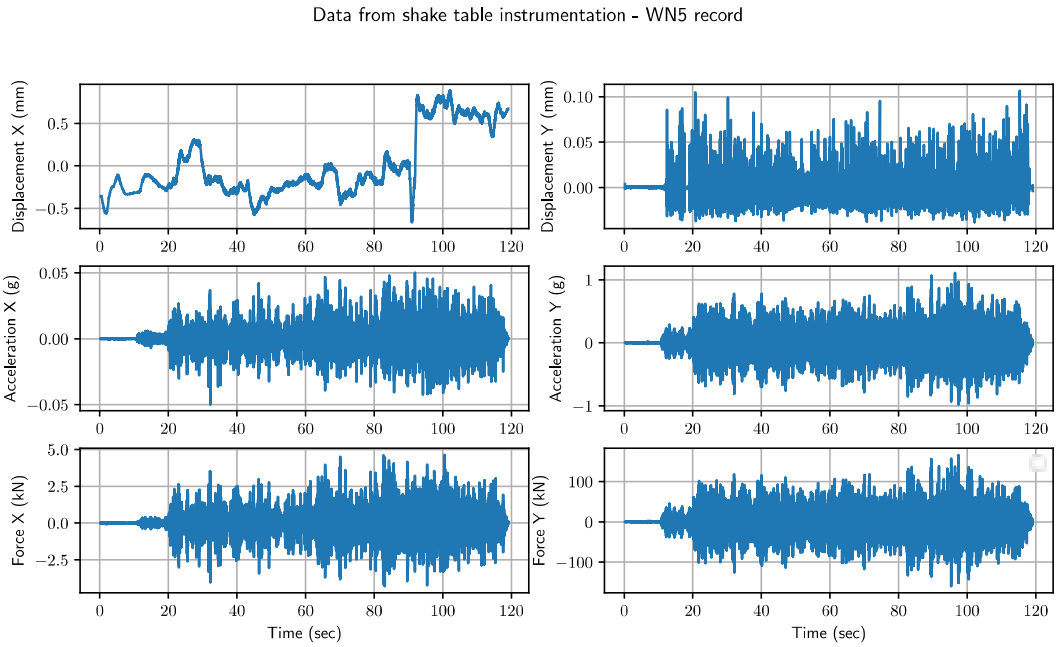

Figure 11: Shake table instrumentation data from $WN5$ record.

1.1 Fourier spectra from acceleration records

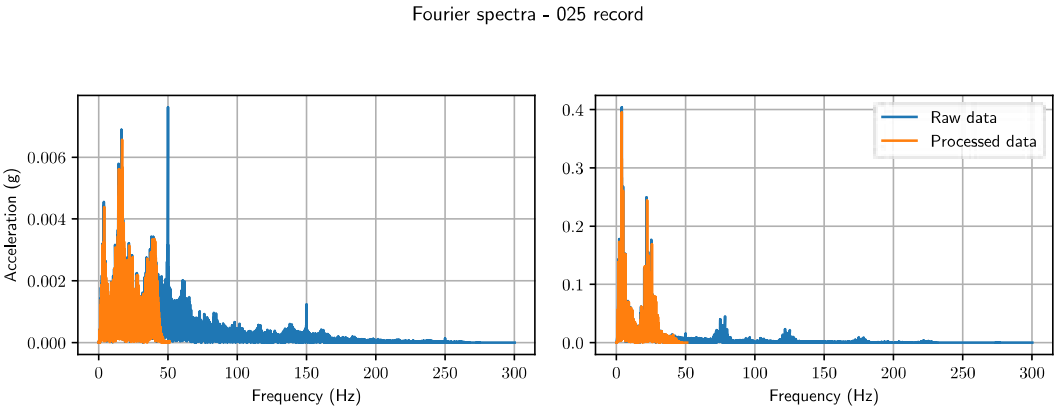

Figure 12: Fourier spectra from 025 record.

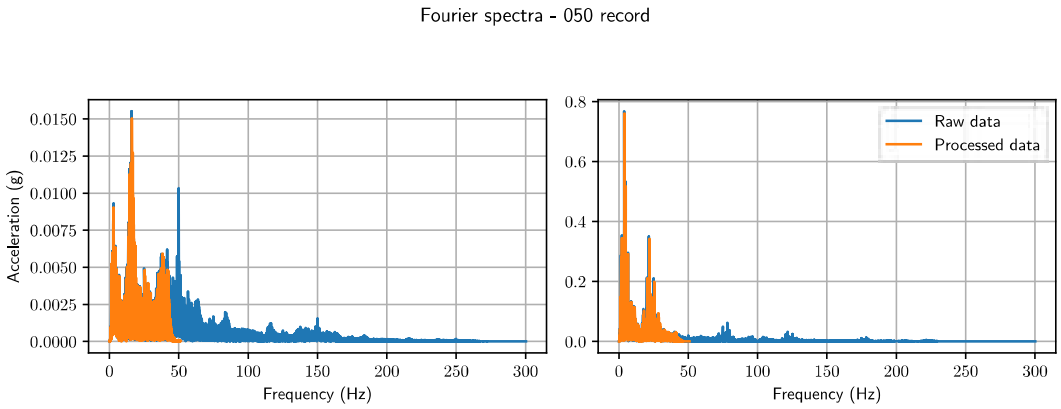

Figure 13: Fourier spectra from 050 record.

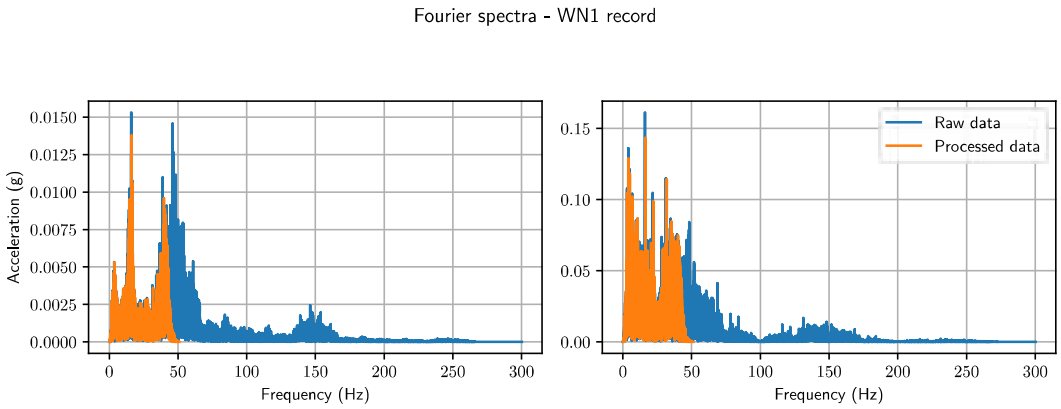

Figure 14: Fourier spectra from $WN1$ record.

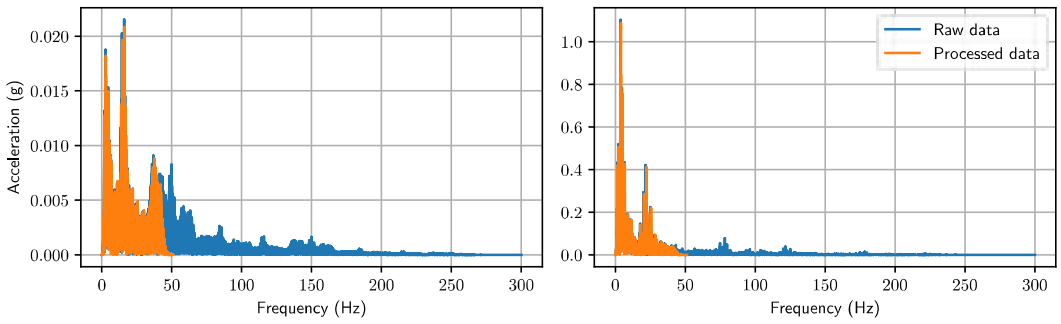

Figure 15: Fourier spectra from 075 record.

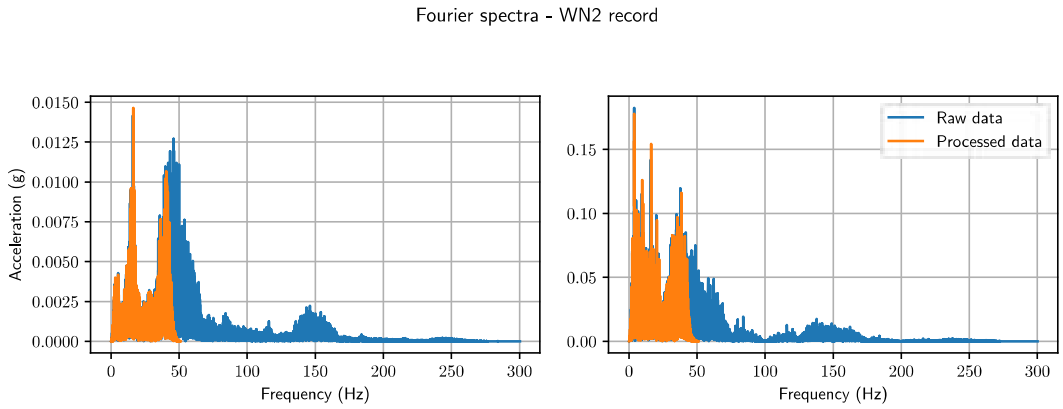

Figure 16: Fourier spectra from $WN2$ record.

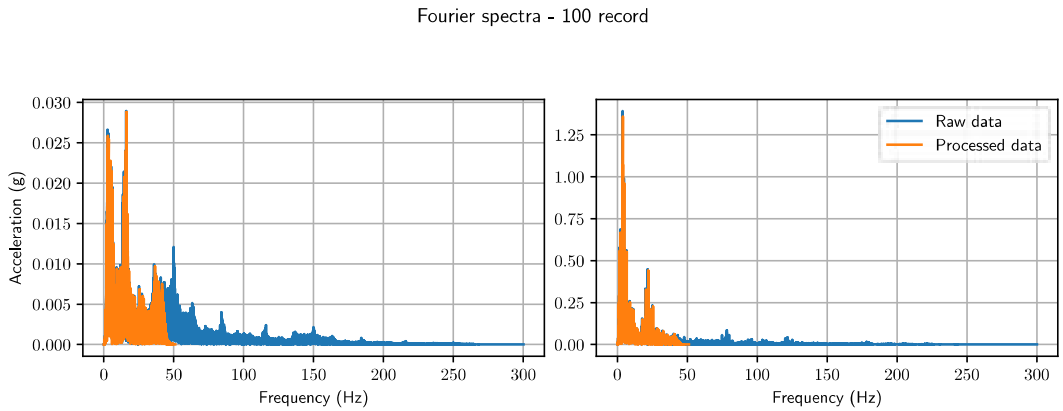

Figure 17: Fourier spectra from 100 record.

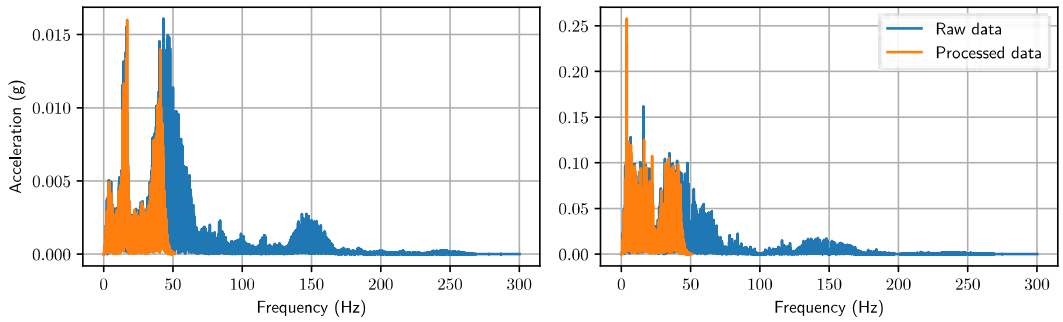

Figure 18: Fourier spectra from $WN3$ record.

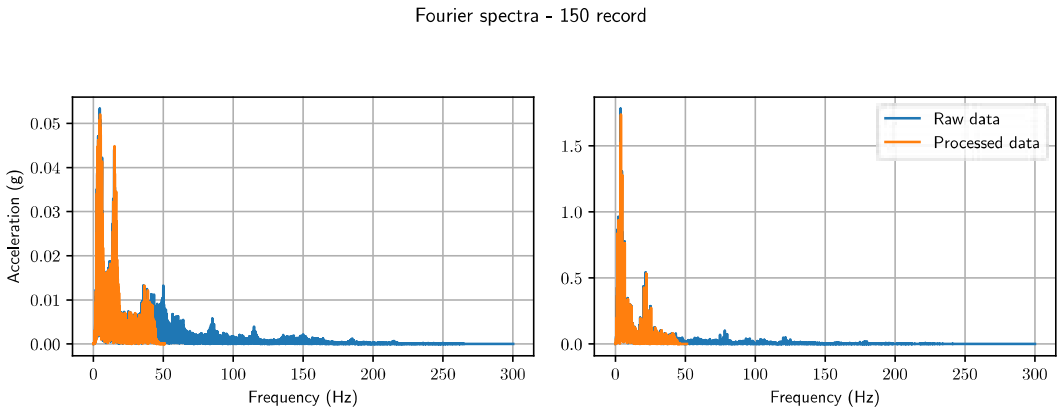

Figure 19: Fourier spectra from 150 record.

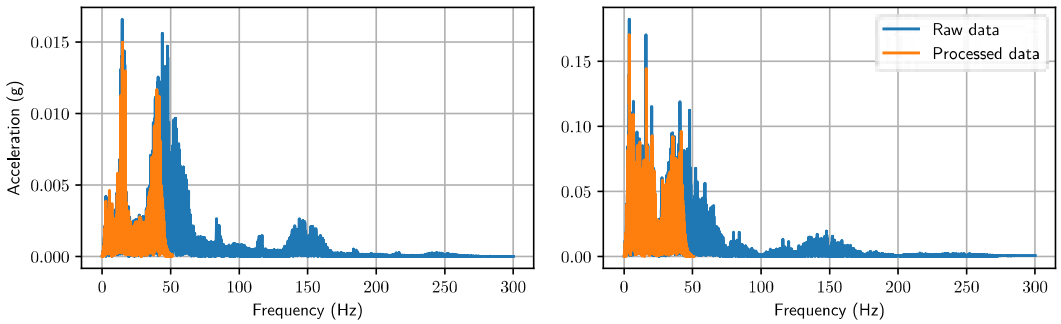

Figure 20: Fourier spectra from $WN4$ record.

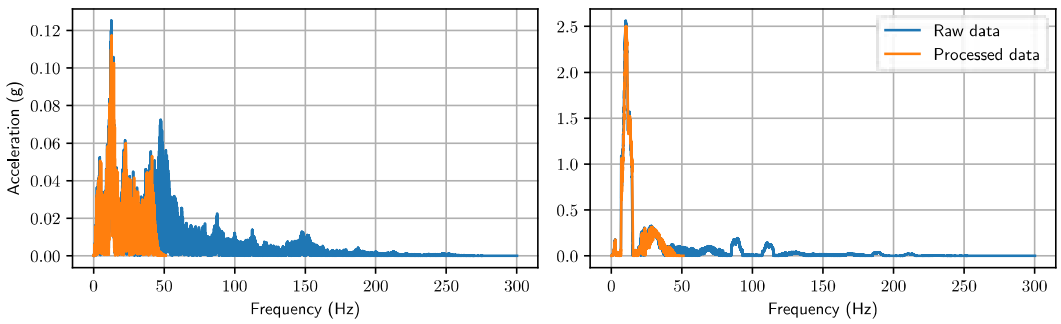

Figure 21: Fourier spectra from $Sine_sweep$ record.

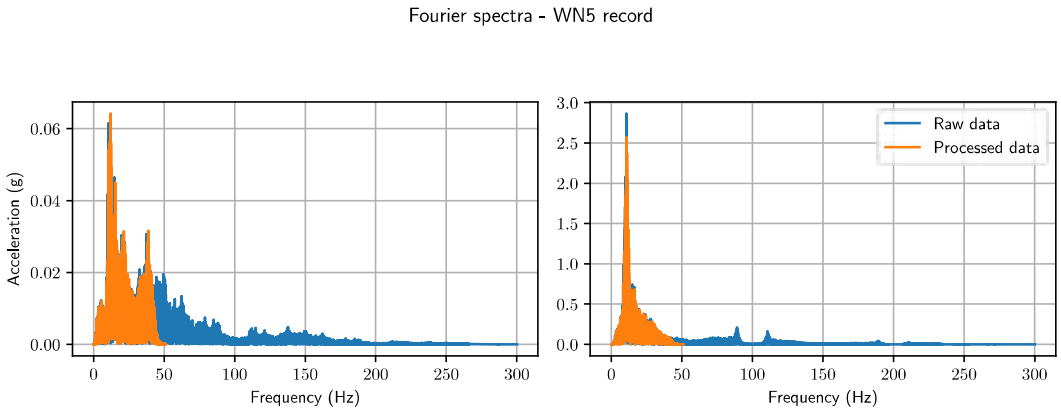

Figure 22: Fourier spectra from $WN5$ record.

1.2 Response spectra from acceleration records

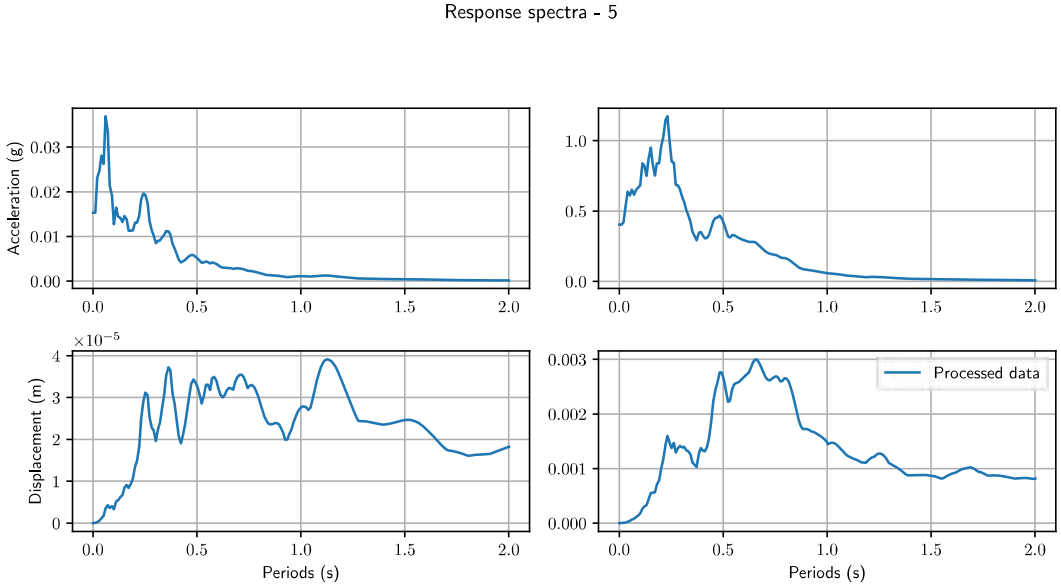

Figure 23: Response spectra from 025 record.

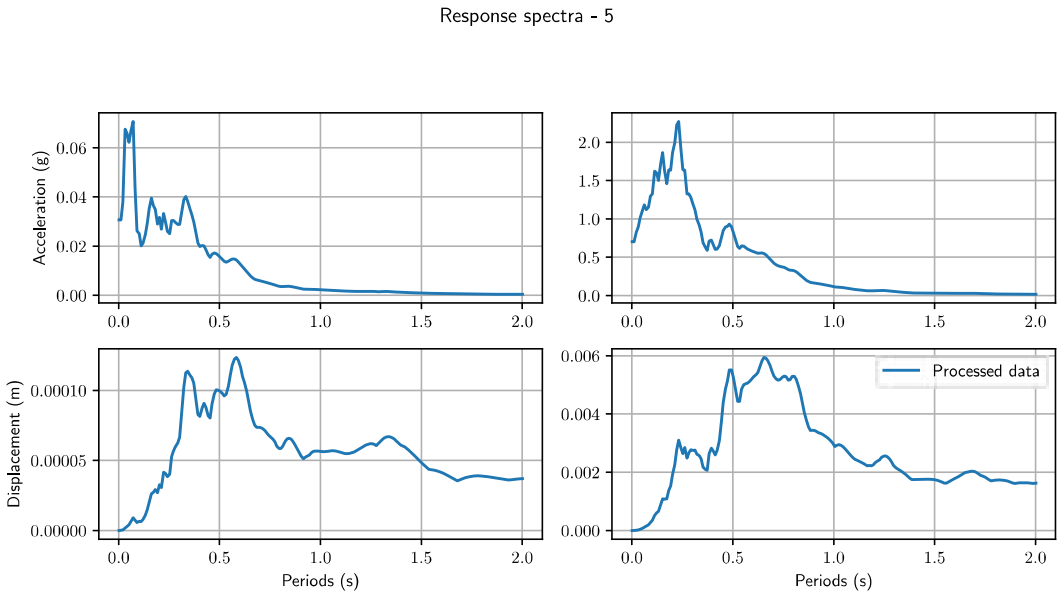

Figure 24: Response spectra from 050 record.

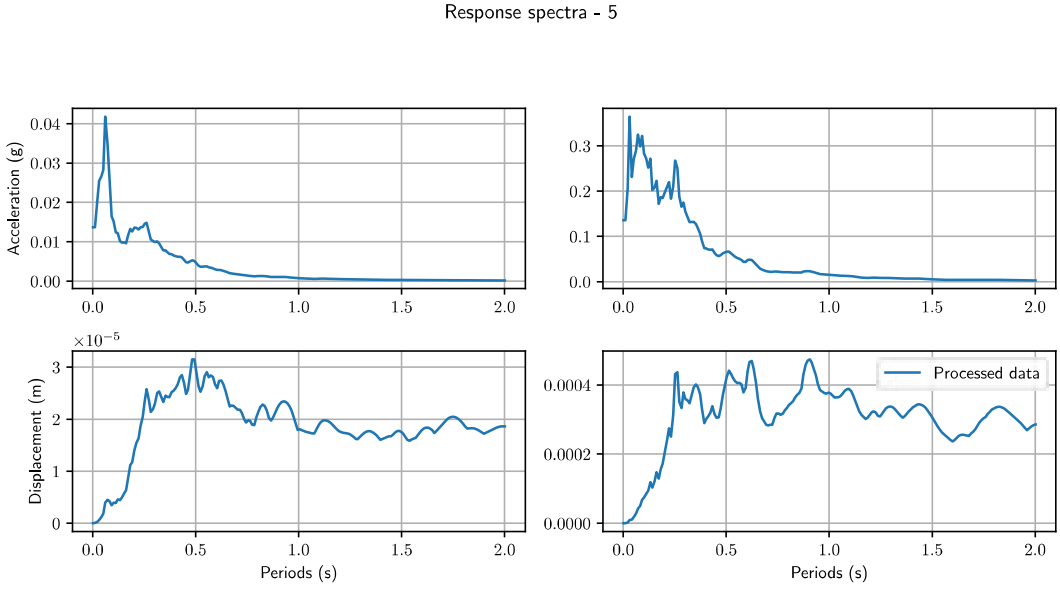

Figure 25: Response spectra from $WN1$ record.

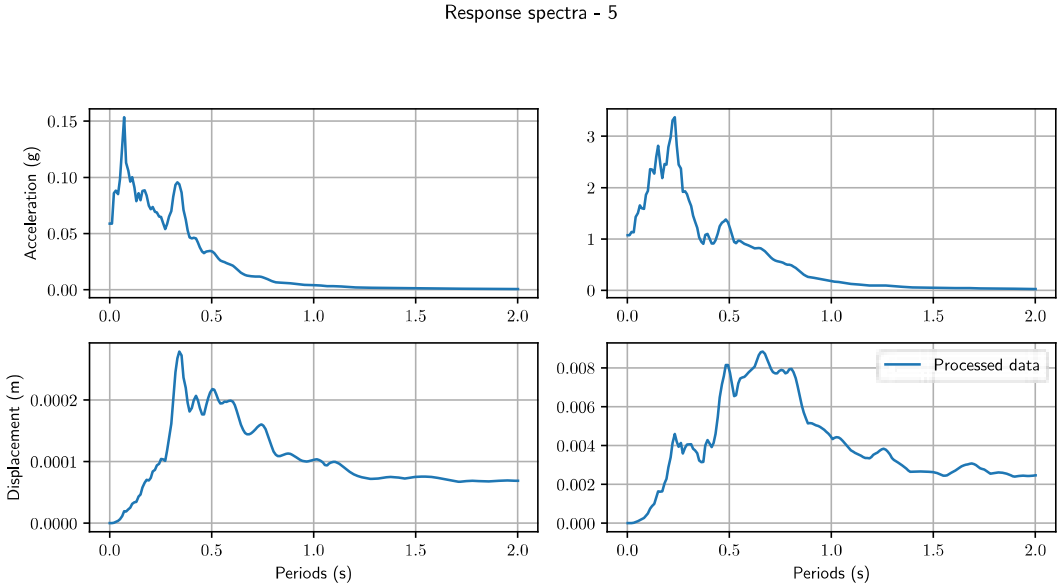

Figure 26: Response spectra from 075 record.

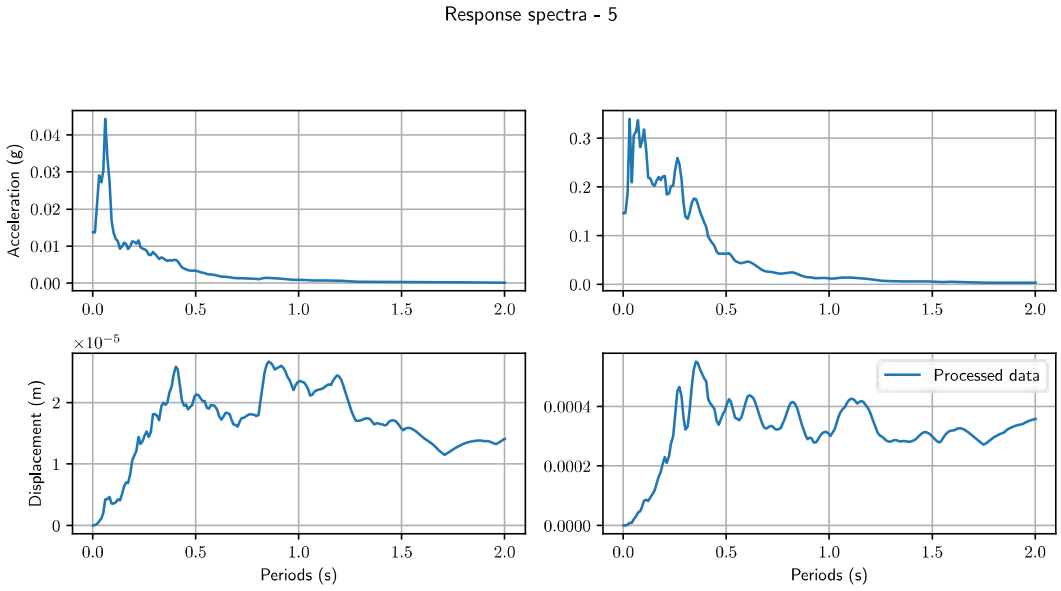

Figure 27: Response spectra from $WN2$ record.

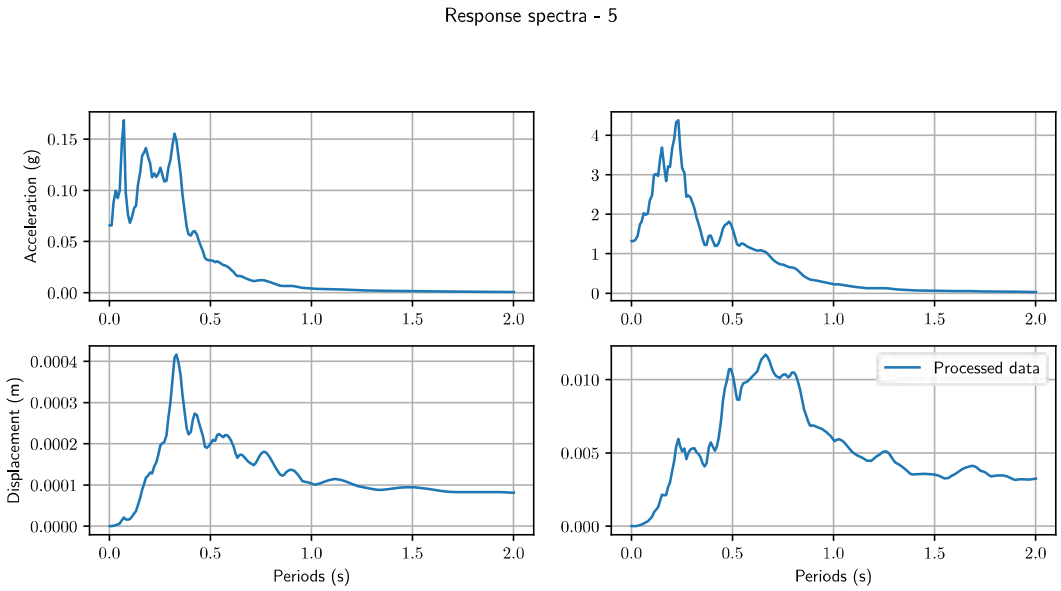

Figure 28: Response spectra from 100 record.

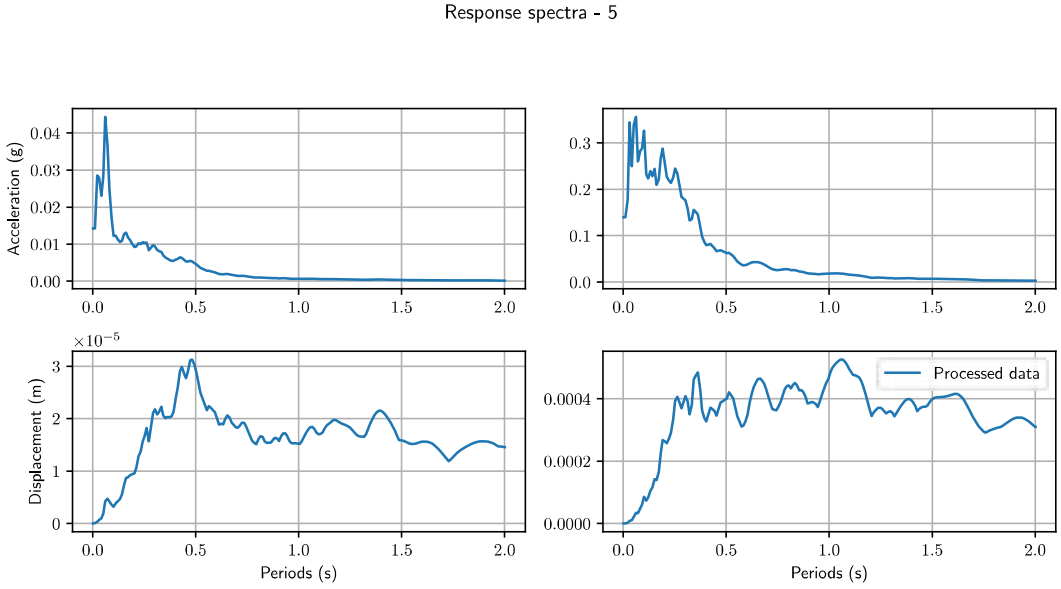

Figure 29: Response spectra from $WN3$ record.

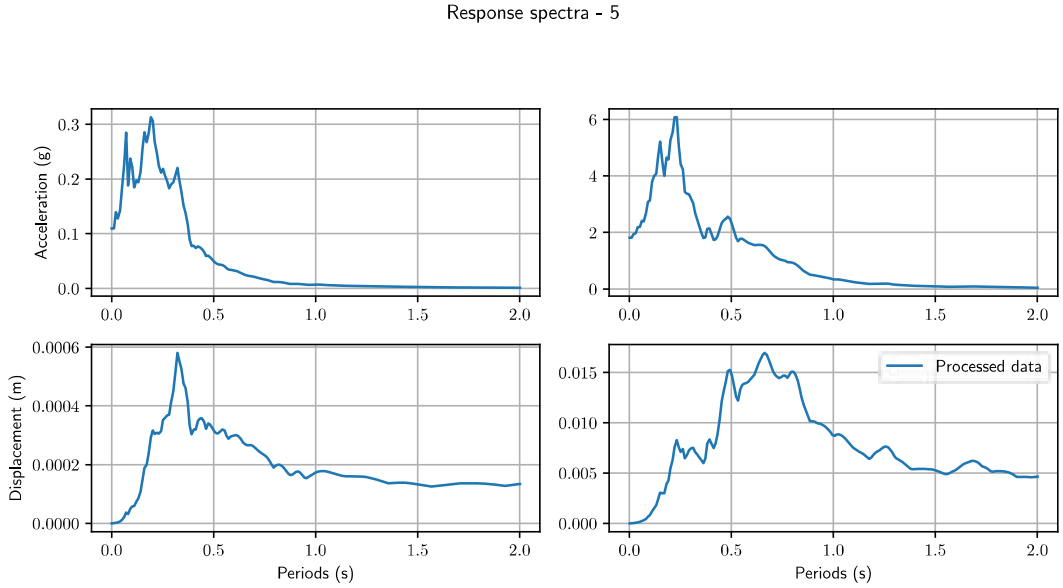

Figure 30: Response spectra from 150 record.

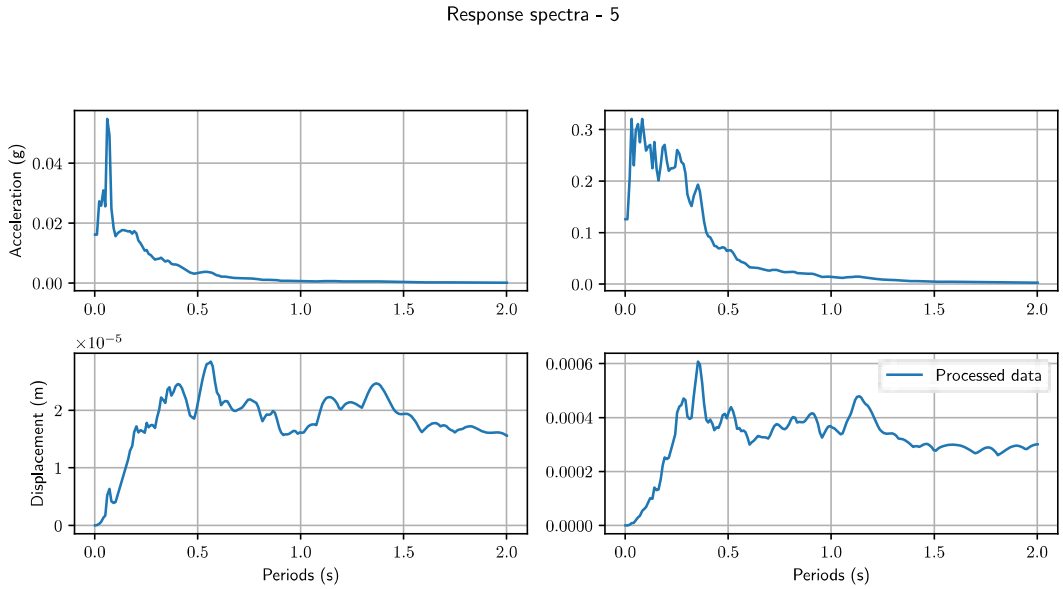

Figure 31: Response spectra from $WN4$ record.

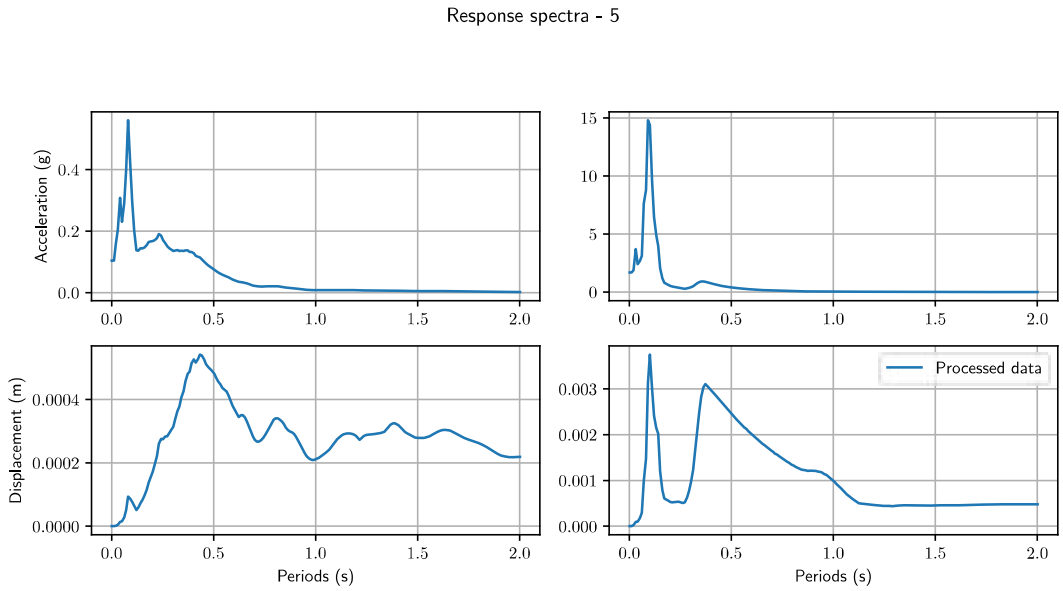

Figure 32: Response spectra from $Sine_sweep$ record.

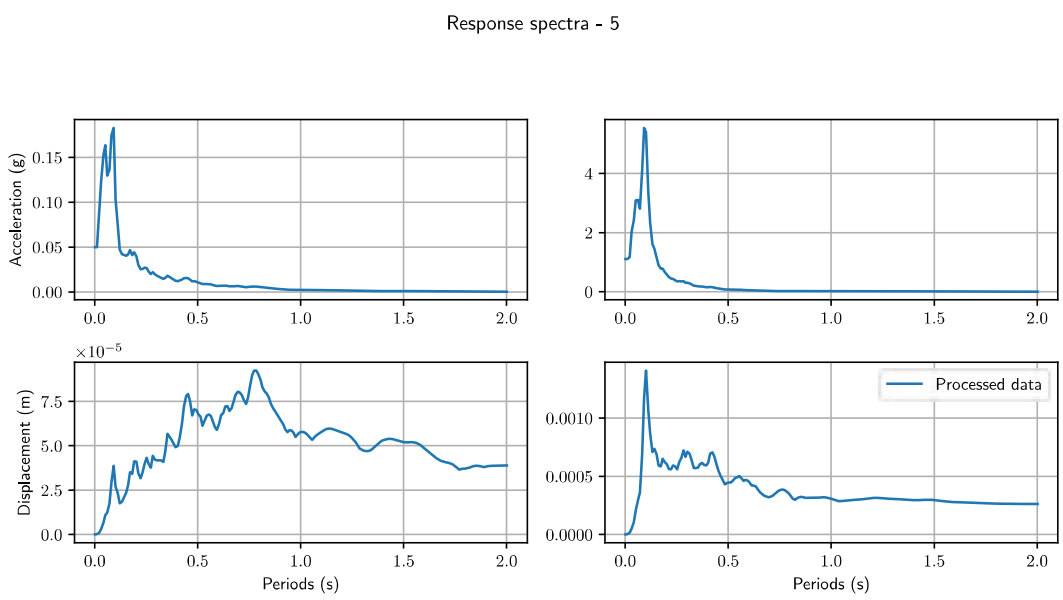

Figure 33: Response spectra from $WN5$ record.

2 Data from instrumentation of Wall 1

2.1 Acceleration records

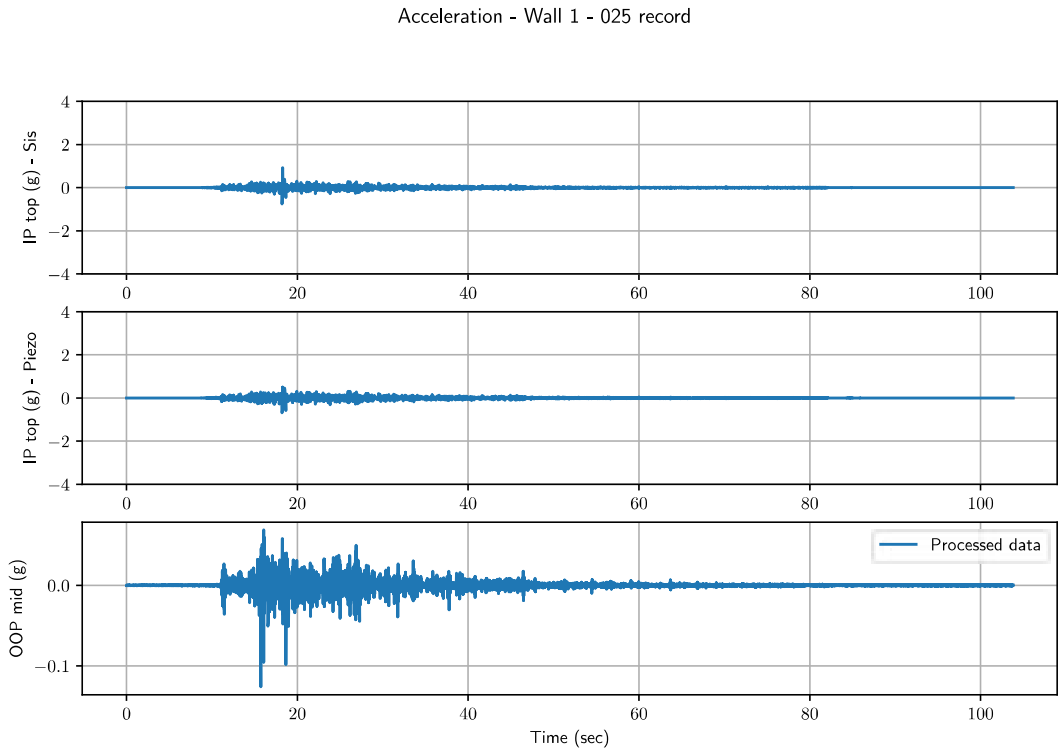

Figure 34: Acceleration records of wall 1 from 025 record.

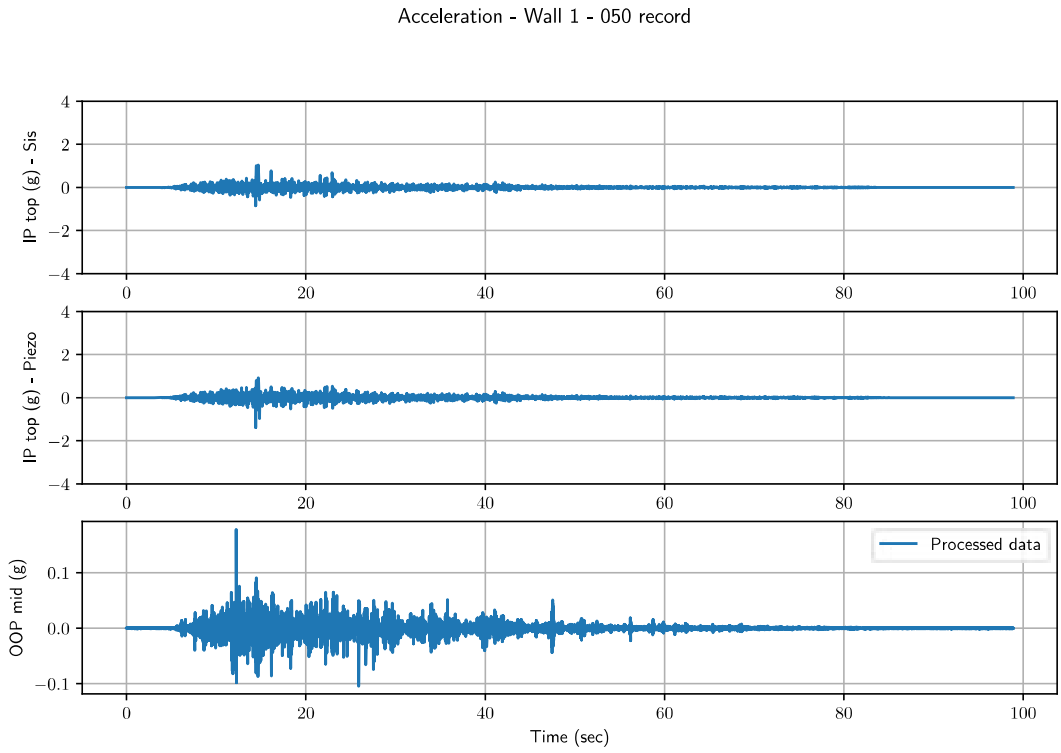

Figure 35: Acceleration records of wall 1 from 050 record.

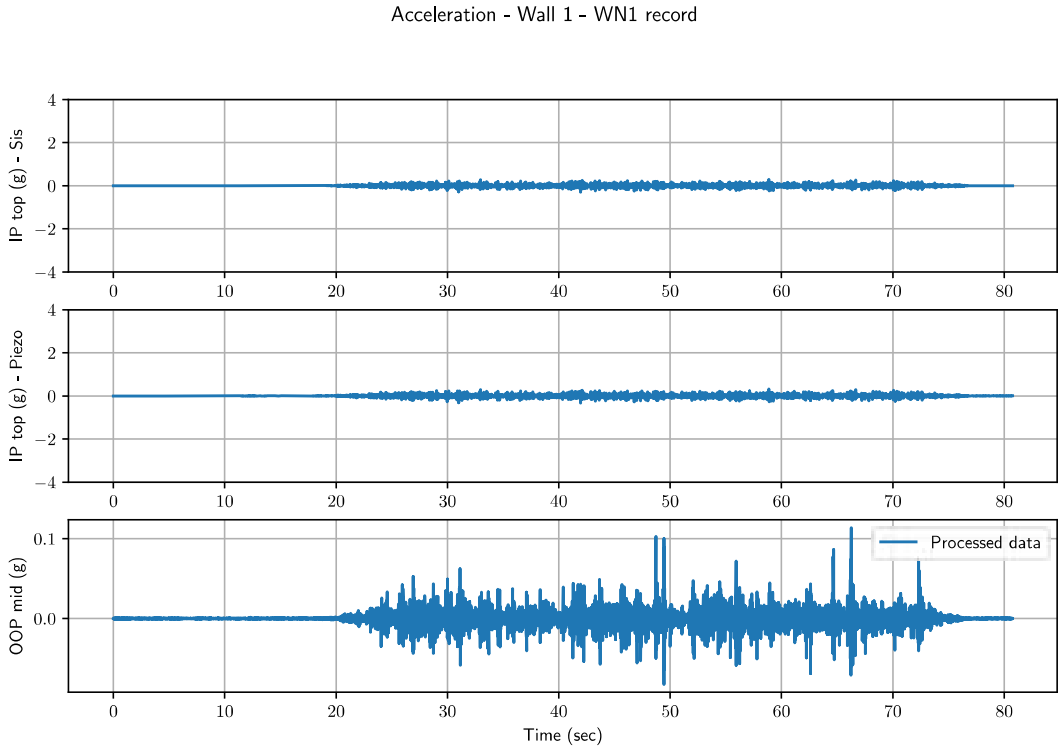

Figure 36: Acceleration records of wall 1 from $WN1$ record.

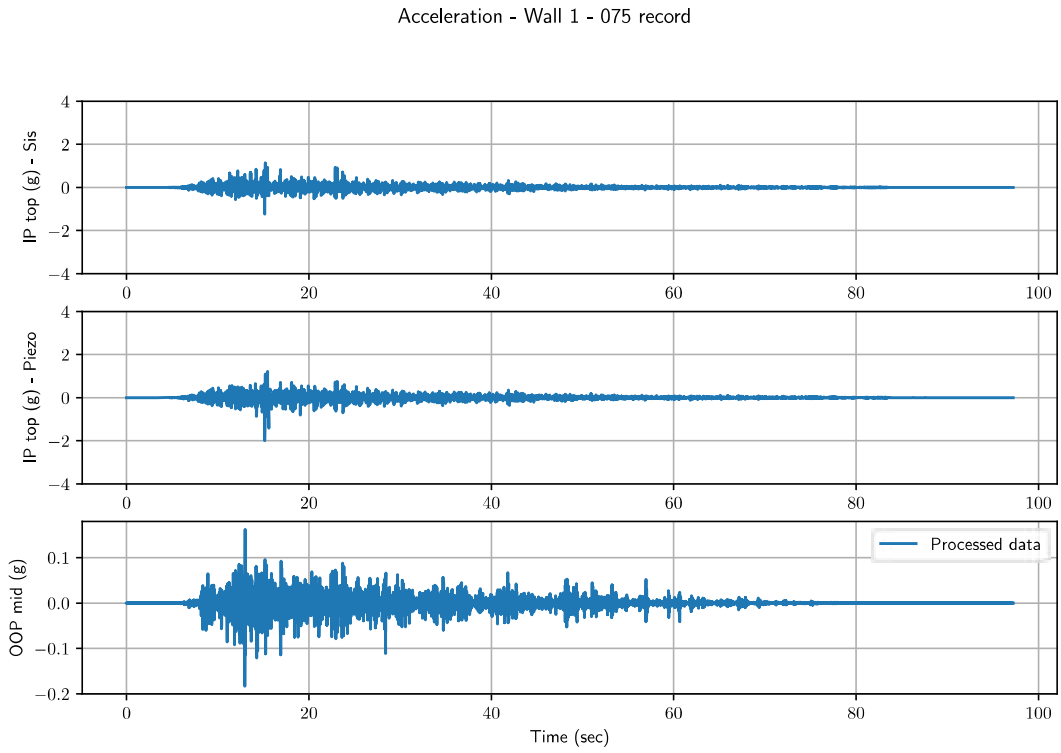

Figure 37: Acceleration records of wall 1 from 075 record.

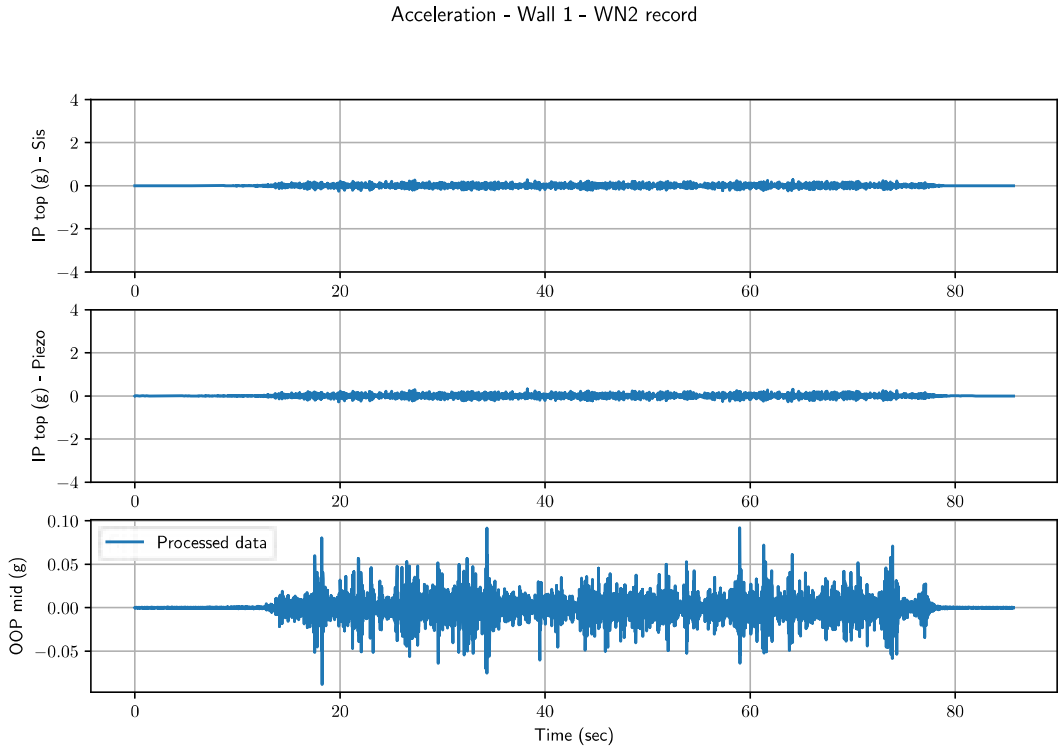

Figure 38: Acceleration records of wall 1 from $WN2$ record.

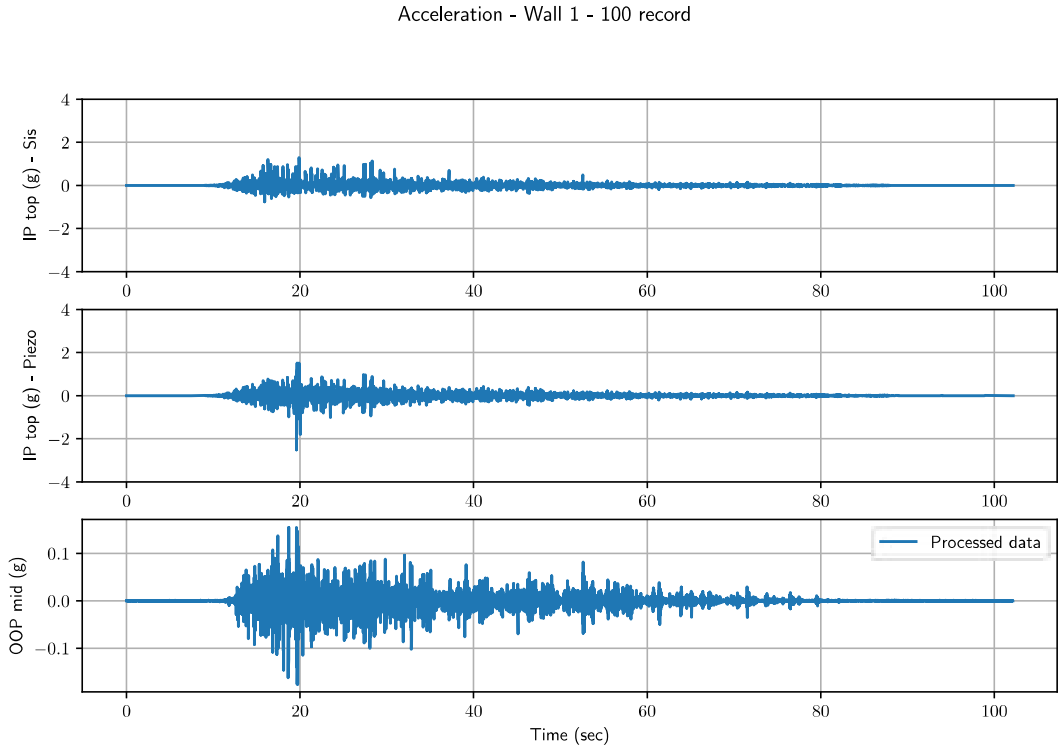

Figure 39: Acceleration records of wall 1 from 100 record.

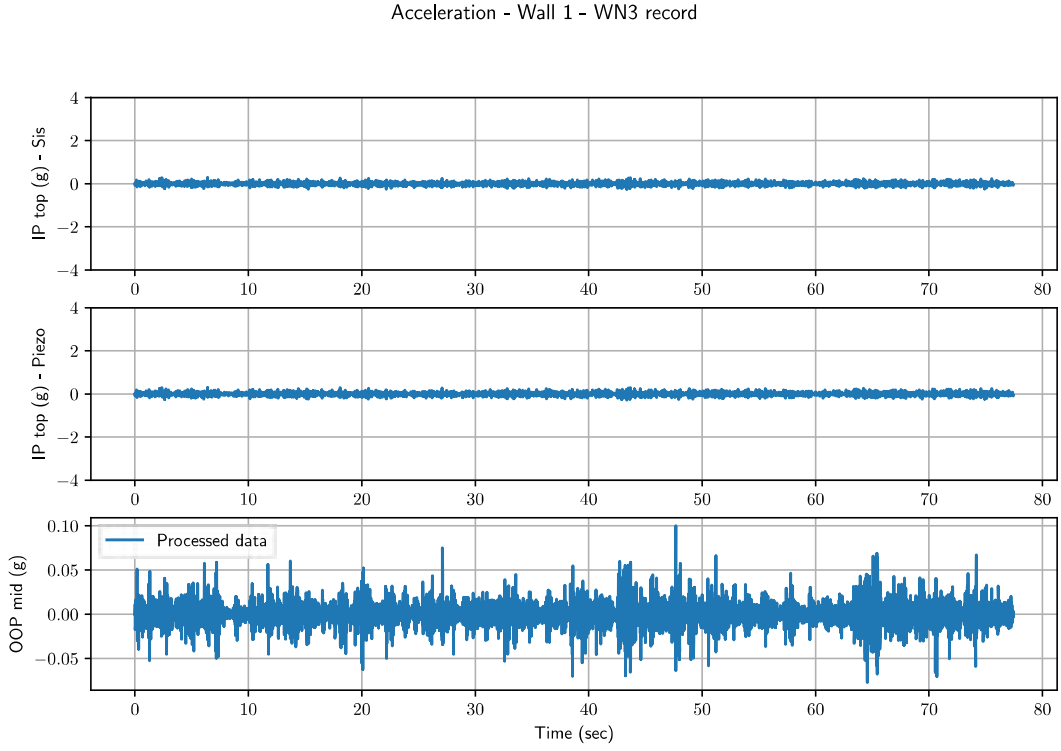

Figure 40: Acceleration records of wall 1 from $WN3$ record.

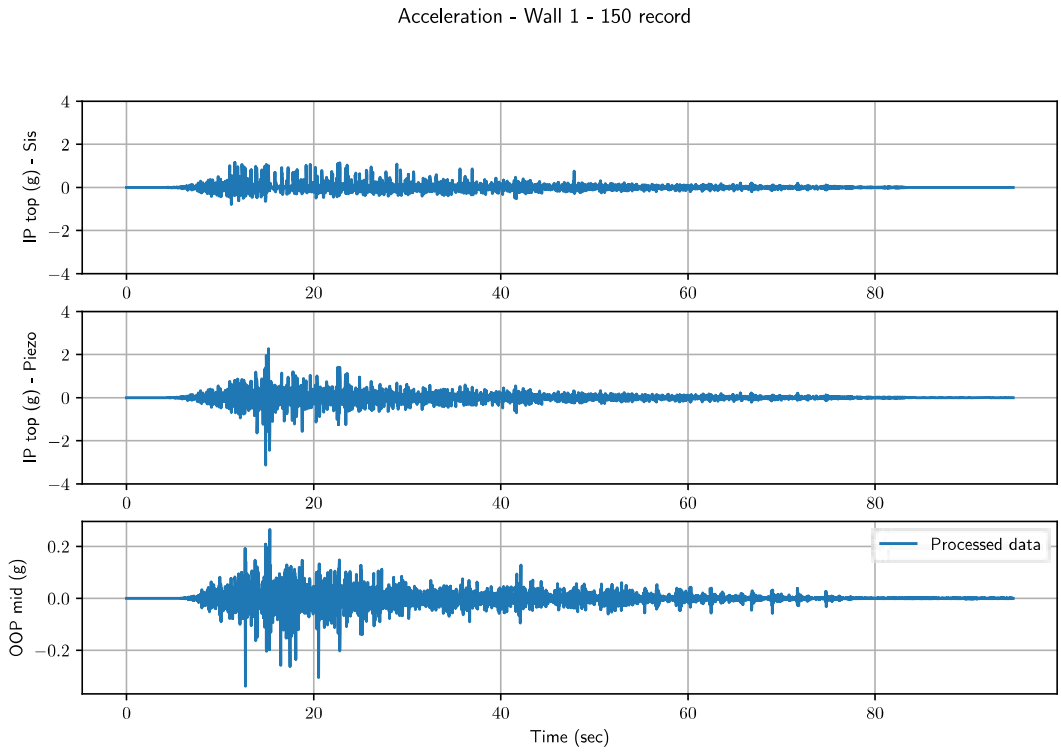

Figure 41: Acceleration records of wall 1 from 150 record.

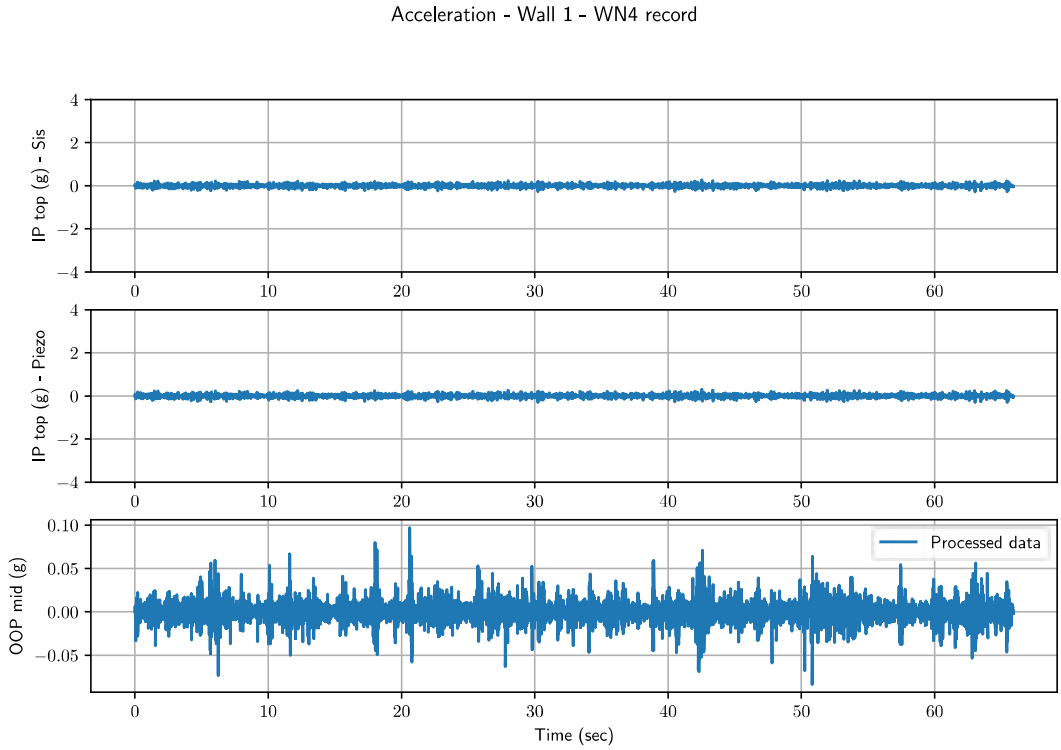

Figure 42: Acceleration records of wall 1 from $WN4$ record.

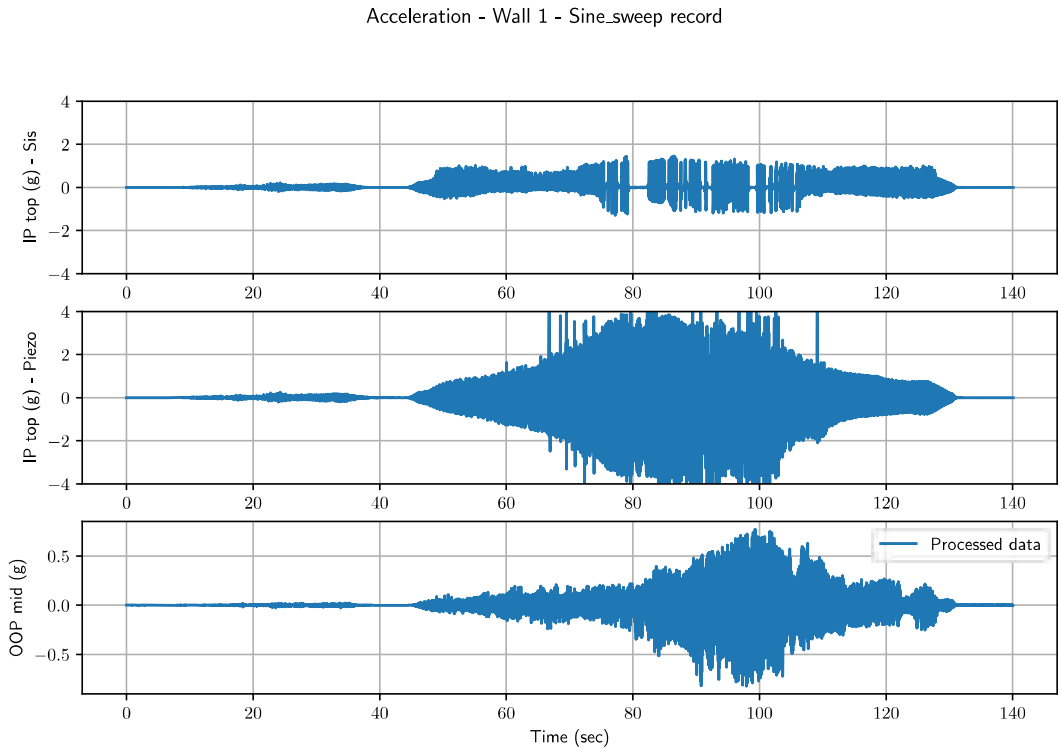

Figure 43: Acceleration records of wall 1 from $Sine_sweep$ record.

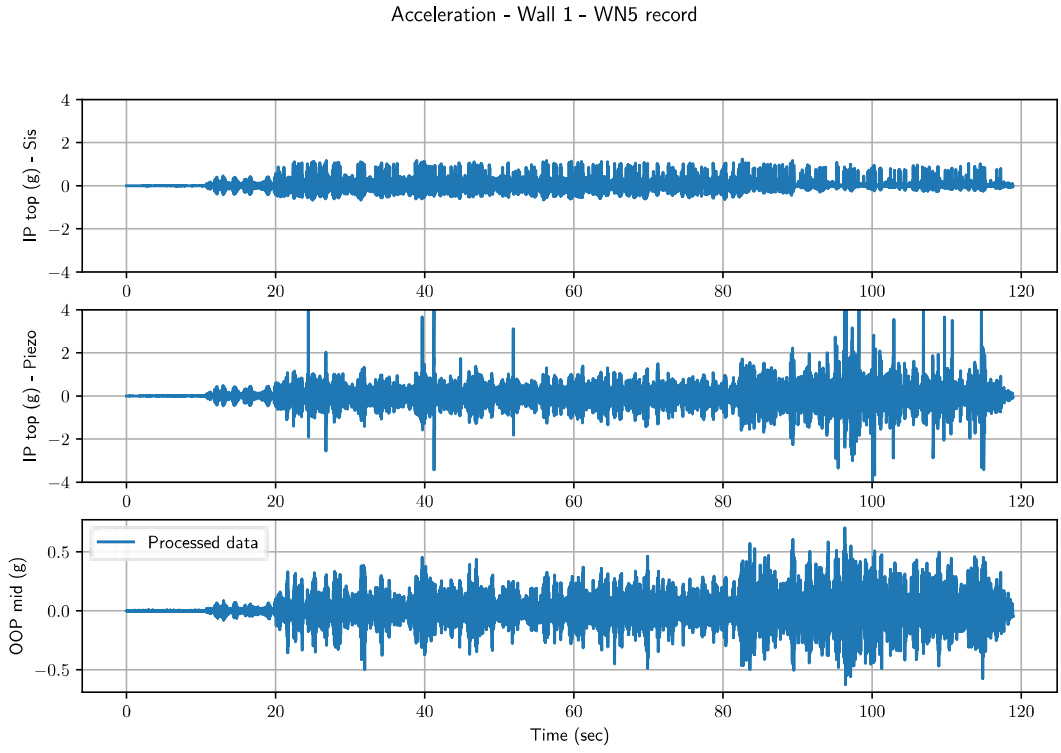

Figure 44: Acceleration records of wall 1 from $WN5$ record.

2.2 Displacement records

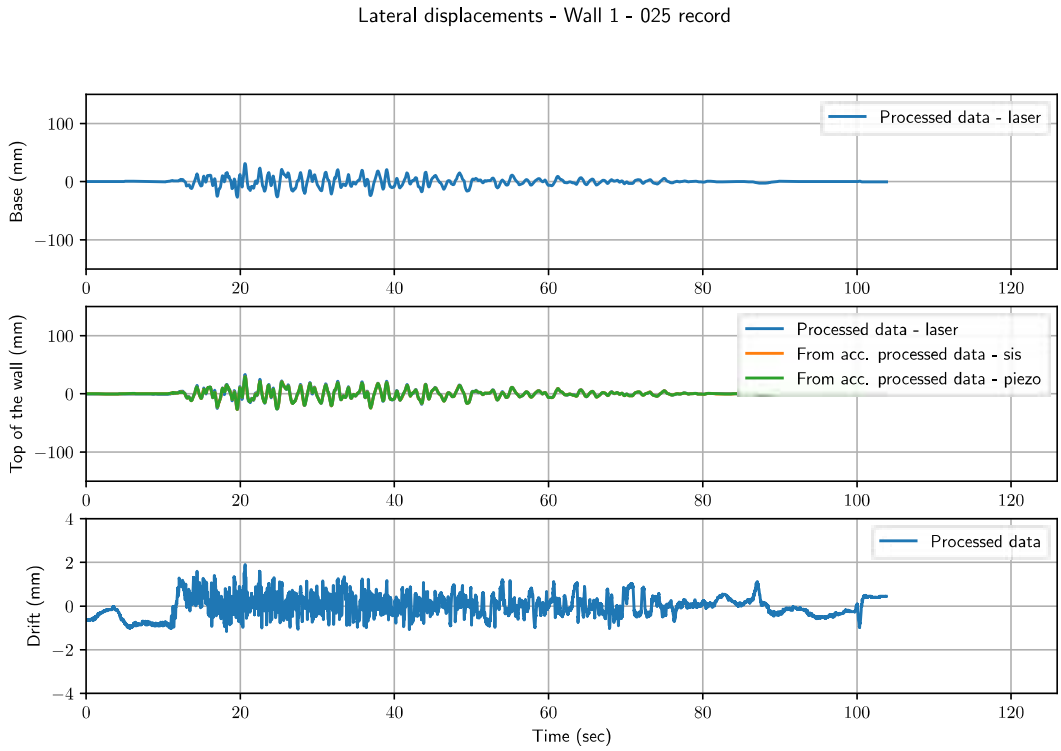

Figure 45: Acceleration records of wall 1 from 025 record.

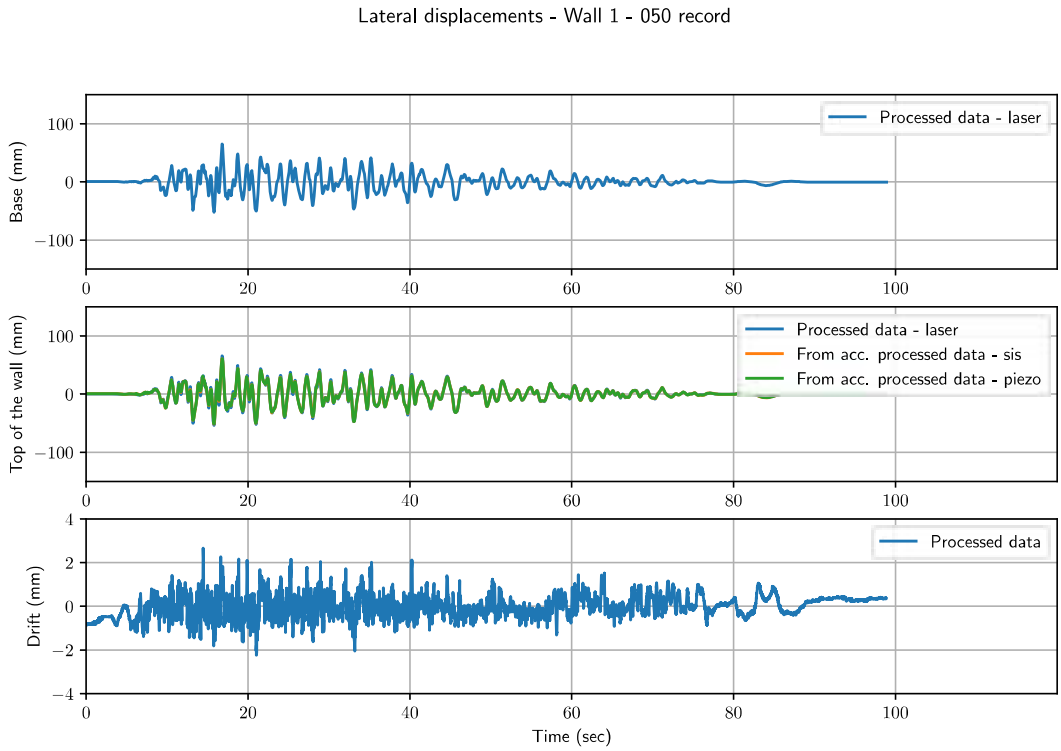

Figure 46: Acceleration records of wall 1 from 050 record.

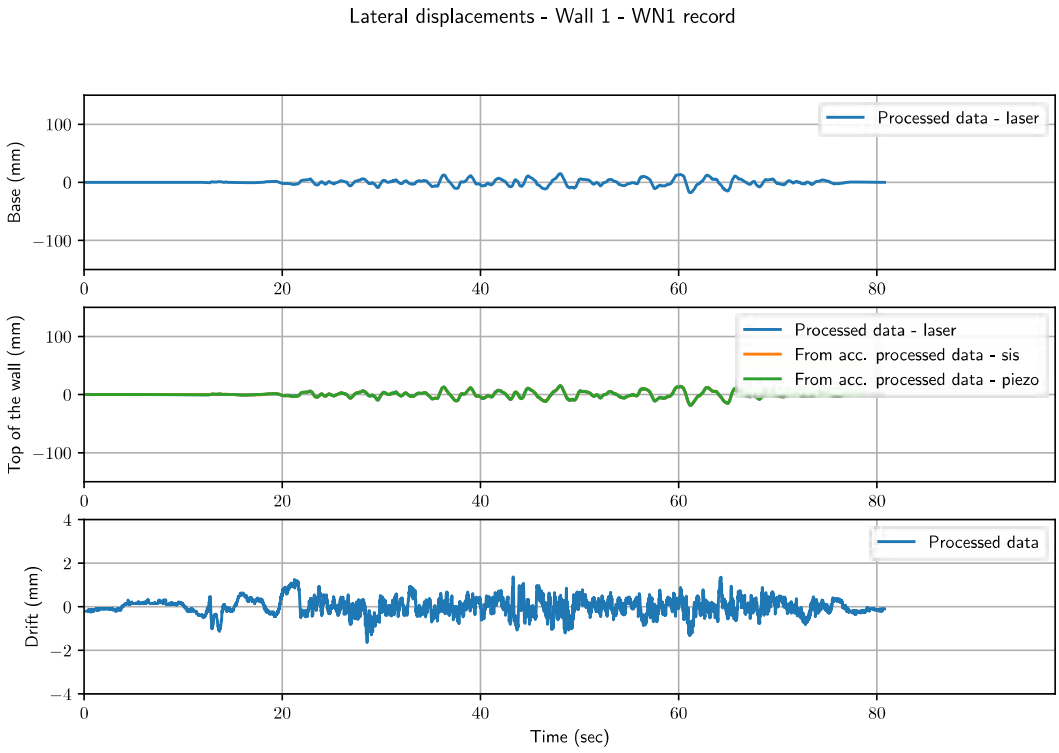

Figure 47: Acceleration records of wall 1 from $WN1$ record.

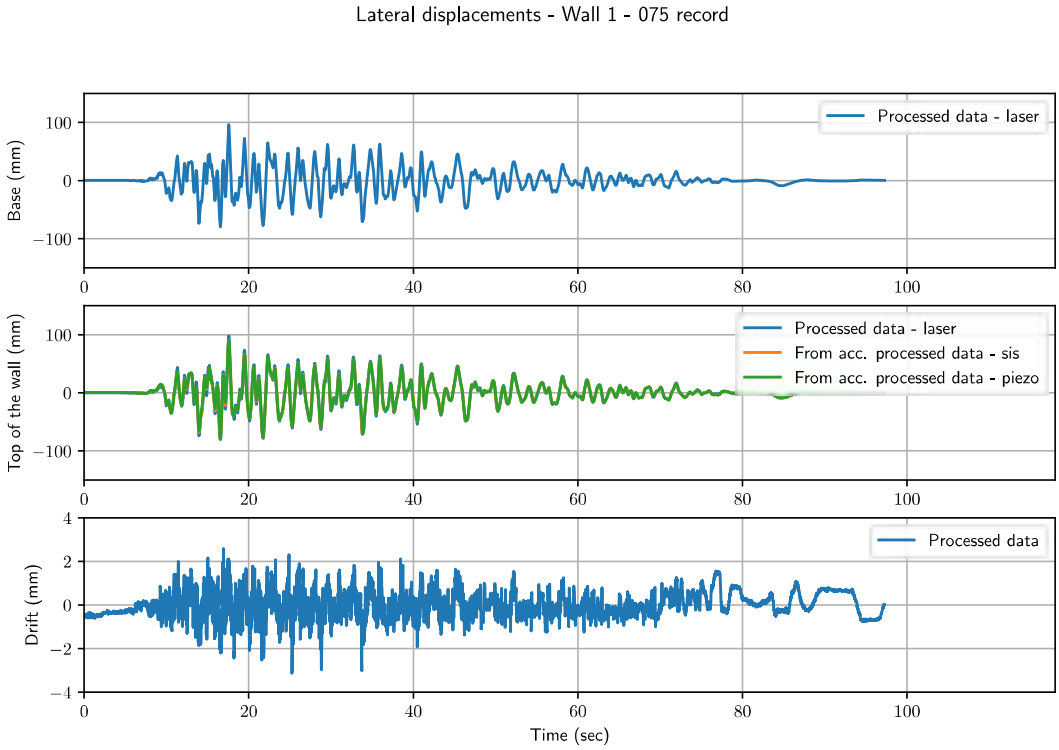

Figure 48: Acceleration records of wall 1 from 075 record.

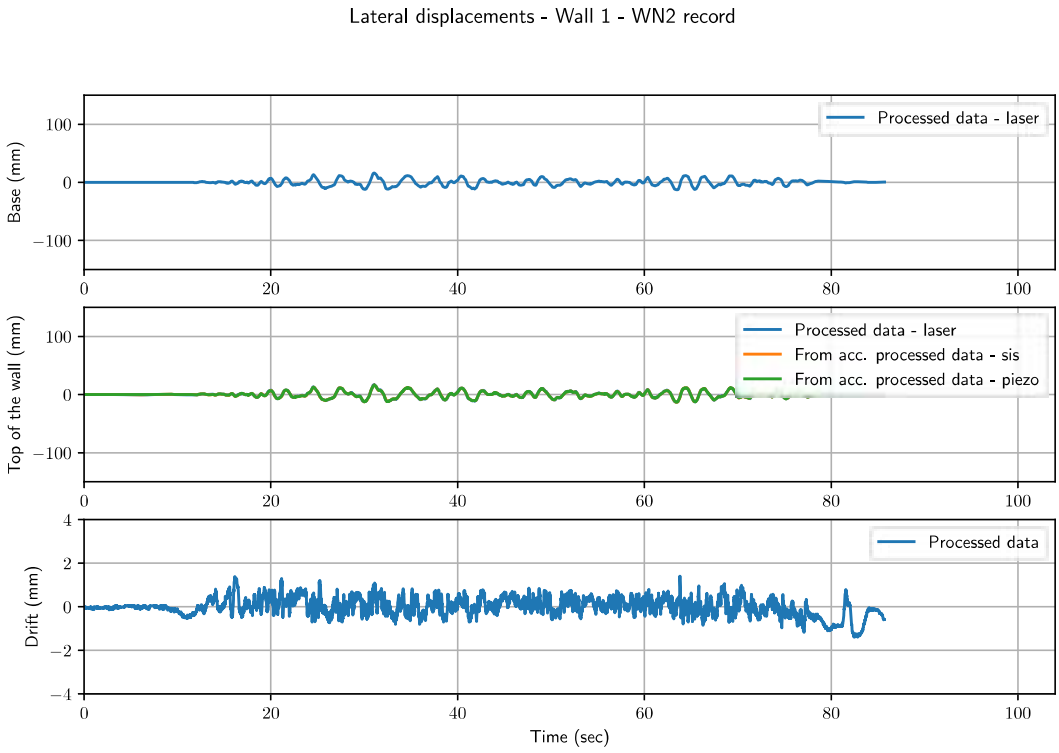

Figure 49: Acceleration records of wall 1 from $WN2$ record.

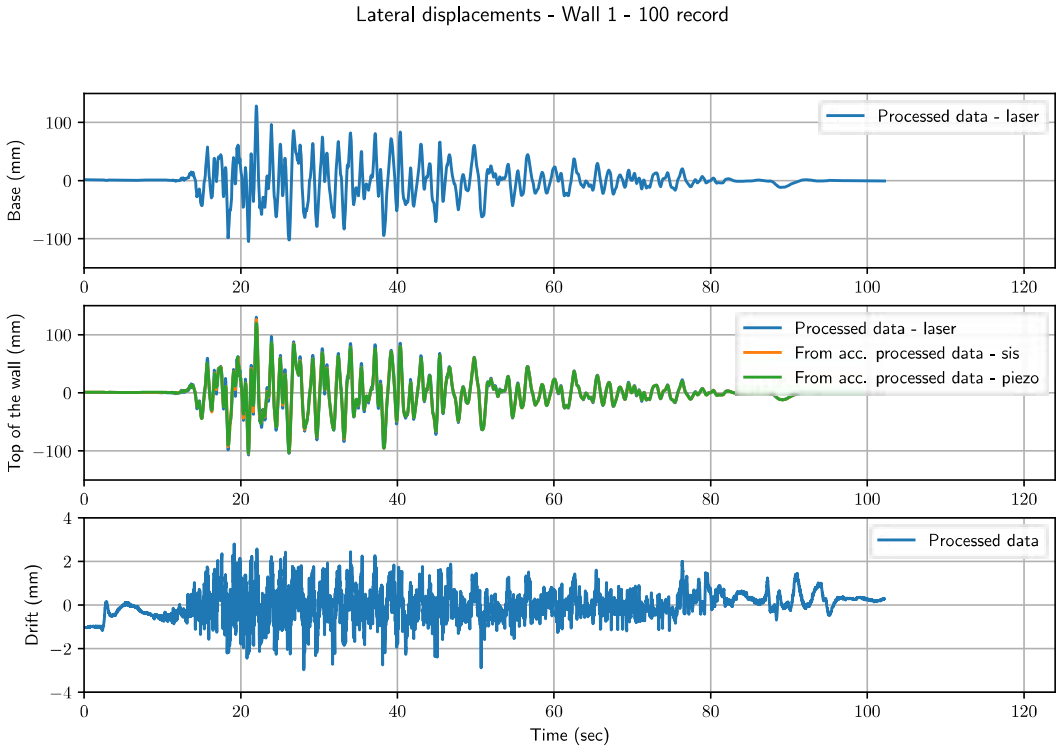

Figure 50: Acceleration records of wall 1 from 100 record.

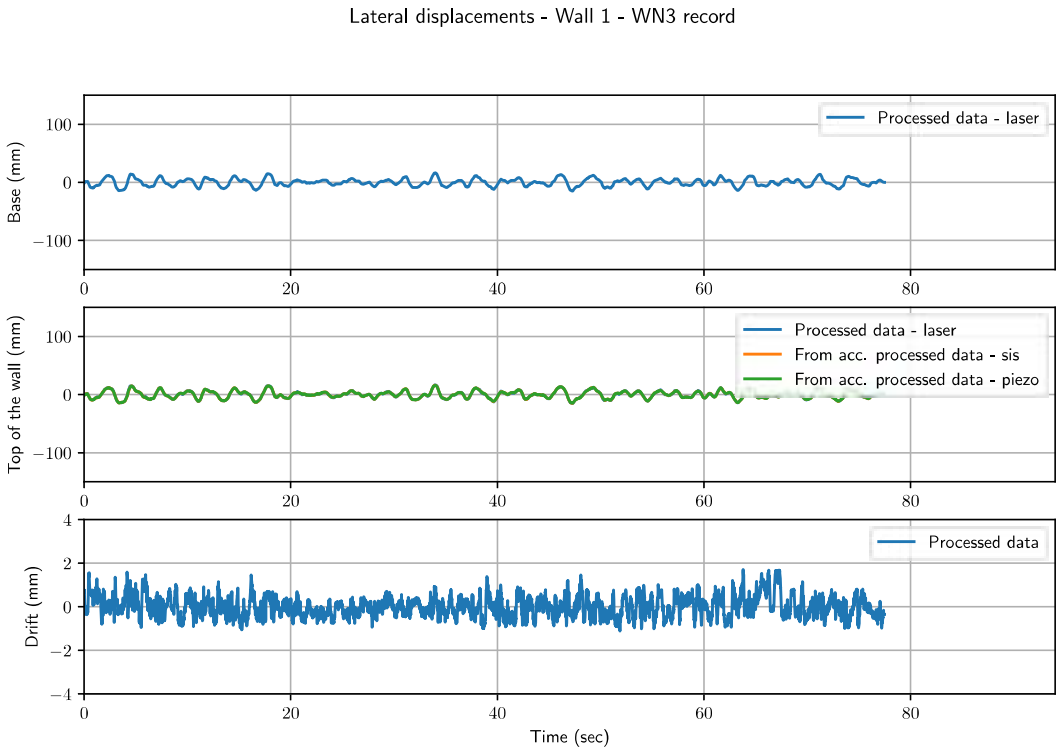

Figure 51: Acceleration records of wall 1 from $WN3$ record.

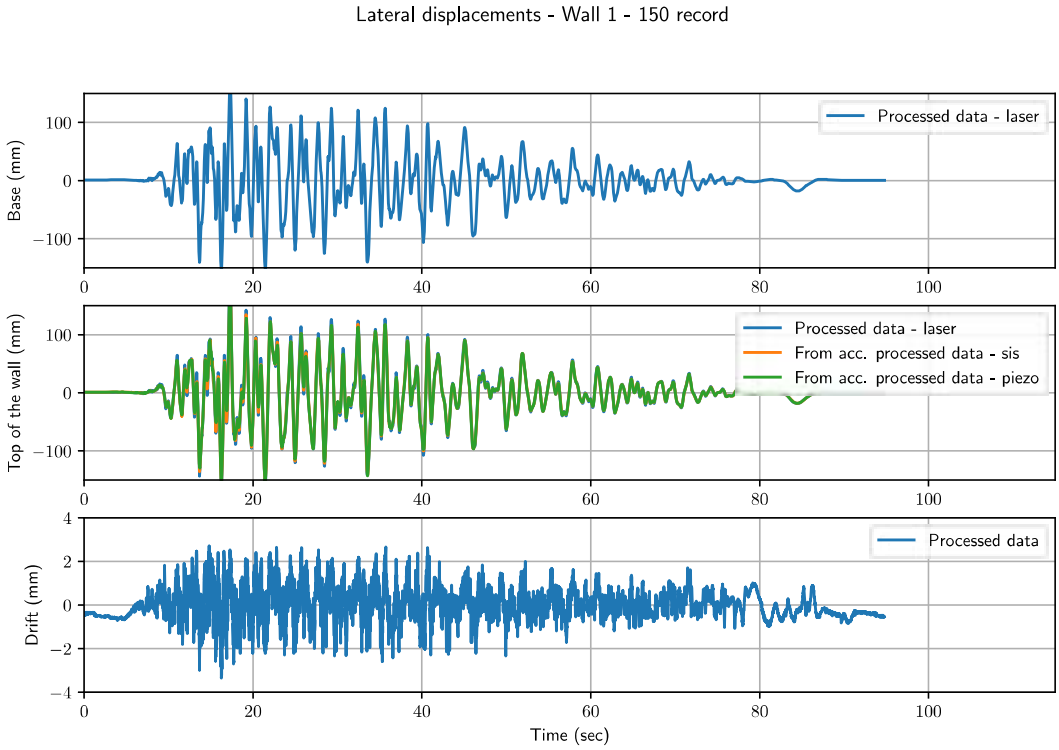

Figure 52: Acceleration records of wall 1 from 150 record.

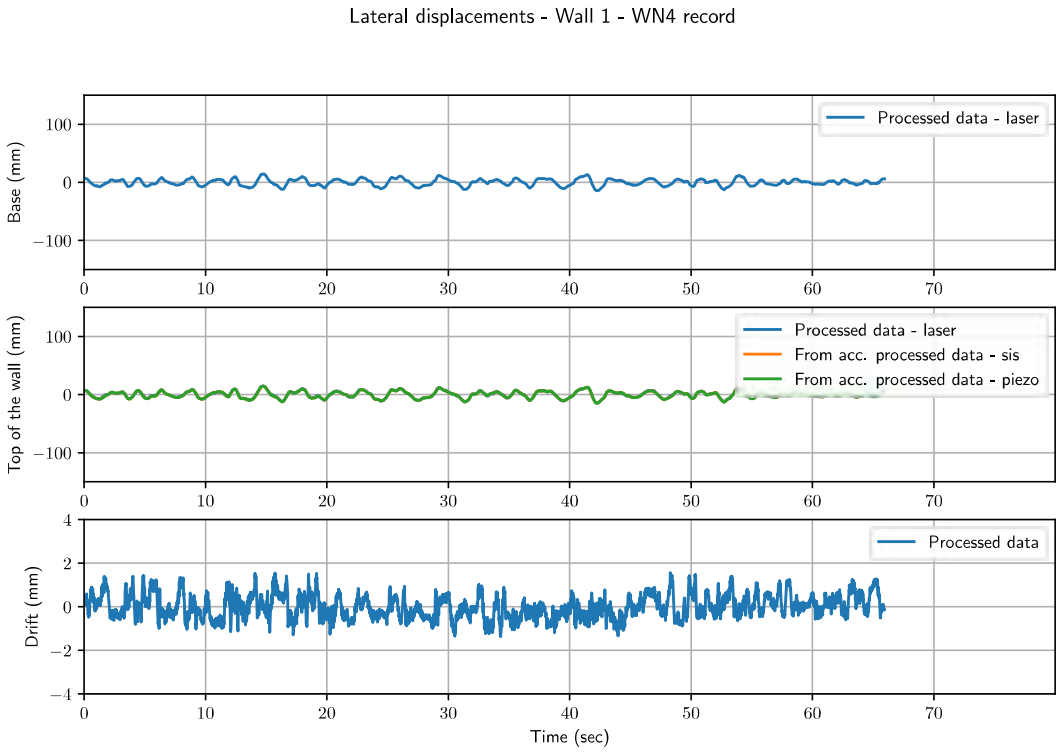

Figure 53: Acceleration records of wall 1 from $WN4$ record.

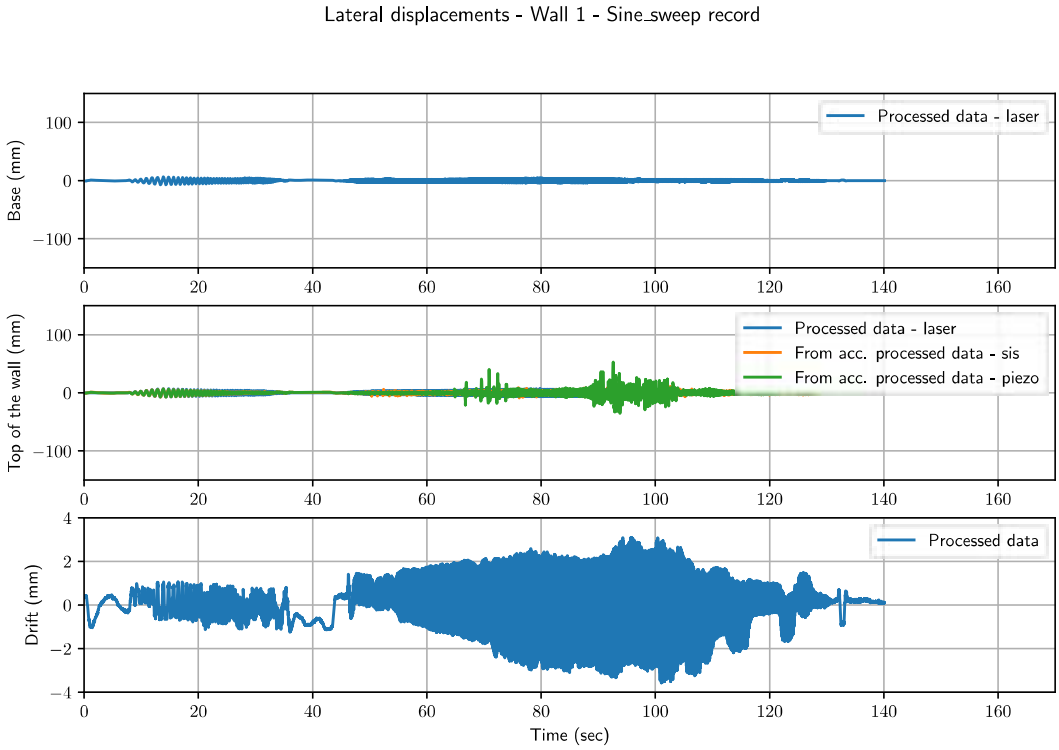

Figure 54: Acceleration records of wall 1 from $Sine_sweep$ record.

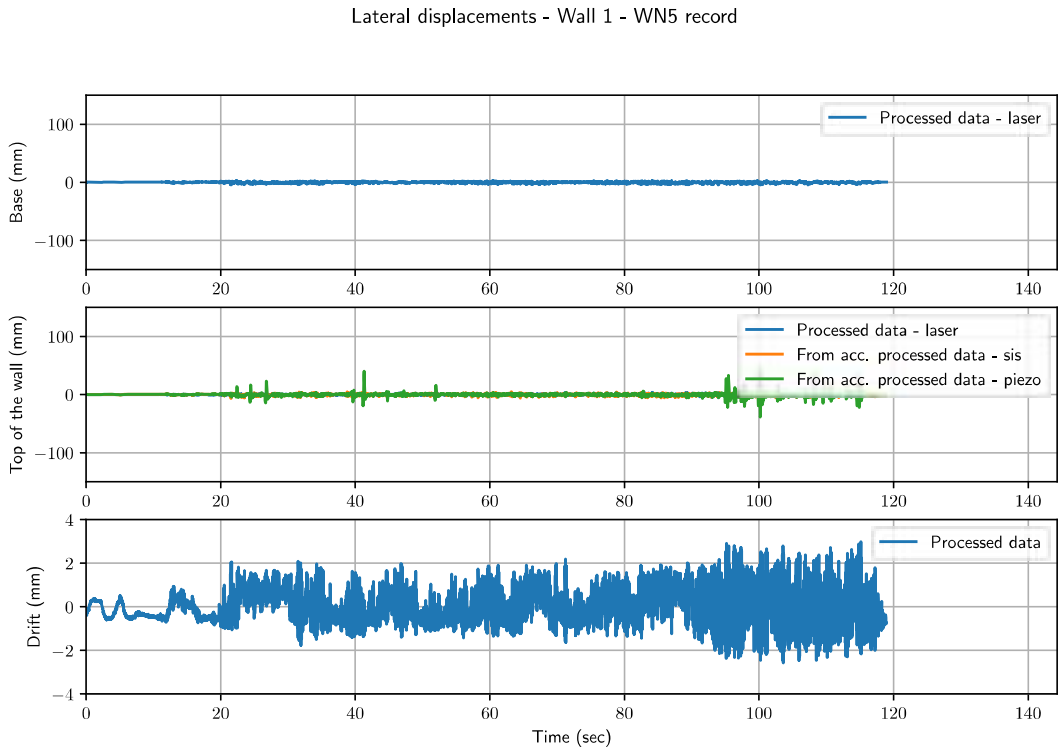

Figure 55: Acceleration records of wall 1 from $WN5$ record.

2.3 Fourier analysis results from acceleration records

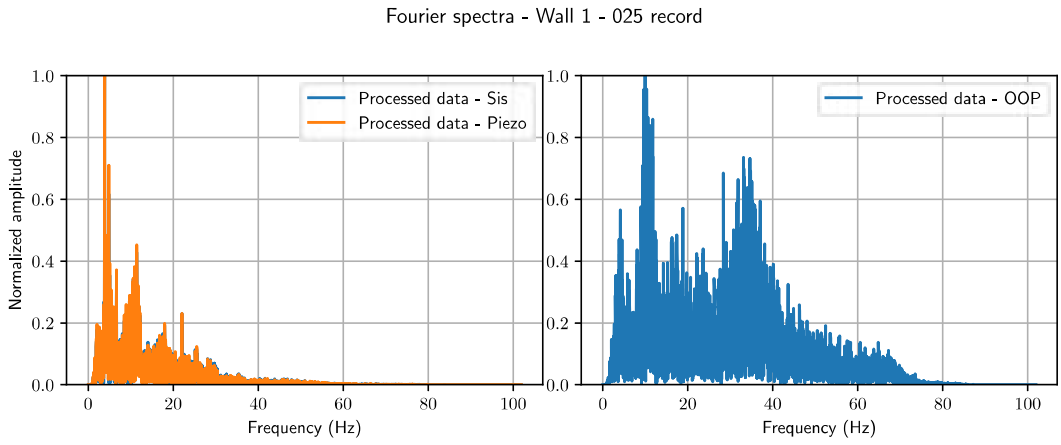

Figure 56: Fourier transformation of wall 1 from 025 record.

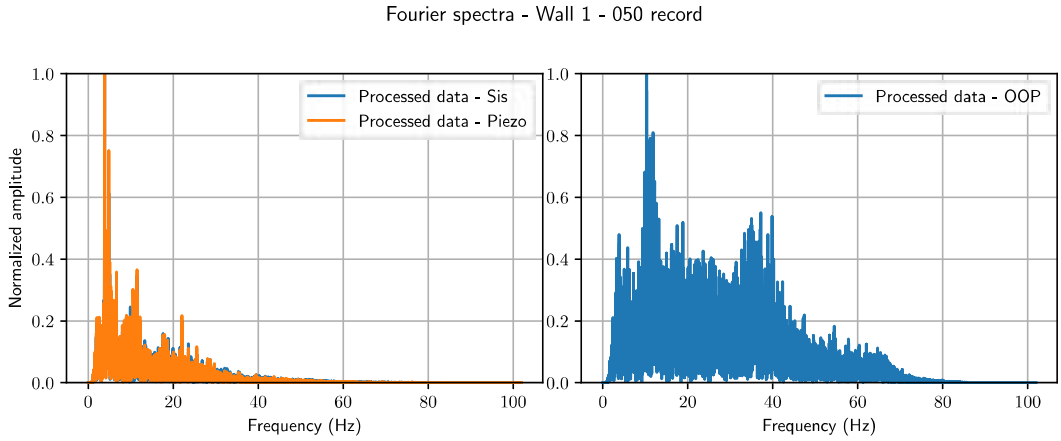

Figure 57: Fourier transformation of wall 1 from 050 record.

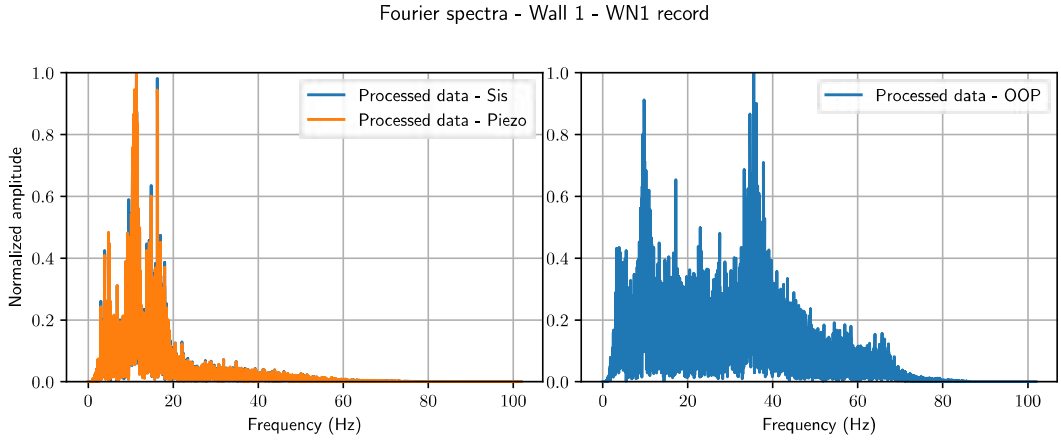

Figure 58: Fourier transformation of wall 1 from $WN1$ record.

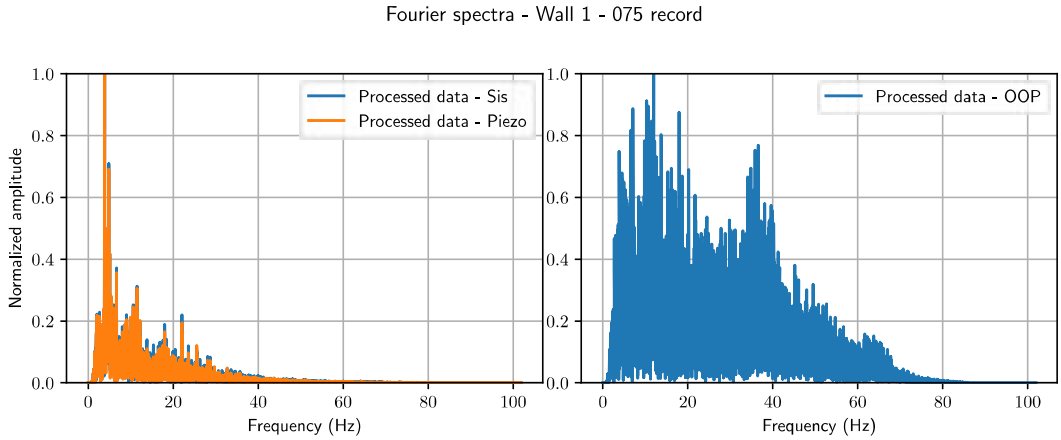

Figure 59: Fourier transformation of wall 1 from 075 record.

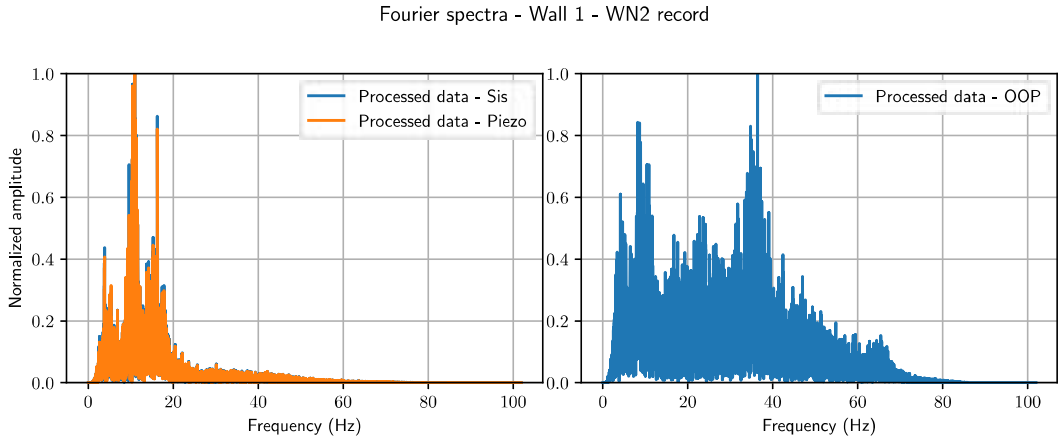

Figure 60: Fourier transformation of wall 1 from $WN2$ record.

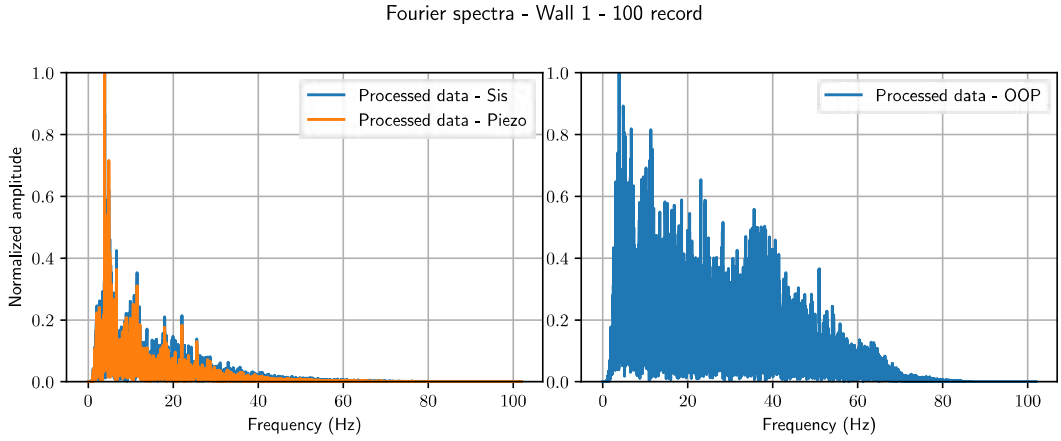

Figure 61: Fourier transformation of wall 1 from 100 record.

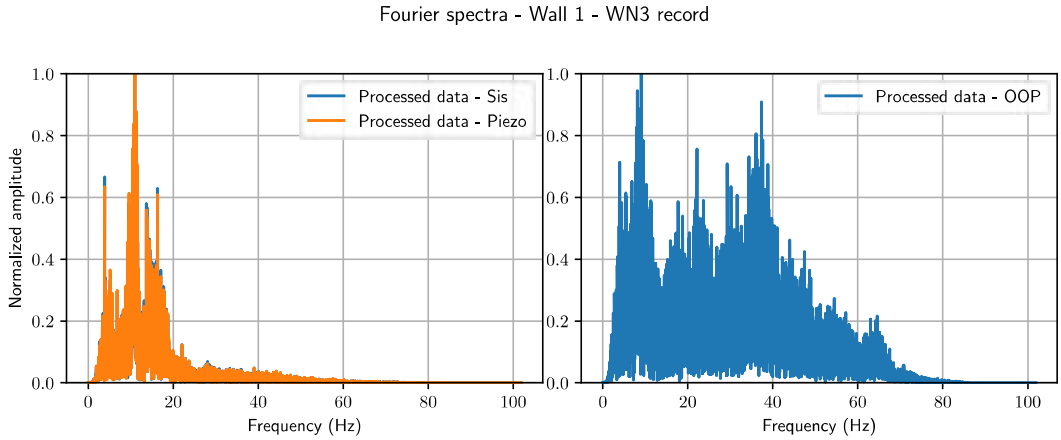

Figure 62: Fourier transformation of wall 1 from $WN3$ record.

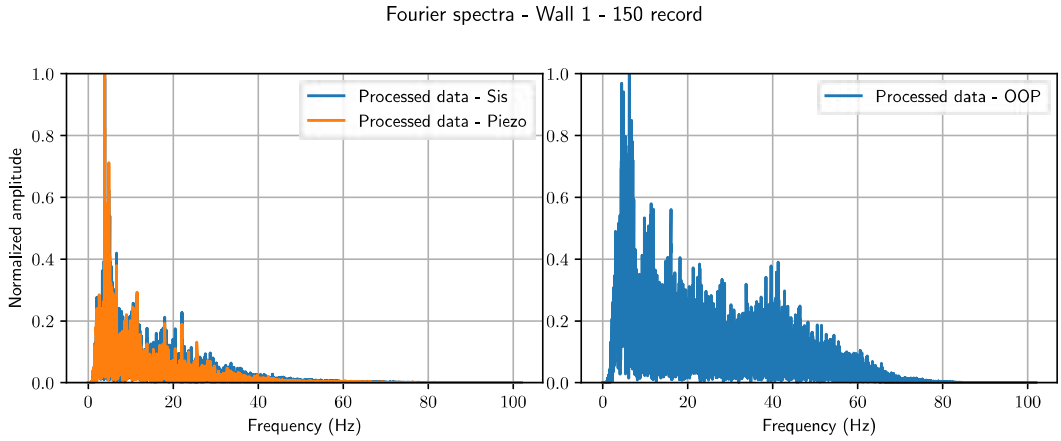

Figure 63: Fourier transformation of wall 1 from 150 record.

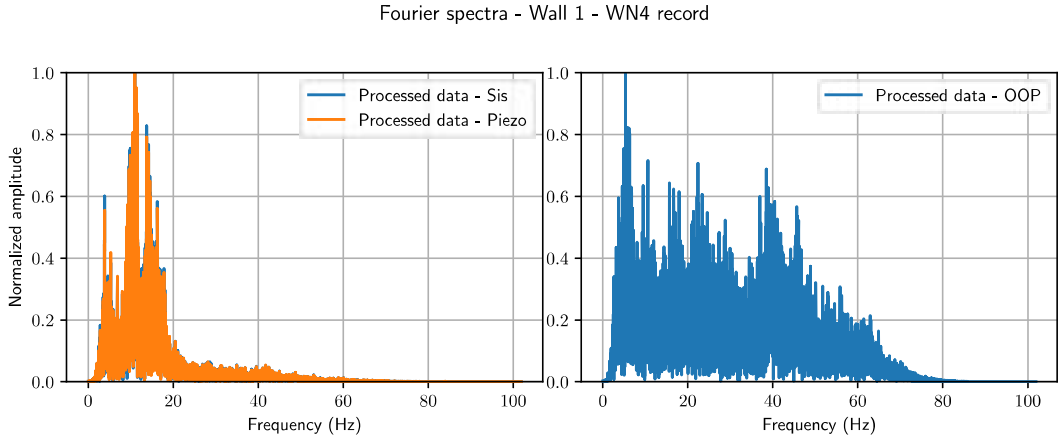

Figure 64: Fourier transformation of wall 1 from $WN4$ record.

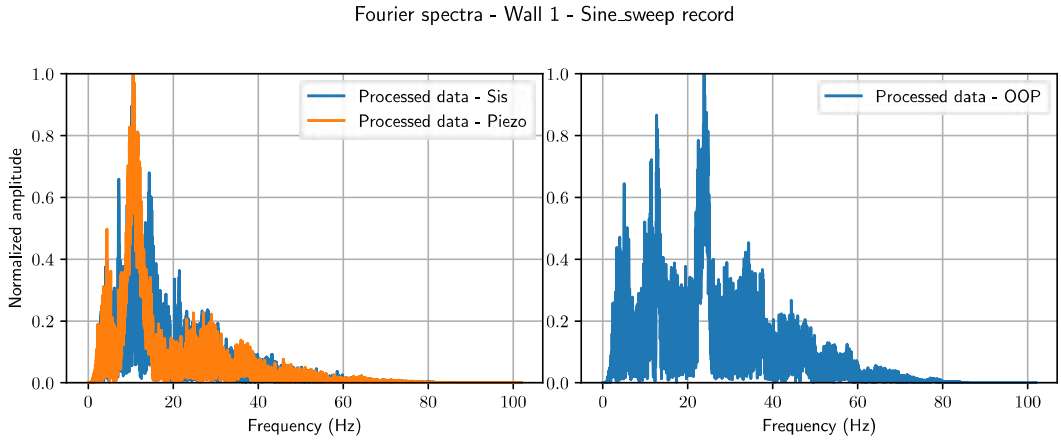

Figure 65: Fourier transformation of wall 1 from $Sine_sweep$ record.

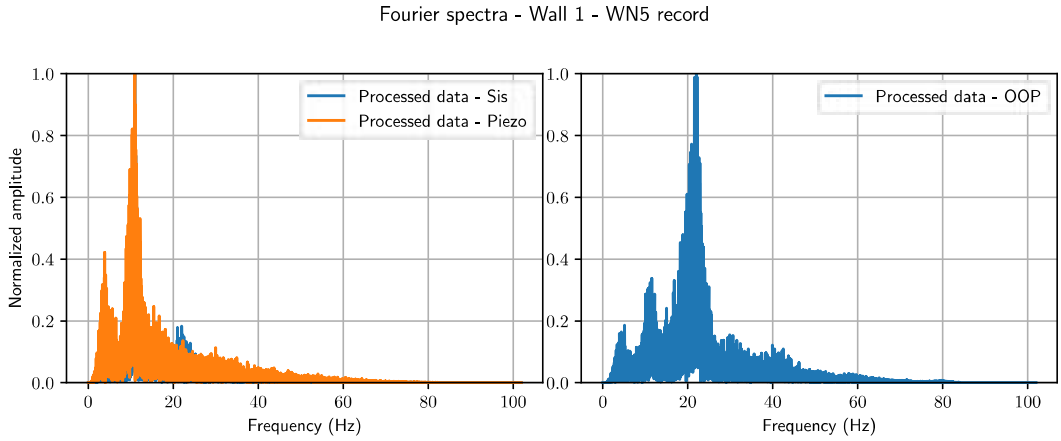

Figure 66: Fourier transformation of wall 1 from $WN5$ record.

2.4 Power density spectra (PDS) from acceleration records

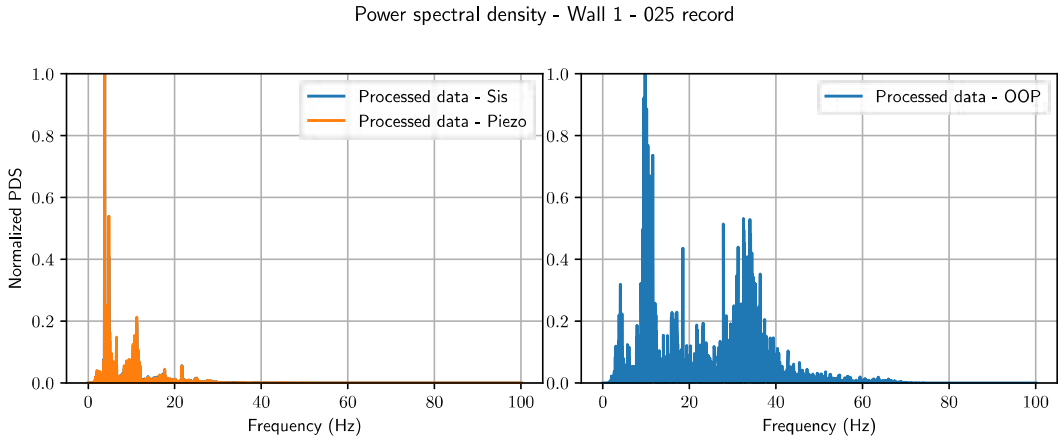

Figure 67: Power density spectra of wall 1 from 025 record.

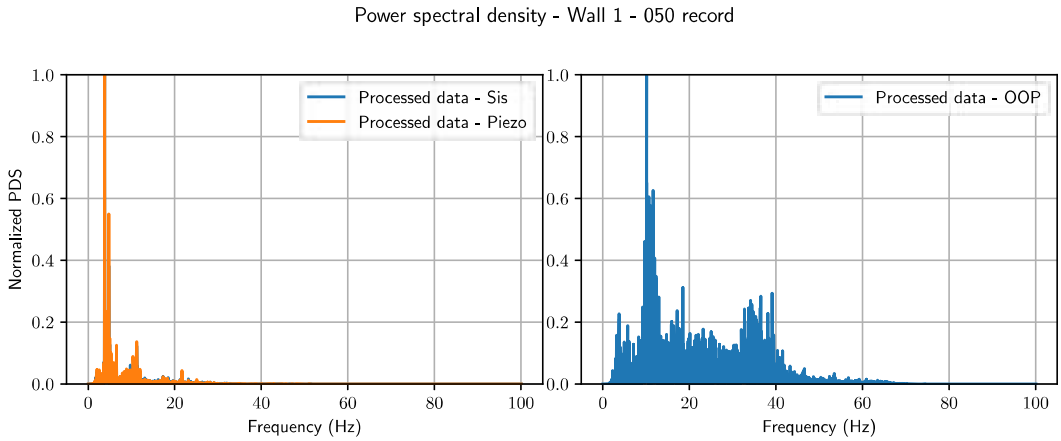

Figure 68: Power density spectra of wall 1 from 050 record.

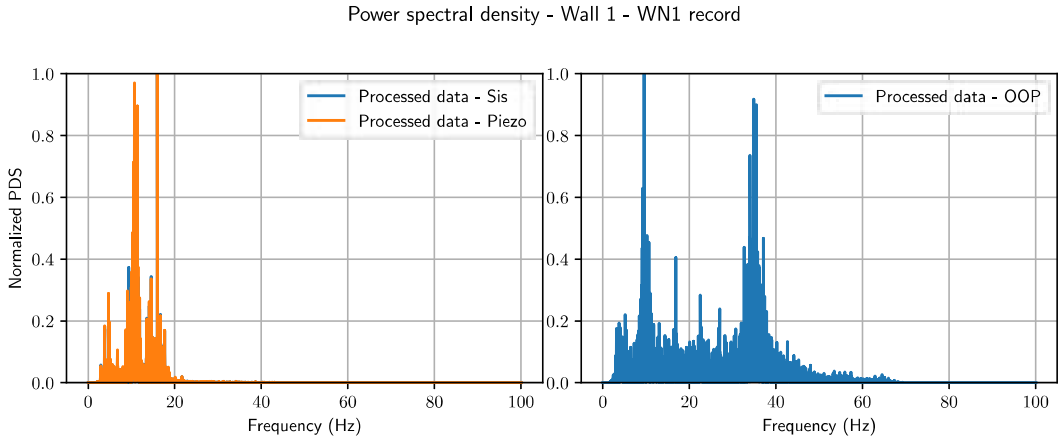

Figure 69: Power density spectra of wall 1 from $WN1$ record.

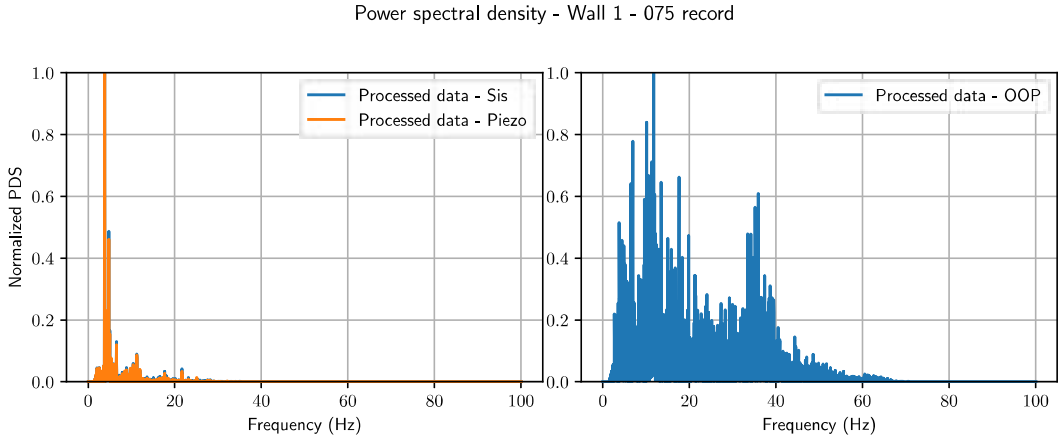

Figure 70: Power density spectra of wall 1 from 075 record.

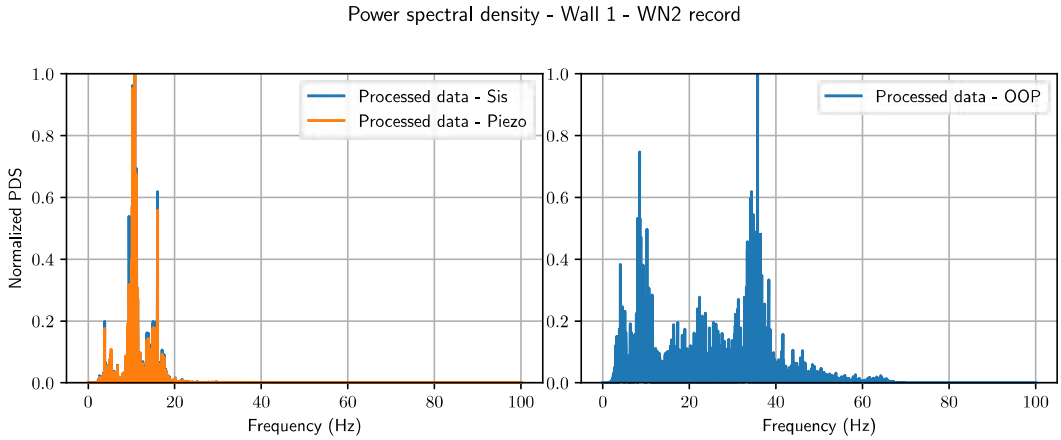

Figure 71: Power density spectra of wall 1 from $WN2$ record.

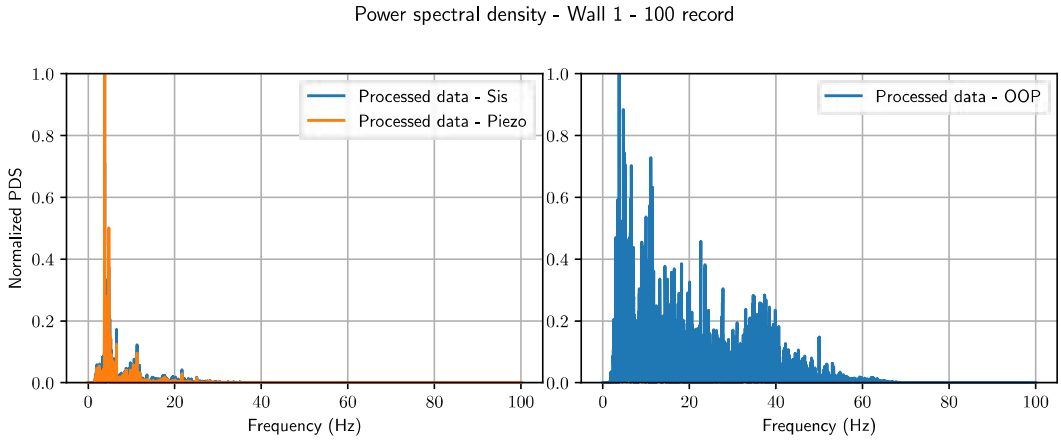

Figure 72: Power density spectra of wall 1 from 100 record.

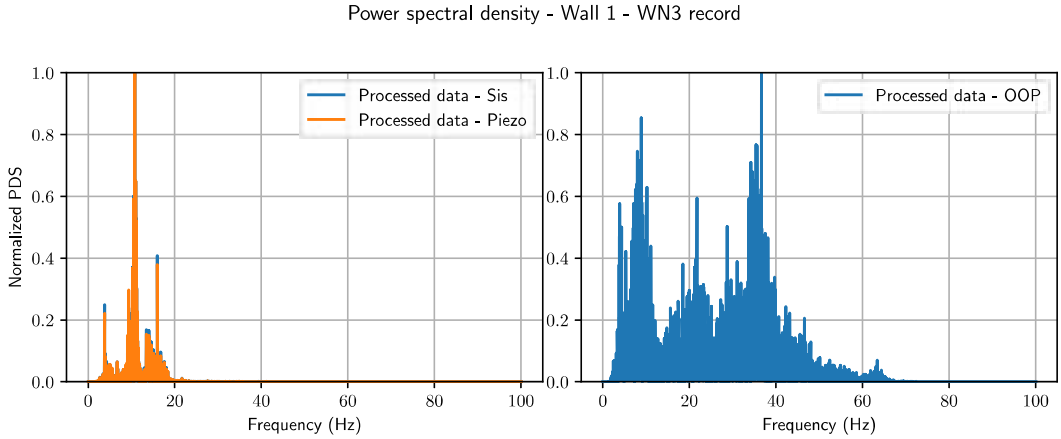

Figure 73: Power density spectra of wall 1 from $WN3$ record.

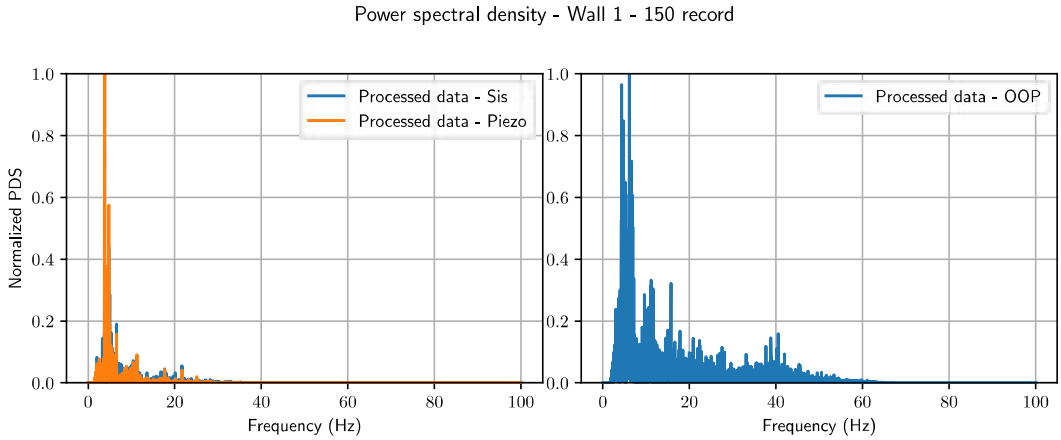

Figure 74: Power density spectra of wall 1 from 150 record.

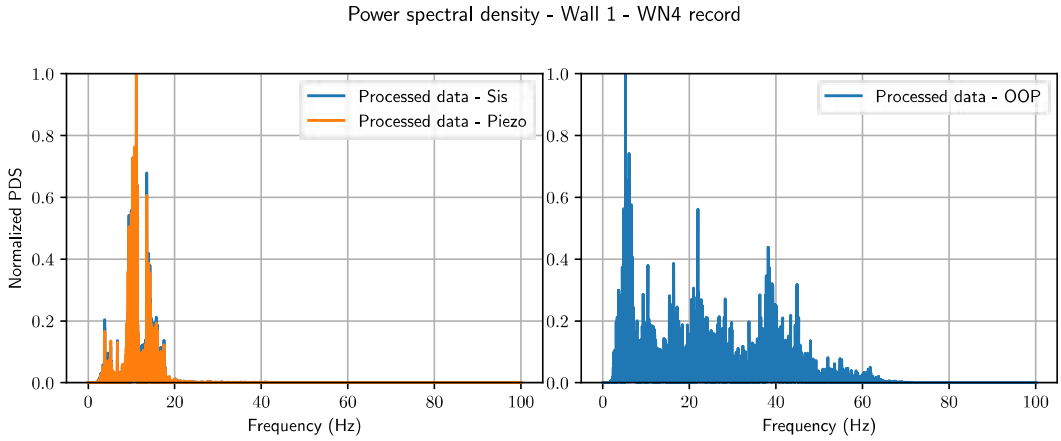

Figure 75: Power density spectra of wall 1 from $WN4$ record.

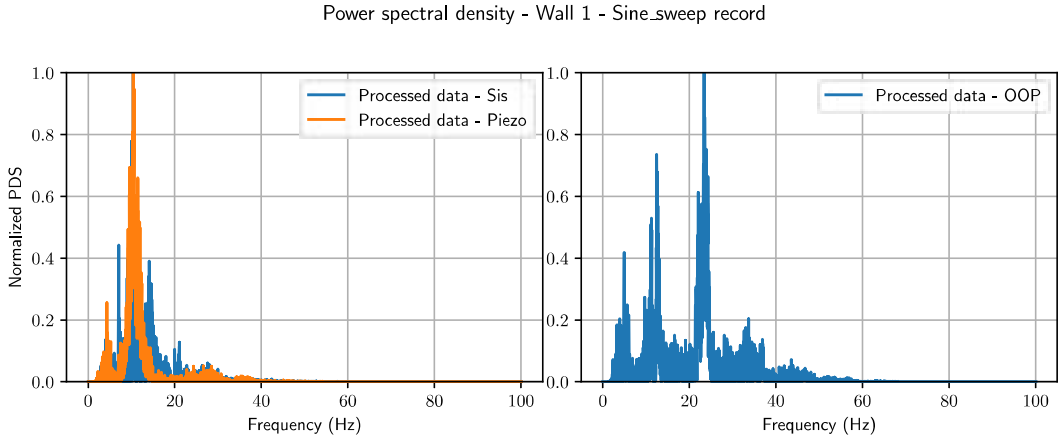

Figure 76: Power density spectra of wall 1 from $Sine_sweep$ record.

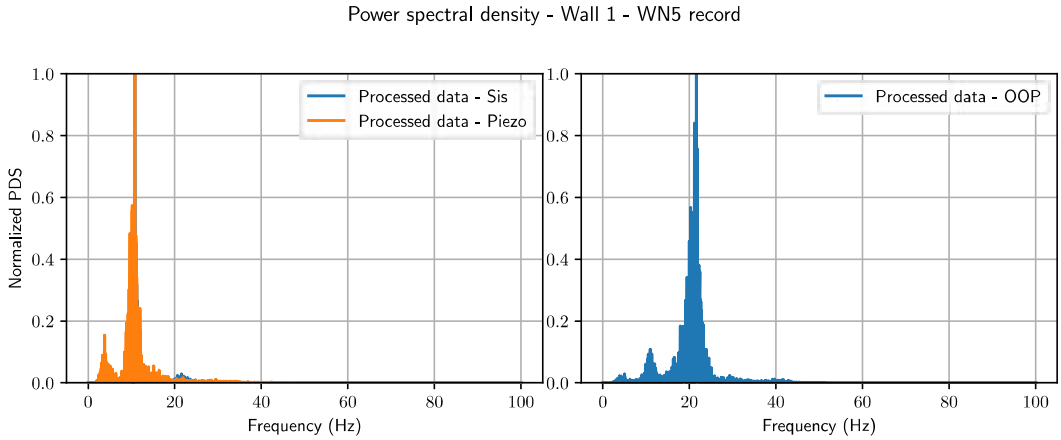

Figure 77: Power density spectra of wall 1 from $WN5$ record.

3 Data from instrumentation of Wall 2

3.1 Acceleration records

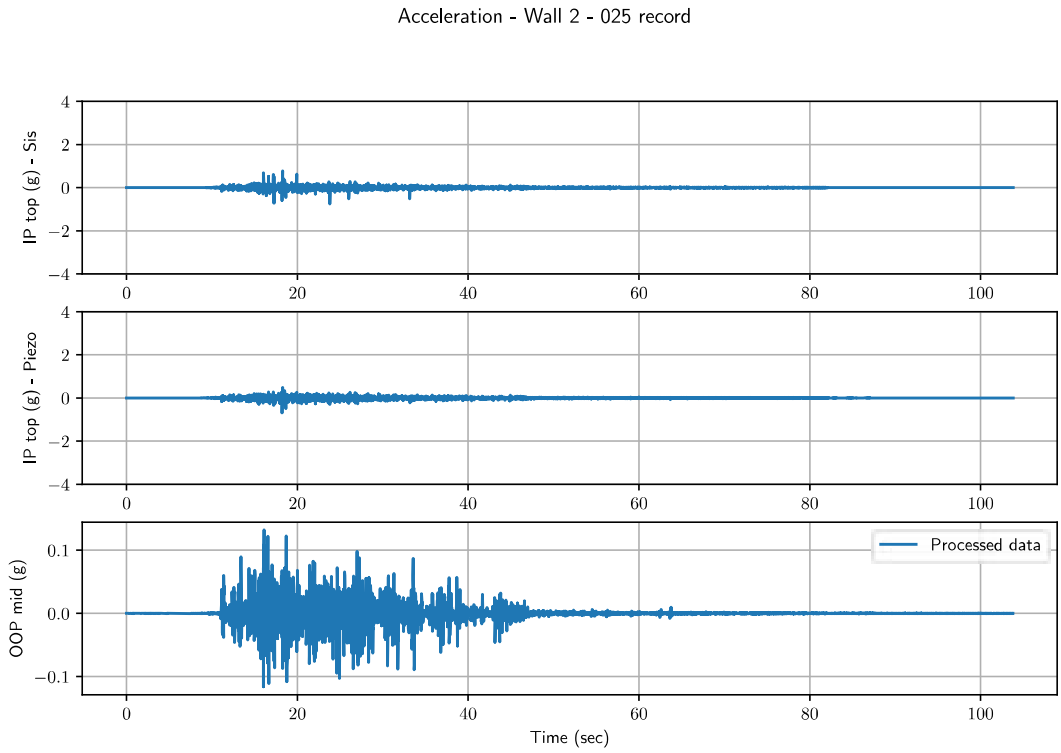

Figure 78: Acceleration records of wall 2 from 025 record.

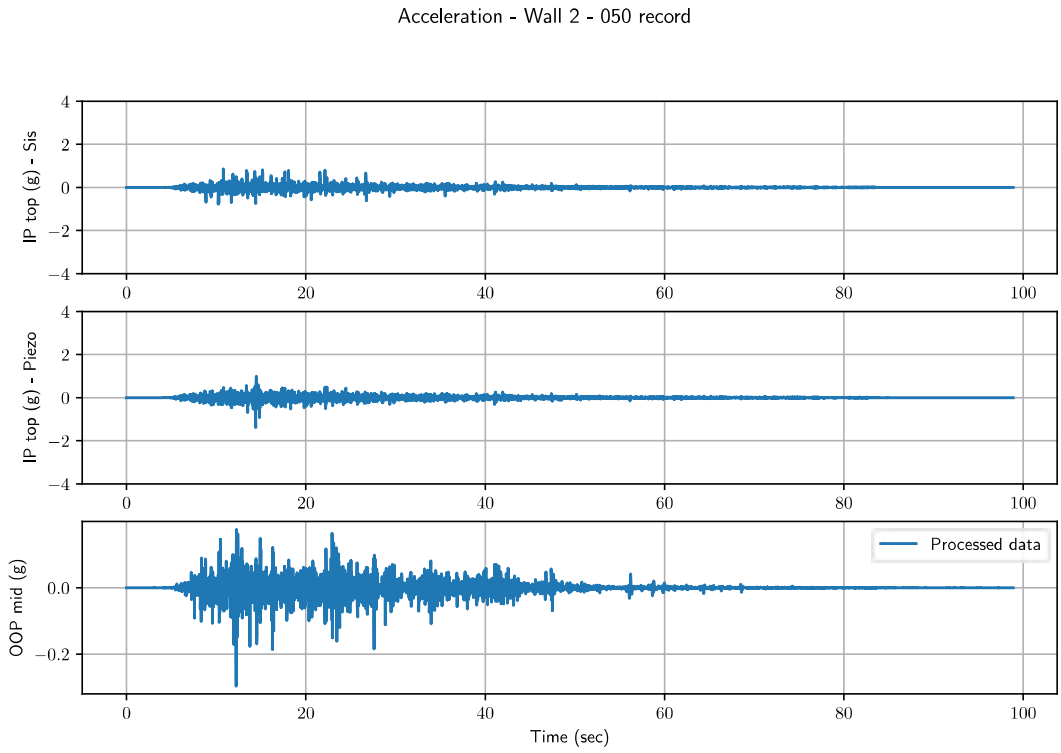

Figure 79: Acceleration records of wall 2 from 050 record.

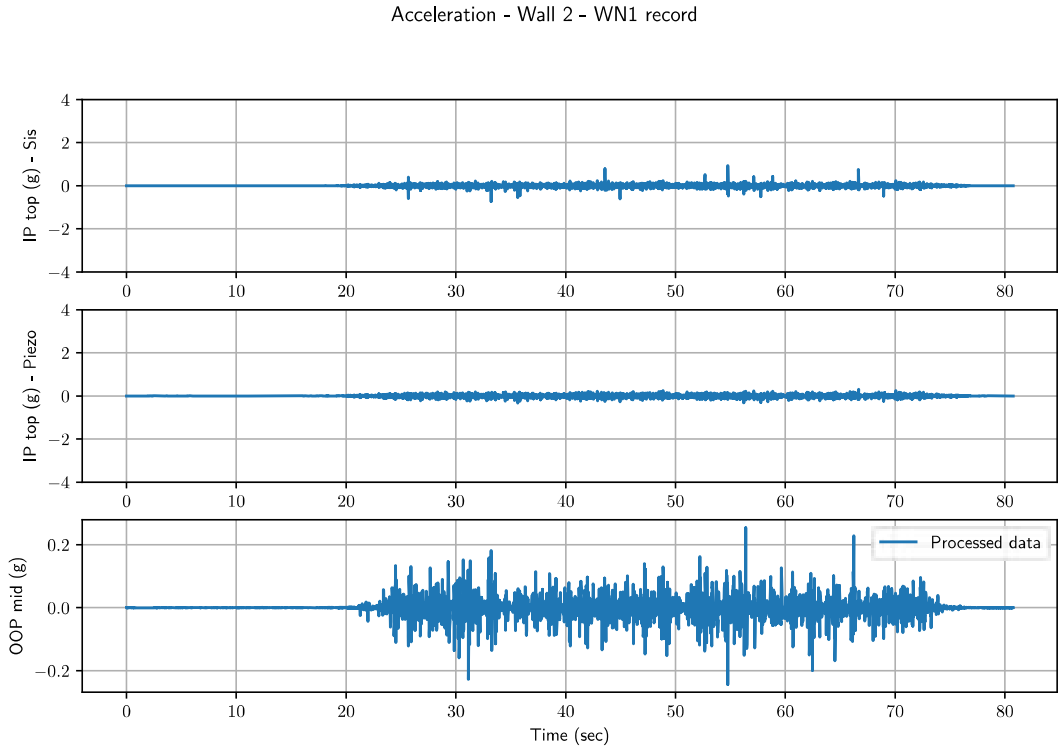

Figure 80: Acceleration records of wall 2 from $WN1$ record.

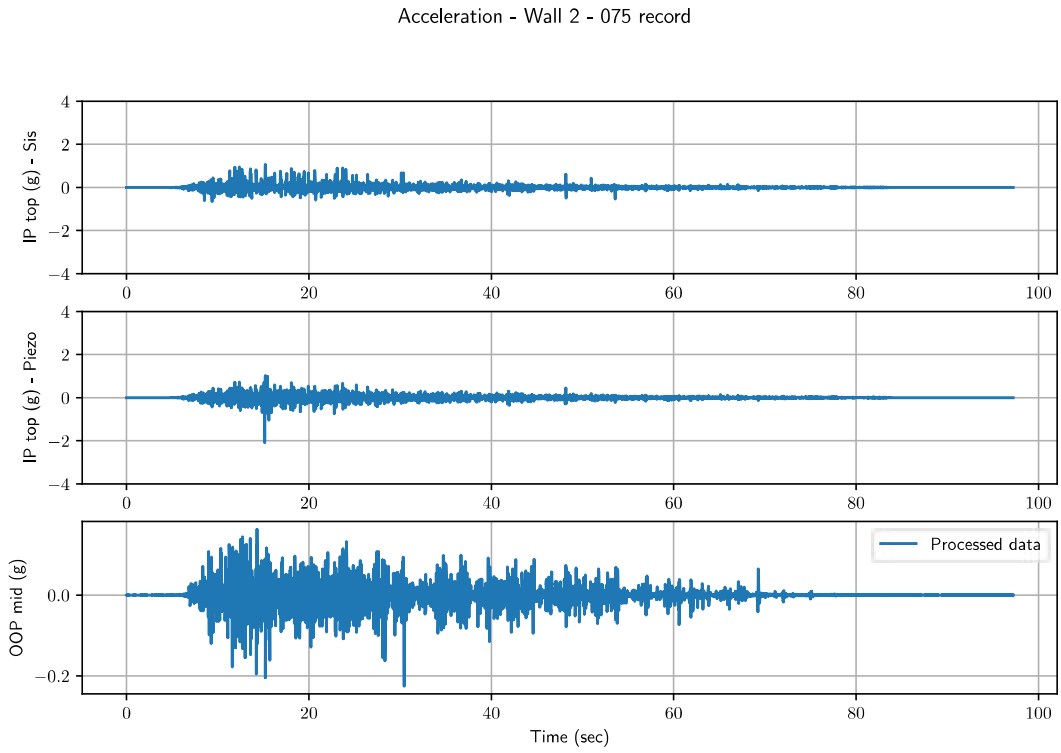

Figure 81: Acceleration records of wall 2 from 075 record.

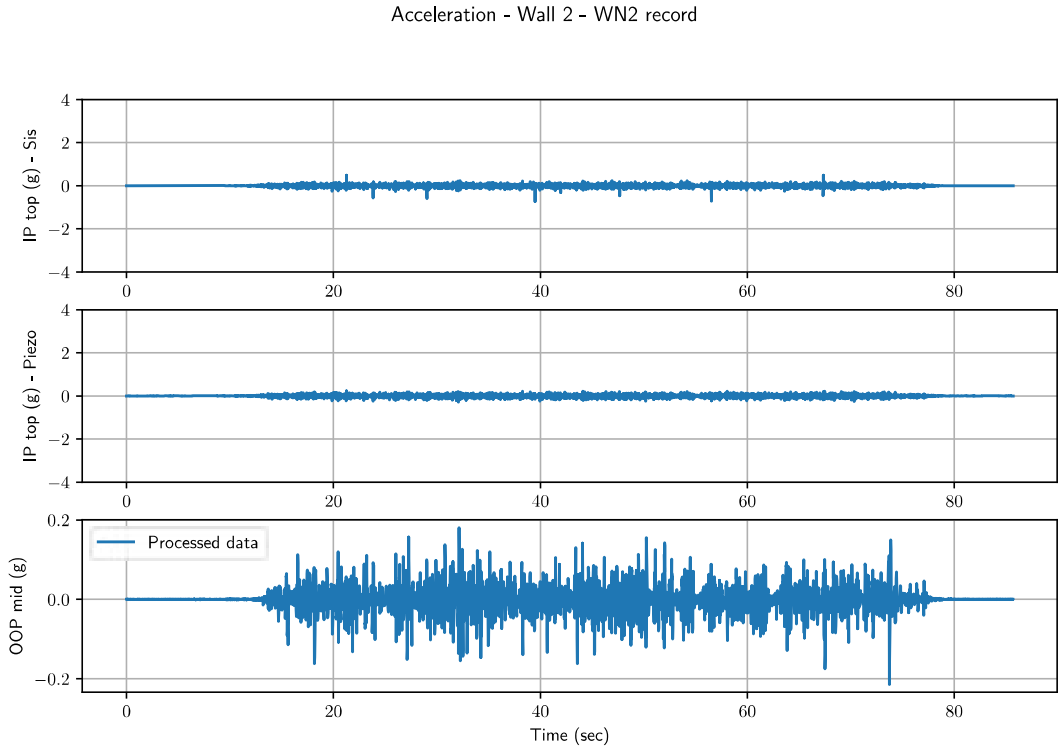

Figure 82: Acceleration records of wall 2 from $WN2$ record.

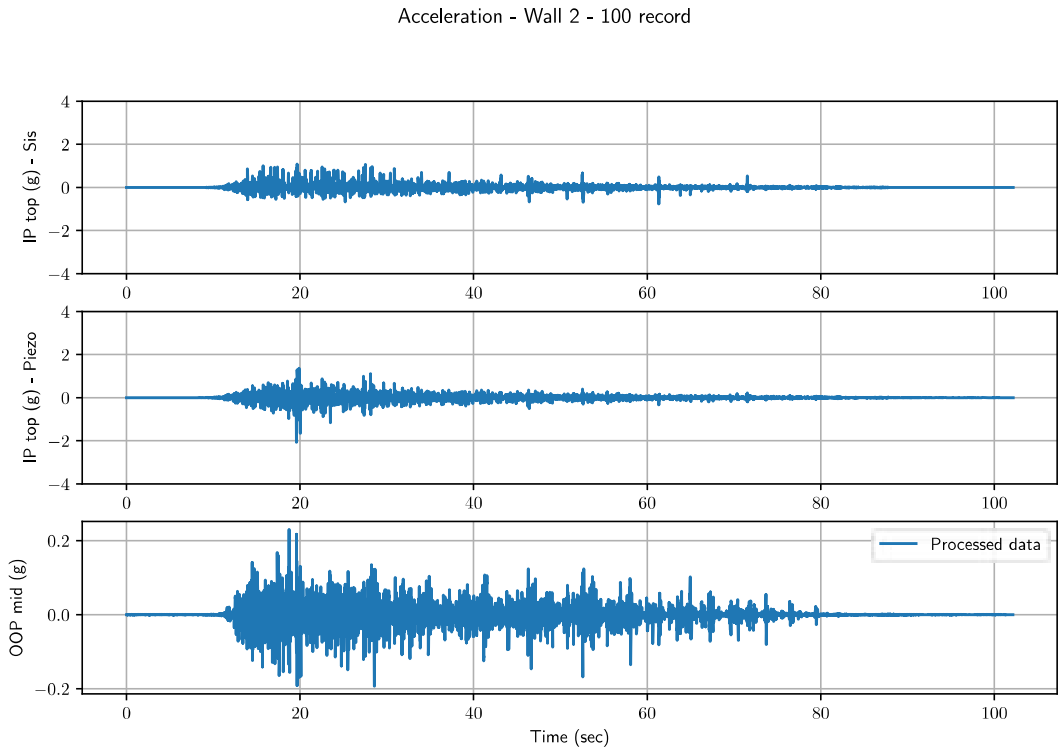

Figure 83: Acceleration records of wall 2 from 100 record.

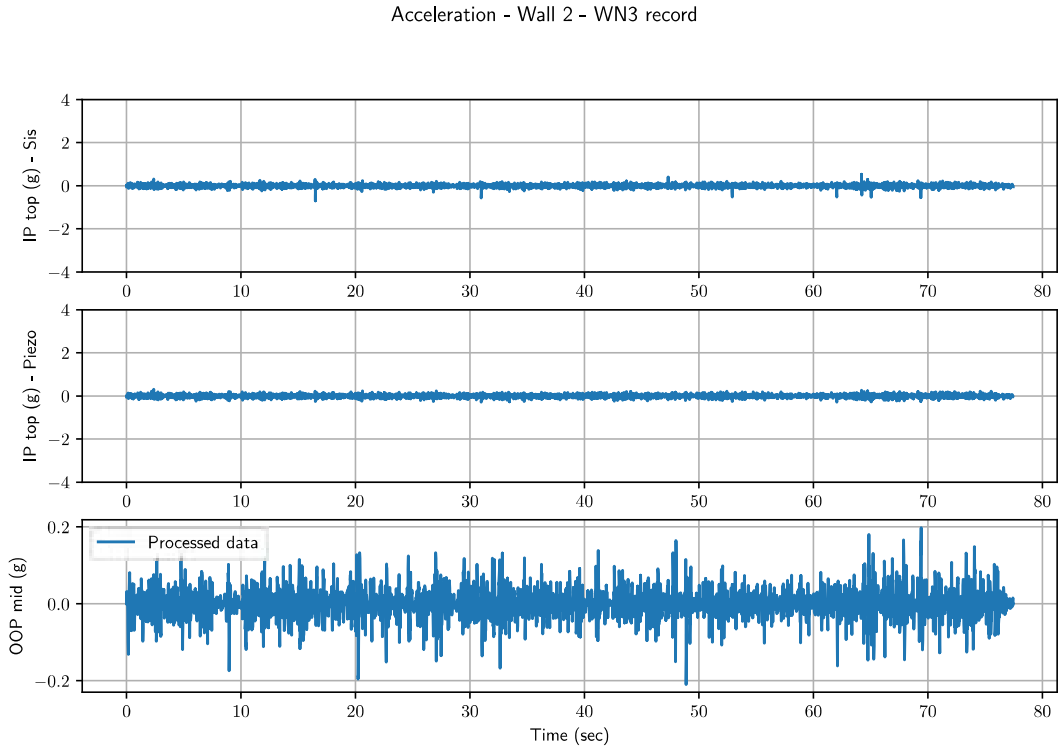

Figure 84: Acceleration records of wall 2 from $WN3$ record.

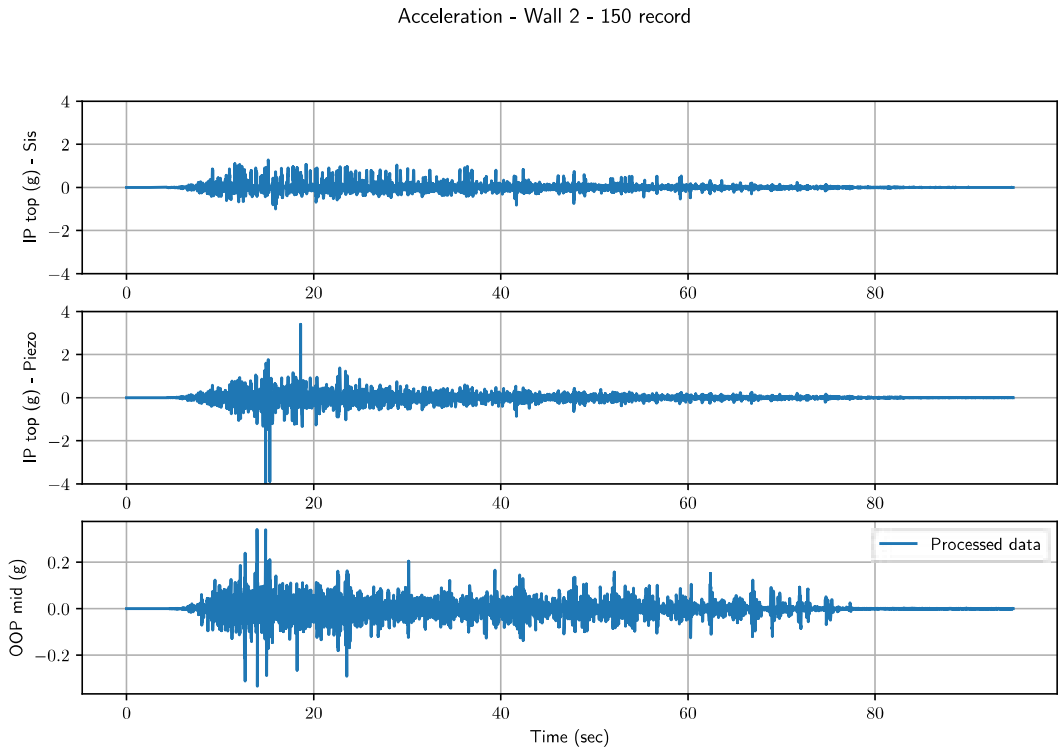

Figure 85: Acceleration records of wall 2 from 150 record.

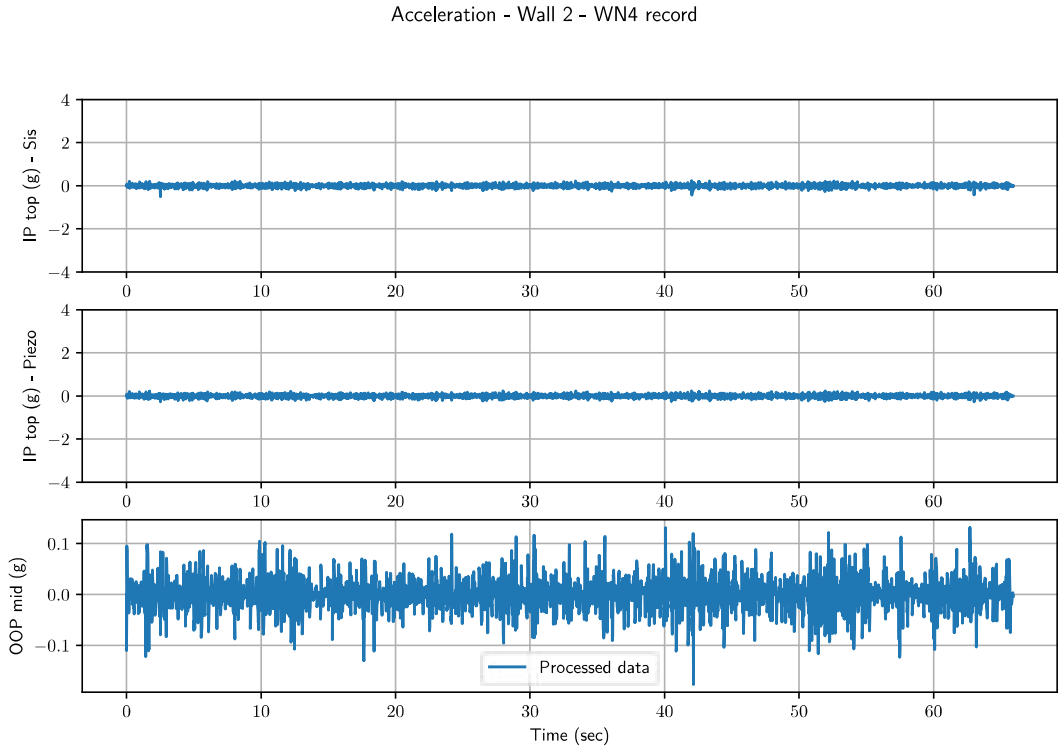

Figure 86: Acceleration records of wall 2 from $WN4$ record.

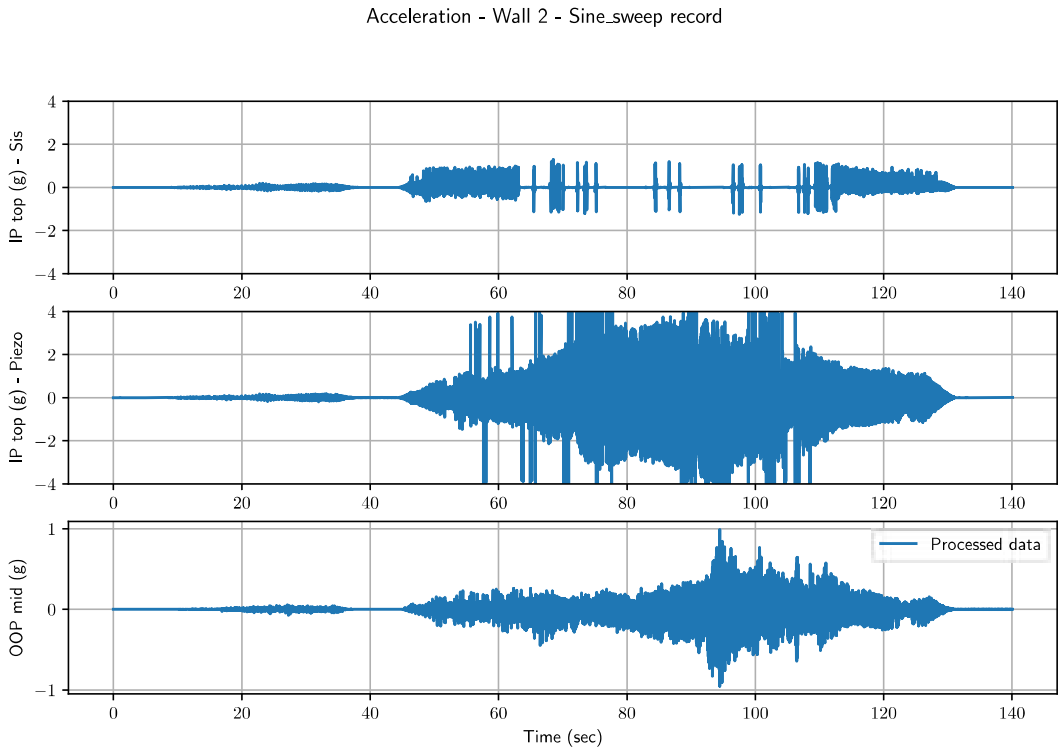

Figure 87: Acceleration records of wall 2 from $Sine_sweep$ record.

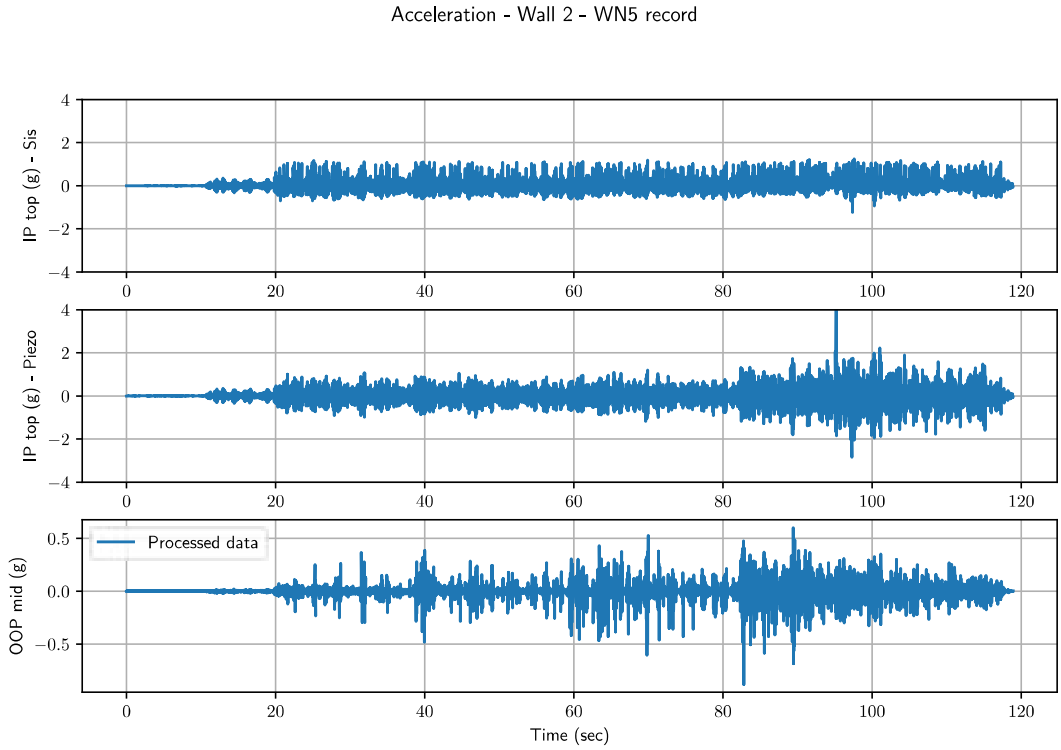

Figure 88: Acceleration records of wall 2 from $WN5$ record.

3.2 Displacement records

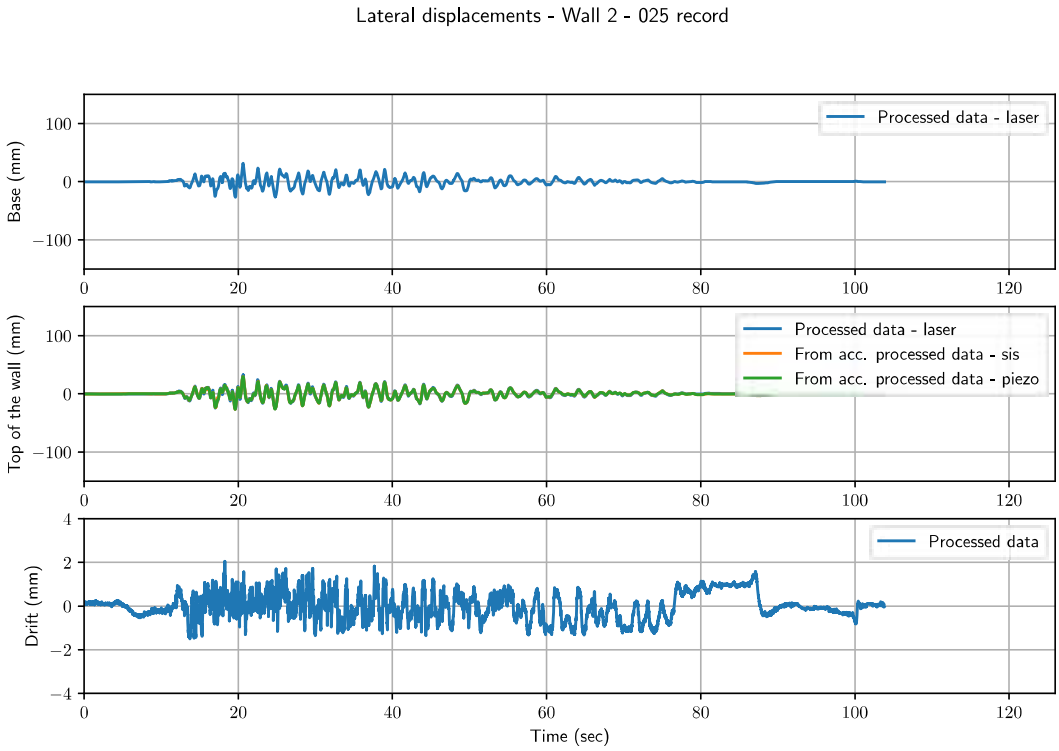

Figure 89: Acceleration records of wall 2 from 025 record.

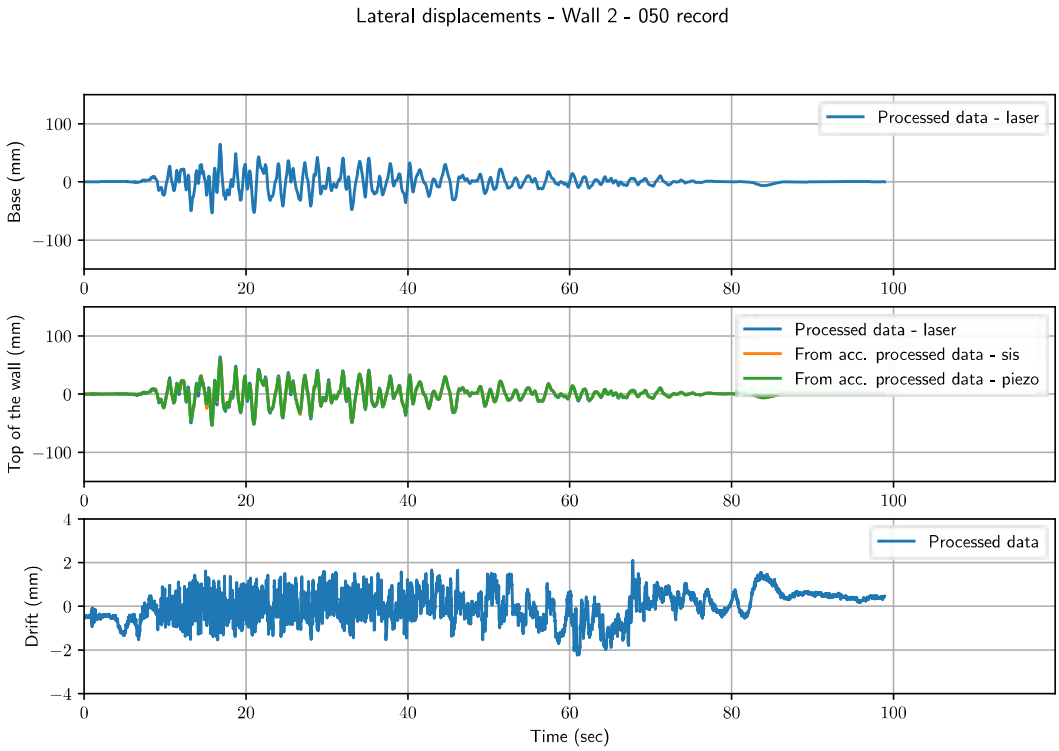

Figure 90: Acceleration records of wall 2 from 050 record.

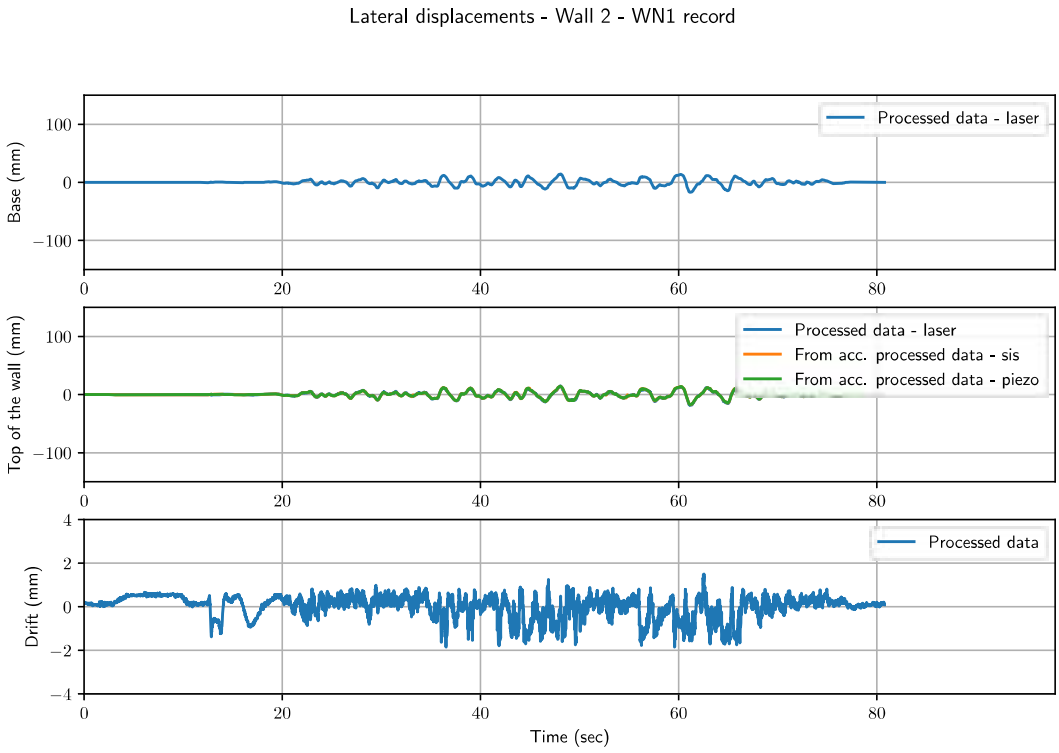

Figure 91: Acceleration records of wall 2 from $WN1$ record.

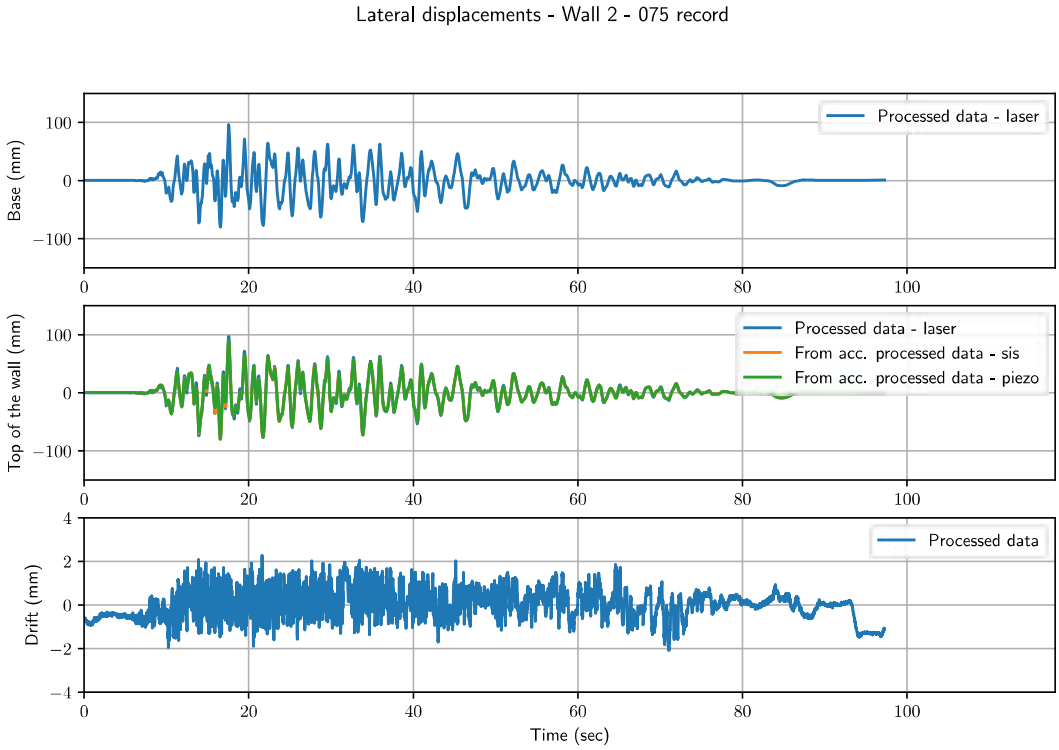

Figure 92: Acceleration records of wall 2 from 075 record.

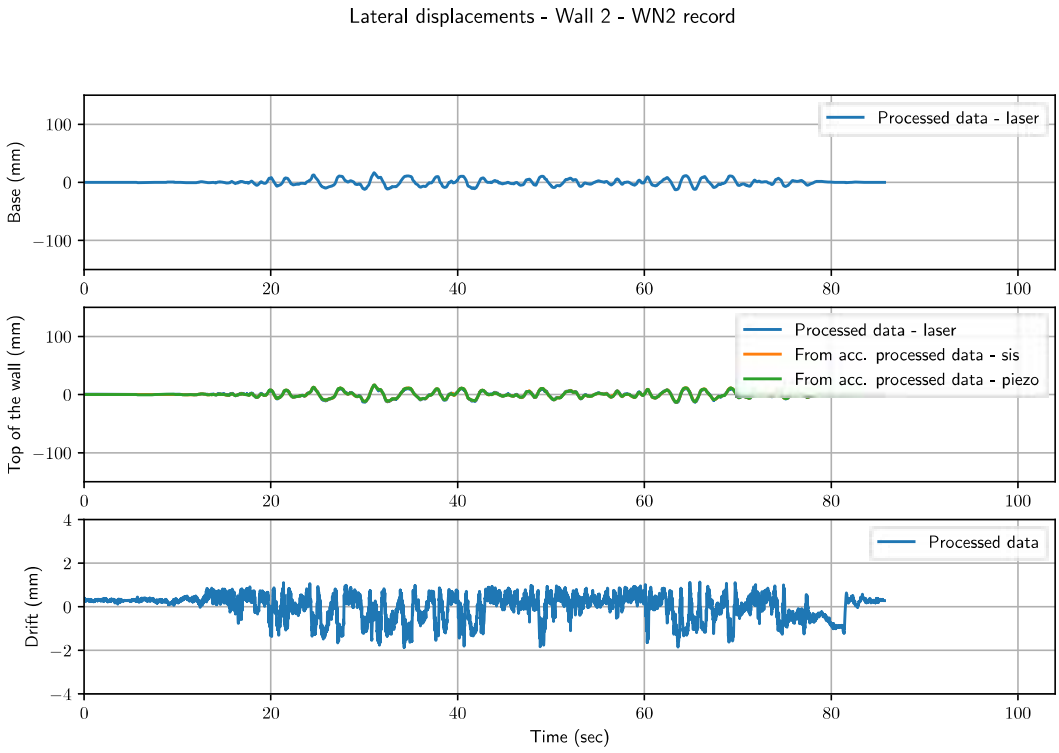

Figure 93: Acceleration records of wall 2 from $WN2$ record.

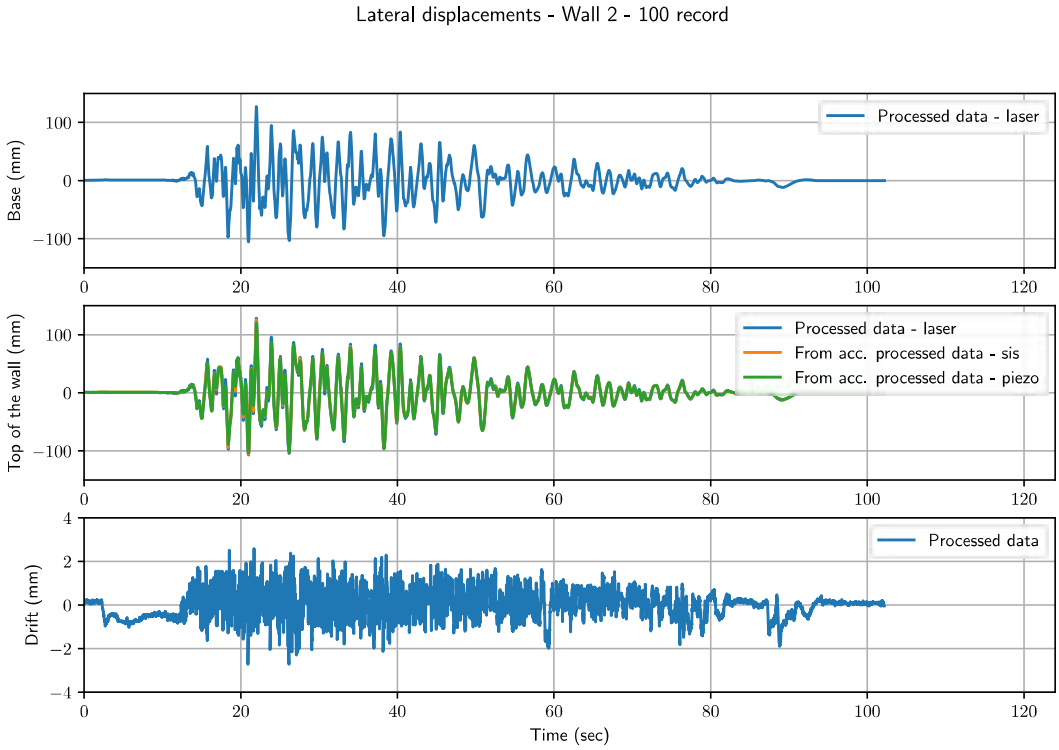

Figure 94: Acceleration records of wall 2 from 100 record.

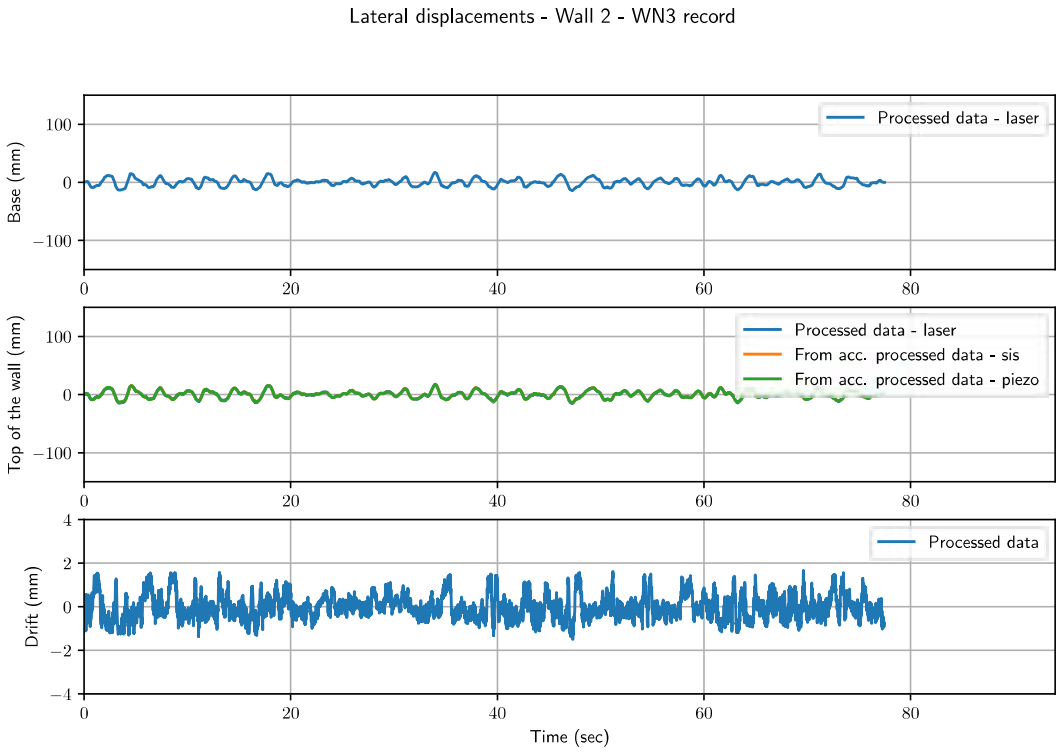

Figure 95: Acceleration records of wall 2 from $WN3$ record.

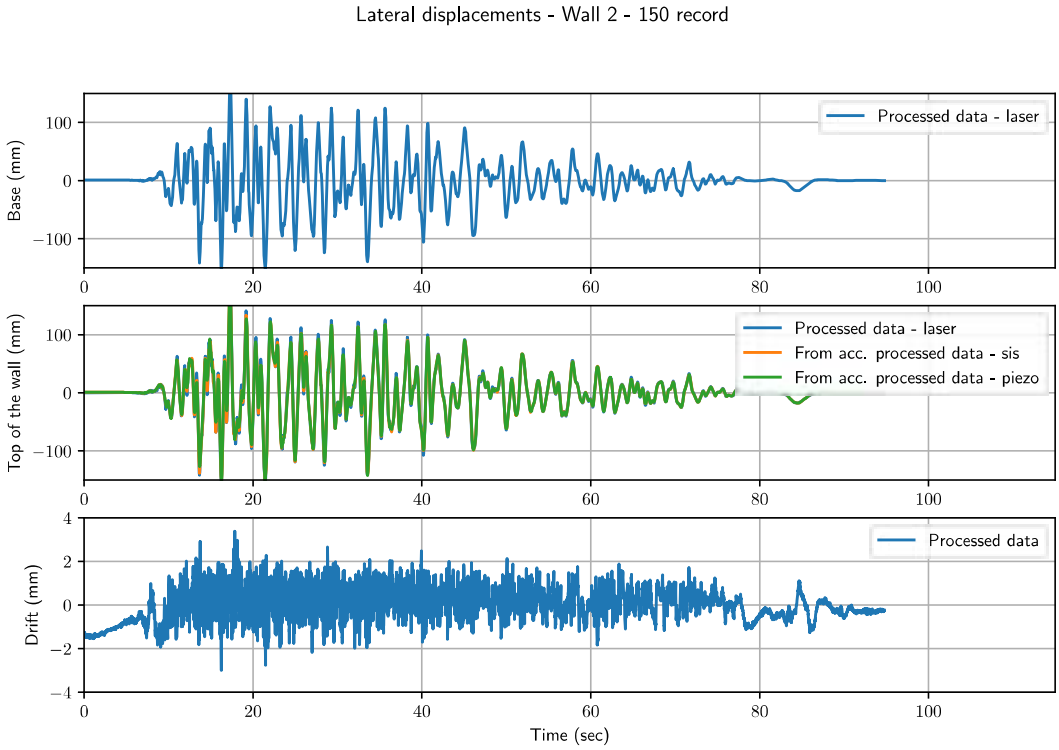

Figure 96: Acceleration records of wall 2 from 150 record.

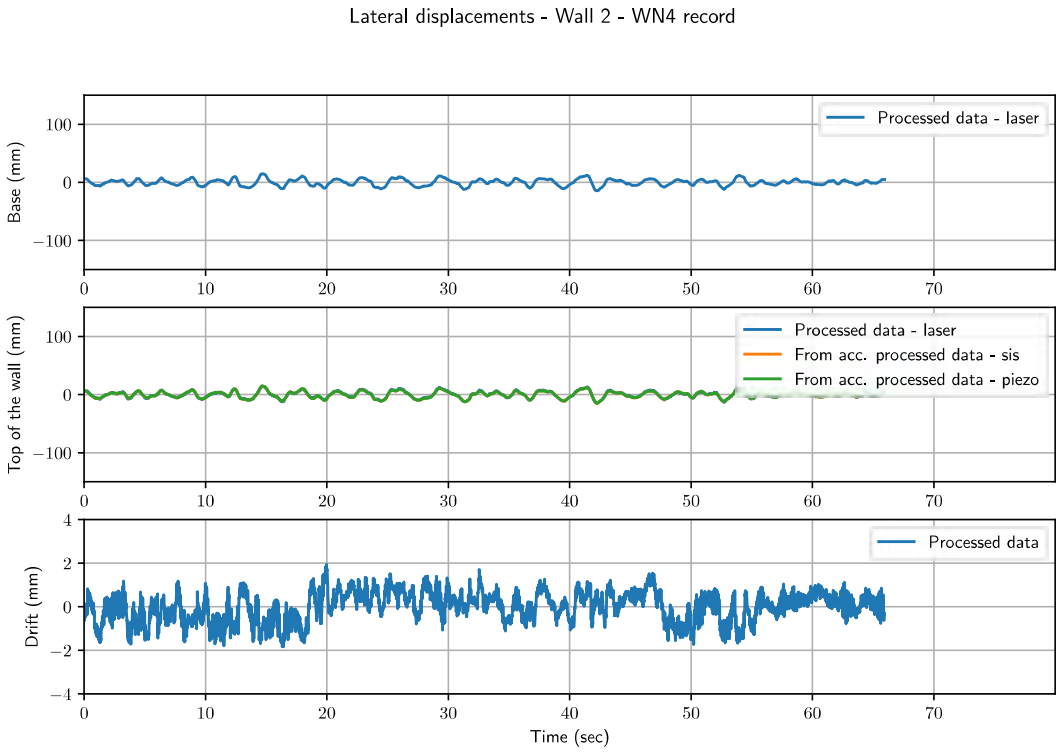

Figure 97: Acceleration records of wall 2 from $WN4$ record.

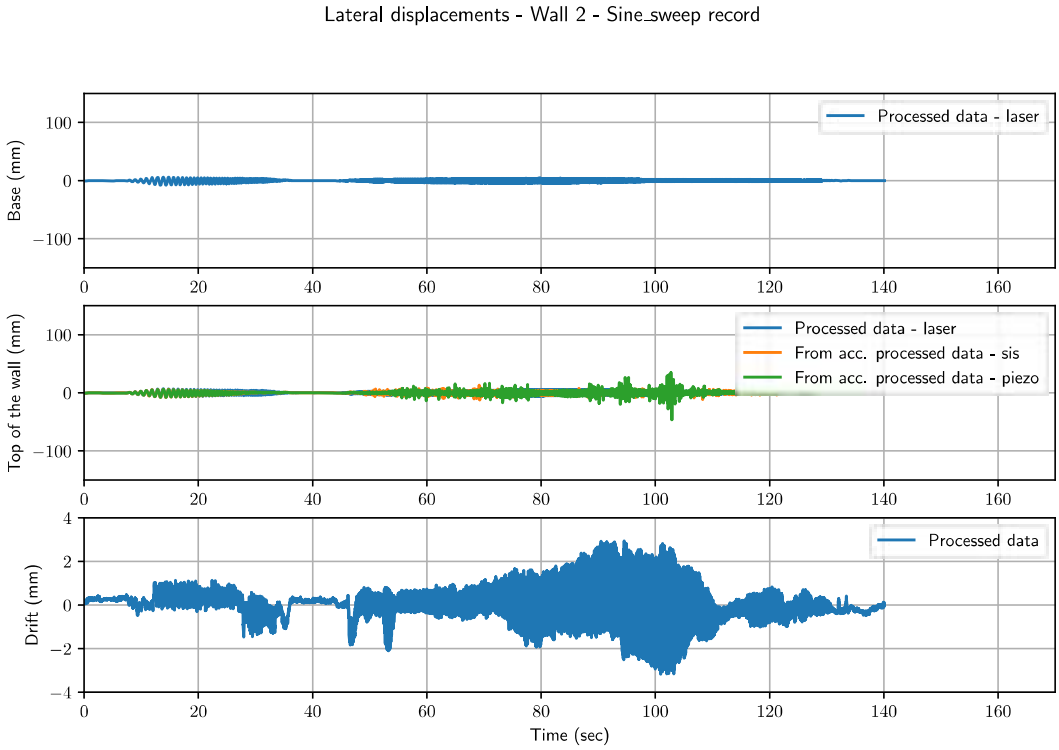

Figure 98: Acceleration records of wall 2 from $Sine_sweep$ record.

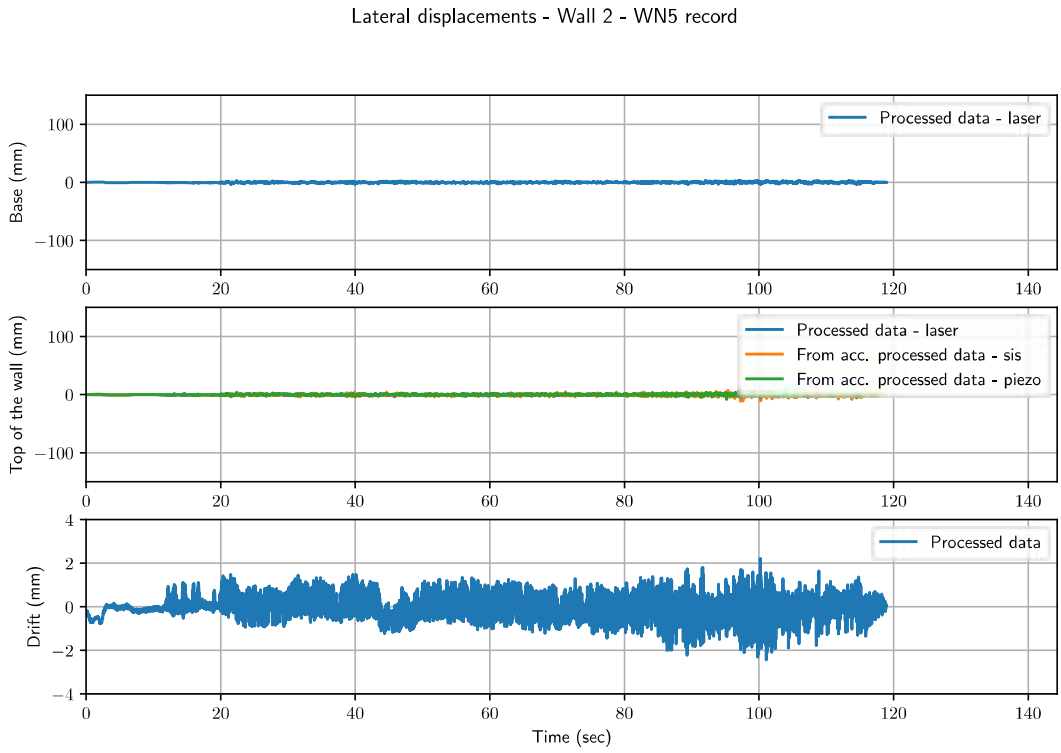

Figure 99: Acceleration records of wall 2 from $WN5$ record.

3.3 Fourier analysis results from acceleration records

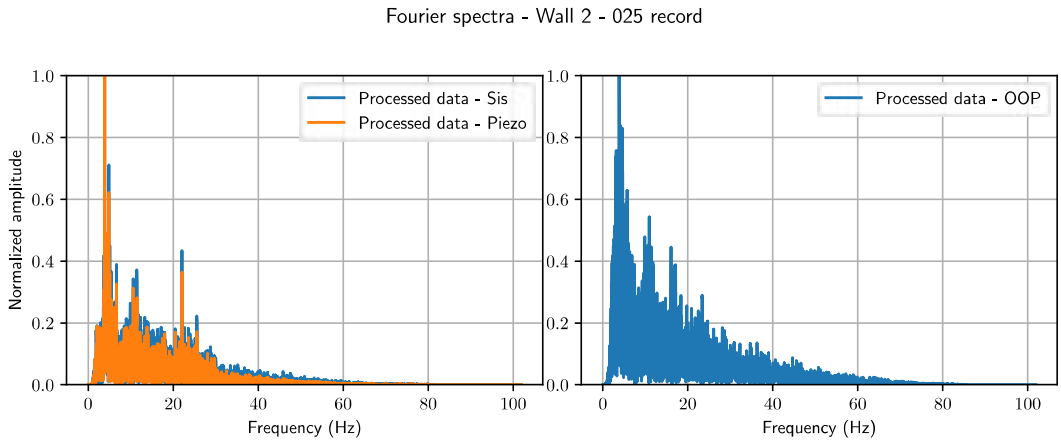

Figure 100: Fourier transformation of wall 2 from 025 record.

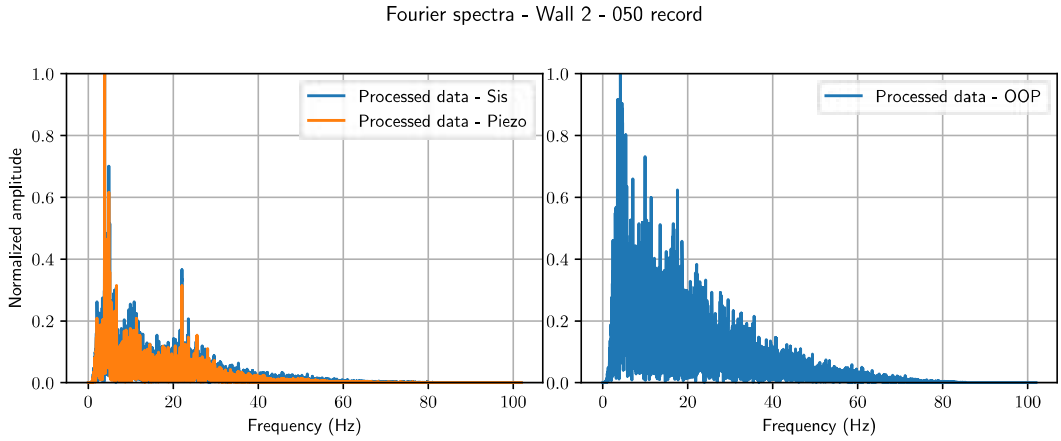

Figure 101: Fourier transformation of wall 2 from 050 record.

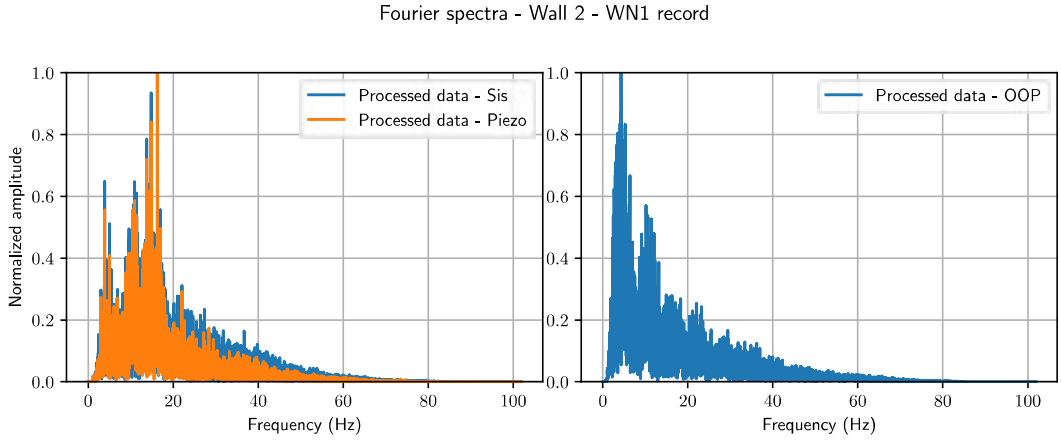

Figure 102: Fourier transformation of wall 2 from $WN1$ record.

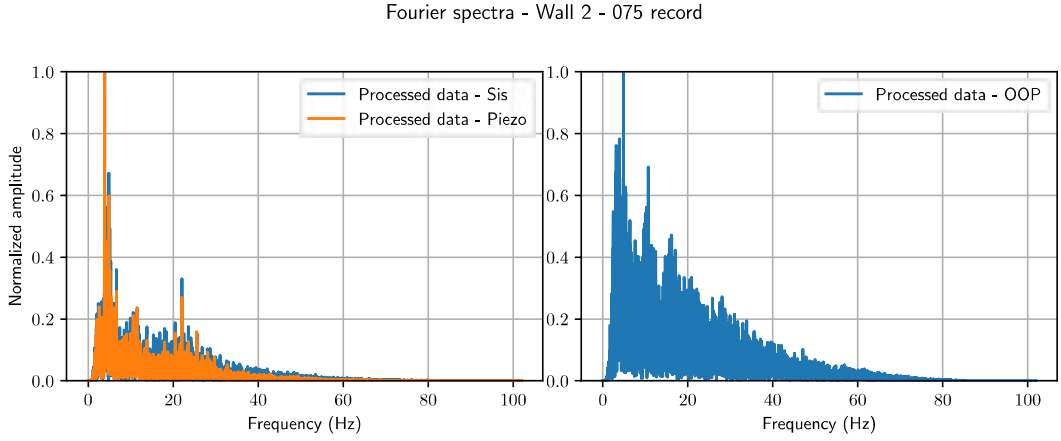

Figure 103: Fourier transformation of wall 2 from 075 record.

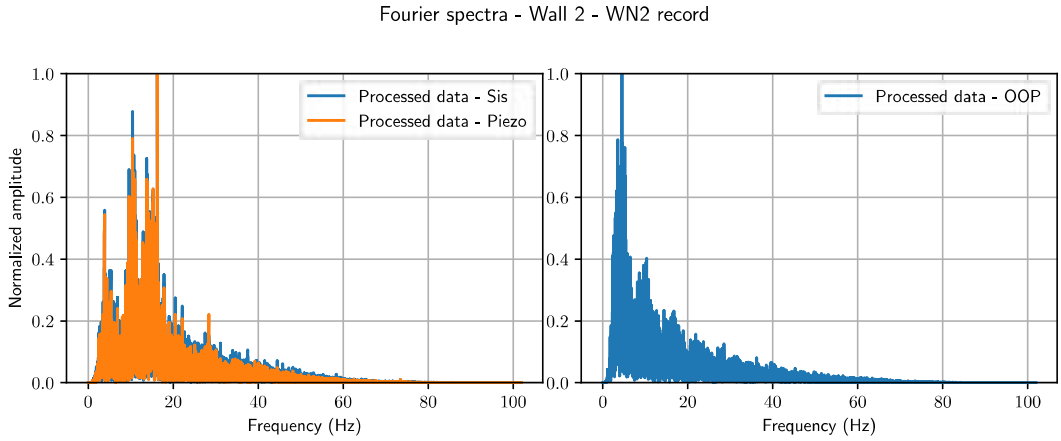

Figure 104: Fourier transformation of wall 2 from $WN2$ record.

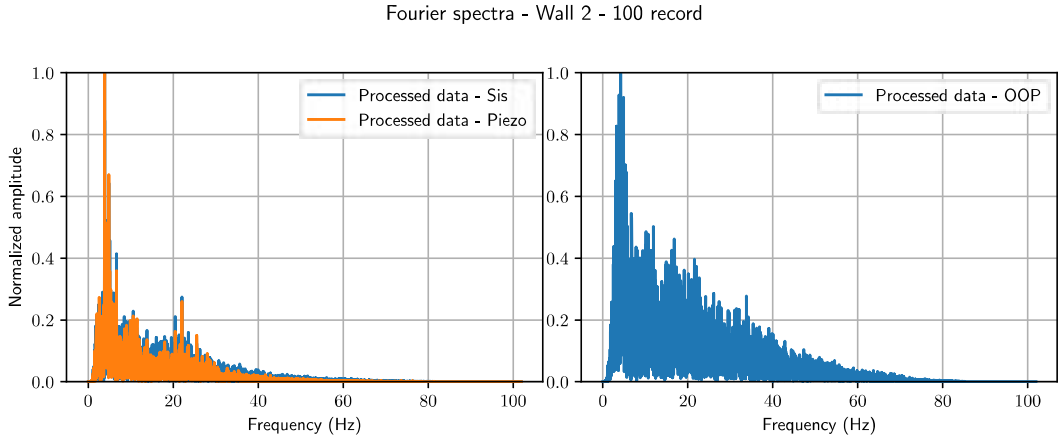

Figure 105: Fourier transformation of wall 2 from 100 record.

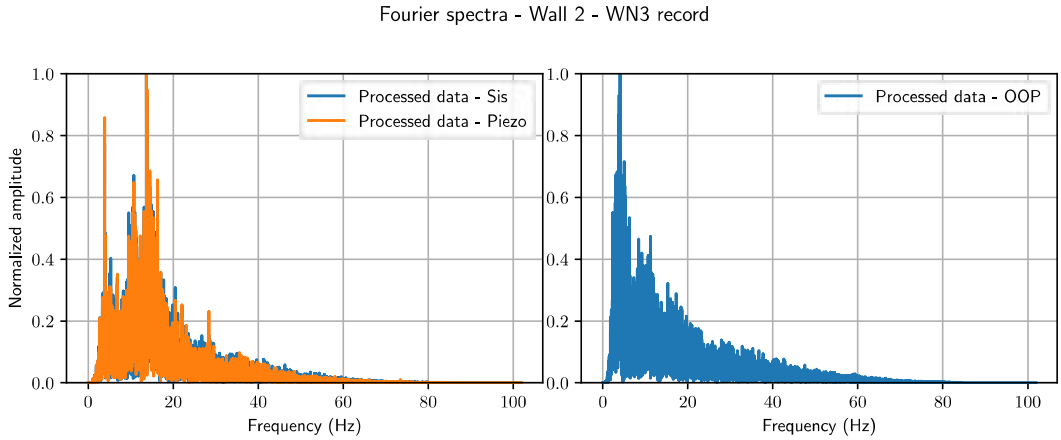

Figure 106: Fourier transformation of wall 2 from $WN3$ record.

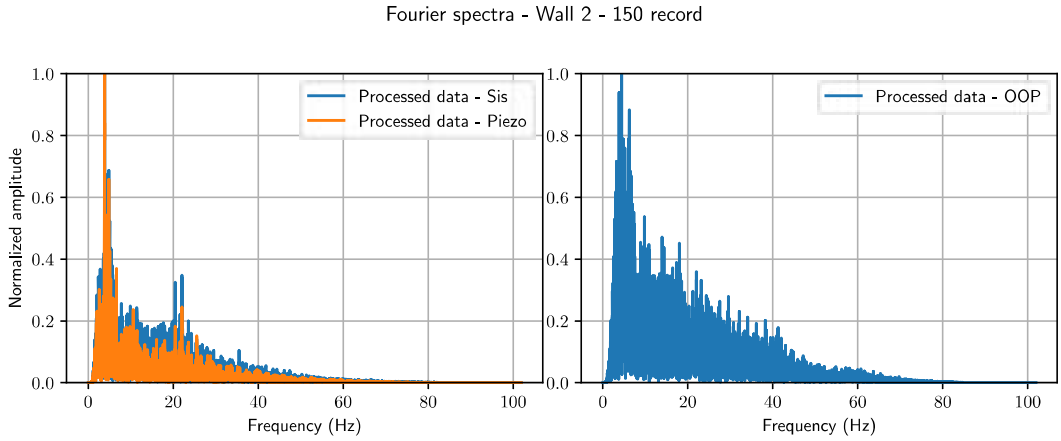

Figure 107: Fourier transformation of wall 2 from 150 record.

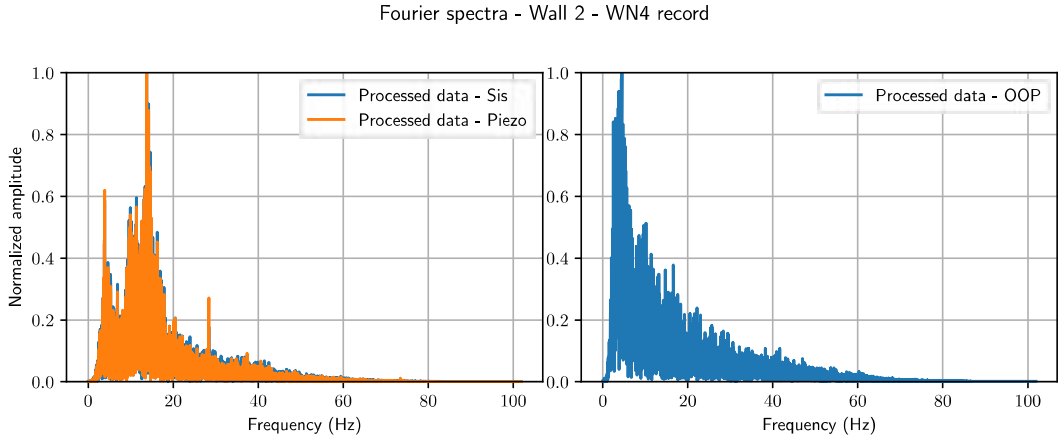

Figure 108: Fourier transformation of wall 2 from $WN4$ record.

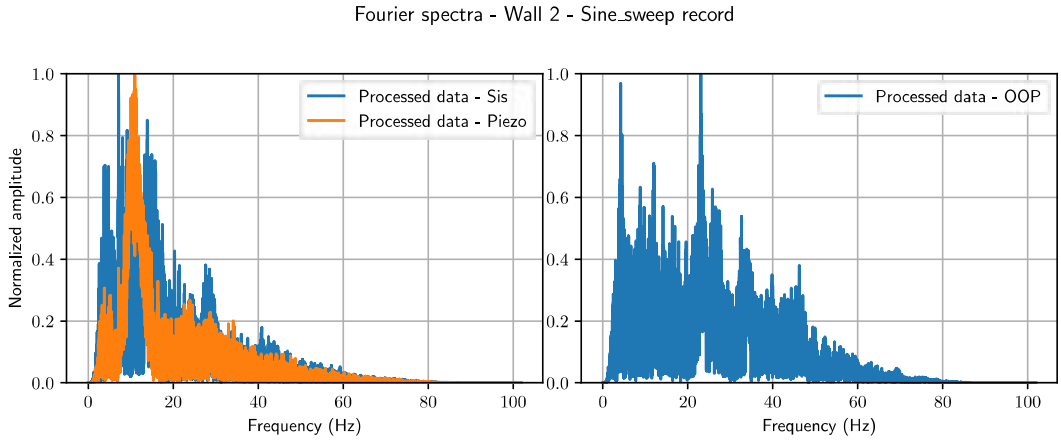

Figure 109: Fourier transformation of wall 2 from $Sine_sweep$ record.

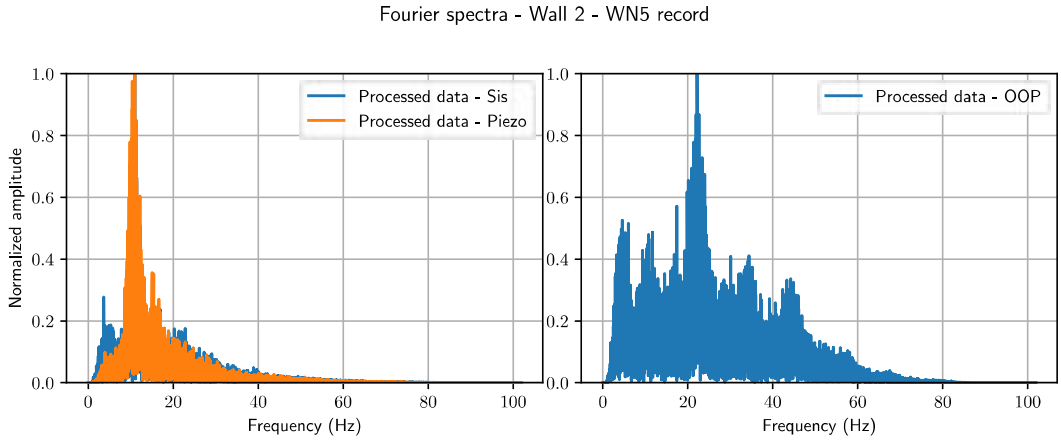

Figure 110: Fourier transformation of wall 2 from $WN5$ record.

3.4 Power density spectra (PDS) from acceleration records

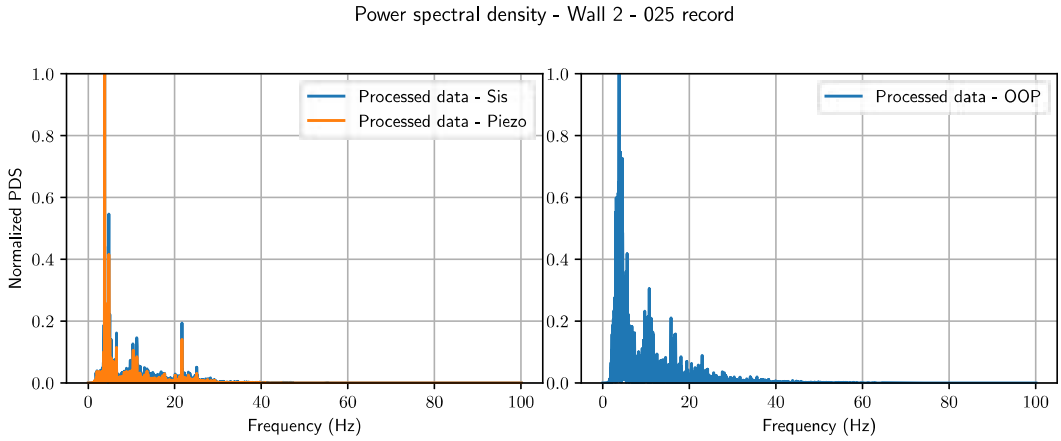

Figure 111: Power density spectra of wall 2 from 025 record.

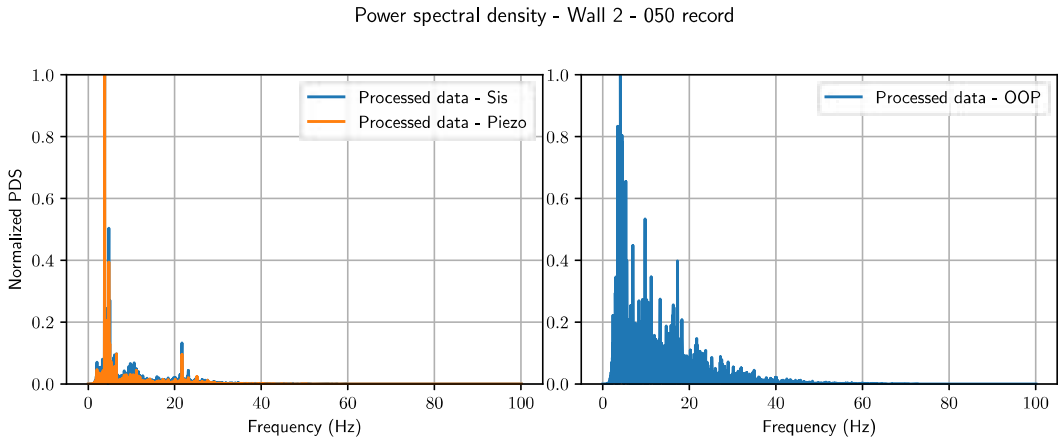

Figure 112: Power density spectra of wall 2 from 050 record.

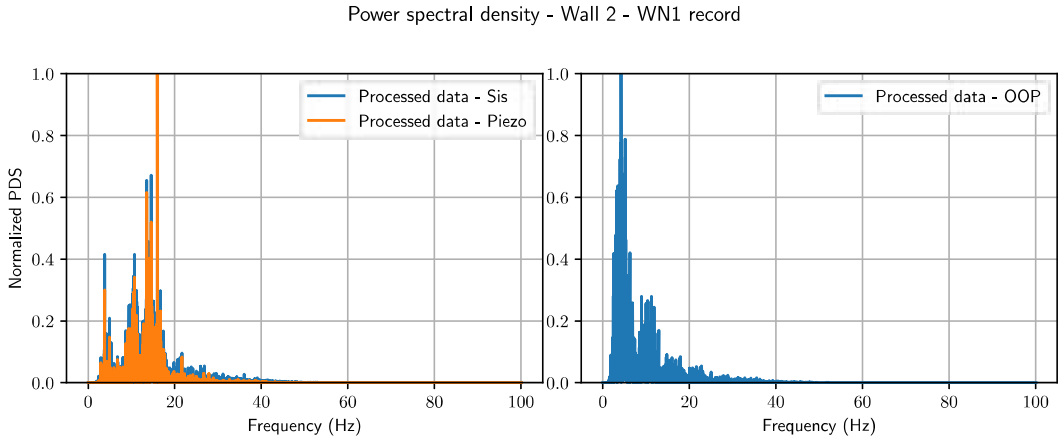

Figure 113: Power density spectra of wall 2 from $WN1$ record.

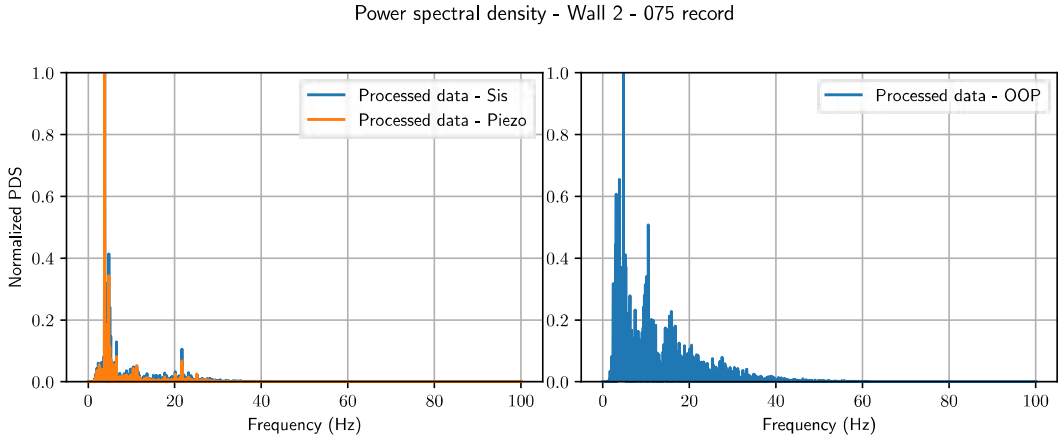

Figure 114: Power density spectra of wall 2 from 075 record.

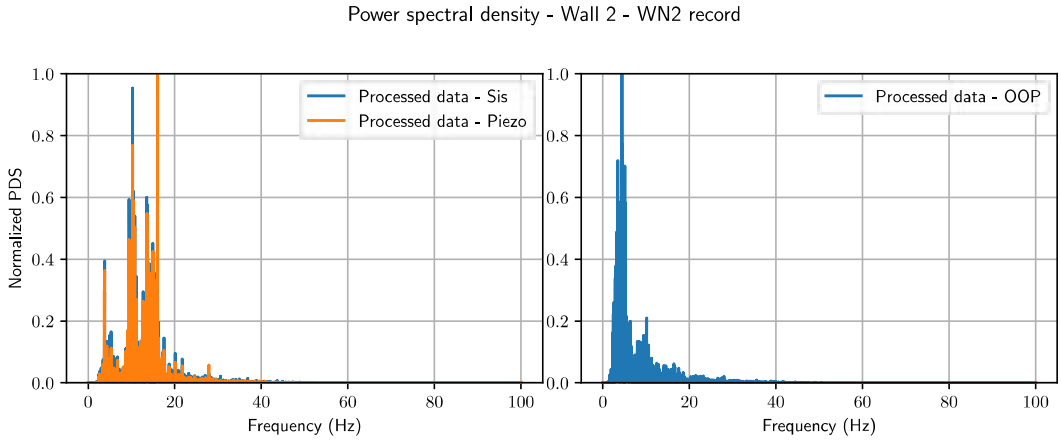

Figure 115: Power density spectra of wall 2 from $WN2$ record.

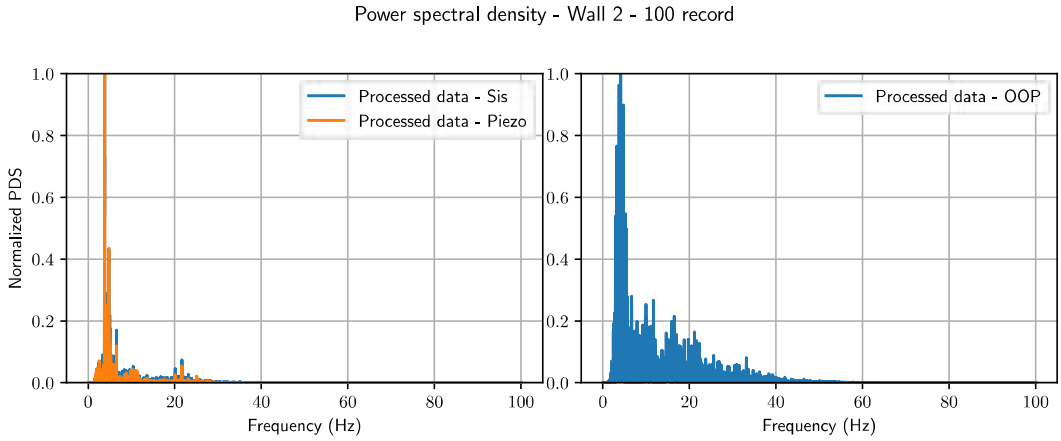

Figure 116: Power density spectra of wall 2 from 100 record.

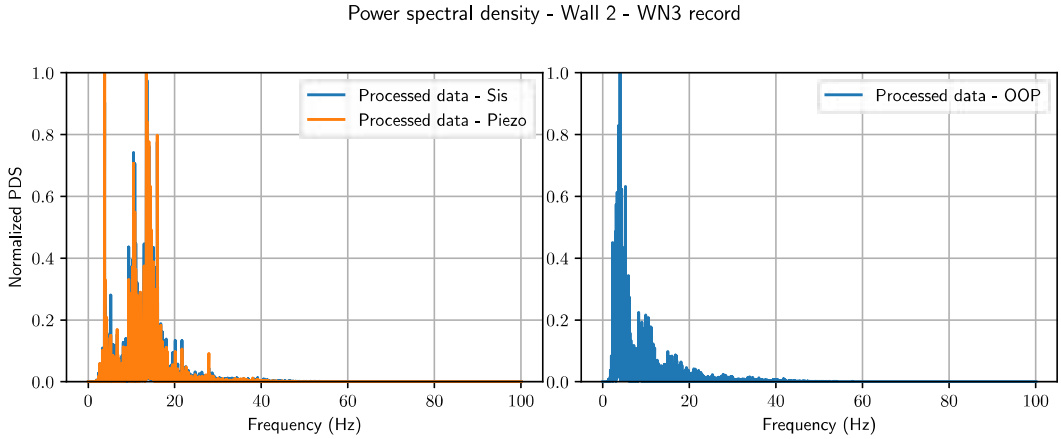

Figure 117: Power density spectra of wall 2 from $WN3$ record.

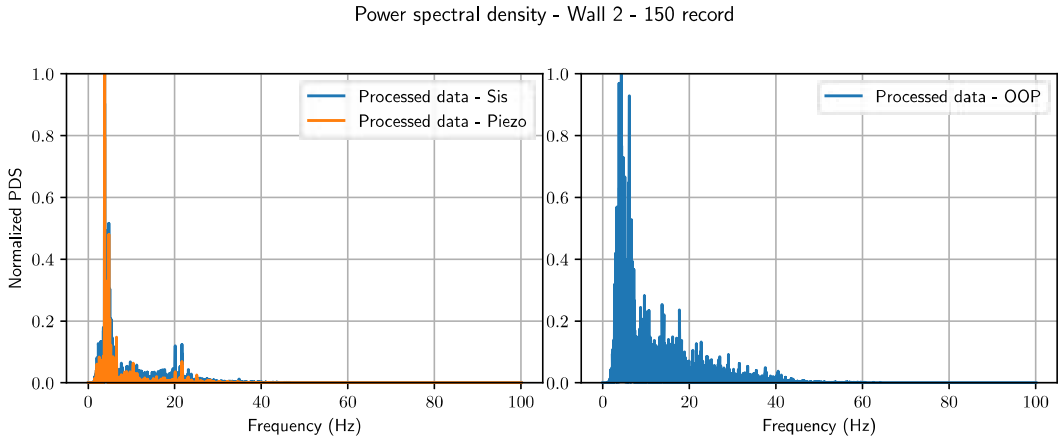

Figure 118: Power density spectra of wall 2 from 150 record.

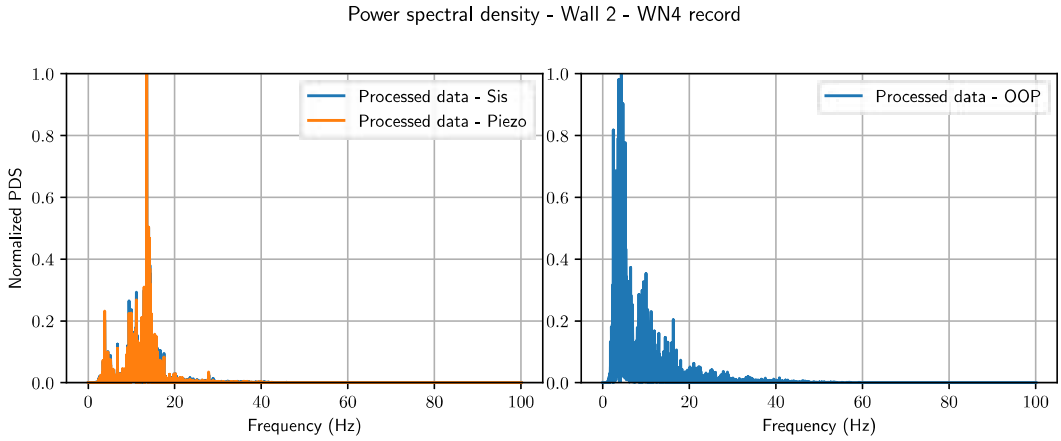

Figure 119: Power density spectra of wall 2 from $WN4$ record.

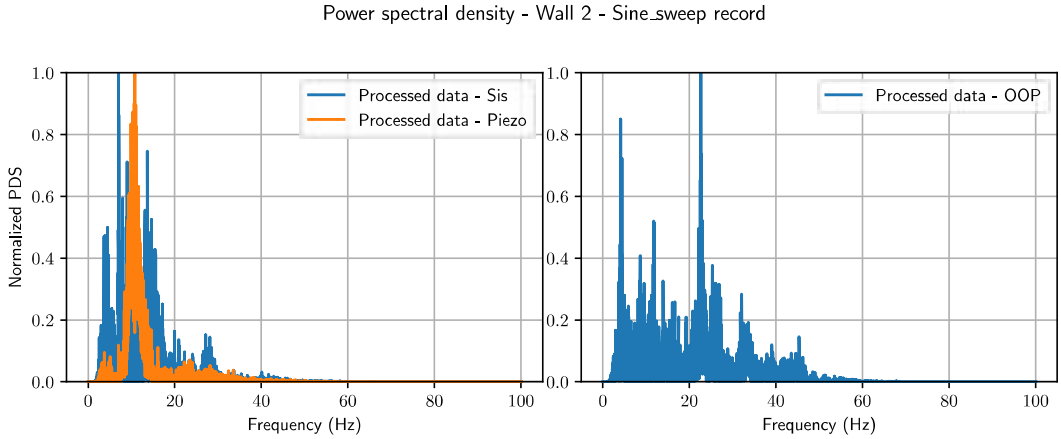

Figure 120: Power density spectra of wall 2 from $Sine_sweep$ record.

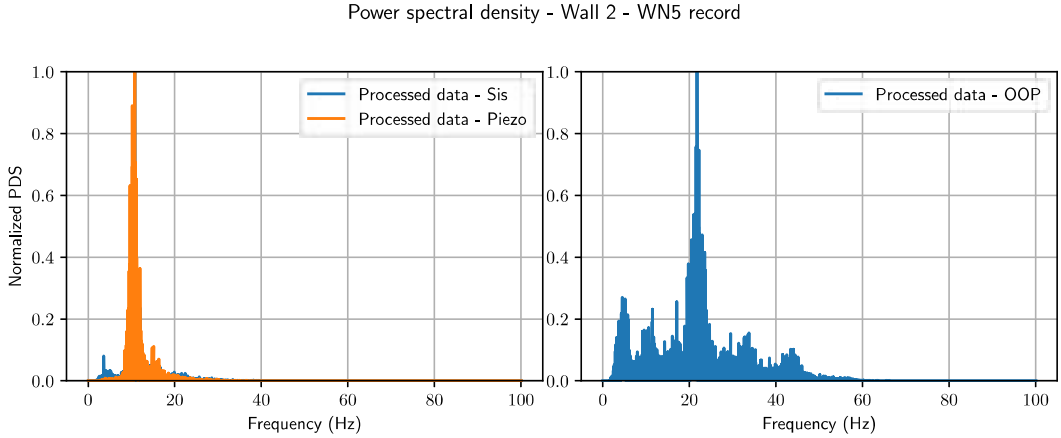

Figure 121: Power density spectra of wall 2 from $WN5$ record.

4 Data from instrumentation of Wall 3

4.1 Acceleration records

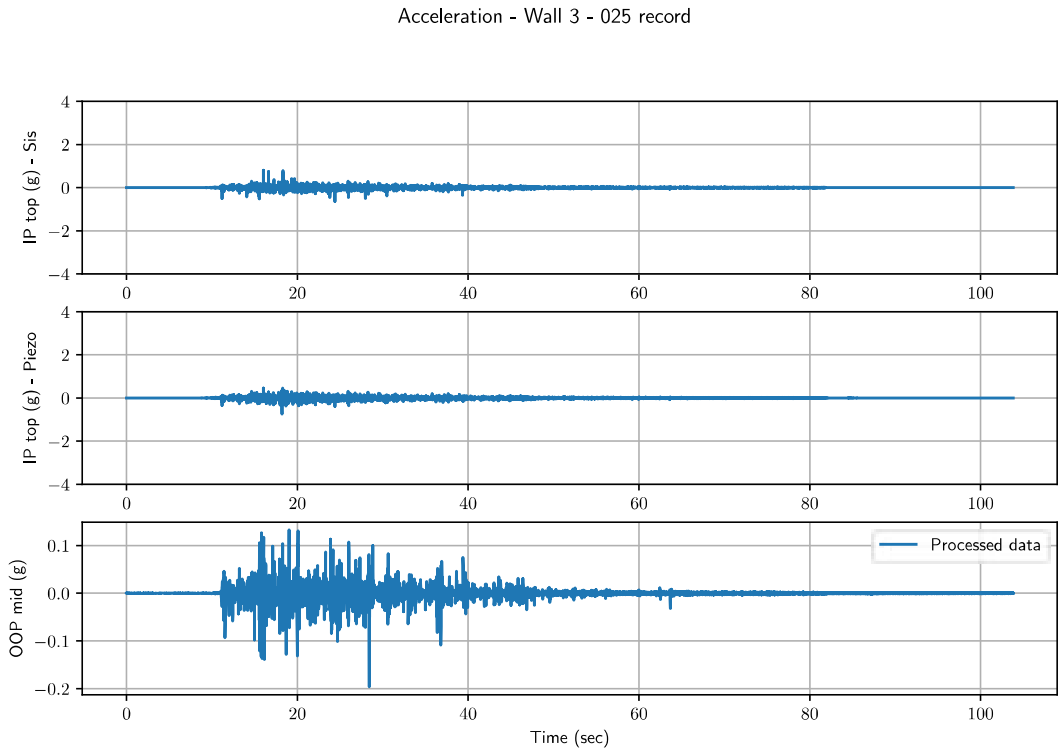

Figure 122: Acceleration records of wall 3 from 025 record.

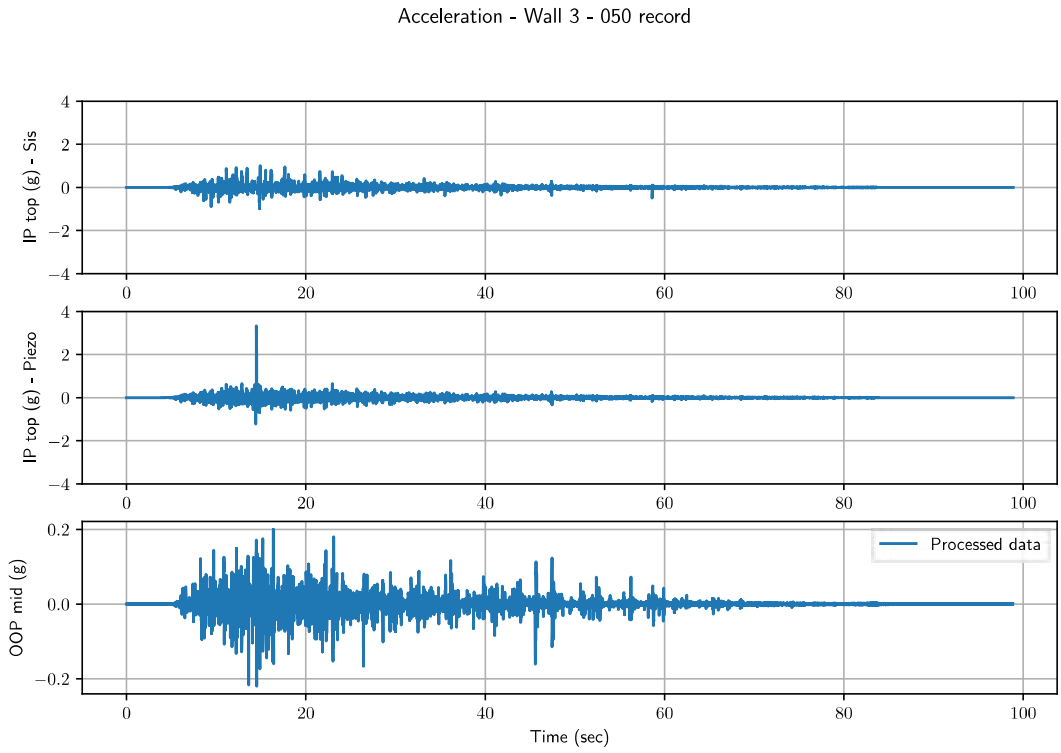

Figure 123: Acceleration records of wall 3 from 050 record.

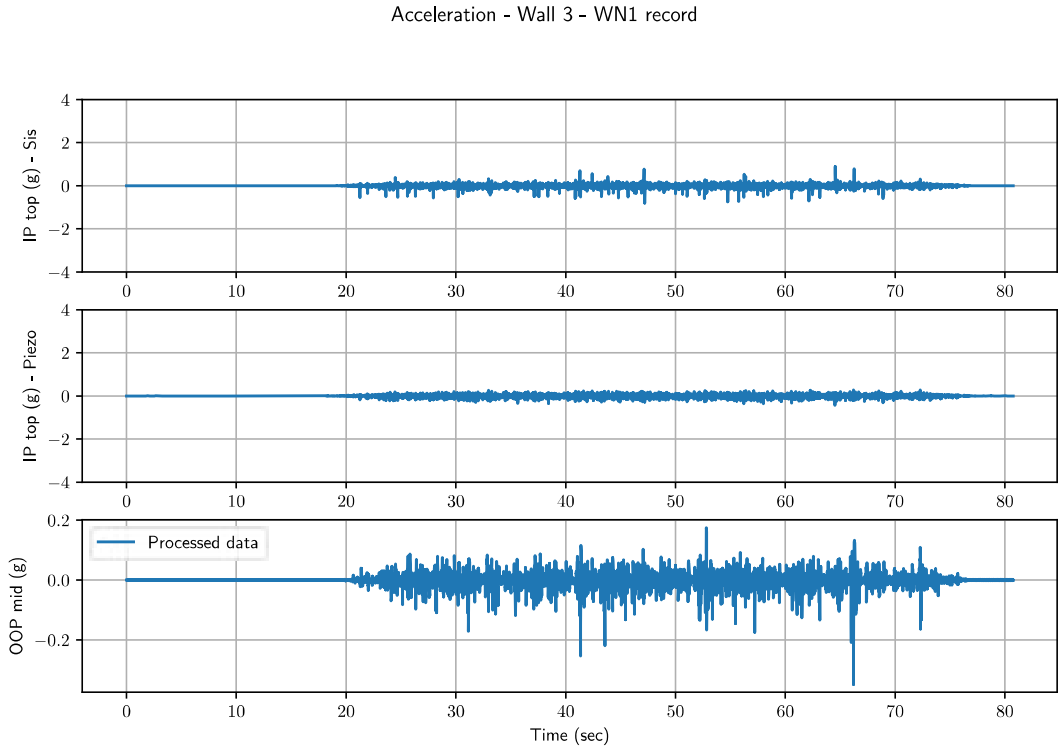

Figure 124: Acceleration records of wall 3 from $WN1$ record.

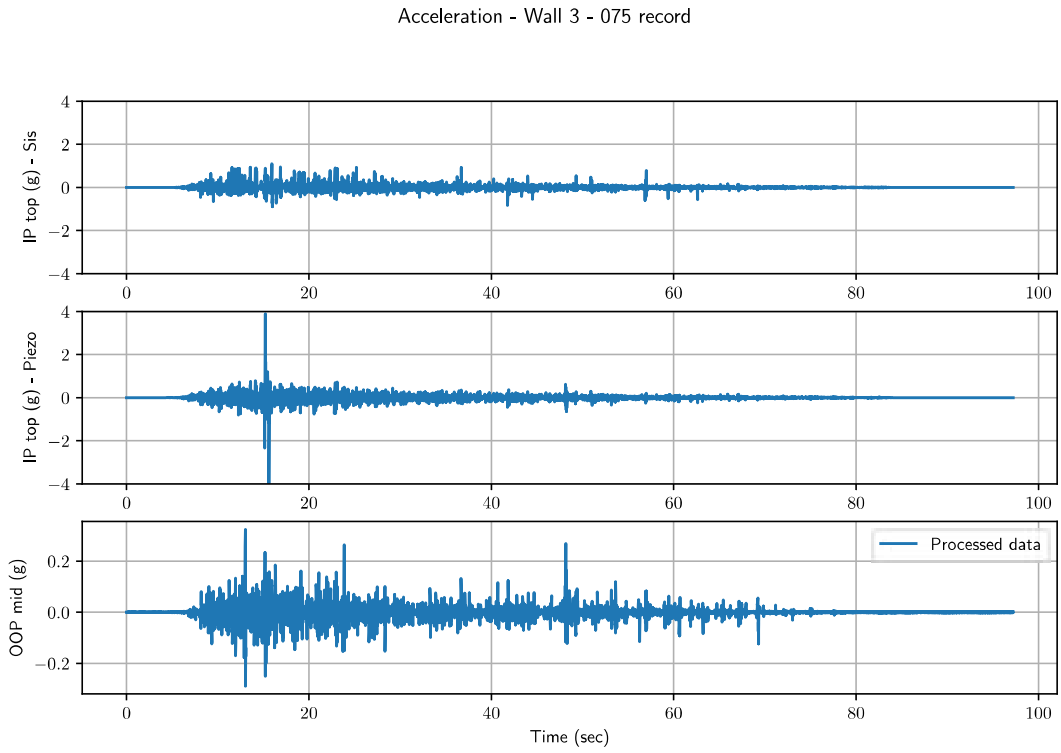

Figure 125: Acceleration records of wall 3 from 075 record.

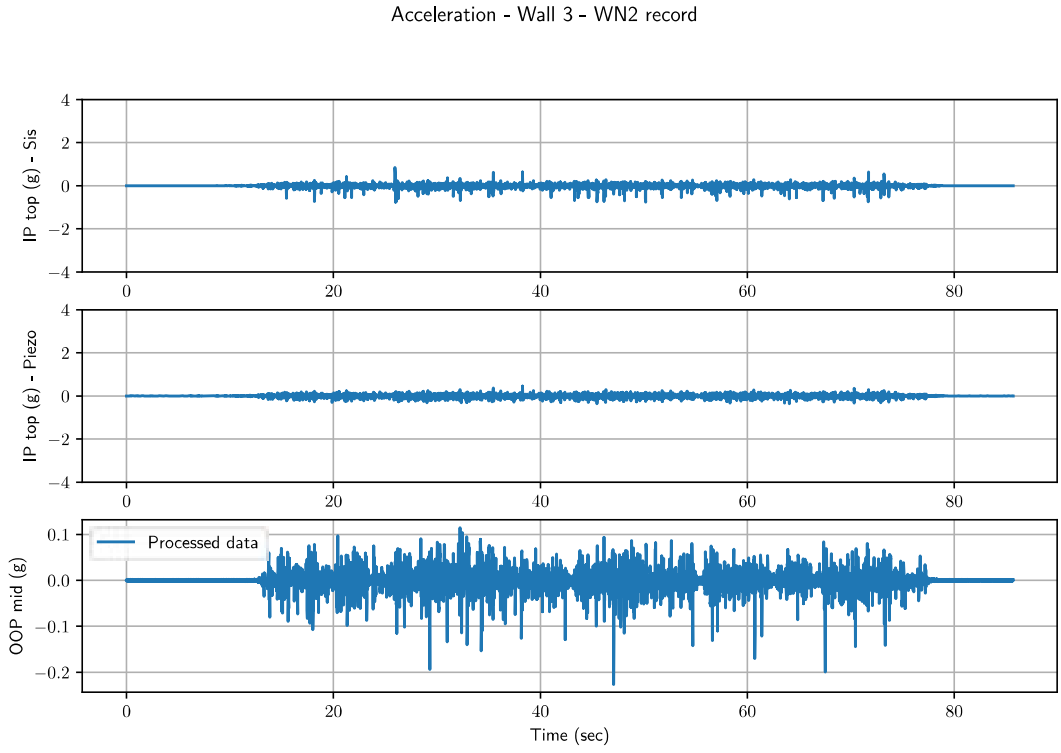

Figure 126: Acceleration records of wall 3 from $WN2$ record.

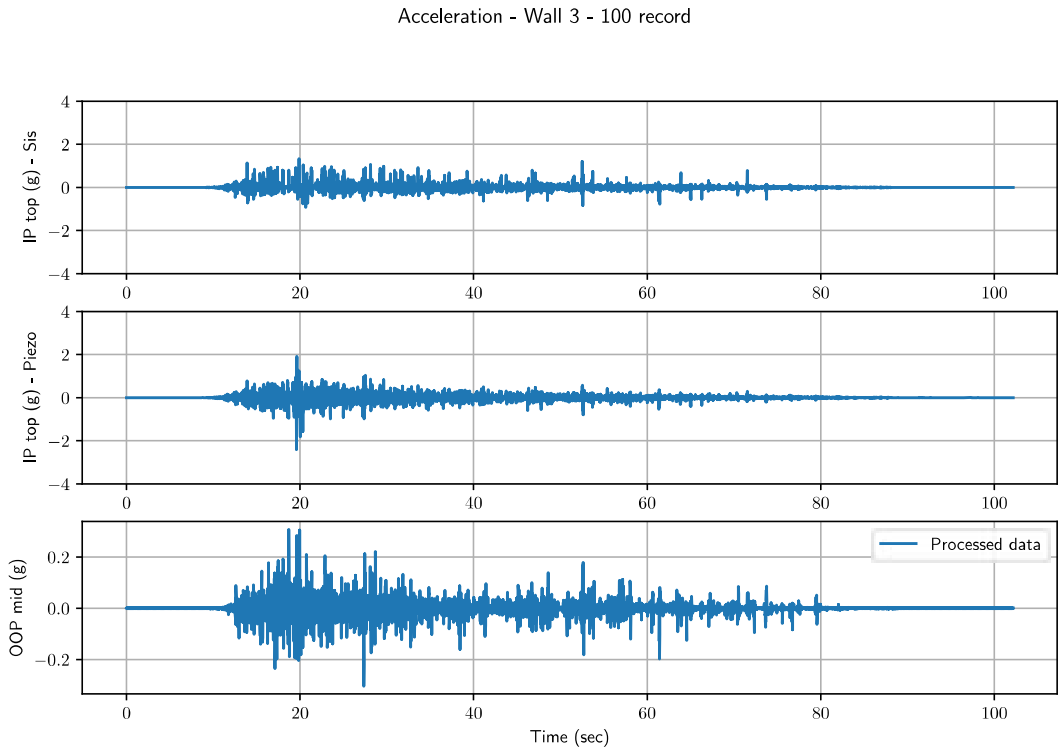

Figure 127: Acceleration records of wall 3 from 100 record.

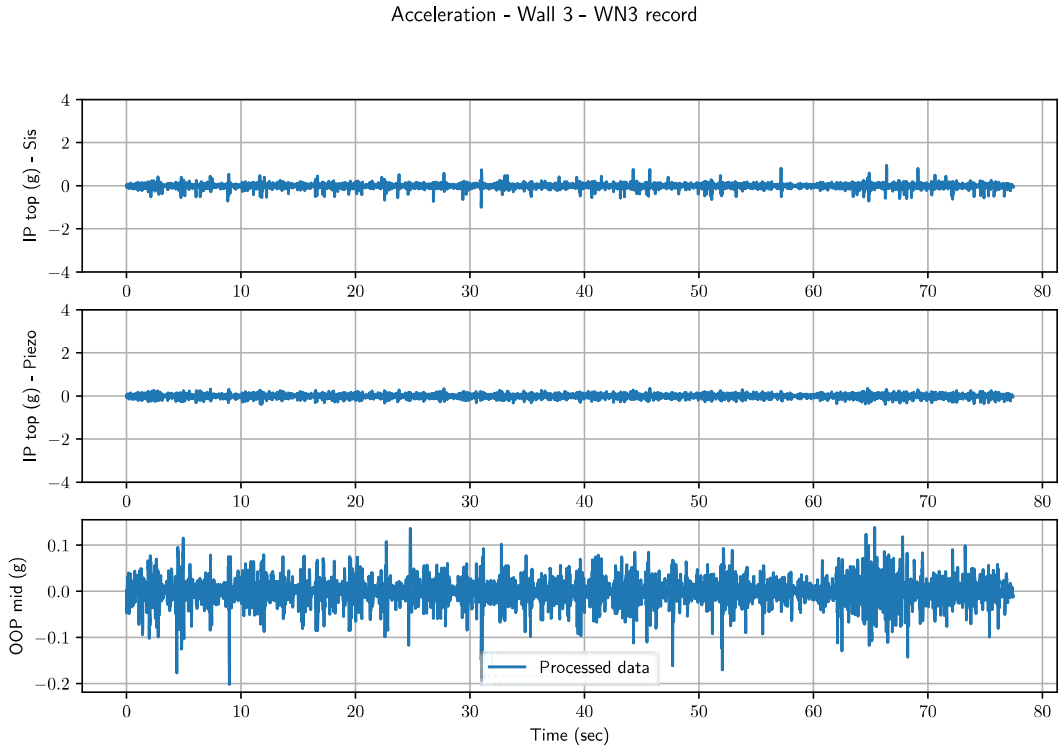

Figure 128: Acceleration records of wall 3 from $WN3$ record.

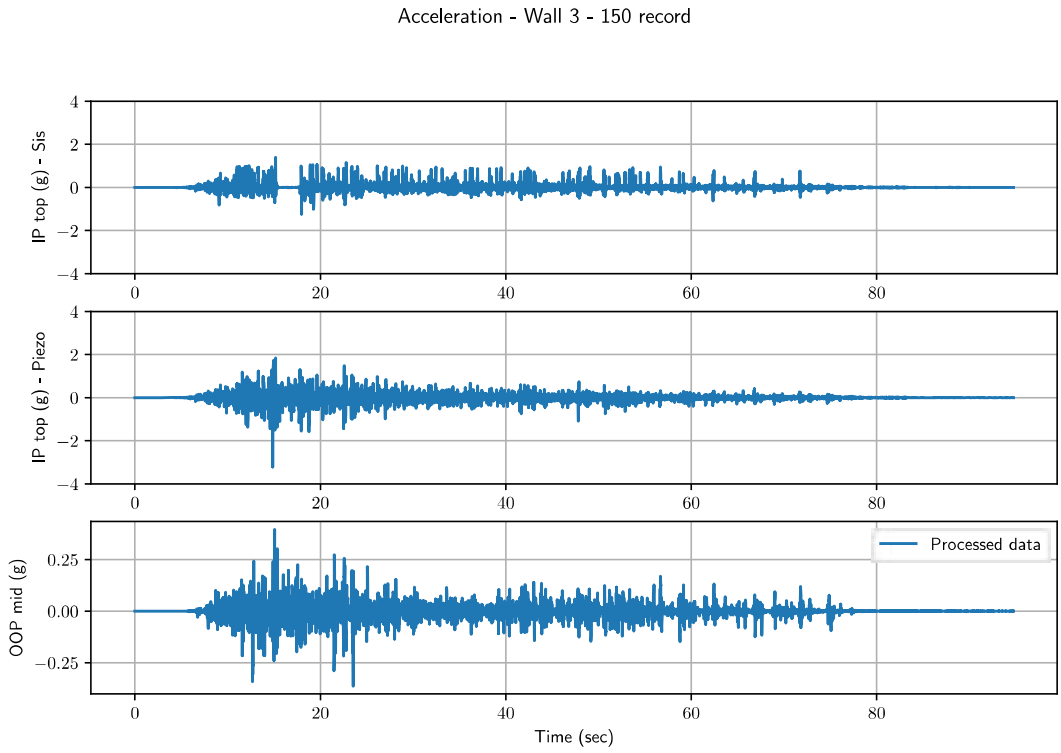

Figure 129: Acceleration records of wall 3 from 150 record.

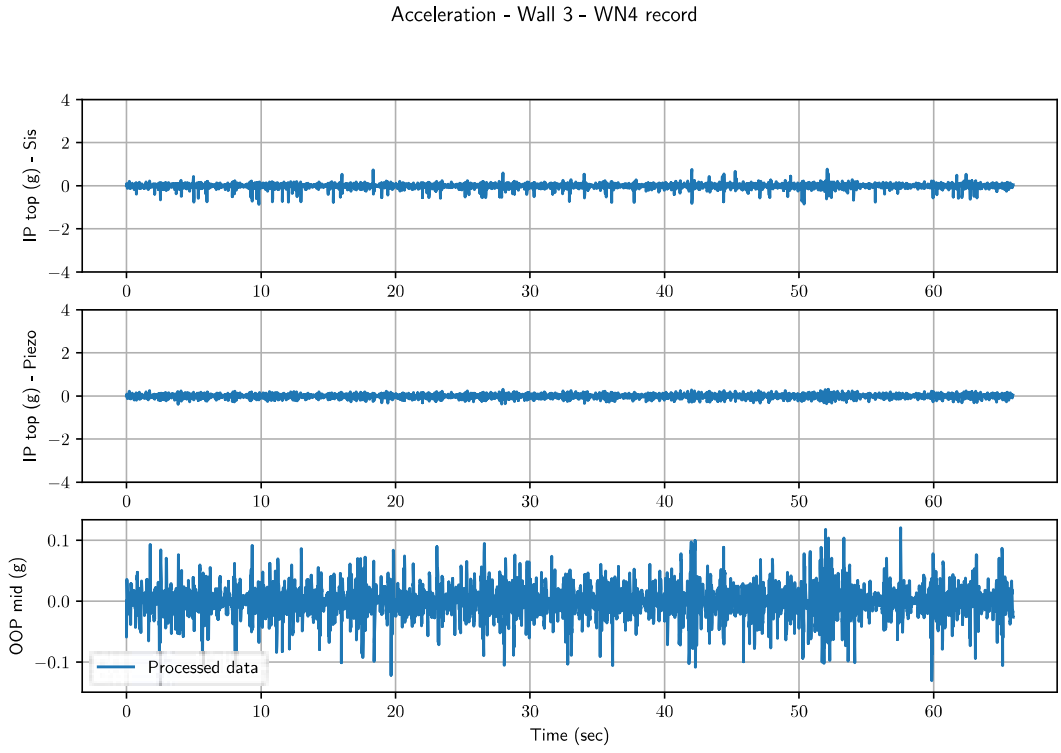

Figure 130: Acceleration records of wall 3 from $WN4$ record.

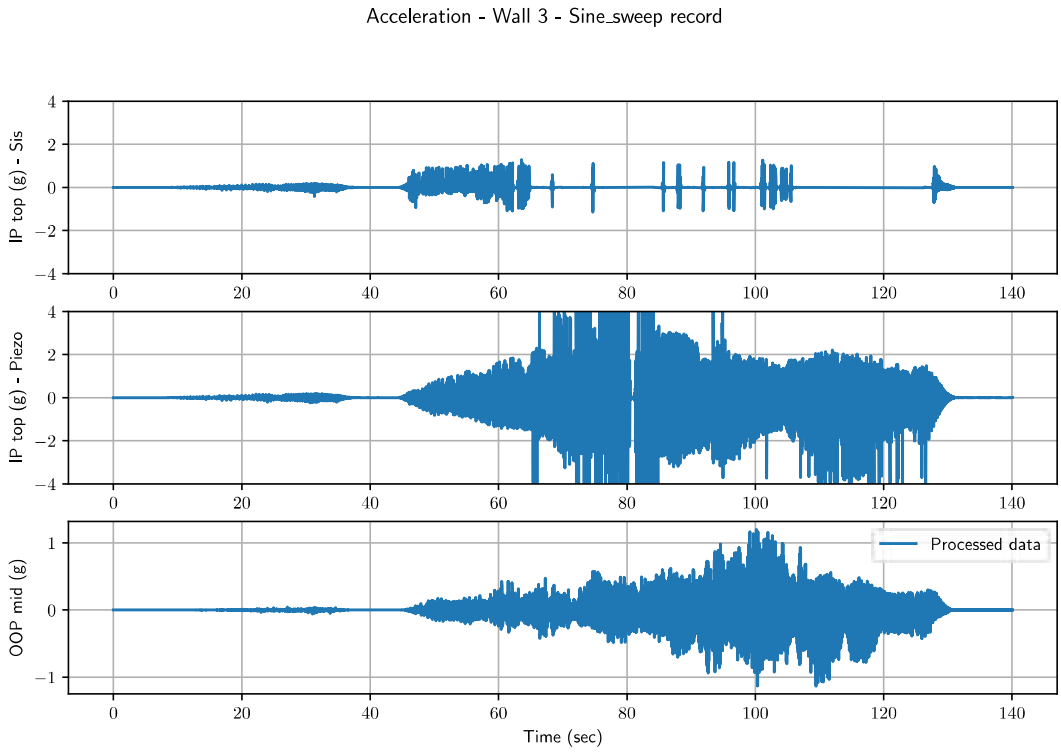

Figure 131: Acceleration records of wall 3 from $Sine_sweep$ record.

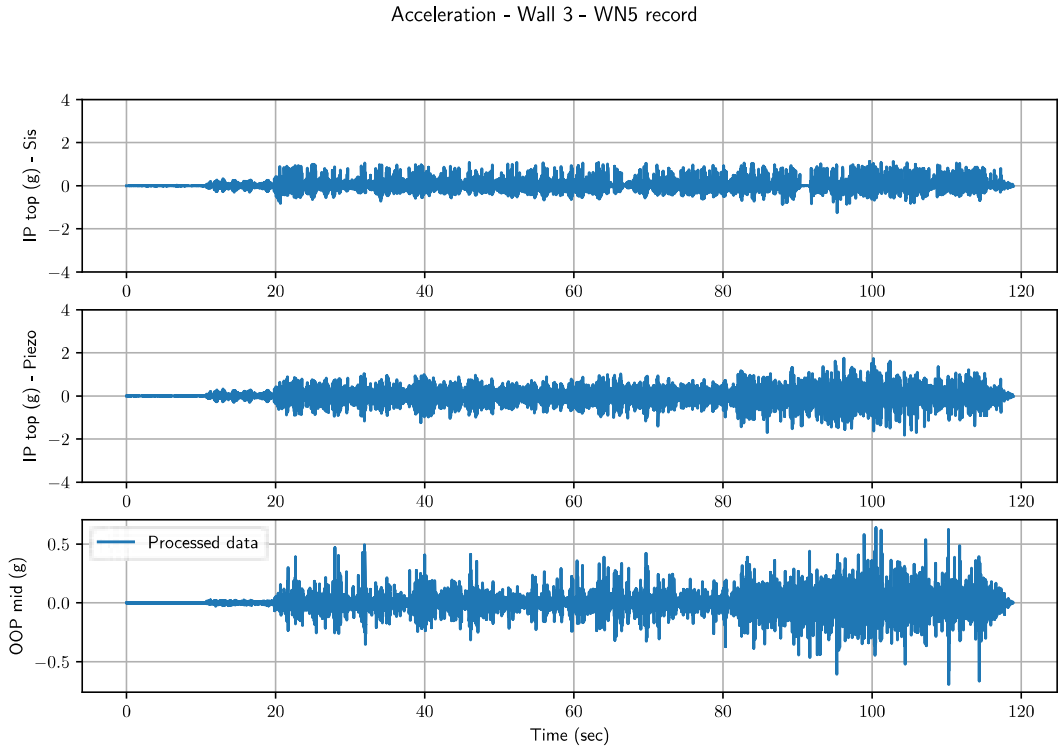

Figure 132: Acceleration records of wall 3 from $WN5$ record.

4.2 Displacement records

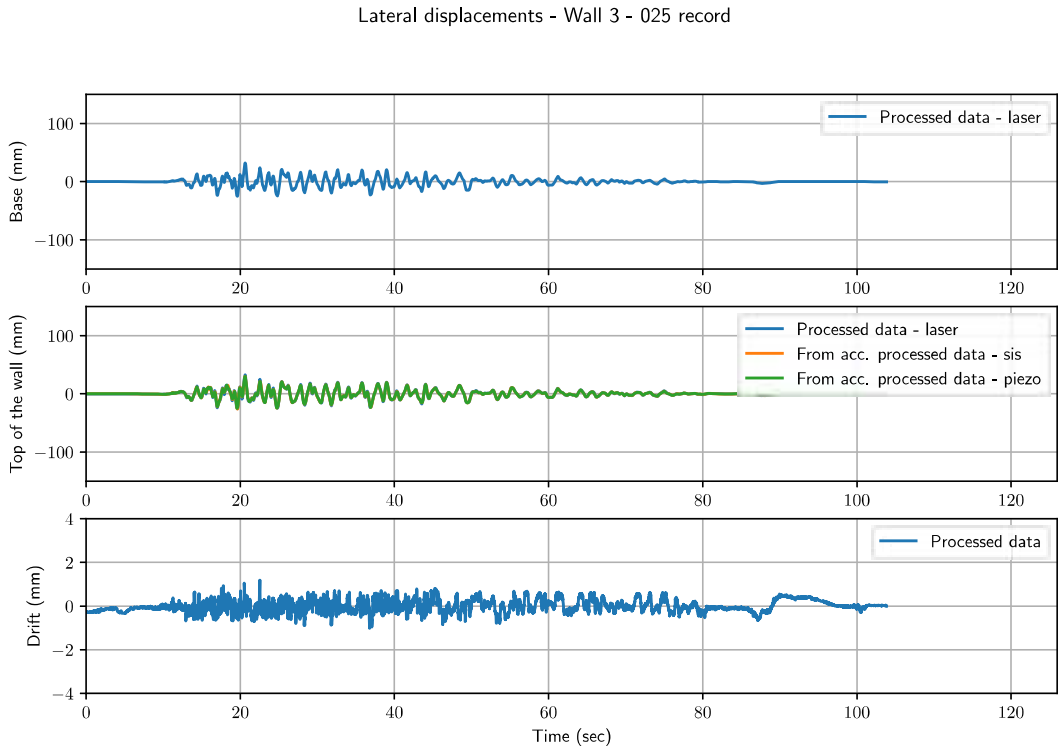

Figure 133: Acceleration records of wall 3 from 025 record.

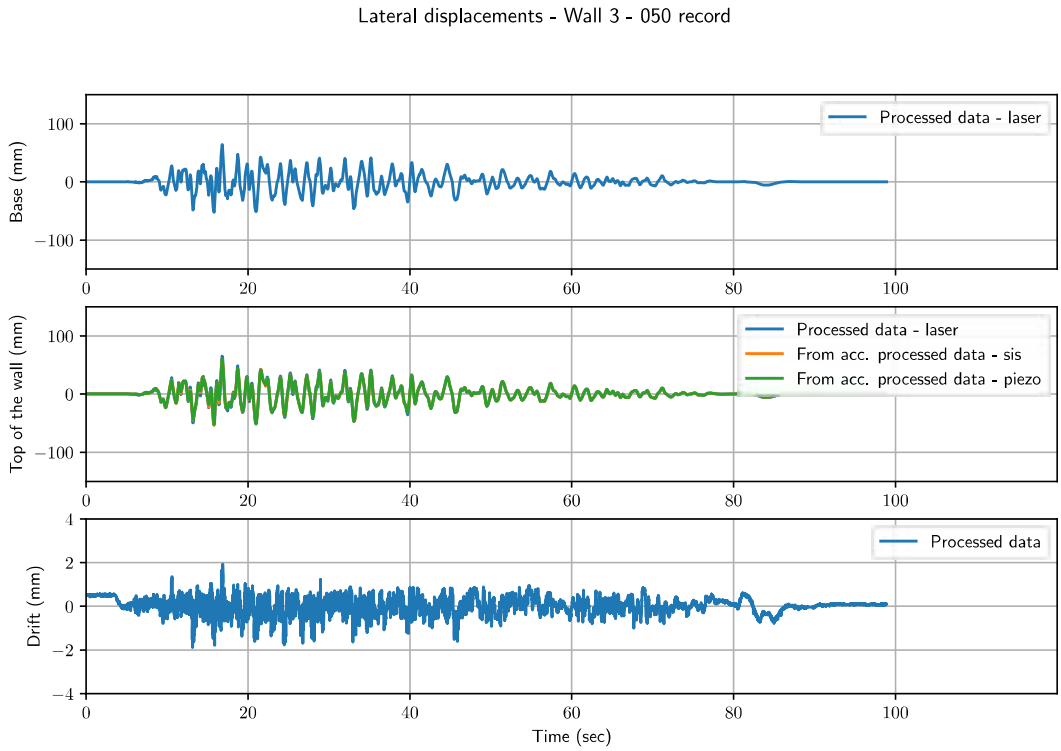

Figure 134: Acceleration records of wall 3 from 050 record.

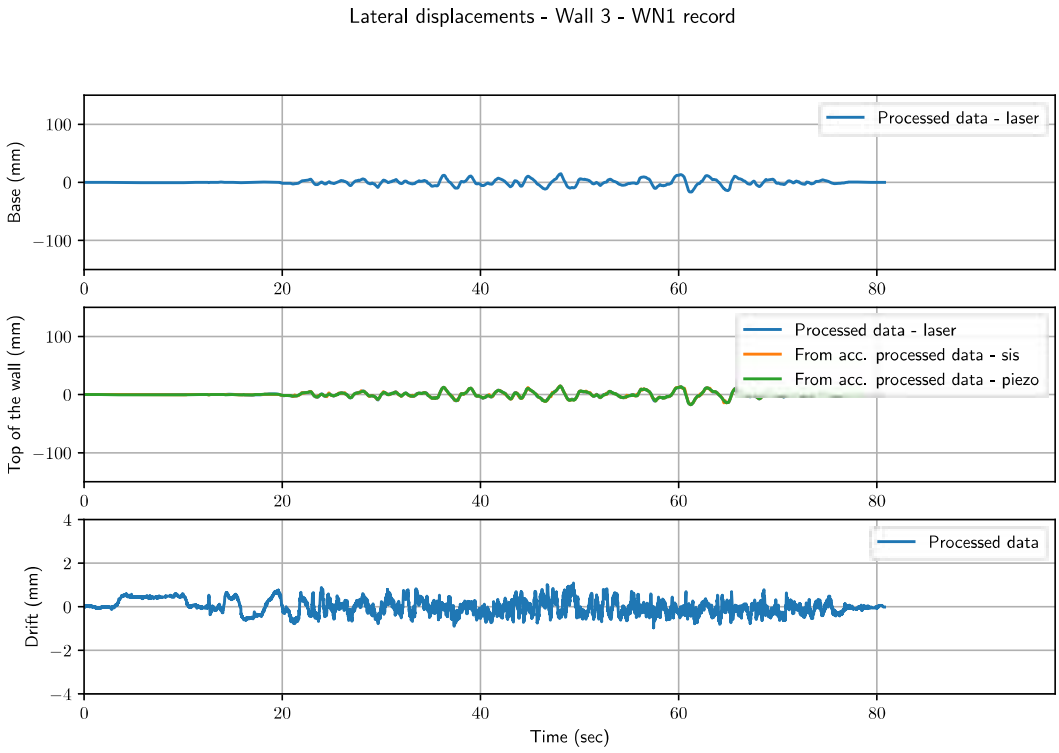

Figure 135: Acceleration records of wall 3 from $WN1$ record.

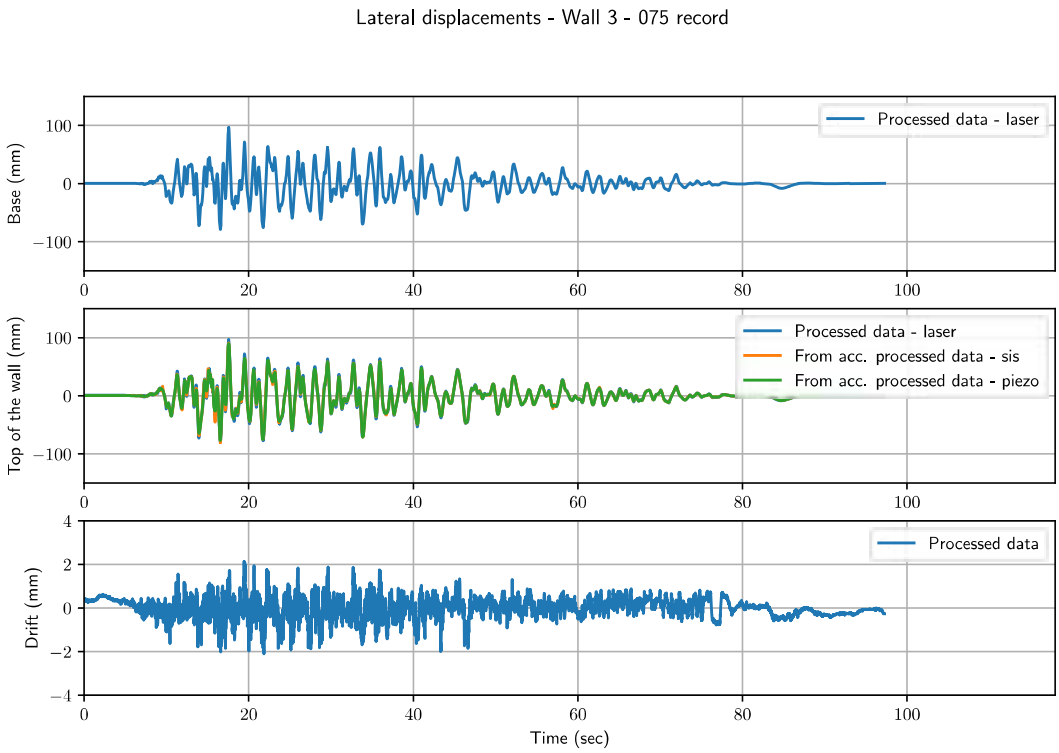

Figure 136: Acceleration records of wall 3 from 075 record.

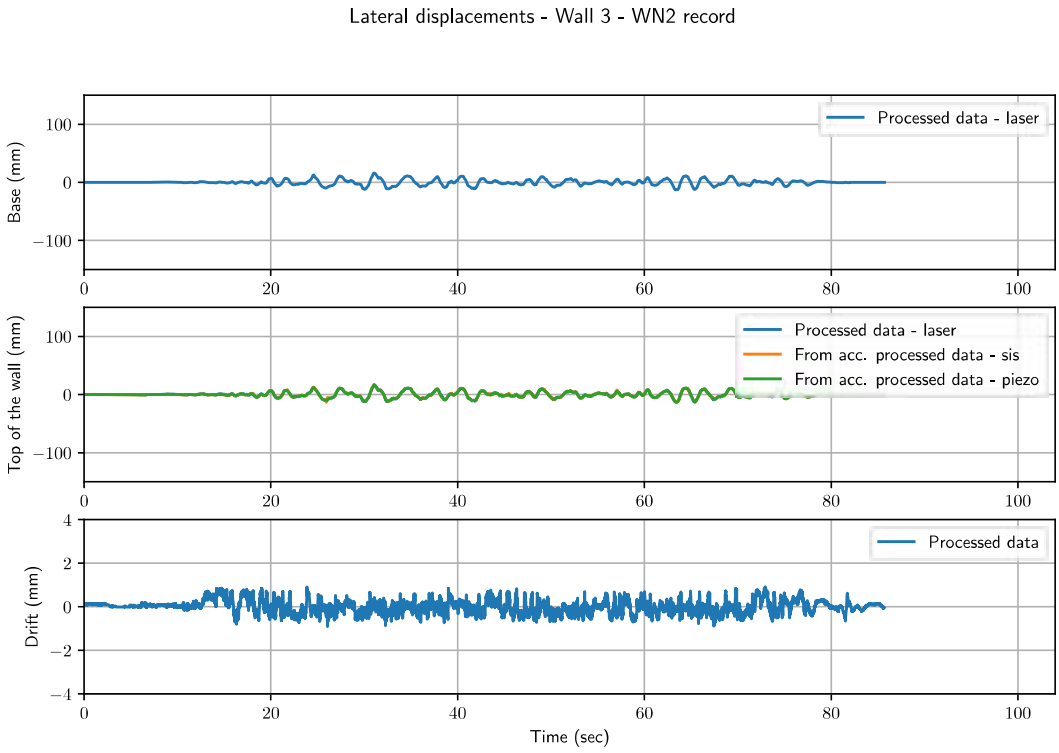

Figure 137: Acceleration records of wall 3 from $WN2$ record.

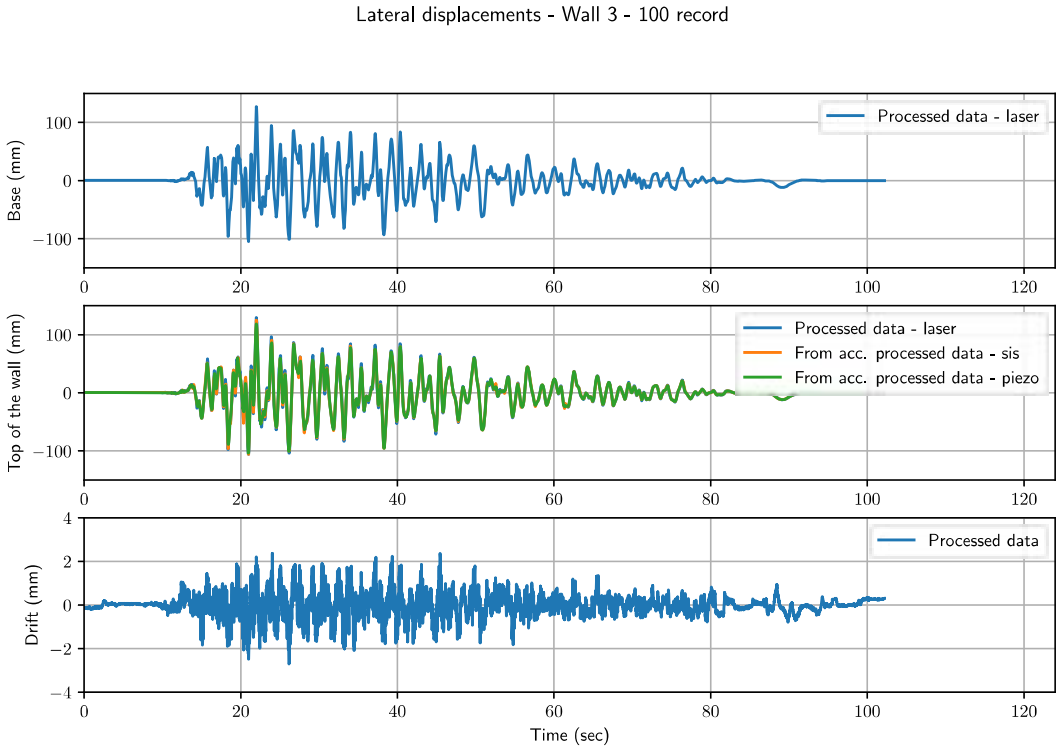

Figure 138: Acceleration records of wall 3 from 100 record.

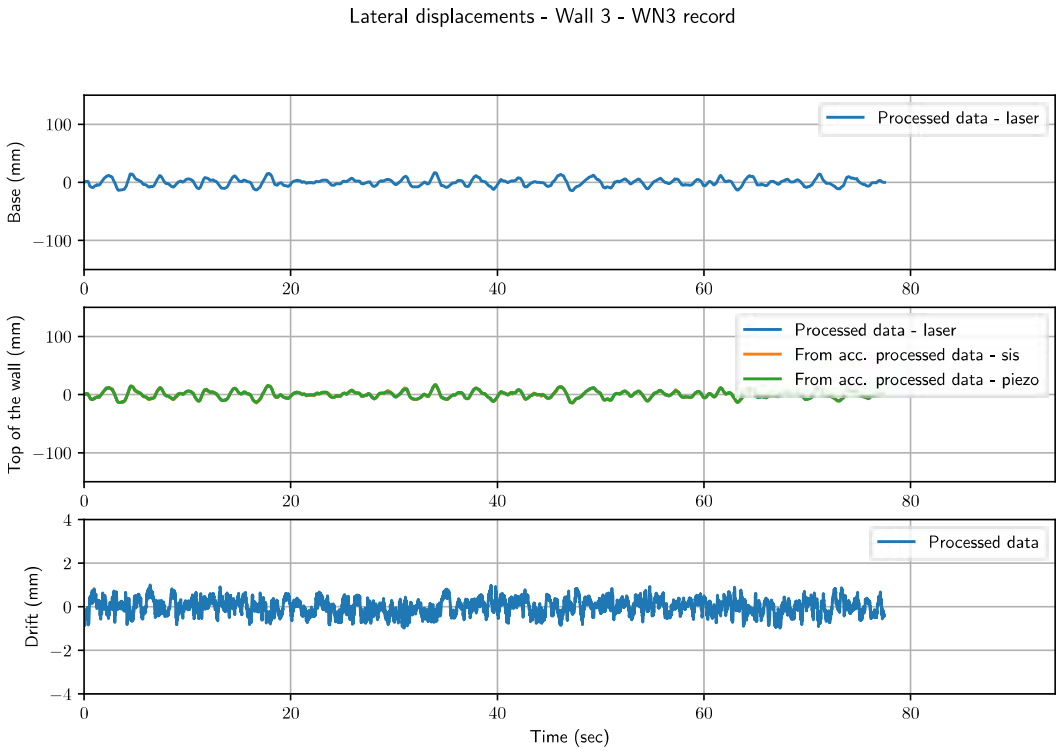

Figure 139: Acceleration records of wall 3 from $WN3$ record.

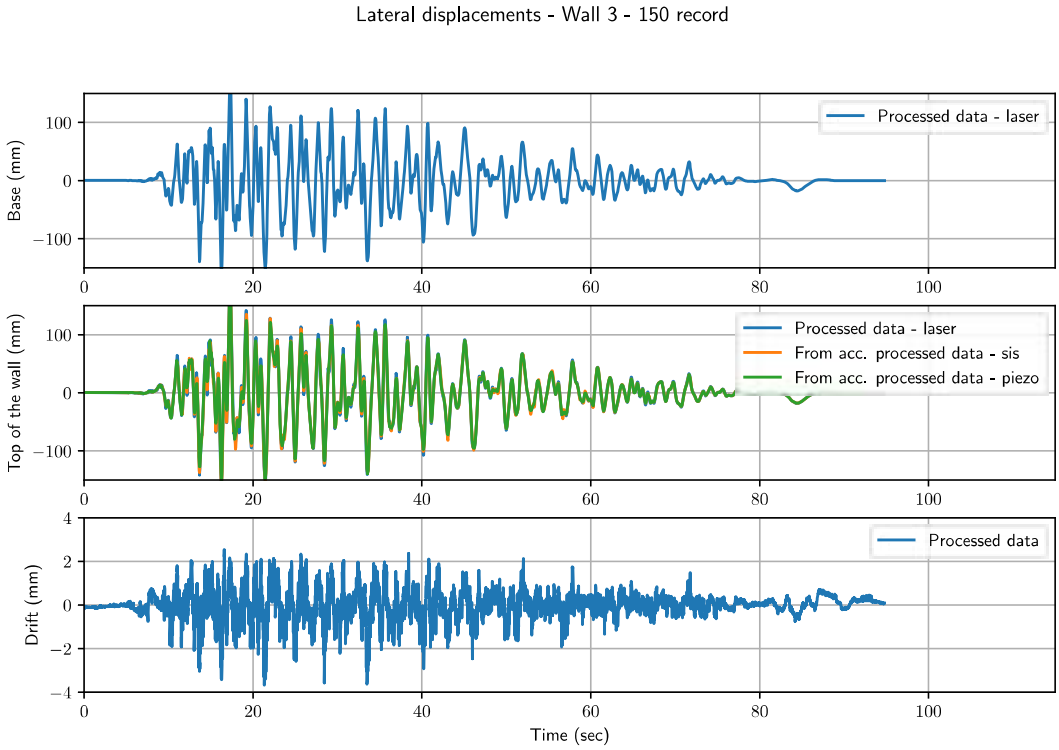

Figure 140: Acceleration records of wall 3 from 150 record.

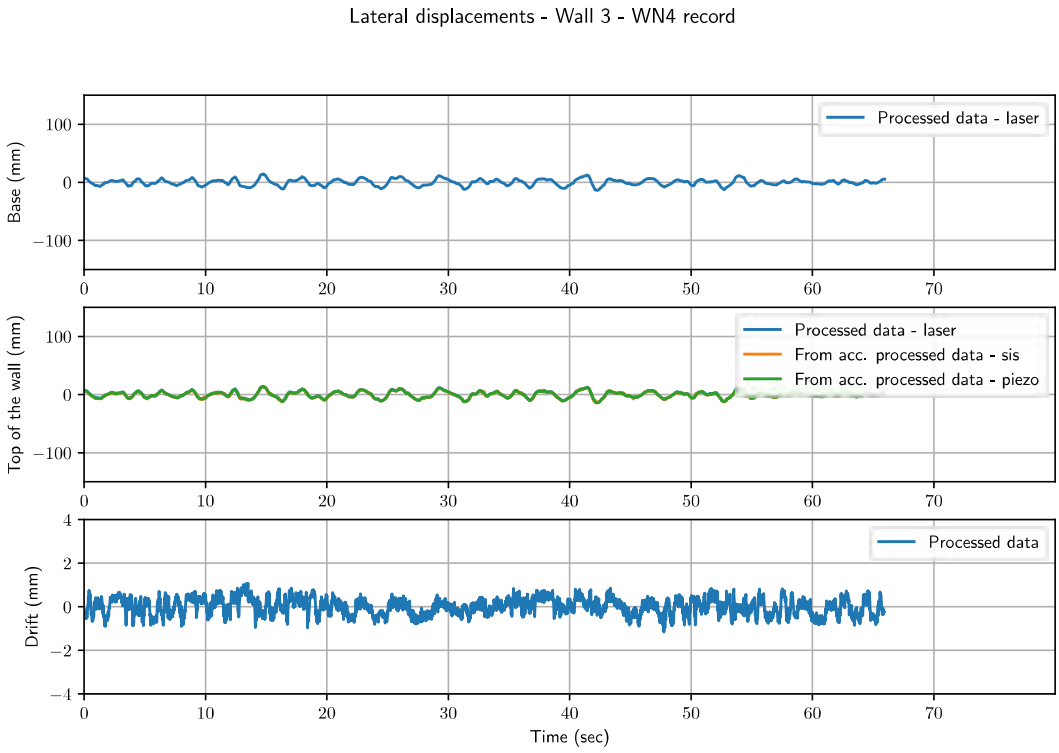

Figure 141: Acceleration records of wall 3 from $WN4$ record.

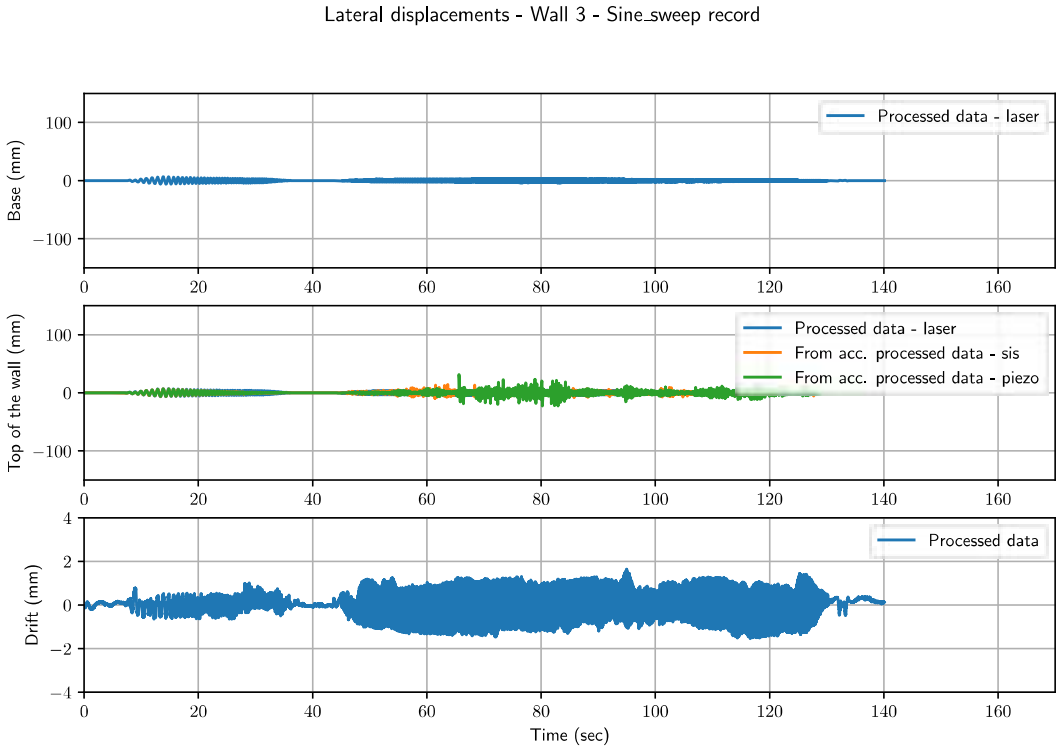

Figure 142: Acceleration records of wall 3 from $Sine_sweep$ record.

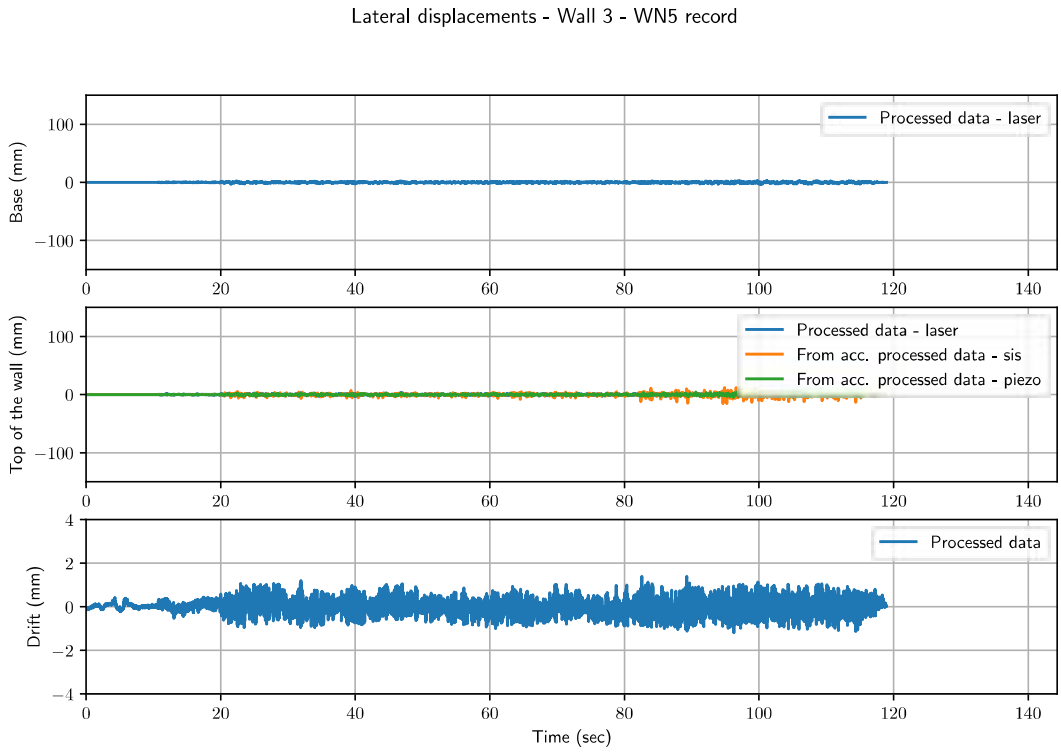

Figure 143: Acceleration records of wall 3 from $WN5$ record.

4.3 Fourier analysis results from acceleration records

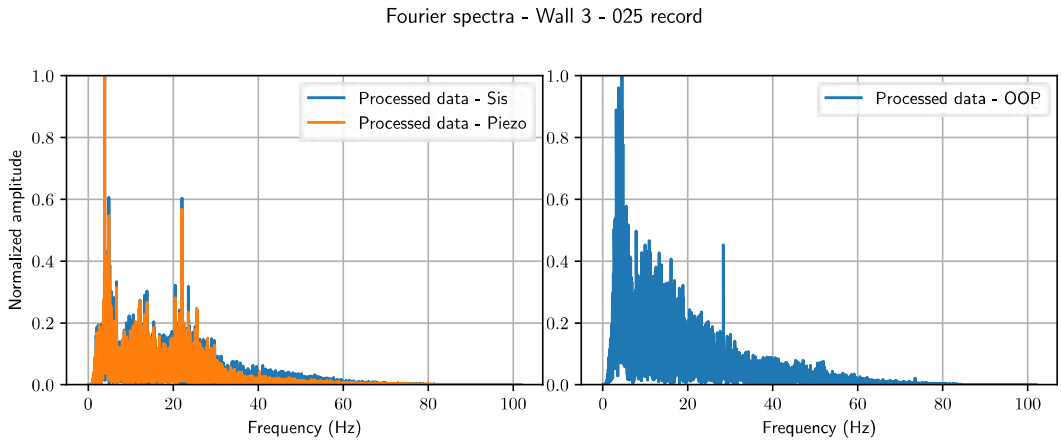

Figure 144: Fourier transformation of wall 3 from 025 record.

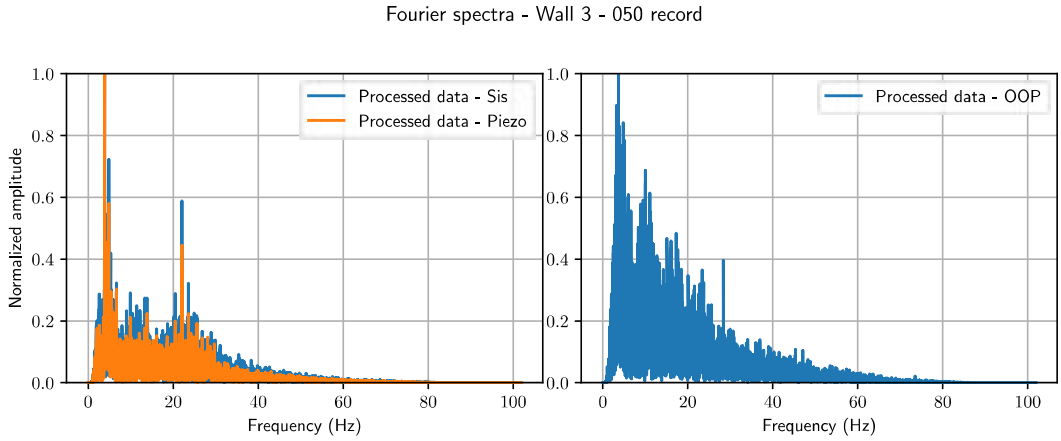

Figure 145: Fourier transformation of wall 3 from 050 record.

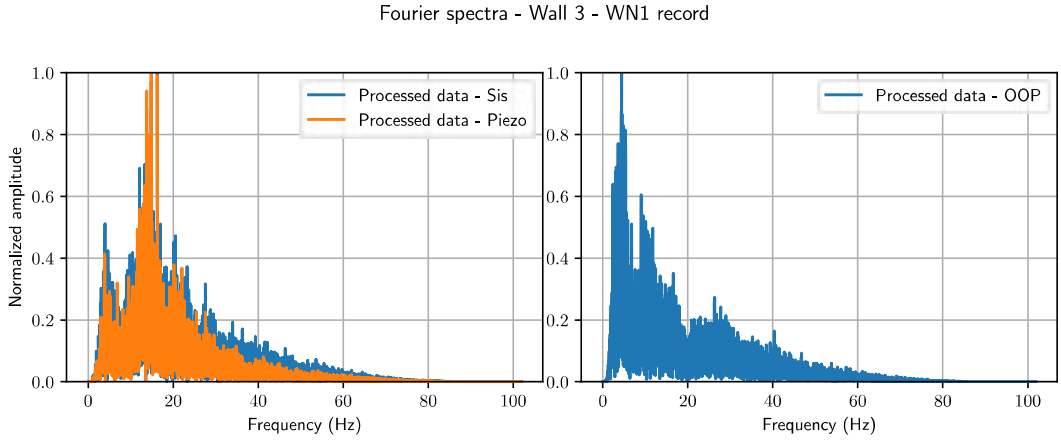

Figure 146: Fourier transformation of wall 3 from $WN1$ record.

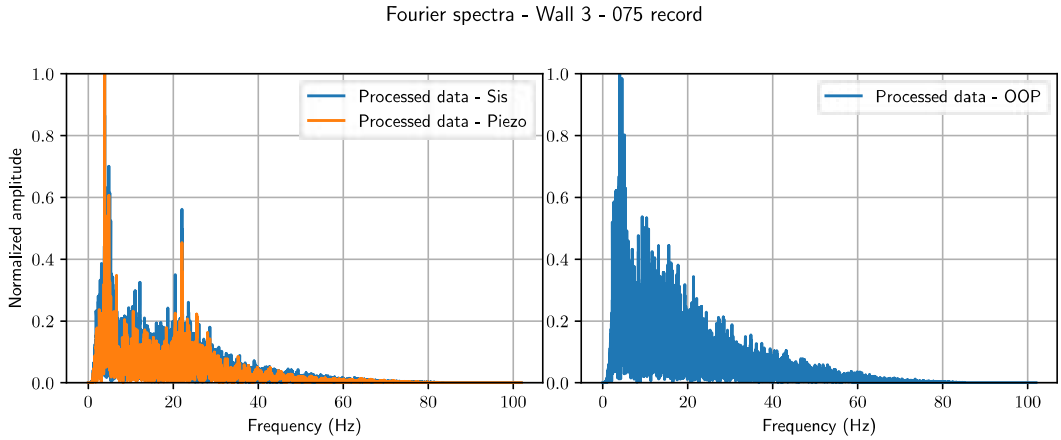

Figure 147: Fourier transformation of wall 3 from 075 record.

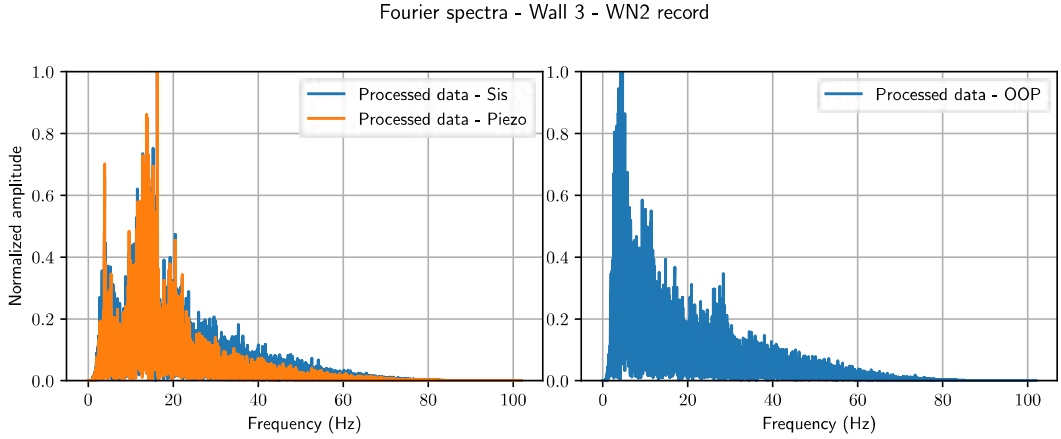

Figure 148: Fourier transformation of wall 3 from $WN2$ record.

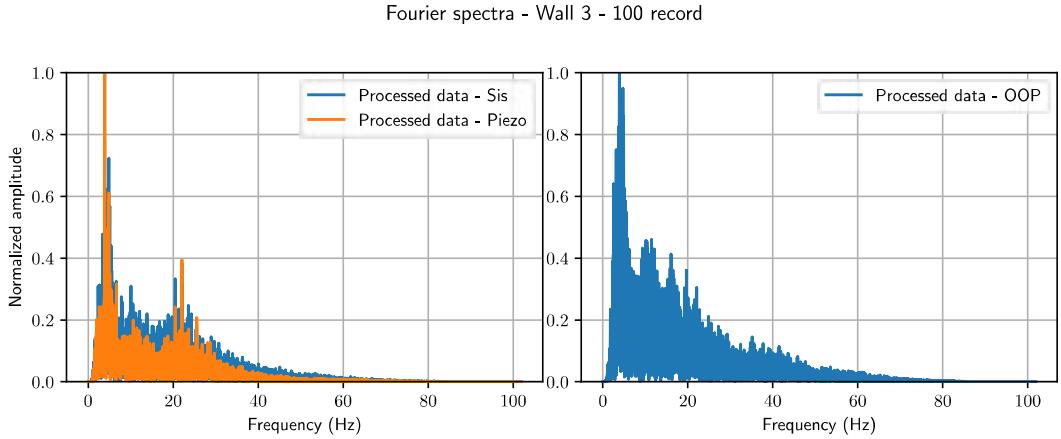

Figure 149: Fourier transformation of wall 3 from 100 record.

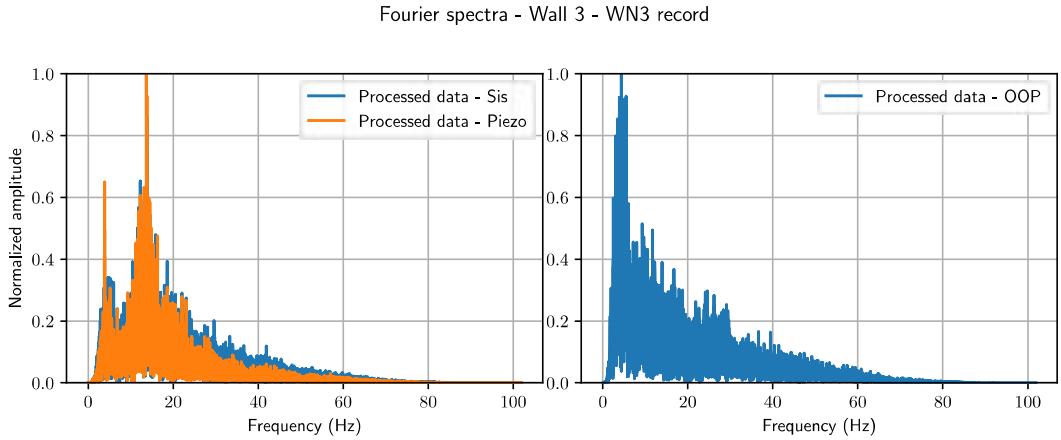

Figure 150: Fourier transformation of wall 3 from $WN3$ record.

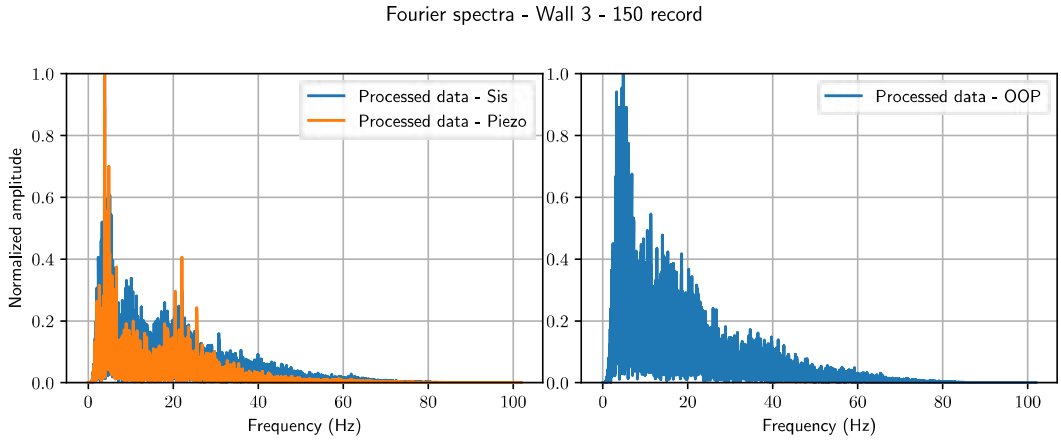

Figure 151: Fourier transformation of wall 3 from 150 record.

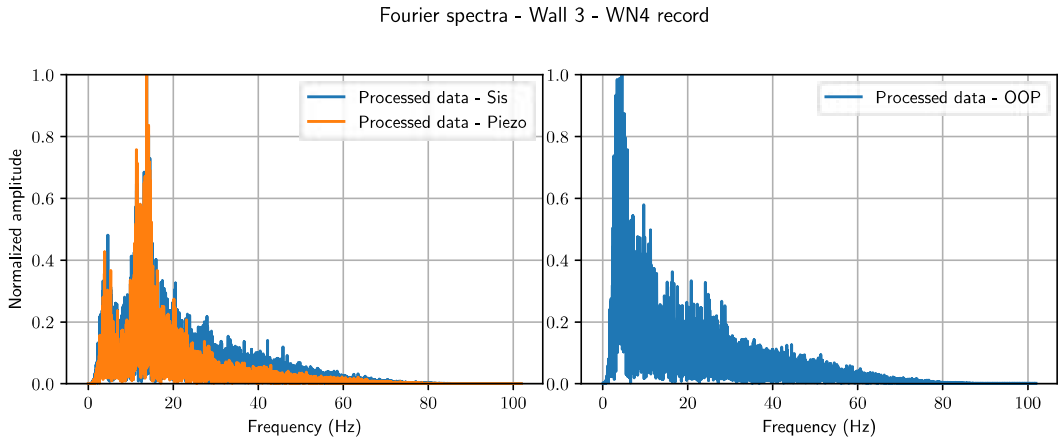

Figure 152: Fourier transformation of wall 3 from $WN4$ record.

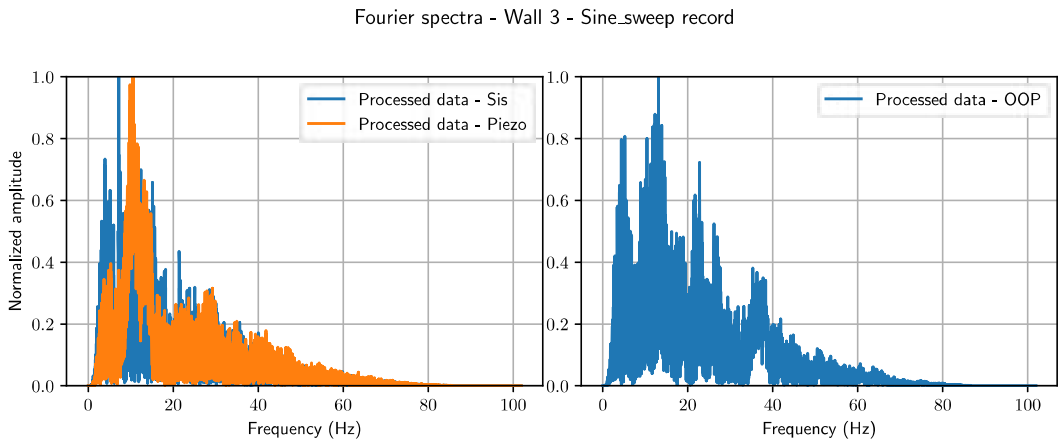

Figure 153: Fourier transformation of wall 3 from $Sine_sweep$ record.

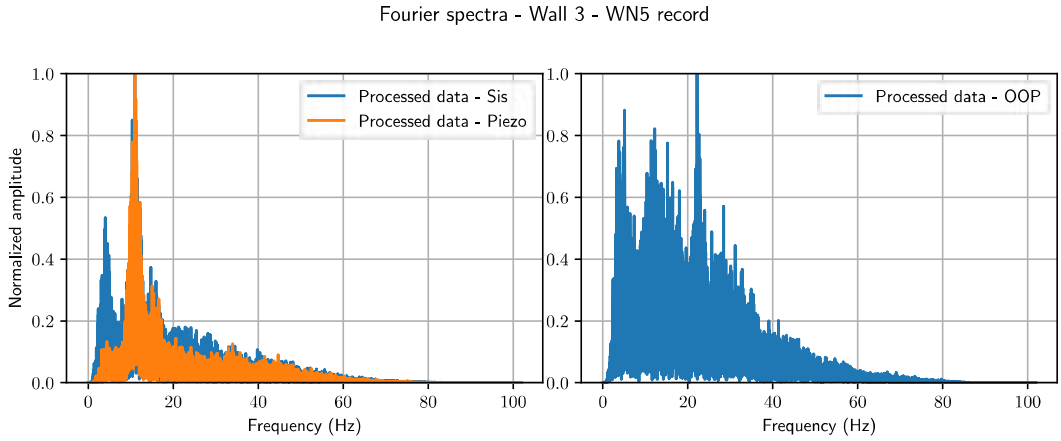

Figure 154: Fourier transformation of wall 3 from $WN5$ record.

4.4 Power density spectra (PDS) from acceleration records

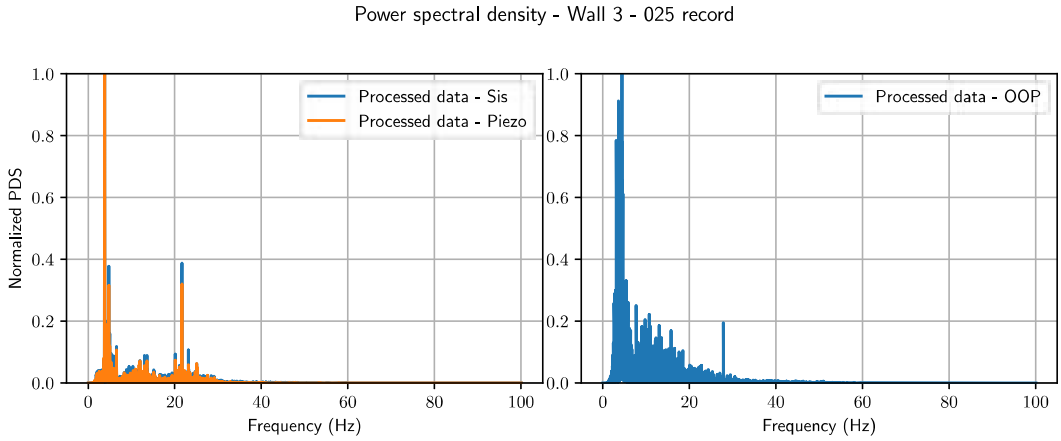

Figure 155: Power density spectra of wall 3 from 025 record.

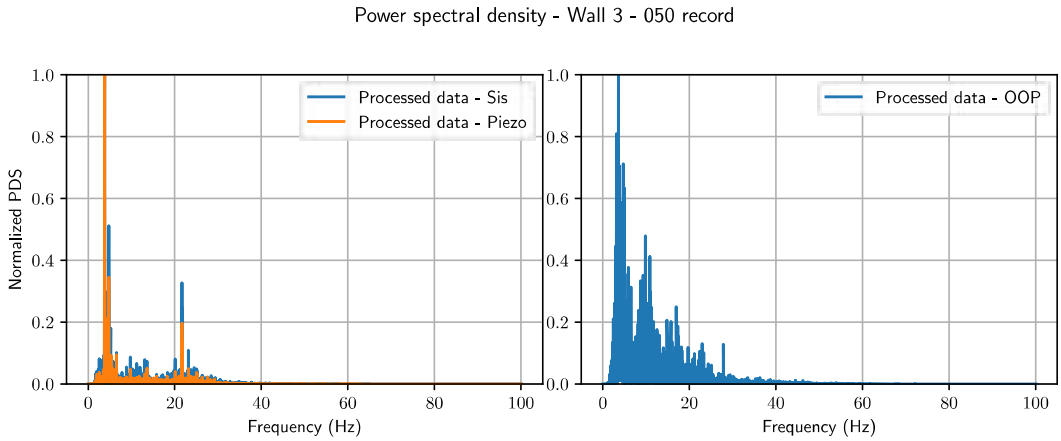

Figure 156: Power density spectra of wall 3 from 050 record.

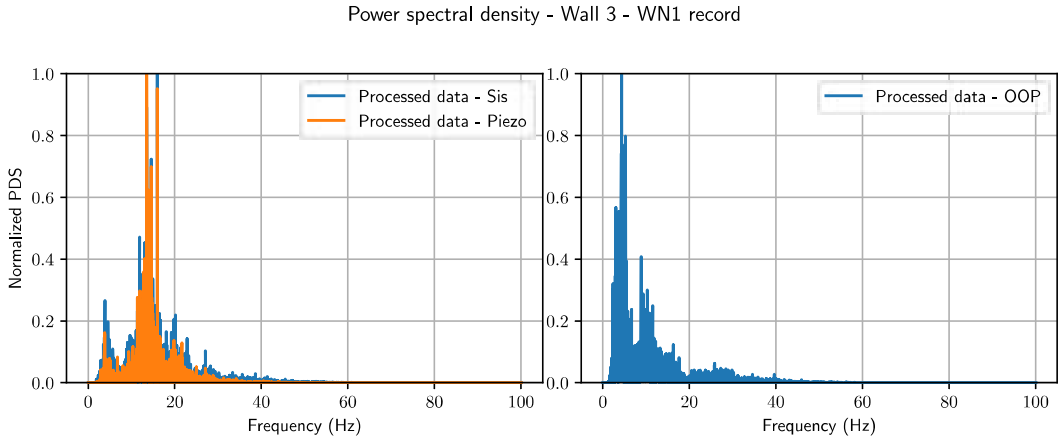

Figure 157: Power density spectra of wall 3 from $WN1$ record.

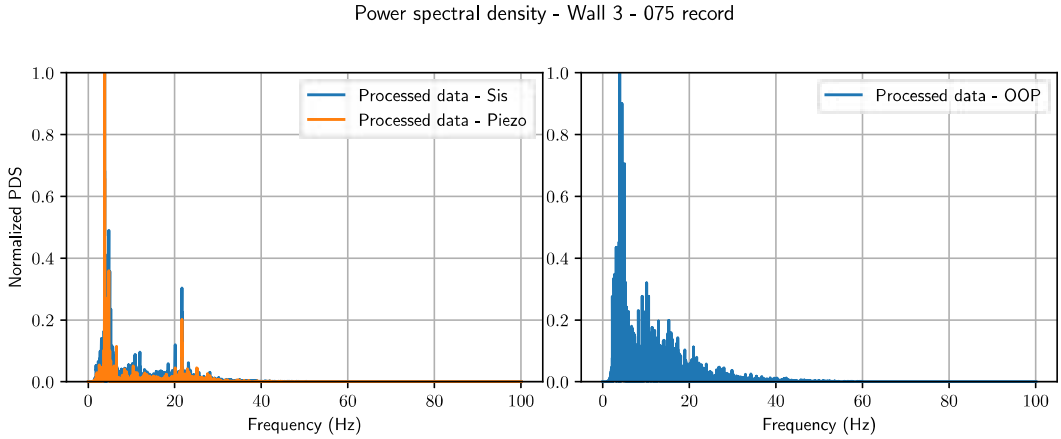

Figure 158: Power density spectra of wall 3 from 075 record.

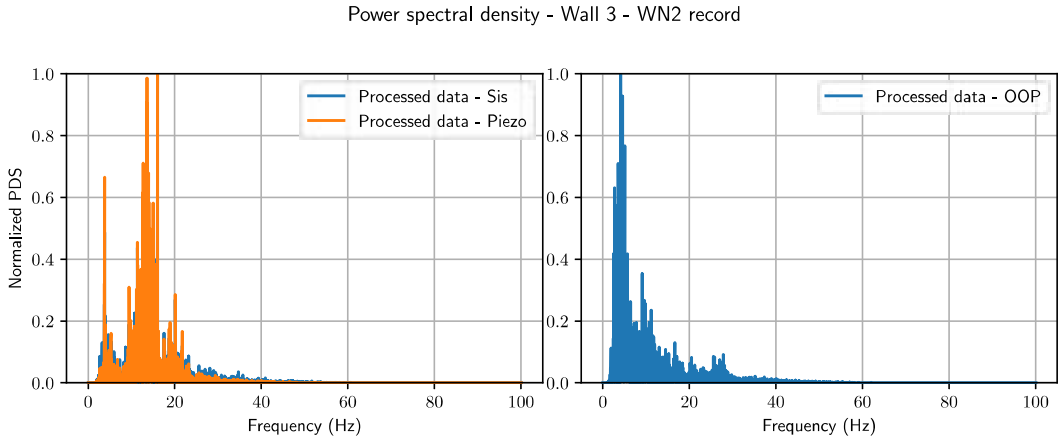

Figure 159: Power density spectra of wall 3 from $WN2$ record.

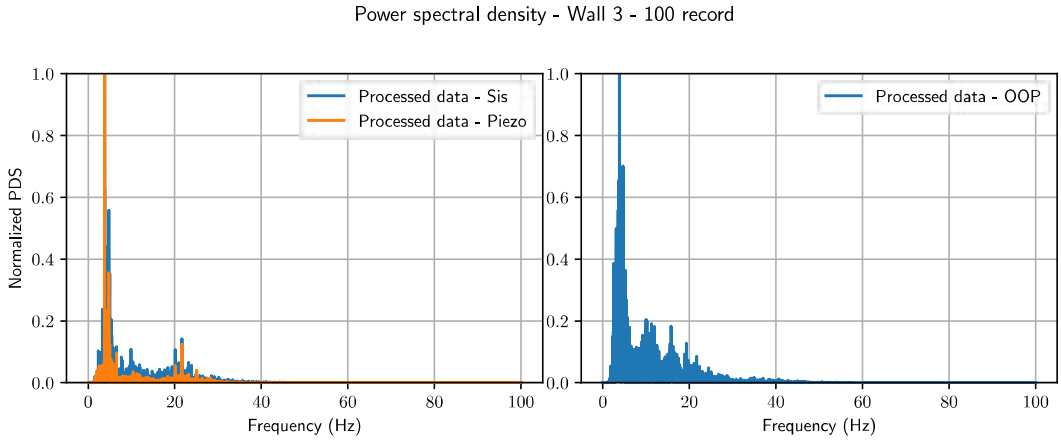

Figure 160: Power density spectra of wall 3 from 100 record.

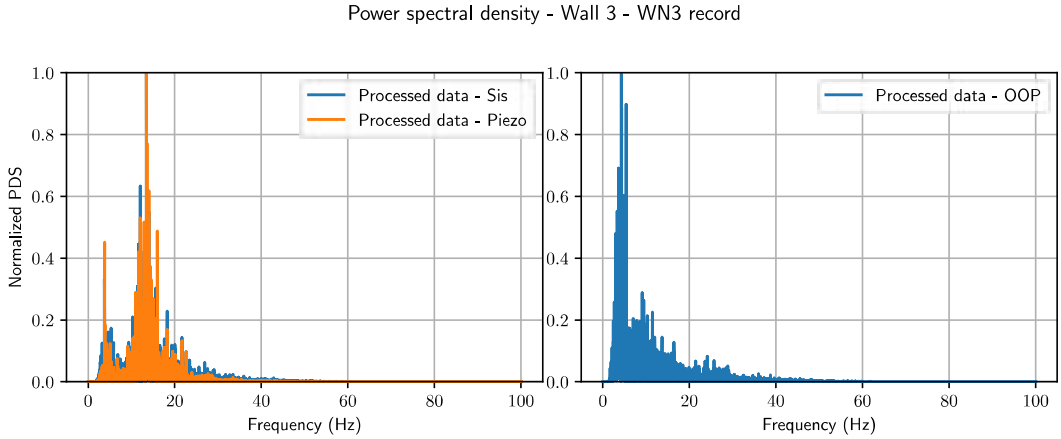

Figure 161: Power density spectra of wall 3 from $WN3$ record.

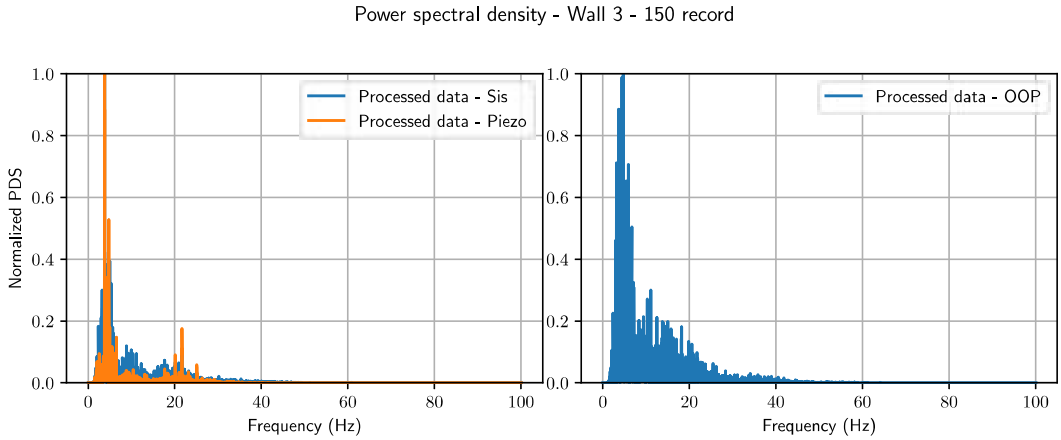

Figure 162: Power density spectra of wall 3 from 150 record.

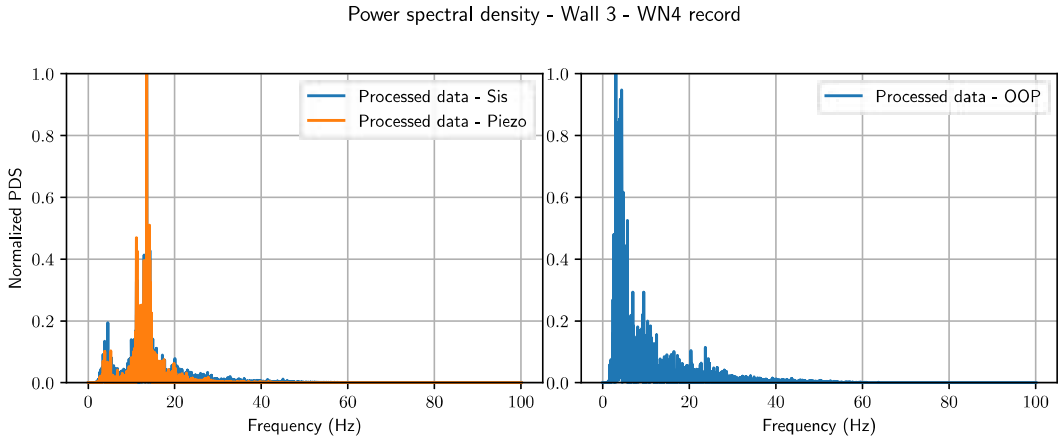

Figure 163: Power density spectra of wall 3 from $WN4$ record.

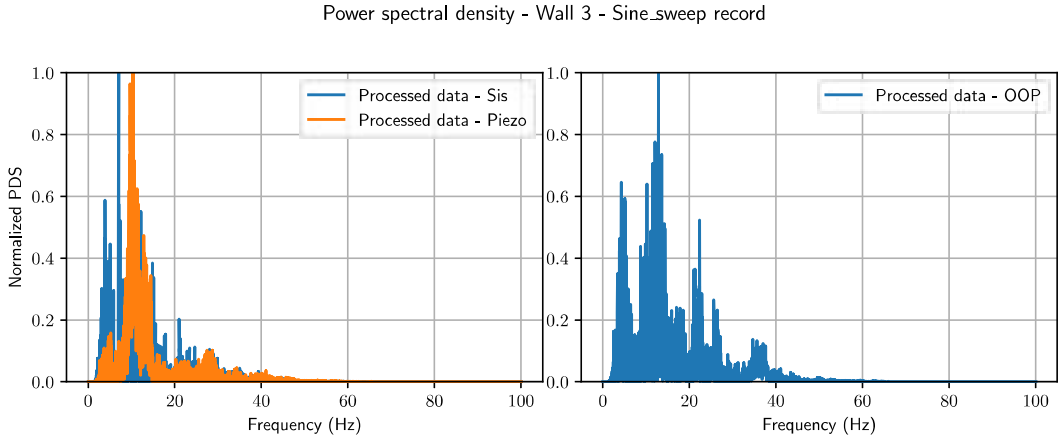

Figure 164: Power density spectra of wall 3 from $Sine_sweep$ record.

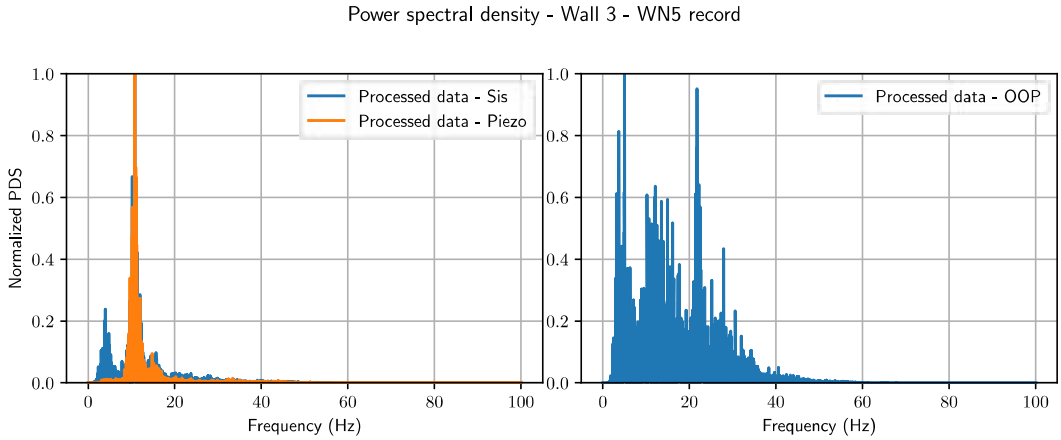

Figure 165: Power density spectra of wall 3 from $WN5$ record.

Appendix B

Summary of contributions

Journal Articles

- Arroyo, O., **Barros, J.**, Ramos, L. Comparison of the reinforced concrete seismic provisions of the design codes of the United States, Colombia and Ecuador for low-rise frames. Earthquake Spectra, Vol 34, pag 441-458, 2018. https://doi.org/10.1193/102116EQS178EP.

- **Barros, J.**, Chiachío, M., Chiachío, J. and Cabanilla, F. Adaptive approximate Bayesian computation by subset simulation for structural model calibration. Comput Aided Civ Inf. 2021; 1– 20. https://doi.org/10.1111/mice.12762

- **Barros, J.**, Chiachío, M., Fernández, J., Morillas, L. and Consuegra, J. Probabilistic shear response modelling of masonry infilled frames. Submitted to Computers and Concrete.

- **Barros, J.**, Chiachío, M., Morillas, L., Torres, W. and Suco, D. A novel semi-empirical approach to non-destructively evaluate the effect of infills on frame buildings. Submitted to Engineering Structures.

- Fernández, J., Chiachío, J., Chiachío, M., **Barros, J.** and Corbetta, M. Physics-Guided Bayesian Neural Networks by ABC-SS: Application to reinforced concrete columns. Engineering Applications of Artificial Intelligence. March 2023. Volume 119. https://doi.org/10.1016/j.engappai.2022.105790

Conference Proceedings (full-papers)

- Rojas, P., Miranda, E., **Barros, J.**, Rosero, D., Márquez, W. and García, L. Seismic performance and rehabilitation of the port of manta after the 2016 Ecuador Earthquake. Ports 2019: Port Engineering, 15th Triennial International Conference, September 15-18, 2019, Pittsburgh, Pennsylvania. ISBN: 9780784482612, pag. 603-615. https://doi.org/10.1061/9780784482612.057.

- Chiachío, M., **Barros, J.** and Chiachío, J. Probabilistic Safety Assessment of concrete columns by approximate bayesian computation. ESREL 2020 and PSAM 15, The 30th European Safety and Reliability Conference, The 15th Probabilistic Safety Assessment and Management Conference, 1-6 Nov., 2020, ISBN: 978-981-14-8593-0. https://www.rpsonline.com.sg/proceedings/esrel2020/pdf/4974.pdf.

- Rojas, P., Retamales, R., Miranda, E., Caballero, M., **Barros, J.** and García, L. Seismic Performance and Rehabilitation of the Solca Hospital Main Buildings after the 2016 Pedernales Earthquake. In proceedings of the 10th International Conference on Behaviour of Steel Structures in Seismic Areas (STESSA), 2022. ISBN: 9783031038112.

- Rojas, P., Miranda, E., **Barros, J.**, Rosero, D., Márquez, W. and García, L. Case History of a Rehabilitated Port Facility after the 2016 Ecuador Earthquake. Ports 2022: Port Engineering, 16th Triennial International Conference, September 18-21, 2022, Honolulu, Hawaii. ISBN: 9780784484395, pag. 93-103. https://doi.org/10.1061/9780784484395.010.

International Conferences

- Ponce, G., **Barros, J.**, Blondet, M. and Chiachío, M. Modelling Cyclic Degradation of Bridge R.C. Columns Subjected to Concurrently Seismic Events. 17th World Conference on Earthquake Engineering (WCEE17), 2021, September 27th to October 2nd, Sendai, Japan.

- **Barros, J.**, Chiachío, M., Barreiro, J. and Consuegra, J. Calibración automatizada de modelos numéricos en base a ensayos de columnas de hormigón. Yachana, Vol. 8, No. 2, pag. 109-118, 2019. ISSN: 1390-7778 (ISSN elctrónico: 2528-8148). http://revistas.ulvr.edu.ec/index.php/yachana/article/view/602/345

Technical seminars as invited speaker

- José Barros. Inferencia de parámetros de modelos numéricos usando ABC. Universidad Técnica de Manabí (UTM). By invitation of Ing. Edgar Menéndez.

- José Barros. Métodos Bayesianos para calibración de modelos y análisis probabilístico de estructuras. Universidad de las Fuerzas Armadas, ESPE. By invitation of Prof. Dr. Roberto Aguiar Falconí.

- José Barros. Evaluación de la probabilidad de colapso de estructuras de pórticos con mampostería frente a sismos. Universidad Católica de Santiago de Guayaquil (UCSG). By invitation of Prof. Dr. Walter Mera Ortiz.

- José Barros. Evaluación sísmica de estructuras de pórticos con mampostería usando ensayos no destructivos. Escuela Politécnica del Litoral (ESPOL). By invitation of Ing. Hugo Landívar.

Bibliography

Adachi, H., Kitajima, K., Ageta, H., and Nakanishi, M. (2000). Pseudo-dynamic test on reinforced concrete frame retrofitted with damper. *12WCEE*, pages 1–8.

Albert, C., Künsch, H. R., and Scheidegger, A. (2015). A simulated annealing approach to approximate bayes computations. *Statistics and computing*, 25(6):1217–1232.

Allemang, R. J. (1983). Experimental modal analysis. *NASA Technical reports*.

American Society of Civil Engineers (2016). *Minimum design loads for buildings and other structures (ASCE/SEI 7)*. ASCE, Reston, VA.

Analog Devices (2009). *Small, Low Power, 3-Axis ±3 g Accelerometer ADXL335*. Analog Devices. Rev. B.

ASCE/COPRI (2014). *Seismic Design of Piers and Wharves*. American Society of Civil Engineers, asce/copri 61-14 edition.

ASCE/SEI 41 (2017). *Seismic Evaluation and Retrofit of Existing Buildings*. American Society of Civil Engineers, asce/sei 41-17 edition.

Au, S. and Beck, J. (2001). Estimation of small failure probabilities in high dimensions by subset simulation. *Probabilistic Engineering Mechanics*, 16(4):263–277.

Awodele, O. and Jegede, O. (2009). Neural networks and its application in engineering. *Sci IT*, pages 83–95.

Baragatti, M., Grimaud, A., and Pommeret, D. (2013). Likelihood-free parallel tempering. *Statistics and Computing*, 23(4):535–549.

Barbosa, A. R., Fahnestock, L. A., Fick, D. R., Gautam, D., Soti, R., Wood, R., Moaveni, B., Stavridis, A., Olsen, M. J., and Rodrigues, H. (2017). Performance of Medium-to-High Rise Reinforced Concrete Frame Buildings with Masonry Infill in the 2015 Gorkha, Nepal, Earthquake. *Earthquake Spectra*, 33(1, SI):S197–S218.

Barreiro, J. (2018). *Calibración de un modelo de elementos finitos de hormigón armado no-lineal para incluir los efectos de degradación por carga cíclica parte 4*. PhD thesis, Universidad Católica de Santiago de Guayaquil.

Barros, J., Chiachío, M., Chiachío, J., and Cabanilla, F. (2021). Adaptive approximate bayesian computation by subset simulation for structural model calibration. *Computer-Aided Civil and Infrastructure Engineering*, n/a(n/a).

Basha, S. H. and Kaushik, H. B. (2016). Behavior and failure mechanisms of masonry-infilled rc frames (in low-rise buildings) subject to lateral loading. *Engineering Structures*, 111:233–245.

Beaumont, M. A., Cornuet, J.-M., Marin, J.-M., and Robert, C. P. (2009). Adaptive approximate bayesian computation. *Biometrika*, 96(4):983–990.

Beck, J. L. (2010). Bayesian system identification based on probability logic. *Structural Control and Health Monitoring*, 17(7):825–847.

Ben Abdessalem, A., Dervilis, N., Wagg, D., and Worden, K. (2019). Model selection and parameter estimation of dynamical systems using a novel variant of approximate bayesian computation. *Mechanical Systems and Signal Processing*, 122:364 – 386.

Benavent-Climent, A., Ramírez-Márquez, A., and Pujol, S. (2018). Seismic strengthening of low-rise reinforced concrete frame structures with masonry infill walls: Shaking-table test. *Engineering Structures*, 165:142–151.

Benker, M., Furtner, L., Semm, T., and Zaeh, M. F. (2020). Utilizing uncertainty information in remaining useful life estimation via bayesian neural networks and hamiltonian monte carlo. *Journal of Manufacturing Systems*.

Bennett, R. M., Flanagan, R. D., Adham, S., Fischer, W., and Tenbus, M. (1996). Evaluation and analysis of the performance of masonry infills during the northridge earthquake. Technical report, The National Science Foundation.

Berry, M., Parrish, M., and Eberhard, M. (2004). *PEER Structural Performance Database User' s Manual (Version 1.0)*. Number January in -. PEER.

Betancourt, M. (2017). A conceptual introduction to hamiltonian monte carlo. *arXiv preprint arXiv:1701.02434*.

Betz, W. (2017). *Bayesian inference of engineering models*. PhD thesis, Technische Universitat Munchen.

Bharti, A. and Pedersen, T. (2019). Calibration of Stochastic Channel Models using Approximate Bayesian Computation. In *IEEE GLOBECOM Workshops*.

Bhatt, A. N. and Shrivastava, N. A. (2021). Application of artificial neural network for internal combustion engines: A state of the art review. *Archives of Computational Methods in Engineering*, 29:897 – 919.

Bianconi, F., Tomassoni, L., Antonini, C., and Valigi, P. (2019). A new Bayesian methodology for nonlinear model calibration in Computational Systems Biology. *bioRxiv*.

Blundell, C., Cornebise, J., Kavukcuoglu, K., and Wierstra, D. (2015). Weight uncertainty in neural network. In *International Conference on Machine Learning*, pages 1613–1622. PMLR.

Bose, S., Martin, J., and Stavridis, A. (2019). Simulation framework for infilled RC frames subjected to seismic loads. *Earthquake Spectra*, 35(4):1739–1762.

Brincker, R., Zhang, L., and Andersen, P. (2000). Output-only modal analysis by frequency domain decomposition. In *Proceedings of ISMA25: 2000 International Conference on Noise and Vibration Engineering*, pages 717–723. Katholieke Universiteit, Leuven.

Cai, G. and Su, Q. (2017). Effect of Infills on Seismic Performance of Reinforced Concrete Frame structures—A Full-Scale Experimental Study. *Journal of Earthquake Engineering*, 00(00):1–29.

Calvi, G. M., Bolognini, D., and Penna, A. (2004). Seismic performance of masonry-infilled rc frames: benefits of slight reinforcements. *Invited lecture to "Sísmica*, 6:14–16.

Cavaleri, L., Zizzo, M., and Asteris, P. G. (2020). Residual out-of-plane capacity of infills damaged by in-plane cyclic loads. *Engineering Structures*, 209(December 2018):109957.

Chiachio, M., Beck, J. L., Chiachio, J., and Rus, G. (2014). Approximate Bayesian computation by subset simulation. *SIAM Journal on Scientific Computing*, 36(3):A1339–A1358.

Christopher, J. D., Wimer, N. T., Lapointe, C., Hayden, T. R. S., Grooms, I., Rieker, G. B., and Hamlington, P. E. (2018). Parameter estimation for complex thermal-fluid flows using approximate Bayesian computation. *Physical Review Fluids*, 3(10):104602.

Coleman, J. and Spacone, E. (2001). Localization issues in force-based frame elements. *Journal of Structural Engineering*, 127(November):1257–1265.

Da Costa, J. M. J., Orlande, H. R. B., and da Silva, W. B. (2018). Model selection and parameter estimation in tumor growth models using approximate Bayesian computation-ABC. *Computational and Applied Mathematics*, 37(3):2795–2815.

De, S., Brewick, P. T., Johnson, E. A., and Wojtkiewicz, S. F. (2019). A hybrid probabilistic framework for model validation with application to structural dynamics modeling. *Mechanical Systems and Signal Processing*, 121:961–980.

De Risi, M. T., Di Domenico, M., Ricci, P., Verderame, G. M., and Manfredi, G. (2019). Experimental investigation on the influence of the aspect ratio on the in-plane/out-of-plane interaction for masonry infills in rc frames. *Engineering Structures*, 189:523–540.

Decanini, L. and Fantin, G. (1986). Modelos simplificados de la mampostería incluida en porticos. *Jornadas Argentinas de Ingeniería Estructural*, 2:817–836.

Del Moral, P., Doucet, A., and Jasra, A. (2012). An adaptive sequential Monte Carlo method for approximate Bayesian computation. *Statistics and computing*, 22(5):1009–1020.

Dhakal, R. and Maekawa, K. (2002). Modeling of post-yield buckling of reinforcement. *ASCE Journal of Structural Engineering*.

Dutta, R., Brotzakis, Z. F., and Mira, A. (2018). Bayesian calibration of force-fields from experimental data: TIP4P water. *Journal of Chemical Physics*, 149(15):1–26.

Fernández, J., Chiachío, M., Chiachío, J., Muñoz, R., and Herrera, F. (2022). Uncertainty quantification in neural networks by approximate bayesian computation: Application to fatigue in composite materials. *Engineering Applications of Artificial Intelligence*, 107:104511.

Fernández, J., Chiachío, J., Chiachío, M., Barros, J., and Corbetta, M. (2023). Physics-guided bayesian neural networks by abc-ss: Application to reinforced concrete columns. *Engineering Applications of Artificial Intelligence*, 119:105790.

Ferretti, F., Ferracuti, B., Mazzotti, C., and Savoia, M. (2019). Destructive and minor destructive tests on masonry buildings: Experimental results and comparison between shear failure criteria. *Construction and Building Materials*, 199:12–29.

Fierro, E. A., Miranda, E., and Perry, C. L. (2011). *Behavior of Nonstructural Components in Recent Earthquakes*, chapter , pages 369–377. ASCE.

Flanagan, R. D. and Bennett, R. M. (1999). In-plane behavior of structural clay tile infilled frames. *Journal of structural engineering*, 125(6):590–599.

Furtado, A., Rodrigues, H., Arêde, A., and Varum, H. (2018). Double-leaf infill masonry walls cyclic in-plane behaviour: experimental and numerical investigation. *The Open Construction & Building Technology Journal*, 12(1).

Gazić, G. and Sigmund, V. (2016). Cyclic testing of single-span weak frames with masonry infill. *Gradevinar*, 68(08):617–633.

Ghahramani, Z. (2015). Probabilistic machine learning and artificial intelligence. *Nature*, 521(7553):452–459.

Ghosh, A. (2011). *Scaling Laws*, pages 61–94. Springer New York, New York, NY.

Gilks, W., Richardson, S., and Spiegelhalter, D. (1996). *Markov chain Monte Carlo in practice*. Chapman and Hall/CRC, Boca Raton.

Gill, W. (1979). *Ductility of rectangular Reinforced Concrete Columns with axial load*. PhD thesis, University of Canterbury.

Goodfellow, I., Bengio, Y., and Courville, A. (2016). *Deep Learning*. MIT Press. `http://www.deeplearningbook.org`.

Guerrero, N., Martinez, M., Picón, R., Marante, M. E., Hild, F., Roux, S., and Flórez-López, J. (2014). Experimental analysis of masonry infilled frames using digital image correlation. *Materials and structures*, 47(5):873–884.

Haider, S. (1995). *In-plane cyclic response of reinforced concrete frames with unreinforced masonry infills*. PhD thesis, Rice University.

Hak, S., Morandi, P., and Magenes, G. (2018). Prediction of inter-storey drifts for regular RC structures with masonry infills based on bare frame modelling. *Bulletin of Earthquake Engineering*, 16(1):397–425.

Harris, J. R., Heintz, J. A., Manager, P., Hooper, J., Porush, A. R., Cranford, S., Haas, K., and Haselton, C. (2009). *Quantification of Building Seismic Performance Factors*. Number June in -. Federal Emergency Management Agency.

Haselton, C. B., Liel, A. B., Lange, S. T., and Deierlein, G. (2008). Beam-Column Element Model Calibrated for Predicting Flexural Response Leading to Global Collapse of RC Frame Buildings. *PEER Report 2007*.

Holmes, M. (1961). Steel frames with brickwork and concrete infilling. *proceedings of the Institution of civil Engineers*, 19(4):473–478.

Huang, H., Burton, H. V., and Sattar, S. (2020). Development and Utilization of a Database of Infilled Frame Experiments for Numerical Modeling. *Journal of Structural Engineering (United States)*, 146(6).

Irfanoglu, A. (2009). Performance of Template School Buildings during Earthquakes in Turkey and Peru. *Journal of Performance of Constructed Facilities*, 23(February):5–14.

Israel, G. D. (1992). Determining sample size. *Fact Sheet*.

Jiang, H., Liu, X., and Mao, J. (2015a). Full-scale experimental study on masonry infilled rc moment-resisting frames under cyclic loads. *Engineering Structures*, 91:70–84.

Jiang, H., Liu, X., and Mao, J. (2015b). Full-scale experimental study on masonry infilled RC moment-resisting frames under cyclic loads. *Engineering Structures*, 91:70–84.

Kalman Šipoš, T., Sigmund, V., and Hadzima-Nyarko, M. (2013). Earthquake performance of infilled frames using neural networks and experimental database. *Engineering Structures*, 51:113–127.

Kam, W. Y., Pampanin, S., Dhakal, R., Gavin, H. P., and Roeder, C. (2010). Seismic performance of reinforced concrete buildings in the september 2010 darfield (canterbury) earthquake. *Bulletin of the New Zealand Society for Earthquake Engineering*, 43(4):340–350.

Karabatsos, G., Leisen, F., et al. (2018). An approximate likelihood perspective on abc methods. *Statistics Surveys*, 12:66–104.

Karthik, M. M. and Mander, J. B. (2011). Stress-block parameters for unconfined and confined concrete based on a unified stress-strain model. *Journal of Structural Engineering*, pages 270–273.

Kaushik, H. B., Rai, D. C., and Jain, S. K. (2006). Code approaches to seismic design of masonry-infilled reinforced concrete frames: A state-of-the-art review. *Earthquake Spectra*, 22(4):961–983.

Kavetski, D., Fenicia, F., Reichert, P., and Albert, C. (2018). Signature-Domain Calibration of Hydrological Models Using Approximate Bayesian Computation: Theory and Comparison to Existing Applications. *Water Resources Research*, 54(6):4059–4083.

Kulakova, L. (2017). *Bayesian Uncertainty Quantification for Data-Driven Applications in Engineering and Life Sciences*. PhD thesis, ETH Zurich.

Lam, H. F., Yang, J. H., and Au, S. K. (2018). Markov chain Monte Carlo-based Bayesian method for structural model updating and damage detection. *Structural Control and Health Monitoring*, 25(4):1–22.

Landívar, H. (2016). Resultado de la inspección visual realizada durante el breve recorrido por las calles de portoviejo en abril 19-2016. Technical report, ASCE, FVL and UCSG.

Lasdon, L. S., Fox, R. L., and Ratner, M. W. (1974). Nonlinear optimization using the generalized reduced gradient method. *RAIRO - Operations Research - Recherche Opérationnelle*, 8(V3):73–103.

Liberatore, L., Noto, F., Mollaioli, F., and Franchin, P. (2018). In-plane response of masonry infill walls: Comprehensive experimentally-based equivalent strut model for deterministic and probabilistic analysis. *Engineering Structures*, 167:533–548.

Maidiawati and Sanada, Y. (2017). R/C frame-infill interaction model and its application to Indonesian buildings. *Earthquake Engineering & Structural Dynamics*, 46(2):221–241.

Mander, J. B., Priestley, N., and Park, R. (1988). Theoretical stress-strain model for confined concrete. *Journal of structural engineering*.

Mansouri, A., Marefat, M. S., and Khanmohammadi, M. (2014). Experimental evaluation of seismic performance of low-shear strength masonry infills with openings in reinforced concrete frames with deficient seismic details. *The Structural Design of Tall and Special Buildings*, 23(15):1190–1210.

Marjoram, P., Molitor, J., Plagnol, V., and Tavare, S. (2003). Markov chain monte carlo without likelihoods. *Proceedings of the National Academy of Sciences*, 100(26):15324–15328.

Markulak, D., Radić, I., and Sigmund, V. (2013). Cyclic testing of single bay steel frames with various types of masonry infill. *Engineering structures*, 51:267–277.

Mazzotti, C., Sassoni, E., and Pagliai, G. (2014). Determination of shear strength of historic masonries by moderately destructive testing of masonry cores. *Construction and Building Materials*, 54:421–431.

McKinley, Trevelyan J. and Vernon, Ian and Andrianakis, Ioannis and McCreesh, Nicky and Oakley, Jeremy E. and Nsubuga, Rebecca N. and Goldstein, Michael and White, Richard G. (2018). Approximate bayesian computation and simulation-based inference for complex stochastic epidemic models. *Statistical Science*, 33(1):4–18.

Mehrabi, A. B., Benson Shing, P., Schuller, M. P., and Noland, J. L. (1996). Experimental evaluation of masonry-infilled rc frames. *Journal of Structural engineering*, 122(3):228–237.

Mengersen, K. L., Pudlo, P., and Robert, C. P. (2013). Bayesian computation via empirical likelihood. *Proceedings of the National Academy of Sciences*, 110(4):1321–1326.

Miran Sensor (2016). *Linear Position Sensor*. Miran.

Misir, I. S., Ozcelik, O., Girgin, S. C., and Yucel, U. (2016). The Behavior of Infill Walls in RC Frames Under Combined Bidirectional Loading. *Journal of Earthquake Engineering*, 20(4):559–586.

Mohamed, H. and Romão, X. (2018). Robust Calibration of Macro-Models for the In-Plane Behavior of Masonry Infilled RC Frames. *Journal of Earthquake Engineering*, 00(00):1–27.

Mohammad Noh, N., Liberatore, L., Mollaioli, F., and Tesfamariam, S. (2017). Modelling of masonry infilled RC frames subjected to cyclic loads: State of the art review and modelling with OpenSees. *Engineering Structures*, 150:599–621.

Morandi, P., Hak, S., and Magenes, G. (2018a). Mechanical characterization and force-displacement hysteretic curves from in-plane cyclic tests on strong masonry infills. *Data in Brief*, 16:886 – 904.

Morandi, P., Hak, S., and Magenes, G. (2018b). Performance-based interpretation of in-plane cyclic tests on RC frames with strong masonry infills. *Engineering Structures*, 156:503–521.

Neal, P. (2012). Efficient likelihood-free bayesian computation for household epidemics. *Statistics and Computing*, 22(6):1239–1256.

Neal, R. (1996). *Bayesian Learning for Neural Networks*. Lecture Notes in Statistics. Springer New York.

Neal, R. M. (1993). Probabilistic inference using markov chain monte carlo methods. Technical Report CRG-TR-93-1, Department of computer science. University of Toronto.

Neutelings, I. (2022). Neural networks.

Nishina, K., Hashimoto, S., Imamura, N., Ohashi, S., Komatsu, M., Kaneko, S., and Hayashi, S. (2018). Calibration of forest 137 Cs cycling model "FoRothCs" via approximate Bayesian computation based on 6-year observations from plantation forests in Fukushima. *Journal of Environmental Radioactivity*, 193-194:82–90.

O'Reilly, G. J., Perrone, D., Fox, M., Monteiro, R., and Filiatrault, A. (2018). Seismic assessment and loss estimation of existing school buildings in Italy. *Engineering Structures*, 168(April):142–162.

Palieraki, V., Zeris, C., Vintzileou, E., and Adami, C. E. (2018). In-plane and out-of plane response of currently constructed masonry infills. *Engineering Structures*, 177(December 2017):103–116.

Panagiotakos, T. B. and Fardis, M. N. (2001). Deformations of reinforced concrete members at yielding and ultimate. *Structural Journal*, 98(2):135–148.

Papaioannou, I., Betz, W., Zwirglmaier, K., and Straub, D. (2015). MCMC algorithms for Subset Simulation. *Probabilistic Engineering Mechanics*, 41(July):89–103.

Park, M., Jitkrittum, W., and Sejdinovic, D. (2016). K2-abc: Approximate bayesian computation with kernel embeddings. In *Artificial Intelligence and Statistics*, pages 398–407. PMLR.

Park, Y.-J. and Ang, A. H.-S. (1985). Mechanistic seismic damage model for reinforced concrete. *Journal of structural engineering*, 111(4):722–739.

Park, Y.-J., Ang, A. H.-S., and Wen, Y. K. (1985). Seismic damage analysis of reinforced concrete buildings. *Journal of Structural Engineering*, 111(4):740–757.

Perrone, D., Calvi, P. M., Nascimbene, R., Fischer, E. C., and Magliulo, G. (2018). Seismic performance of non-structural elements during the 2016 Central Italy earthquake. *Bulletin of Earthquake Engineering*.

Pirsaheb, H., Javad Moradi, M., and Milani, G. (2020). A Multi-Pier MP method for the non-linear static analysis of out-of-plane loaded masonry walls. *Engineering Structures*, 223(November 2019):111040.

Prangle, D. (2016). Lazy abc. *Statistics and Computing*, 26(1-2):171–185.

Pratap, P. and Pujol, S. (2021). Dynamic tests of an idealized long-period structure. *DEEDS*.

Reynders, E. (2012). System Identification Methods for (Operational) Modal Analysis: Review and Comparison. *Archives of Computational Methods in Engineering*, 19(1):51–124.

Rutter, C. M., Ozik, J., DeYoreo, M., and Collier, N. (2019). Microsimulation model calibration using incremental mixture approximate bayesian computation. *Annals of Applied Statistics*, 13(4):2189–2212.

Sala, M. and Soriguera, F. (2020). Lane-changing and freeway capacity: A bayesian inference stochastic model. *Computer-Aided Civil and Infrastructure Engineering*, 35(7):719–733.

Sattar, S. and Liel, A. B. (2016a). Seismic performance of nonductile reinforced concrete frames with masonry infill walls - I: Development of a strut model enhanced by finite element models. *Earthquake Spectra*, 32(2):795–818.

Sattar, S. and Liel, A. B. (2016b). Seismic performance of nonductile reinforced concrete frames with masonry infill walls - II: Collapse assessment. *Earthquake Spectra*, 32(2):819–842.

Schneider, S. P., Zagers, B. R., and Abrams, D. P. (1998). Lateral strength of steel frames with masonry infills having large openings. *Journal of Structural Engineering*, 124(8):896–904.

Sigmund, V. and Penava, D. (2014). Influence of openings, with and without confinement, on cyclic response of infilled rc frames—an experimental study. *Journal of earthquake engineering*, 18(1):113–146.

Singaucho, J., Laurendeau, A., Viracucha, C., and Ruiz, M. (2016). Observaciones del sismo del 16 de abril de 2016 de magnitud Mw 7.8, intensidades y aceleraciones. *Revista Politécnica*, 38(1):–.

Sisson, S. A., Fan, Y., and Beaumont, M. (2018). *Handbook of approximate Bayesian computation*. CRC Press.

Sisson, S. A., Fan, Y., and Tanaka, M. M. (2007). Sequential monte carlo without likelihoods. *Proceedings of the National Academy of Sciences*, 104(6):1760–1765.

Song, M., Behmanesh, I., Moaveni, B., and Papadimitriou, C. (2019). Modeling error estimation and response prediction of a 10-story building model through a hierarchical bayesian model updating framework. *Frontiers in Built Environment*, 5(January):1–15.

Stafford Smith, B. and Carter, C. (1969). A method of analysis for infilled frames. *Proceedings of the institution of civil engineers*, 44(1):31–48.

Tarque, N., Candido, L., Camata, G., and Spacone, E. (2015). Masonry infilled frame structures: state-of-the-art review of numerical modelling. *Earthquakes and Structures*, 8(3):733–759.

Tasnimi, A. A. and Mohebkhah, A. (2011). Investigation on the behavior of brick-infilled steel frames with openings, experimental and analytical approaches. *Engineering Structures*, 33(3):968–980.

Tiboaca, O.-D. (2016). *On the Application of the Reversible Jump Markov Chain Monte Carlo Method within Structural Dynamics by Oana-Daniela Tiboaca*. PhD thesis, University of Sheffield.

TMS 402/602 (2016). *TMS 402/602 Building Code Requirements and Specifications for Masonry Structures, 2016 (Formerly ACI 530)*. The Masonry Society.

Toni, T., Welch, D., Strelkowa, N., Ipsen, A., and Stumpf, M. P. (2009). Approximate bayesian computation scheme for parameter inference and model selection in dynamical systems. *Journal of The Royal Society Interface*, 6(31):187–202.

Urich, A. J. and Beauperthuy, J. L. (2012). Protagonism of the Infill Walls on Seismic Performance of Venezuela Buildings. *15th World Conference on Earthquake Engineering (15WCEE)*.

Varum, H., Furtado, A., Rodrigues, H., Dias-Oliveira, J., Vila-Pouca, N., and Arêde, A. (2017). Seismic performance of the infill masonry walls and ambient vibration tests after the Ghorka 2015, Nepal earthquake. *Bulletin of Earthquake Engineering*, 15(3):1185–1212.

Villalobos, E., Sim, C., Smith-Pardo, J. P., Rojas, P., Pujol, S., and Kreger, M. E. (2018). The 16 April 2016 Ecuador earthquake damage assessment survey. *Earthquake Spectra*, 34(3):1201–1217.

Zhao, J. and Sritharan, S. (2007). Modeling of strain penetration effects in fiber-based analysis of reinforced concrete structures. *ACI structural journal*, 104(2):133.

Zhu, M., McKenna, F., and Scott, M. H. (2018). Openseespy: Python library for the opensees finite element framework. *SoftwareX*, 7:6–11.

Zhu, W., Marin, J. M., and Leisen, F. (2016). A bootstrap likelihood approach to bayesian computation. *Australian & New Zealand Journal of Statistics*, 58(2):227–244.

Zovkic, J., Sigmund, V., and Guljas, I. (2013). Cyclic testing of a single bay reinforced concrete frames with various types of masonry infill. *Earthquake Engineering & Structural Dynamics*, 42(8):1131–1149.